UNIVERSITY OF LONDON THESIS

Degree PhD Year 2006 Name of Author ATTI, Olukemi Francis

Modelling Outflow and Low Temperature Induced Crack Propagation in Pressurised Pipelines

A thesis submitted to the University of London for the degree of Doctor of Philosophy

By

OLUFEMI FRANCIS ATTI

Department of Chemical Engineering
University College London
Torrington Place
London WC1E 7JE

April 2006

ProQuest LLC
789 East Eisenhower Parkway
P.O. Box 1346
Ann Arbor, MI 48106-1346

ABSTRACT

This thesis describes the development and refinement of a rigorous mathematical model for simulating outflow following the failure of pressurised single pipelines and pipeline networks containing multi-component hydrocarbon mixtures. The same model is then extended to simulate the progression of a defect in the pipeline into a running fracture.

The outflow model is based on homogeneous equilibrium assumption with the conservation equations resolved using the Method of Characteristics (MOC). The model addresses some of the shortcomings associated with the incorrect posing of boundary conditions reported in earlier works. Both types of failures including pipeline puncture as well as full-bore rupture are modelled. Typical pressurised pipeline inventories include permanent gases and liquids, condensable gases, flashing liquids as well as two-phase liquid gas mixtures.

Model validation is performed against the Isle of Grain field data as well as those logged during the Piper Alpha tragedy. In cases where real data are not available, a mass conservation index is determined to assess the accuracy of the numerical simulation. In most cases, good agreement between the simulated and field data along with reasonable mass conservation indices (close to unity) are observed.

A significant aspect of the work involves the development of methodologies for reducing the computation run time. This has involved the use of various numerical grid discretisation schemes such as simple and nested grids as well as the development of a quadratic interpolation scheme. Investigations using different types of pipeline inventories show that the nested grid system is primarily effective in reducing the computation run time when used in conjunction with long pipelines (*ca.*>10 km) containing gases. For other cases, the use of the simple grid system is recommended.

The interpolation scheme involves the construction of a database encompassing a pre-defined fluid pressure/enthalpy range. This method is found to be universally effective

in reducing the computational run time by as much as 80 % for all types of inventories without a loss in accuracy. This computational run time saving is made in comparison to when actual flash calculations are made.

The crack propagation model invokes fracture mechanics principles and accounts for the important processes taking place during depressurisation including the thermal, and pressure stresses in the pipe wall to simulate the progression of a simple defect into a running fracture.

The application of the model to an isolated exposed pipeline, where the released inventory freely moves away from the discharge plane shows rapid localised cooling of the pipe wall to temperatures well below its ductile to brittle transition temperature. The resulting drop in the fracture toughness coupled with the pressure stresses at the defect plane suggests that catastrophic pipeline failure through a running fracture can arise. In the case of buried pipelines, such effects are found to be even more pronounced due to the additional thermal stresses in the pipe wall. The latter is brought about as a result of the cooling the pipe wall by the confined escaping gas.

The above study for the first time quantitatively highlights the importance of taking into account the expansion induced cooling effects as a credible failure scenario when undertaking safety assessment of pressurised pipelines.

DEDICATION

To the one who created me... that I may show forth His glory.

To the one who died... that I may live.

To the one who lights my path...that I may stumble not.

To God the Father, the Son, and the Holy Spirit.

ACKNOWLEDGEMENTS

I wish to thank the following people and organisations who have contributed so much in many ways to facilitate the completion of this thesis.

To God Almighty, the giver of life and the source of all wisdom. Thank you for everything.

To my very dear parents for all your sacrifice, prayers, and guidance.

My supervisor, Prof. Haroun Mahgerefteh for the opportunity given me to study in this field, your excellent supervision, and for ensuring my well-being.

To the EPSRC and the graduate school for the financial assistance. Thank you very much. I couldn't have done it without you.

Special thanks to Dr Adeyemi Oke for establishing my feet during the early days and for all the interesting discussions we had. I'm truly grateful.

Professors Yuri Rykov and Lokesh Dharani.

My colleagues, both past and present with whom we shared the same office. It was a pleasure meeting you all.

The technical and admin. staff of the department of Chemical engineering, UCL.

Maggie Baldry, for the proofreading the various versions of this thesis.

To my darling wife Bimbola...for your undying love, support and steadfastness. Words cannot fully express my gratitude.

Finally, to my little Miss, the jewel in my crown, my beautiful daughter Ayomide..for the incessant joy you've brought into my life. You're simply the best.

LIST OF CONTENTS

CHAPTER 1

INTRODUCTION

The increase in demand for fossil fuels and their derivatives as a source of energy and raw materials has led to more pipelines systems being laid in order to facilitate their transportation.

Pipelines are considered an efficient and relatively safe method for transporting hydrocarbons. However, the combination of high pressures, significant amounts of inventory and high flammability pose significant risk to the public and the environment if a line break occurs.

Pipeline accidents are more common than conventionally thought. According to data published by the US Department of Transport (1982-1997), even short, simple pipelines will have a reportable accident during a 20-year lifetime. Operators of long pipelines (1,000 km or over) can expect failures at a frequency of at least one per year. The Office of Pipeline Safety in the United States reported (Vahedi, 2003) that during 1986 and 2000, there were 3,116 natural gas pipeline incidents. These resulted in 309 fatalities, 1,398 injuries and 478 million dollars of damage to property.

Studies (Montiel et al., 1996) have indicated that the most common causes of pipeline damage include mechanical failure (e.g. from corrosion), impact failure (e.g. from excavating machinery and heavy objects), human error and external events (e.g. sabotage and subsidence). Such failures may be in the form of full-bore rupture, simple puncture or longitudinal tear. Of these, though the least likely, full-bore rupture (FBR) - in which the pipeline is split into two across its circumference is by far the most catastrophic due to the ensuing massive release rate.

One of the most catastrophic consequences of a pipeline rupture is the ignition of the released inventory aptly exemplified by the Piper Alpha tragedy (Cullen, 1990), which resulted in the loss of 167 lives. The impact of pipeline failure on the environment can also be equally devastating. It is reported that on average, over 6.3

million gallons of oil and other hazardous liquids are released from pipelines each year (Environmental Defence, 1999). Other cases in which pipeline failures have led to numerous fatalities and damage to infrastructure and environment have also been reported (see for example Bond (2002)). Consequently, record fines exceeding hundreds of millions of dollars are now being imposed on pipeline operators causing damage to the environment (Fletcher, 2001a; True, 2001).

In 1996, the Pipeline and Safety Regulation (HMSO, 1996) was introduced in the UK as a single set of goal setting, risk-based regulations enveloping the health and safety aspects of both the onshore and offshore pipelines. Notably, pipeline operators must be able to demonstrate through the safety case that all hazards arising from pipeline rupture are addressed and satisfactorily accommodated.

Central to this type of analysis is the evaluation of the release rate and its variation with time as the result of a pipeline failure. Such data has an important bearing on the design and operation of the pipeline, and assists the pipeline operator or local authority in preparing emergency plans in the event of an accident.

Apart from modelling outflow, the simulation of the fluid properties such as temperature and pressure along the pipeline are also important. For example, low fluid temperatures as a result of rapid depressurisation following full bore rupture can lead to hydrate or wax formation, which may in turn block fluid flow. Knowledge of the fluid pressure profile within the pipeline on the other hand can provide accurate predictions of the activation times for pressure actuated emergency shut down valves placed at various distances along the pipeline.

The modelling of the release process following pipeline rupture is complex due to the highly transient nature of the discharge process as well as the large number of interacting parameters involved. This can be further complicated when choking and two-phase flows are involved.

Many models have been reported in the literature for predicting the fluid dynamics following pipeline failure, each having its own strengths and weaknesses. The discrepancies between the results are due to the assumptions made in developing the

partial differential equations of flow, subsequent simplifications, the thermodynamic model used, the hydrodynamics correlation, and the numerical method employed in solving the partial differential equations (Kimambo and Thorley, 1995). Of these only few (e.g. Oke et al., 2003) are in principle capable of modelling non-axisymmetric release following pipeline puncture. A number of simple models that attempt to simulate this type of failure treat the pipeline as a vessel discharging through an orifice, thereby ignoring the effects of the ensuing pressure and fluid flow transients within the pipeline (see for example Woodward and Mudan, 1991). These simplistic models are also incapable of simulating un-isolated release failure where pumping of the pressurised inventory continues despite puncture.

More thermodynamically and mechanically rigorous models have focused on full-bore rupture and/or puncture at one end of single pipelines (Chen, 1993; Chen et al., 1995a,b; Mahgerefteh et al., 1997, 1999). The fact that in reality, fluids are conveyed in a network of pipelines rather than in a single pipeline limits the applicability of these single pipeline models.

In addition, when simulating the complete blowdown of long pipelines (ca. $\geq$ 10 km), the computational expense involved in employing the rigorous models may become prohibitive, requiring the use of expensive computational resources (Chen, 1993; Saha, 1997).

Finally, most of the models described above employ simple heat transfer models, which fail to adequately account for the transient heat transfer process occurring across the pipeline wall. Consequently, limited qualitative and quantitative judgement on the effect of depressurisation and the attendant cooling on the thermo-physical properties of the pipeline wall and flowing fluid can be made.

During the past decade, researchers at University College London (see for example Mahgerefteh et al., 1997,1999; Oke et al., 2003,Oke ,2004) have developed a numerical simulation tool for simulating the fluid dynamics following the rupture of pressurised pipelines, including networks. The model accounts for the important processes taking place during depressurisation, including real fluid behaviour,

frictional effects, radial and axial flow in the proximity of puncture as well as the accompanying rapid pressure and thermal transients. Significant reduction in computational run times have been achieved through the development of fast numerical solution techniques. The comparative results between model and real data show very good agreement. This model was later translated into a robust computer programme, PipeTech.

The present study deals with the further development and the refinement of the above outflow model in terms of increasing the range of application, accuracy, as well as further reduction in the computational run time. This is then followed by the extension of the model for simulating low temperature induced failure in pressurised pipelines.

This thesis is divided into 7 chapters.

Chapter 2 is a review of the mathematical models available in the open literature for simulating pipeline failure. This includes the evaluation of their strengths and weaknesses in terms of robustness, computational efficiency and accuracy.

In chapter 3, the theoretical basis for the pipeline outflow model presented in this thesis together with its assumptions and justifications are presented. The chapter begins with the derivation of the basic equations governing flow followed by a review of the methods for the resolution of the conservative equations, including the method of characteristics (MOC) adopted in this study. The energy balance model employed for estimating transient heat transfer across the pipeline wall and the isothermal steady state flow model are presented.

Chapter 4 deals with the application of the MOC to develop an updated model based, on the work of Oke (2004), capable of simulating full-bore rupture or puncture in pipeline networks for both isolated and un-isolated flows. The appropriate boundary conditions for puncture, full-bore rupture, connectors or junctions between pipes are presented. In addition, an interpolation technique for reducing the computational expense without sacrificing accuracy is developed.

In chapter 5, the pipeline rupture model performance is validated by comparing the output data with field measurements. The numerical interpolation technique presented in chapter 4 for reducing the computational run time is evaluated by comparing its output data and computational run time against the standard model. Furthermore, the applicability of the nested grid scheme (Mahgerefteh et al., 1999) in reducing computational run time is fully investigated.

Other failure scenarios including comparison of outflow behaviour following rupture in straight pipelines as compared to rupture in pipeline networks are presented and discussed. For cases where experimental data are not available a mass conservation index is used to obtain a measure of accuracy of simulated results.

Chapter 6 deals with the development of a depressurisation induced crack propagation model. This work is initiated in the first instance because of the observed significant reduction in the fluid temperature and hence the surrounding pipe-wall following puncture. This model accounts for the accompanying thermal and pressure stresses as well as the reduction in the fracture toughness to simulate the conditions for the transition of an initial through-wall defect into a propagating fracture. The model is applied under the two conditions of exposed (isolated and un-isolated flows) and buried pipelines in order to highlight any differences in the pipelines susceptibility to depressurisation induced crack propagation.

Chapter 7 deals with general conclusions and suggestions for future work.

CHAPTER 2

PIPELINE FAILURE OUTFLOW MODELLING LITERATURE REVIEW

2.1 Introduction

The literature relating to modelling outflow following pipeline failure is extensive spanning over a number of decades. Historically, the modelling of accidents involving pipelines has its origins in the nuclear industry, which is primarily concerned with the evaluation of loss of coolant accidents (LOCAs) in Pressurised Water Reactors (PWRs).

In recent years however, there have been numerous pipeline rupture accidents in the oil and gas industry. Consequently, there have been subsequent stricter safety design regulations and heavy financial penalties. With easy access to relatively fast and inexpensive computational resources, strong interest has been stimulated in this topic.

This chapter presents a review of the pertinent models for simulating the transient fluid dynamics following the failure of pressurised pipelines. These are reviewed based on formulation of the governing equations for transient flow, the mathematical methods employed to solve such equations, thermodynamics, and where appropriate, comparison of the model results with experimental data.

Six models that have found widespread use in industry and academia for simulating outflow following pipeline failure are reviewed in detail. For completeness, the review also briefly covers other simplistic models published in the open literature in view of their potential advantages in terms of low computational run time.

In chronological order, the models reviewed are:

1. APIGEC Models [(TRANSFLOW and Exponential equation), APIGEC (1978,1979)]

2. British Gas Model [DECAY; Jones and Gough (1981)]
3. OLGA [Bendiksen et al. (1986,1991)]
4. PLAC [Philbin and Govan (1990); Philbin (1991); Hall et al. (1993)]
5. Imperial College London Models [BLOWDOWN (Haque et al.; Richardson et al., 1991-1996), META-HEM, MSM (Chen et al., 1992-1995)]
6. University College London Models [Mahgerefteh et al. (1997-2000), Vahedi (2003), Oke et al. (2003)]
7. Other models (1970 - to date)

2.2 APIGEC Models (TRANSFLOW and Exponential Equation)

In 1978, a study was conducted by the Alberta Petroleum Industry, Government Environmental Committee (APIGEC, 1978) to evaluate and improve H_2S isopleth prediction techniques. Three phases involved in gas release including blowdown, atmospheric dispersion and plume rise from a pipeline following failure were considered. The last two phases are not of interest to this study, hence only the blowdown stage is herein discussed. Two blowdown models were employed to create the common blowdown curves, which were later used for dispersion calculations. These models were the TRANSFLOW blowdown model, and a simplified exponential blowdown model.

The TRANSFLOW model, based on mass, momentum, and energy balances employs a numerical simulator to calculate the time curve defining the rate of gas blowdown from the pipeline. The model accounts for valve closure, frictional effects and gas flow rate in the line before rupture. No further information about the model's theoretical basis including the thermodynamics, fluid flow dynamics and how the numerical simulator solves the conservation equations, are supplied. It is therefore difficult to comment on the validity and the range of applicability of the model.

The second APIGEC blowdown model that was employed for calculating the discharge rate was a simplified exponential equation given by:

$$Q = A.e^{(-B.t)} \tag{2.1}$$

Where Q and t are the gas flowrate in m^3/s and time in seconds respectively. A and B are constants depending on pipeline dimension, fluid inventory, initial pressure, and temperature.

The above equation however lacks theoretical basis and does not allow for valve closure, or gas flow or the associated pressure drop within the pipeline.

Figure 2.1 shows the variation of mass flowrate with time obtained by comparing the results of the TRANSFLOW model with field data. The data was obtained during the blowdown of a 168 mm diameter pipeline at an initial pressure of 69 bara. No information regarding the inventory composition or pipeline length was given. From the figure, it may be observed that the model underestimates the blowdown rate, with the total mass released being approximately 12% lower than experimental results.

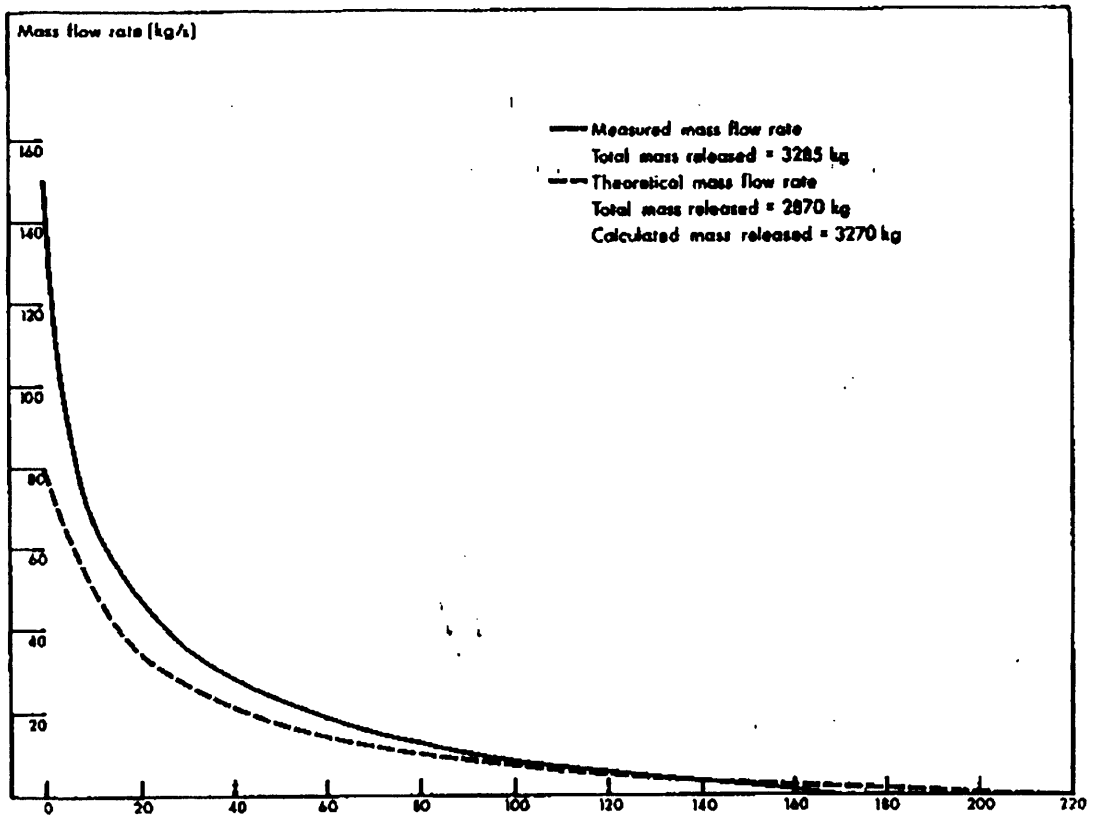

Figure 2.1: Mass flow rate from a 168.3 mm ruptured pipe at an initial pressure of 69 bar and gas temperature 10°C (APIGEC, 1979).

By applying the TRANSFLOW blowdown model to various hypothetical cases, the authors observed that the pipeline length strongly affects the overall shape of the blowdown curve. However, this has no effect on the release rate during the early stages (ca 0 – 10 s) of blowdown. It was also observed that the initial release portion of the curve was strongly influenced by line pressure, however, gas temperature and initial fluid velocity have little effect on the blowdown behaviour.

The authors compared the results generated by the two blowdown models (TRANSFLOW and the exponential equation (2.1)) and concluded that they compared reasonably well considering the simplicity of the exponential model.

The main drawbacks of the APIGEC models are that they have been developed solely for gaseous flows, and hence cannot be applied to a two-phase or liquid discharge. In addition, the exponential model is incapable of simulating the fluid properties such as temperature and pressure both within the pipeline as well as at the rupture plane. Such data are essential for simulating other important consequences of pipeline rupture including brittle fracture, wax or hydrate formation.

2.3 British Gas Model (DECAY)

Jones and Gough (1981) reported on a model named DECAY for analysing high-pressure natural gas decompression behaviour following pipeline rupture. The model is based on isentropic and homogeneous equilibrium fluid flow, and assumes the pipeline to be horizontal. It accounts for wave propagation along the length of the pipeline and uses the Soave-Redlich-Kwong equation of state (SRK EoS) to obtain fluid property data.

In order to validate their model, Jones and Gough (1981) conducted a series of shock tube experiments using different fluid compositions. An instrumented 36.6 m long, 0.1 m diameter tube, was used for this purpose. Depressurisation was initiated by detonating an explosive charge located at the end of the tube resulting in a full-bore rupture.

Based on the variations of pressure with time along the tube length as shown in figures 2.2 and 2.3 respectively, the authors reported good agreement between the simulated results and experimental data.

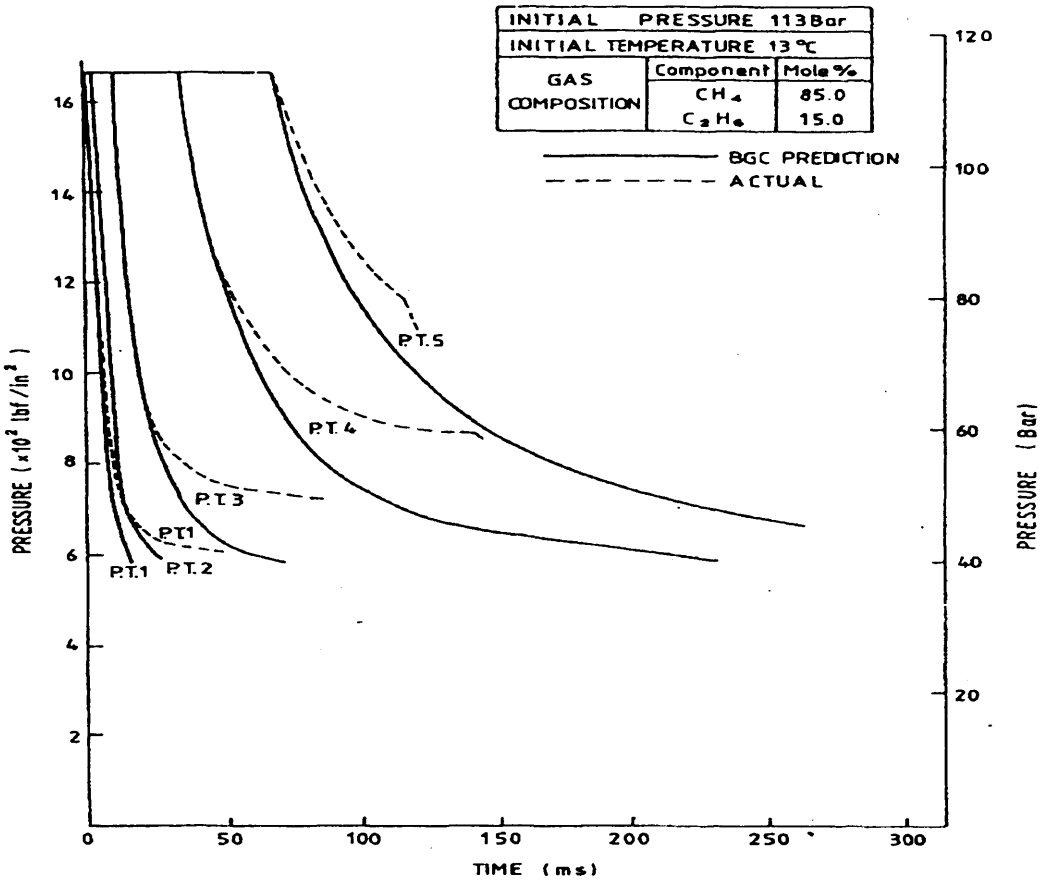

Figure 2.2: Comparison between British Gas model [DECAY] and experimental data (Jones and Gough, 1981).

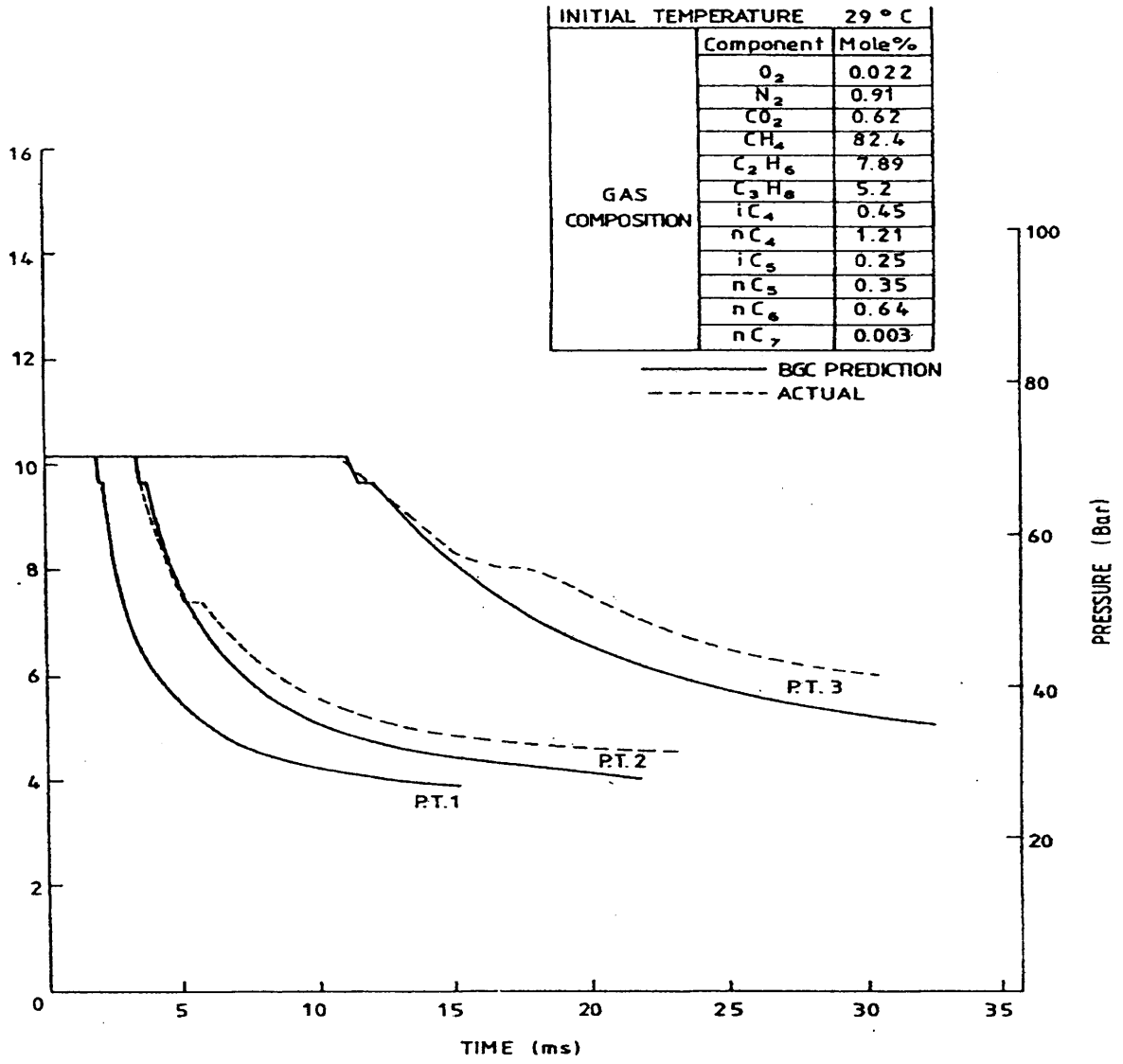

Figure 2.3: Comparison between British Gas model [DECAY] and experimental data (Jones and Gough, 1981).

Although good agreement was obtained with experimental data, the performance of the model is uncertain with respect to the blowdown of long pipelines, including those conveying flashing fluids. More so, neglecting the effects of friction and heat transfer irrespective of the depressurising fluid and pipeline length can result in errors in simulated results (Kimambo and Thorley, 1995).

2.4 OLGA

The development of OLGA for the hydrocarbon industry started as a project for Statoil to simulate slow transients associated with terrain-induced slugging, pipeline start-up and shut-in, and variable production rates.

Although the original OLGA model was capable of successfully simulating the bubble/slug flow regime adequately, it was incapable of simulating stratified/annular flows. Bendiksen et al. (1991), as well as addressing the above limitation by accounting for a drop field moving at approximately the gas velocity, extended OLGA to deal with hydrocarbon mixtures.

In the model, separate conservation equations are applied for gas, liquid bulk and liquid droplets, which may be coupled through interfacial mass transfer. Two momentum equations are used; a combined equation for the gas and possible liquid droplets and a separate one for the liquid film. A mixture energy conservation is used and fluid properties predictions are based on Peng-Robinson (Peng and Robinson, 1976) or Soave-Redlich-Kwong (Soave, 1972) equations of state.

Wall heat transfer is accounted for with the user supplying a heat transfer coefficient, and different frictional factors ascribed to the various flow regimes. An implicit finite difference numerical scheme is used to solve the pertinent conservation equations. However, this gave rise to numerical diffusion of sharp slug fronts and tails thus failing to predict correct slug sizes. This problem was addressed in a later version of OLGA (Nordsveen and Haerdig, 1997) by introducing a Langrangian type front tracking scheme.

Bendiksen et al. (1991) presented some results relating to the validation of OLGA in conjunction with naphtha/nitrogen and with nitrogen /diesel systems in 0.19 m ID pipes with total lengths of 450 m at pressures up to 10 MPa. These showed generally good agreement with laboratory obtained data. However, these tests were confined to steady state conditions comparing pressure drops, liquid hold up and flow-regime transitions. Detailed description of the experimental facilities are described elsewhere (Bendiksen et al., 1986).

Further validation of OLGA under transient conditions was presented in a publication by Shoup et al. (1998). The mixture composition is not given. The results of the simulation are compared against field test data for 'slow' and 'rapid' blowdown of a 5279 m, 0.1 m diameter onshore gas condensate pipeline at 48 bar. The discharge orifices were - 12.7 mm and 25.4 mm for the slow and rapid blowdown tests respectively. Results showing the variations of pressure with time for the 'slow' and 'rapid' blowdown scenarios are shown in figures 2.4 and 2.5. As may be observed from the figures, reasonable agreement is obtained during slow blowdown, however, the model performs relatively poorly when simulating rapid blowdown.

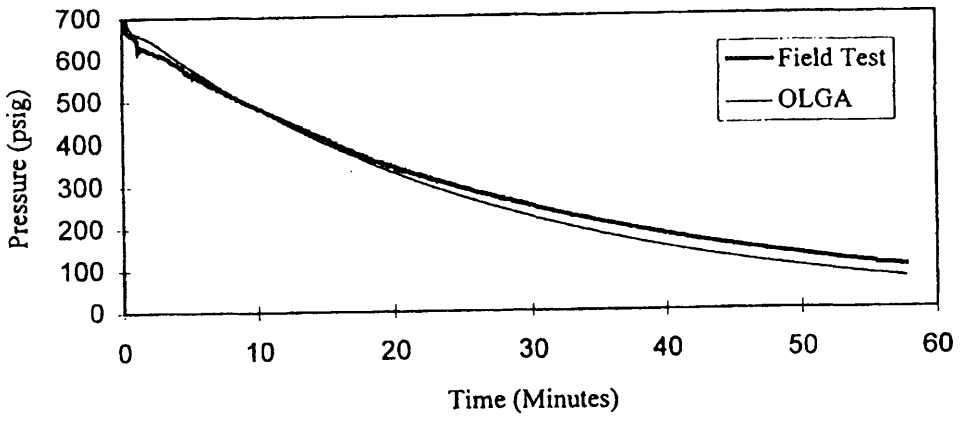

Figure 2.4: Pressure versus time for the rapid blowdown (Pressure at Site 6) OLGA simulations versus Field Test (Shoup et al., 1998).

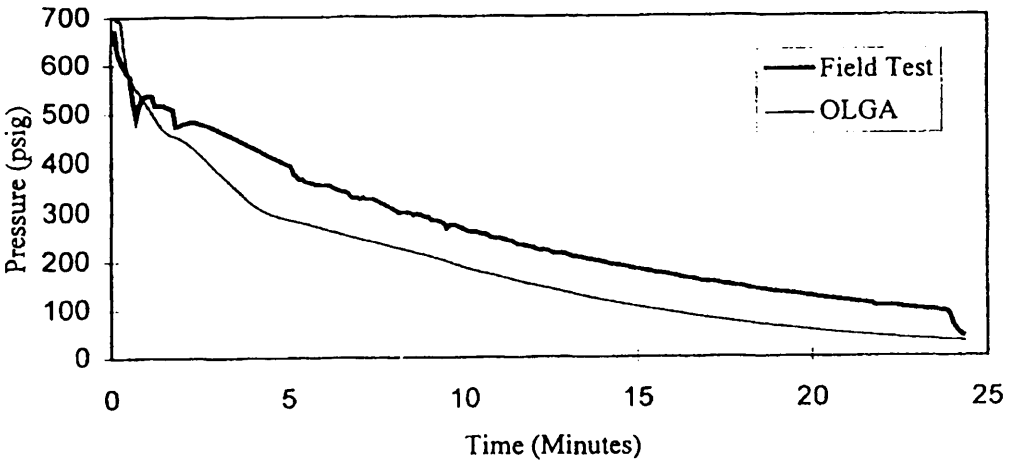

Figure 2.5: Pressure versus time for the rapid blowdown (Pressure at Site 6) OLGA simulations versus Field Test (Shoup et al., 1998).

It is noteworthy that the discharge rate during the FBR of the test pipeline is expected to be much greater than that for the 'rapid' blowdown. This is so because the area available for flow during FBR is 16 times greater than that of the 'rapid blowdown scenario. As such, it would be reasonable to expect an even greater discrepancy when simulating FBR.

No information is available publicly on OLGA's computational run time. However considering the fact that the simulation is numerically based, coupled with use of separate conservation equations for the various fluid phases, its computational run time is expected to be relatively high - particularly when simulating the rupture of long pipelines containing multi-component hydrocarbon mixtures.

2.5 PLAC

PLAC (Pipe Line Analysis Code) has its origins in the TRAC-PFI (Transient Reactor Analysis Code; 1979) code, originally developed for the nuclear industry to simulate rapid transients within the cooling system pipe-work following prescribed failure scenarios (Peterson et al., 1985). PLAC can be regarded as a general transient two-phase model whose original purpose was the modelling of terrain-induced slugging in

transportation pipelines. Furthermore, it is claimed (Hall et al., 1993; Philbin, 1991) that PLAC has the capacity to simulate transients resulting from start-up, shutdown, ruptures and severe slugging. A recent upgrade of PLAC, PROFES Transient (Hyprotech Ltd, 2001) is said to have the additional capability of simulating leaks from pipelines, although no publicly available literature has been discovered on the pertaining theory or validation of PROFES.

PLAC is based on a full three-dimensional two-fluid representation allowing for friction and other dynamic interactions between phases. The formulation employs six conservation equations (two each for mass, momentum and energy) plus an equation of state. These allow the possibility to distinguish between the gas and liquid phase properties, and hence characterisation of their inter-phase thermodynamics. The conservation equations are solved using the semi-implicit finite difference method.

At the rupture plane, PLAC makes use of the homogenous frozen flow model as the critical flow boundary condition. Chen et al. (1995a,b) refers to this assumption as physically unrealistic, and is proposed to contribute significantly to the poor performance of PLAC as a predictive tool for simulating FBR of pipelines.

Furthermore, available literature (Offshore Technology Report, 1998) suggests that PLAC cannot accommodate compositional variation with time along the pipeline. This limitation implies that the code cannot handle ruptures of pipelines whose inventory composition are expected to vary along the pipe. The above limitation poses serious doubt as to PLAC's claimed capability to model non-equilibrium flow interactions in pipelines.

Philbin (1991) presented a comparison of PLAC's predictions with data obtained by Cunliffe (1978) on a production rate change in a Marlin gas condensate trunk line near Melbourne. The line was subjected to an increase in flow-rate from 155-mmscf per day to 258-mmscfd. The details of the composition of the fluid in the line are not given. A comparison between the actual and calculated condensate outflow is given in figure 2.6. As it may be observed from the data, PLAC seriously underestimates the initial surge following the change in the flow-rate. Philbin (1991) attributed this to a correlation (Andritsos, 1986) used for interfacial friction, which over-predicts at high

pressures. PLAC's failure to simulate such fluctuations is surprising - particularly in view of its perceived strength in successfully simulating such terrain induced dynamic behaviour.

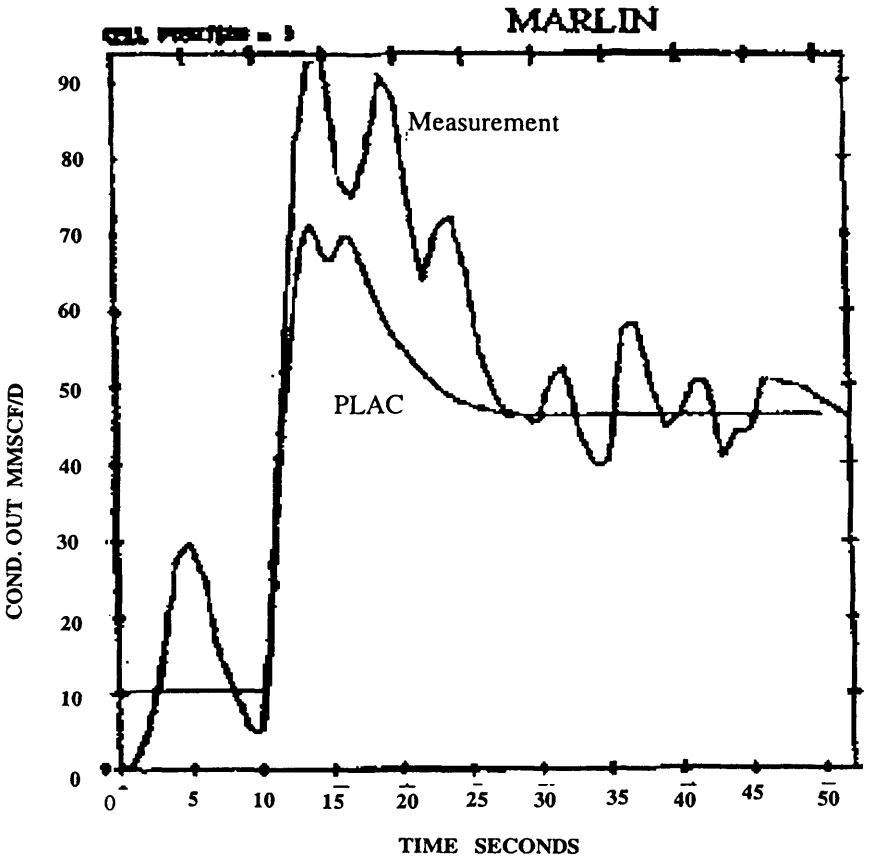

Figure 2.6: Condensate Flow Rate Out versus Time for the Marlin Gas-condensate Trunkline (Philbin, 1991).

Chen et al. (1995b) and Mahgerefteh et al. (1999) also carried out some assessment of PLAC's performance in predicting outflow following pipeline rupture. The results, which in general show poor agreement with field data, are presented later (see section 2.6.3).

The thermodynamic package employed in PLAC seems to be incapable of determining the phase boundaries and fluid states accurately (Chen et al., 1995b). These are considered as the main contributory factors in PLAC's rather poor performance in simulating real data during FBR.

The fully optimised code, run on a SUN Sparc2 workstation has a typical run time of 0.25 s per time step using 100 cells. Philbin (1991) claims 1 to 5 hours for a blowdown simulation. However, no mention of either the length, or the pressure of the pipeline is made. Considering the fact that PLAC utilises separate conservation equations for liquid and vapour phases as well as the additional complexities introduced due to its adoption of a non- equilibrium model, the computational run time for PLAC is expected to be exceptionally long.

2.6 Imperial College London Models

2.6.1 BLOWDOWN

Haque et al., (Haque et al., 1992a,b) at Imperial College London developed a computer model, BLOWDOWN for simulating the quasi-adiabatic expansion process following the blowdown of pressure vessels. The phase equilibrium relations and thermophysical properties of the fluids are provided by an in-house computer programme PREPROP. It incorporates a corresponding states principle (CSP) based on an accurate equation of state for methane, coupled with the Peng-Robinson (Peng and Robinson, 1976) equation of state (PR-EoS). PR-EoS is considered to be generally more efficient than CSP, while CSP predicts more accurate properties for 'methane like mixtures' (Saville and Szczepanski, 1982).

BLOWDOWN still remains the most comprehensive model available for depressurisation of vessels, although Mahgerefteh and Wong (1999) recently introduced a modification incorporating various equations of state.

BLOWDOWN accounts for non-equilibrium effects between the constituent phases, heat transfer between each fluid phase and their corresponding sections of vessel wall, inter-phase fluxes due to evaporation and condensation, and the effects of sonic flow

at the orifice. Critical choking is modelled by carrying out an energy balance across the release orifice.

BLOWDOWN has since found wide popularity in industry. It was later extended by Chen et al. (1993) to simulate the blowdown of pipelines by accounting for frictional pressure drop.

The extended 'pipeline version' of BLOWDOWN was validated with a reasonable degree of success by comparison with the data from a series of LPG blowdown tests. This was conducted jointly by BP and Shell Oil on the Isle of Grain (Tam and Cowley, 1988). These tests (FBR and orifice discharge) involved the blowdown of a number of 100 m pipelines with diameters of 0.15 m and 0.5 m. The pipelines were made of carbon steel and instrumented to record the pressure, temperature and fluid inventory. The inventory comprised primarily of LPG (ca. 95-mole % propane and 5-mole % butane) in a pressure range of 8 - 21 bar. The results obtained for one of the experiments (test P42) is presented here for the purpose of this review.

Figures 2.7a-c show the variation of the fluid temperature, pressure and inventory with time. As may be observed, reasonable agreement is obtained between the measured and experimental data although relatively large discrepancies in temperature profiles are observed towards the end of the blowdown. In addition, the predicted inventory remaining in the pipeline is consistently greater than the measured value. This, according to the authors, may be as a result of the quasi-steady and homogeneous flow assumption made in BLOWDOWN.

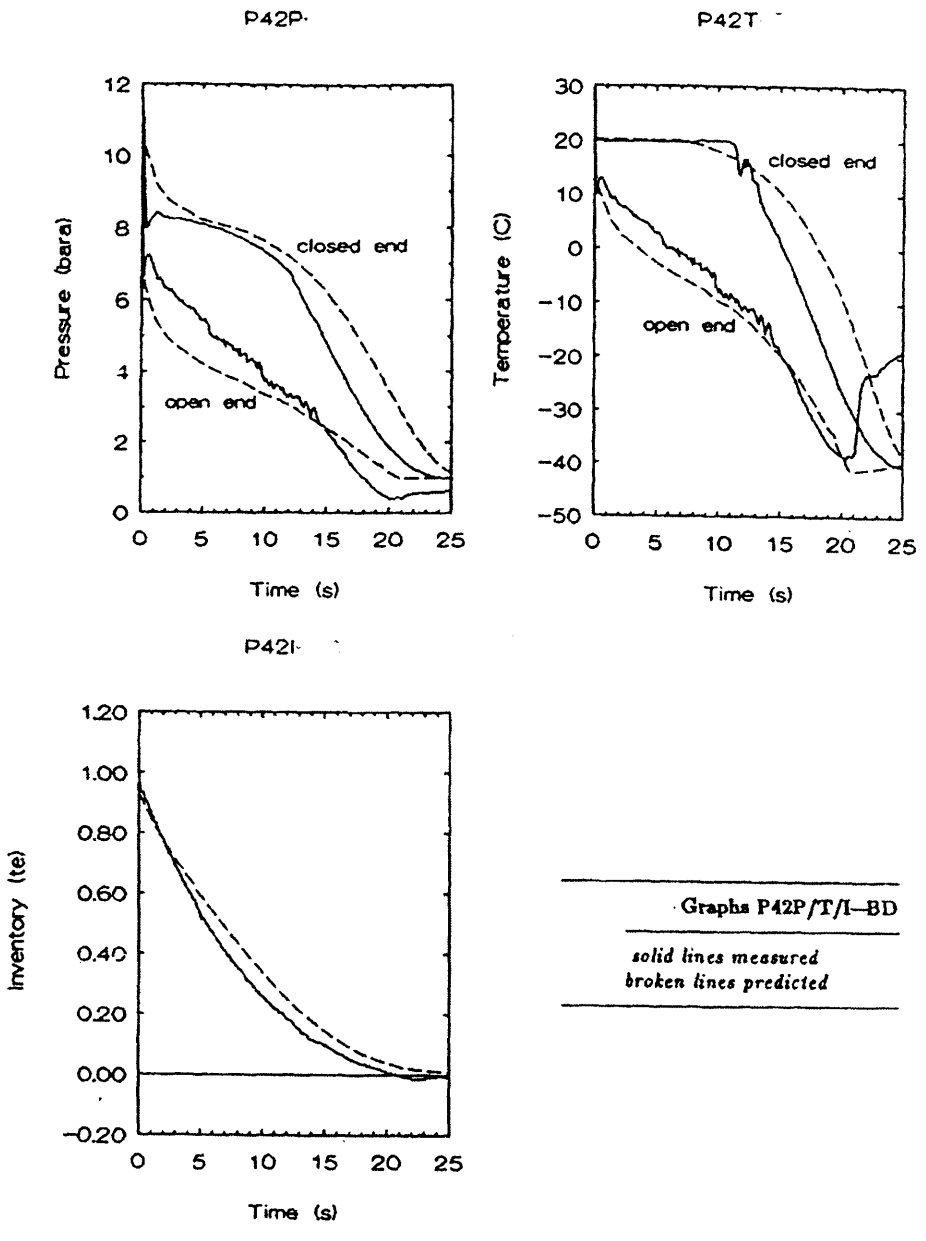

Figures 2.7 (a - c): Results of blowdown of pipeline containing LPG mixture; Isle of Grain depressurisation tests P42 (Richardson and Saville 1996b).

Although BLOWDOWN produces reasonable agreement with field data, the model does not account for the rupture induced expansion wave propagation. Such phenomena have a significant effect on the discharge process especially in case of the blowdown of long pipelines (see section 5.7).

BLOWDOWN typically requires a 'few' hours to simulate an Isle of Grain test, while the more refined model in which the quasi-steady state assumption is relaxed takes a 'few' days. The above CPU run times reported are based on the simulations performed on a 386 computer fitted with an 860 co-processor.

2.6.2 Chen et al., 1992 (MOC Based Model)

Chen et al. (1992) simulated the blowdown of pipelines containing perfect gases following full-bore rupture using the Method of Characteristics (MOC). Four different algorithms were employed in order to investigate their effect on the computational run time and accuracy. These were the hybrid method, the hybrid method with multigrid system, wave tracing and multiple wave tracing (MWT) method (see Zucrow and Hoffmann, 1976). The MOC (see chapters 4 and 5) is in principle capable of handling pipeline punctures and blowdown from a network of pipelines in conjunction with suitable boundary conditions.

Heat transfer is accounted for in terms of a simple heat conduction equation for a cylindrical geometry based on the assumption that the pipe wall thickness is small and that it is at the same temperature as the fluid. The frictional loss on the other hand is estimated using a standard equation for gas flow in pipes.

The multiple wave-tracing (MWT) algorithm was found to be the most efficient and accurate when compared to the other methods for simulating long gas line rupture problems. A nested grid system is used in which finer grid spaces are employed near the rupture plane. As compared to the other solution techniques, the MWT is found to reduce the computational load by a factor of about 5 depending on the length of the pipeline.

The ideal gas blowdown simulation results were validated against field data obtained during the Piper Alpha tragedy following the FBR of the sub-sea gas line between the Piper Alpha and MCP-01 platforms (Richardson and Saville, 1991). (See section 5.3.3, table 5.2-5.3 for blowdown conditions.)

The results obtained were found to be in poor agreement with actual data, with the discrepancy being attributed to ignoring real fluid behaviour (see figure 2.11). The simulation run time using the MWT algorithm was 16 hours on a SUN SPRAC workstation.

2.6.3 Chen et al., 1995a,b (HEM, MSM)

In this work Chen et al. (1995a,b) accounted for real fluid behaviour using an in-house computer program-PREPROP. The authors also investigated the effects of assuming homogenous equilibrium as compared to heterogeneous equilibrium between the constituent phases on the accuracy of their simulations. As opposed to heterogeneous equilibrium, homogenous equilibrium assumes that all phases are at thermal and mechanical equilibrium, and move at the same velocity. This assumption ensures the maximum possible mass transfer rate during any phase process, significantly simplifying the requirement of modelling the interfacial heat/mass transfer processes into a simple phase equilibrium calculation.

Using the hetergenoues equilibrium model, the authors also investigated the effects of assuming stratified (liquid at the bottom with vapour at the top) as opposed to bubbly flow on the blowdown results.

The flow regime transitions are specified empirically by using a flow regime map. The flow channel is discretised using staggered meshes where the flow velocity is defined at the cell edge and all other variables defined at cell centre. Furthermore, the density in the mass conservation equation is eliminated using a locally linearised equation of state so that the discretised conservation laws can be reduced to two difference equations in terms of mixture enthalpy and pressure only.

Figures 2.8a-d show the results of the heterogeneous equilibrium model, referred to as META-MSM (META Marginal Stability Model, with META referring to the name of the main computer program) as well as homogenous equilibrium model (HEM) as compared to the Isle of grain depressurisation test P42 data. (See section 5.3; table 5.1, for full depressurisation conditions.)

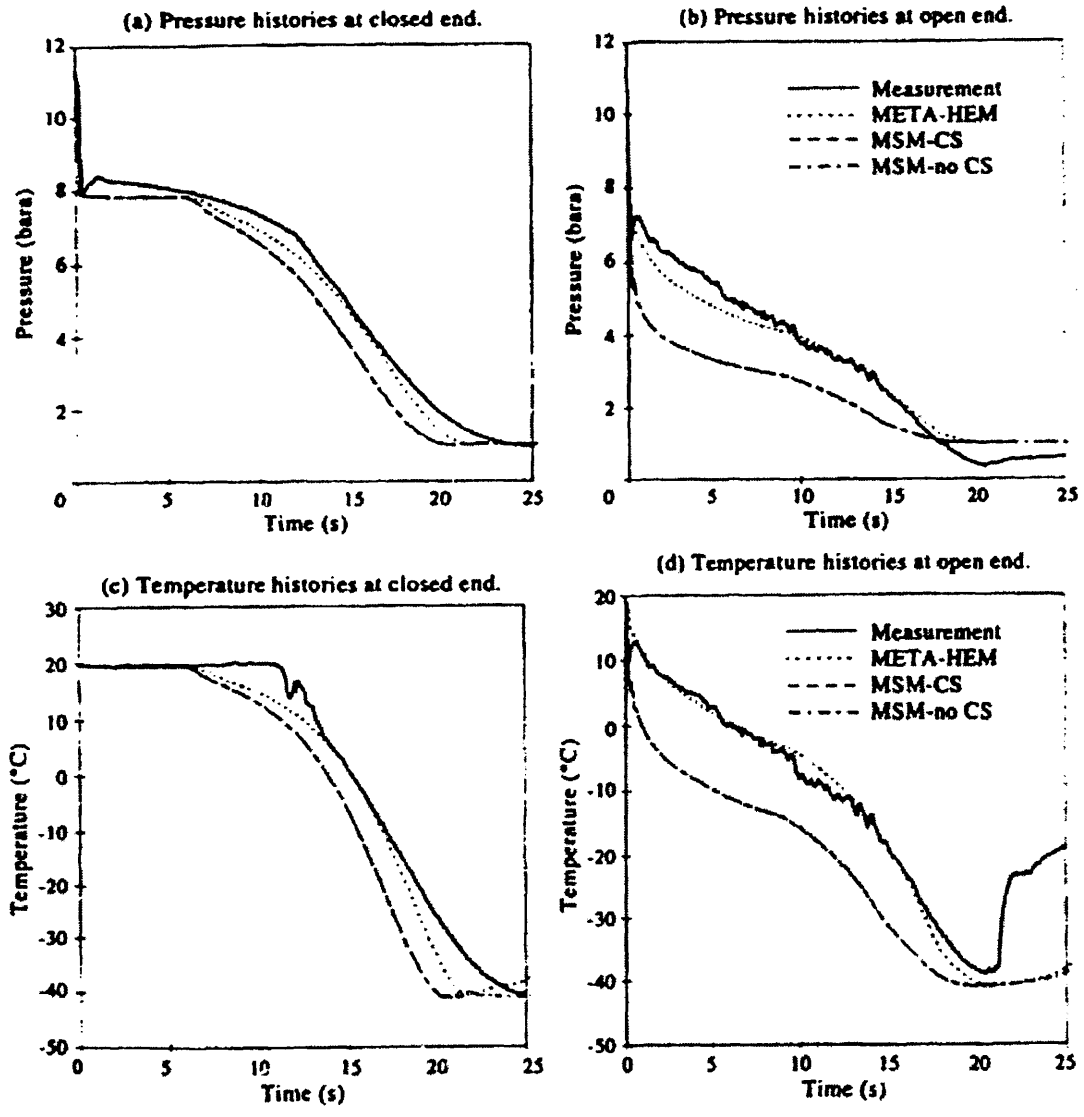

Figures 2.8 (a - d): Results of blowdown of pipeline containing LPG mixture (Isle of Grain depressurisation tests P42) (Chen et al., 1995b).

Good agreement between META- HEM and field data is obtained. This agreement is in fact better than those obtained using either of the non-equilibrium-based models (MSM-Concentration Stratification [CS] and MSM-no CS). The poor performances of heterogeneous models are probably as a consequence of the uncertainties associated with the large amount of empirical correlations used for the generation of the hydrodynamic data for the various flow regimes.

Based on the reasonably good performance of the HEM, it can be concluded that the homogenous equilibrium assumption is valid in the case of the FBR depressurisation of long (>100 m) pipelines.

Furthermore, agreement between the MSM-CS and MSM-no CS models indicates that the effect of concentration stratification can be ignored.

Figure 2.9 shows the performance of PLAC against the META-HEM, MSM-CS (Marginal Stability Model-Concentration Stratification) and BLOWDOWN codes for the variation of the total line inventory with time for LPG blowdown test P42. META-HEM, MSM-CS and BLOWDOWN agree relatively well in comparison to field data, with PLAC performing quite poorly.

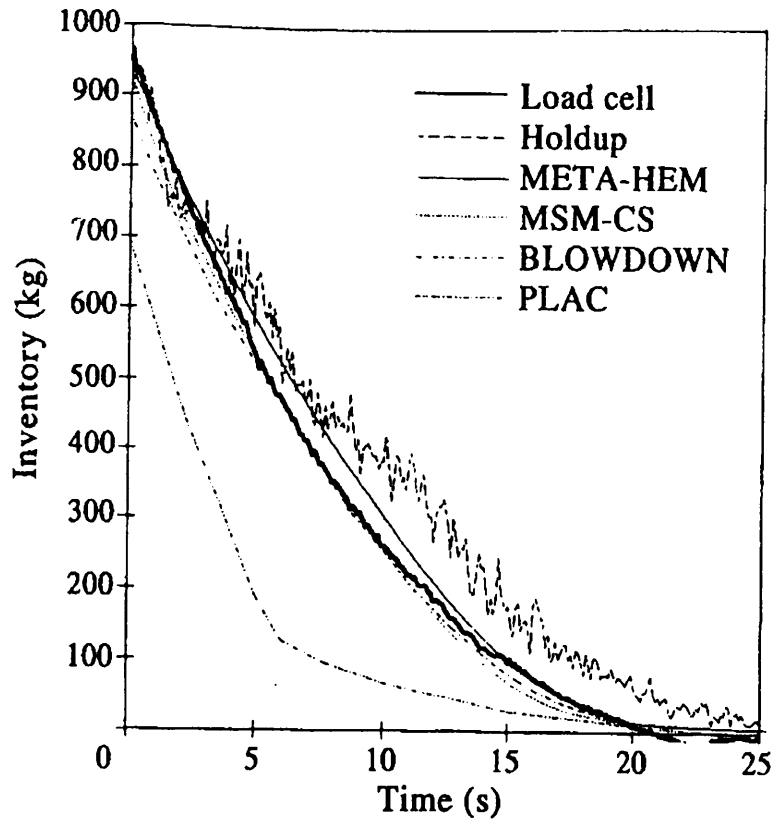

Figure 2.9: Comparison of results of HEM, MSM, BLOWDOWN and PLAC with the Isle of Grain depressurisation test P42 (Chen et al., 1995b).

25 uniform meshes were used in the simulation of the Isle of Grain depressurisation tests on a DEC 5000/240 workstation. The corresponding computation time for the META-MSM and the HEM model was *ca.* 20 hrs and 8 hrs respectively. Hence it is expected that the application of the above models (MSM and HEM) in simulating the complete blowdown of long pipelines would take many days to execute.

2.7. University College London Models

2.7.1 Mahgerefteh et al., 1997-2000

Between 1997 and 2000, Mahgerefteh et al. published three papers relating to transient modelling of outflow following pipeline rupture.

The model of Mahgerefteh et al. (1997) is based on the solution of conservation equations for one-dimensional flow based on the classical inverse marching method of Characteristics (Zucrow and Hoffmann, 1976). The dynamic response of both check and ball valves during emergency isolation are simulated. The inventory is treated as an ideal gas in order to illustrate the various dynamic effects in gas transmission pipelines.

Check valve closure is modelled by introducing closed end boundary conditions at the required time and space co-ordinates while for the ball valve, the authors account for the variation of flow rate as a function of time during valve closure.

Valve response following emergency isolation was modelled in conjunction with a real North Sea pipeline containing methane of length and diameter 145 km and 0.87 m respectively. The initial flow velocity is 10 m/s and the line pressure and temperature are 133 bar and 283 K respectively. Under such conditions, the inventory will remain in the gas phase. The pipeline is partially insulated with an assumed heat transfer coefficient of 5 W/m^2K.

The authors investigated the effect of valve proximity to the rupture plane on the total amount of inventory released. Figure 2.10 shows the data for a ball valve and a check valve. For the sake of an example, the ball valve is designed to activate closure at a

pressure of 10 bar below the normal working pressure and close at a rate of 2.54 cm/s. The check valve on the other hand is assumed to close instantaneously, upon the detection of flow reversal. The data indicates that for valves positioned in close proximity (up to 5 km) to the rupture plane, a check valve offers a much better degree of protection in terms of limiting the total amount of inventory released. For valves positioned at larger distances, the difference in performance becomes progressively unremarkable.

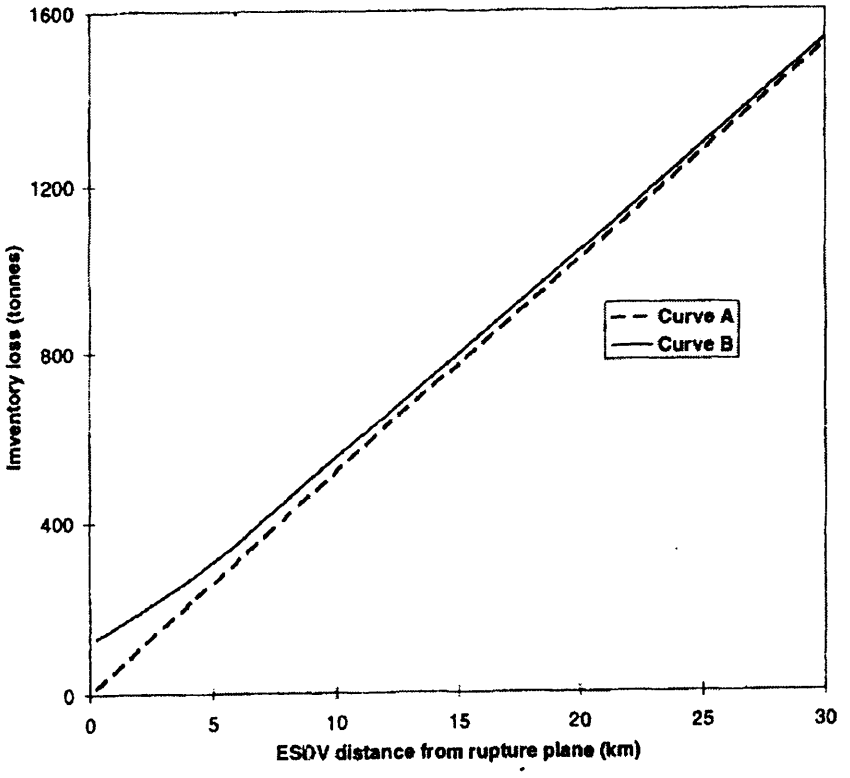

Figure 2.10: The variation of inventory loss as a function of ESDV proximity to the rupture plane: Curve A: Check valve; Curve B: Ball valve.

(Mahgerefteh et al., 1997).

In their second paper (Mahgerefteh et al., 1999), real fluid behaviour is accounted for using the PR-EoS incorporating the pertinent hydrodynamic equations for two-phase flows. In addition, curved characteristics are employed in which the characteristics

lines are replaced by arcs of parabolas. These are claimed to overcome the errors introduced as a result of using linear characteristics, which essentially assume a linear variation of thermo-physical properties between the various discretisation grid points. Based on earlier observations (Chen et al., 1995a,b), the homogeneous equilibrium model (HEM) in which all phases are assumed to be at thermal and mechanical equilibrium is assumed.

The problem of long CPU times associated with the numerical solution was largely addressed by using a compound nested grid system (CNGS) in which the penultimate, and the last grid next to the rupture plane are subdivided further.

The model presented in the 1999 publication (Mahgerefteh et al., 1999) was validated against intact end pressure data for the Piper Alpha riser as well as two sets of test results (P40 and P42) obtained from the Isle of Grain depressurisation tests. The results of the Piper Alpha simulation and test P40 are reviewed herewith.

Figure 2.12 shows the measured intact end pressure-time history following the FBR of the Piper Alpha to MCP-01 sub sea line. Curve A shows measured data whereas curve B shows the predictions using Compound Nested Grid System Method of Characteristics (CNGS-MOC). Curve C shows the corresponding data (CNGS-ideal) generated using linear characteristics in conjunction with the ideal gas assumption, as reported in a previous publication (Mahgerefteh et al., 1997). As it may be observed, the inclusion of real fluid behaviour results in good agreement with field data.

Comparing the CPU run times for the Piper Alpha simulation as shown in figure 2.11, it is difficult to rationalise the significantly shorter CPU run time for the CNGS-MOC ideal gas model as compared to CNGS-MOC real gas model (c.f 1.5 minutes with 6 days). This is more so considering the Chen et al. (1992) MOC based ideal gas model (section 2.6.2.) similar to CNGS-ideal took 16 hrs to execute.

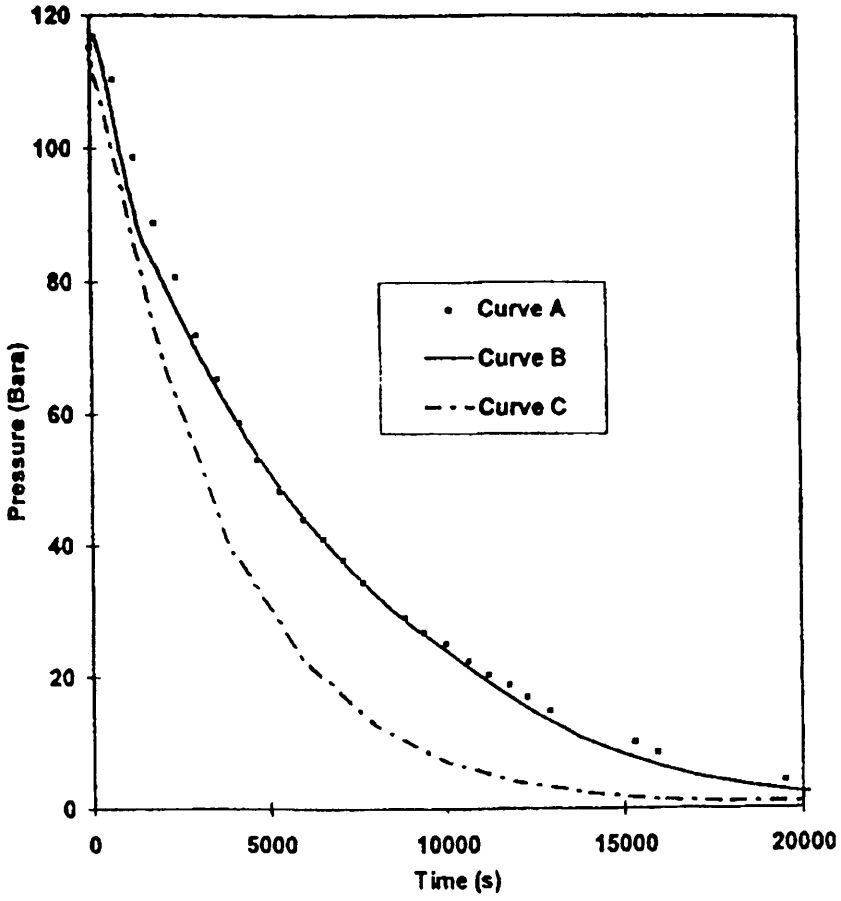

Figure 2.11: Intact end pressure vs. time profiles for the Piper Alpha-MCP pipeline (Mahgerefteh et al., 1999).

Curve A: Field Data; Curve B: CNGS-MOC, CPU time = 6 days; Curve C: CNGS-MOC ideal gas, CPU time = 1.5 min.

Figures 2.12 and 2.13 respectively show predictions for the open and closed end temperature-time and pressure-time histories for the LPG mixture test P40 as compared to experimental data. Curves A and B show the measured data whereas curves C and D represent the corresponding simulated data using CNGS-MOC. These show relatively good agreement with the experimental data. It may be observed from the temperature profile data in figure 2.12 that there is a large discrepancy towards the end of the blowdown process. This is most likely due to the use of a constant heat

transfer coefficient, and hence ignores the dependence of the heat transfer coefficient on the fluids' phase and properties during the discharge process. The authors attribute the other finite discrepancies between theory and experiment to the uncertainty associated with the measurement data, the inaccuracies associated with the prediction of VLE data, as well as the lack of accurate information on the fluid composition.

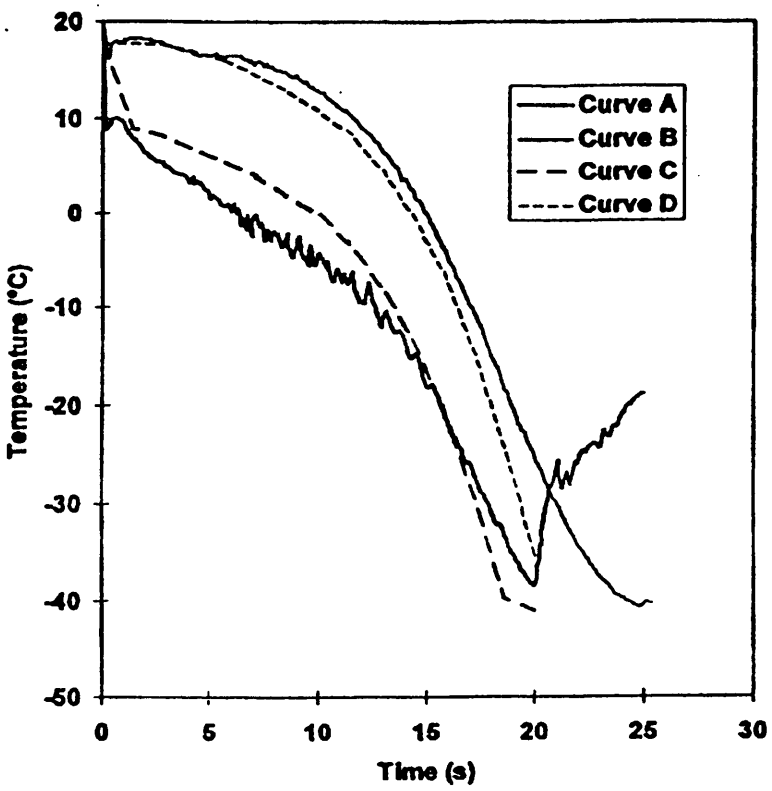

Figure 2.12: Temperature-time profiles at the open and closed ends for the P40 (LPG) test (Magerefteh et al., 1999).

Curve A: Field data (open end); Curve B: Field data (closed end); Curve C: CNGS-MOC (open end); Curve D: CNGS-MOC (closed end).

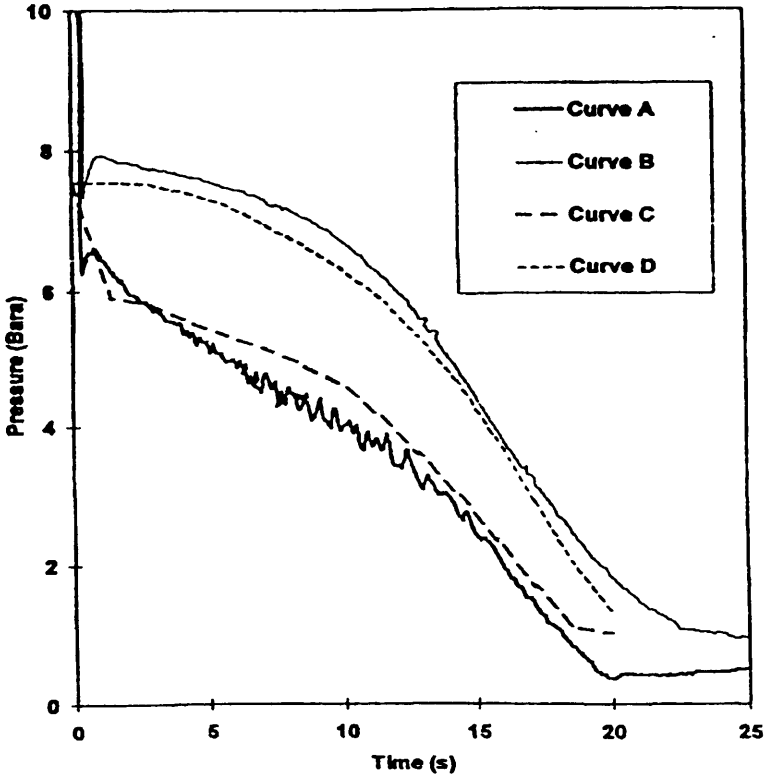

Figure 2.13: Pressure-time profiles at the open and closed ends for the P40 (LPG) test (Magerefteh et al., 1999).

Curve A: Field data (open end); Curve B: Field data (closed end); Curve C: CNGS-MOC (open end); Curve D: CNGS-MOC (closed end).

Finally, using MOC, Mahgerefteh et al. (2000) employed a real fluid model to predict the effect of phase transition on the dynamic behaviour of emergency shut down valves.

The authors conclude that a transition from gas to two-phase flow during blowdown results in a delay in valve activation. This is turn leads to more inventory loss following pipeline failure as compared to a permanent gaseous inventory. The

pressure surge upstream of the closed valve was simulated using the Joukowsky equation and the results reported.

2.7.2 Vahedi, 2003

Vahedi (2003) developed a model based on the Method of Characteristics to determine the effects of inclination and pipeline enlargement (non-uniform pipe diameter) on outflow characteristics. A comparison was made between the results generated using linear as opposed to curved characteristics and the author also studied the effect of using different friction factor correlations on the simulated results. Fluid thermodynamic properties are calculated with the aid of the Peng- Robinson equation of state, and the fluid phases are assumed to be in homogenous equilibrium.

Vahedi's (Vahedi, 2003) pipeline rupture model was validated against the Isle of Grain experimental data and those recorded during the Piper Alpha tragedy. Good agreement between field and experimental data was obtained with the degree of agreement being similar to that obtained by Mahgerefteh et al. (1999) (see figure 2.11, curve B).

A hypothetical scenario involving the rupture of an enlarged pipeline, containing methane at an initial pressure of 50 bara was also investigated. Figure 2.14 gives a schematic representation of the pipeline and the rupture location.

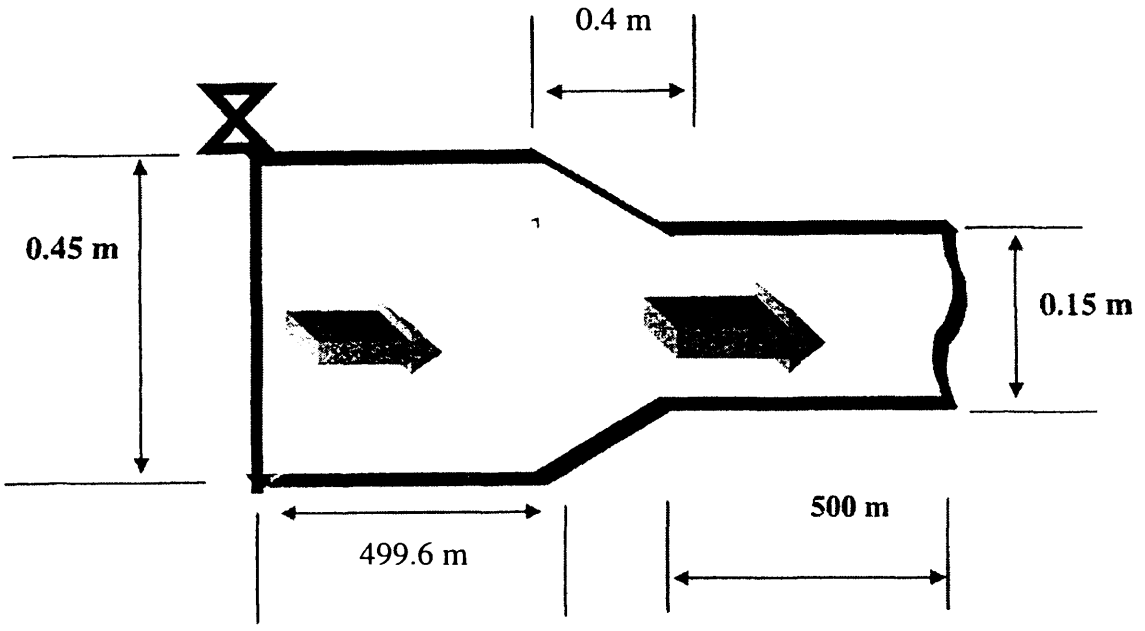

Figure 2.14: Schematic representation of enlarged pipeline simulation (Vahedi 2003).

The simulation results for the above configuration were then compared with those obtained using a uniform diameter pipeline of the same length, containing the same amount of inventory.

Figure 2.15 shows the variation of pipeline inventory with time following the rupture of the uniform and the enlarged pipeline. As it may be observed from figure 2.15, the enlarged pipeline depressurises at a significantly slower rate when it is compared to the uniform diameter pipeline. The author hence concludes that reducing the pipeline diameter or 'bottlenecking' may be used as an effective way of reducing hazards following FBR by reducing the discharge rate.

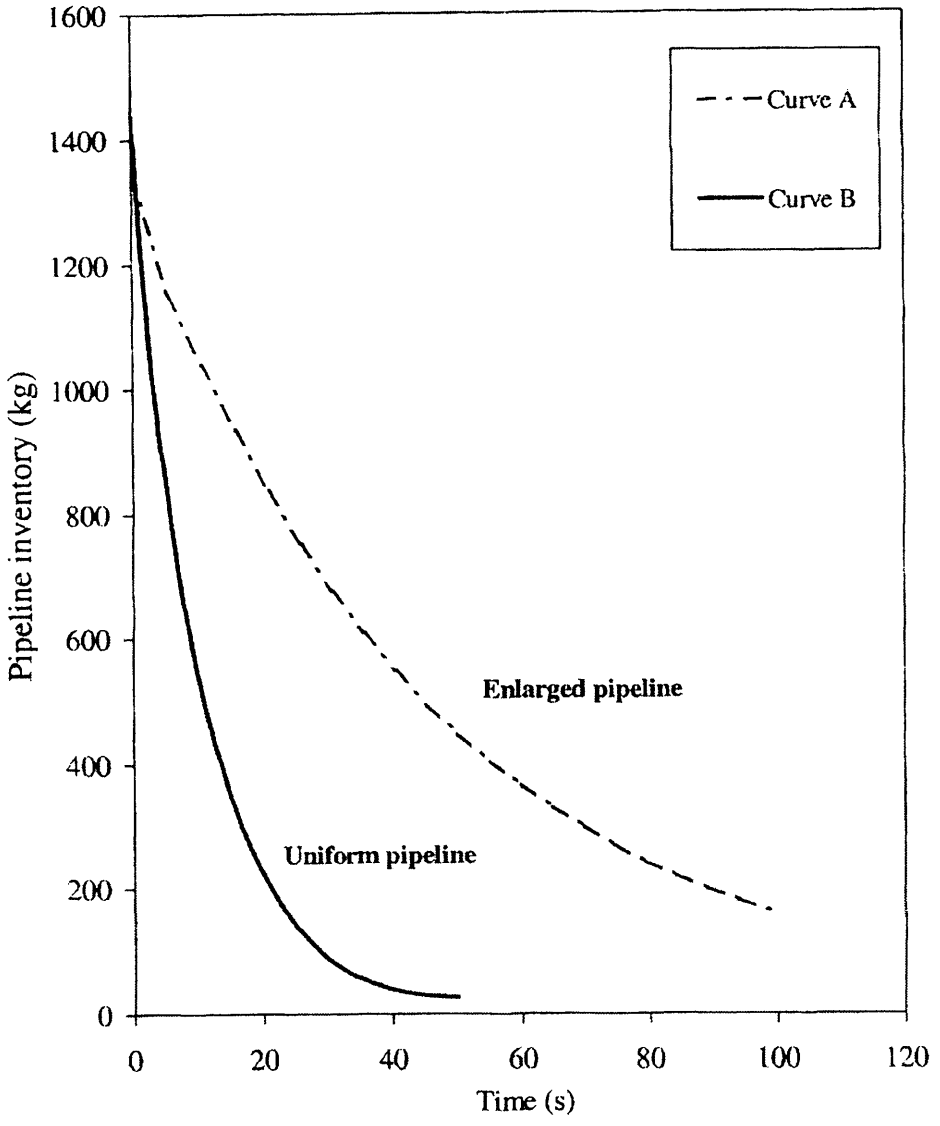

Figure 2.15: Pipeline inventory variation with time for methane following FBR (Vahedi, 2003).

Curve A: Enlarged pipeline.

Curve B: Uniform pipeline.

Other investigations made by the Vahedi (2003) include the use of curved as opposed to linear characteristics on the simulation accuracy and CPU run times. It was observed that for two-phase flows, the linear characteristics provide consistently better predictions and executed faster in comparison to curved characteristics. However, for gaseous media either methodology yields practically the same result with similar computational run times.

On the study of the effect of pipeline inclination, the author concludes that the pressure wave propagation during top end rupture is slower in inclined pipelines as compared to horizontal pipelines, with the converse holding for bottom end rupture.

2.7.3 Oke et al., 2003; Oke, 2004

The model developed by Oke et al. (2003) and Oke (2004) dealt with outflow characteristics following the puncture and rupture of pipeline networks. The model is also based on the MOC and assumes homogenous equilibrium between phases. However, the conservation equations were posed in terms of pressure, enthalpy and velocity (PHU) in contrast to the conventional pressure, density and velocity (PDU) formulation used by previous workers (Zucrow and Hoffmann, 1976, Tiley, 1989; Chen et al., 1992; Mahgerefteh et al., 1997, etc). A pressure, entropy velocity (PSU) based formulation was also presented and all three (PDU, PHU and PSU) models were compared in terms of accuracy and CPU run times. In addition, the effect of adopting quadratic as opposed to linear interpolations along the space co-ordinate was examined. Boundary conditions were imposed at pertinent grid points to allow closure of the characteristic equations.

Oke's (2004) model was validated against the Isle of Grain and Piper Alpha pipeline rupture data. The PDU, PHU and PSU based conservation equations were used to simulate the Isle of Grain depressurisation tests in order to investigate the effect of the choice of primitive variables on model accuracy and computational run time. Figure 2.16 shows the variation of discharge pressure with time for the Isle of Grain test P40 as compared to the simulation results. As it may be observed, in general, the PHU model performs best in terms of accuracy, followed by the PSU and PDU models. The PHU model also required the least CPU run time, requiring 12 minutes to execute, while the PSU and PDU models required 13 minutes and 86 minutes respectively on an IBM Pentium IV 2400 MHz PC. Based on these results, the PHU model was thus used for all the subsequent simulations presented. The use of quadratic as opposed to linear interpolations although very marginally improved the model predictions, resulted in longer simulation run time.

Good agreement between field and experimental data was obtained for the Piper Alpha simulation, with the accuracy similar to that obtained by other workers (Mahgerefteh et al., 1999; Vahedi, 2003). The execution time using the PHU model was *ca.* 28 hrs.

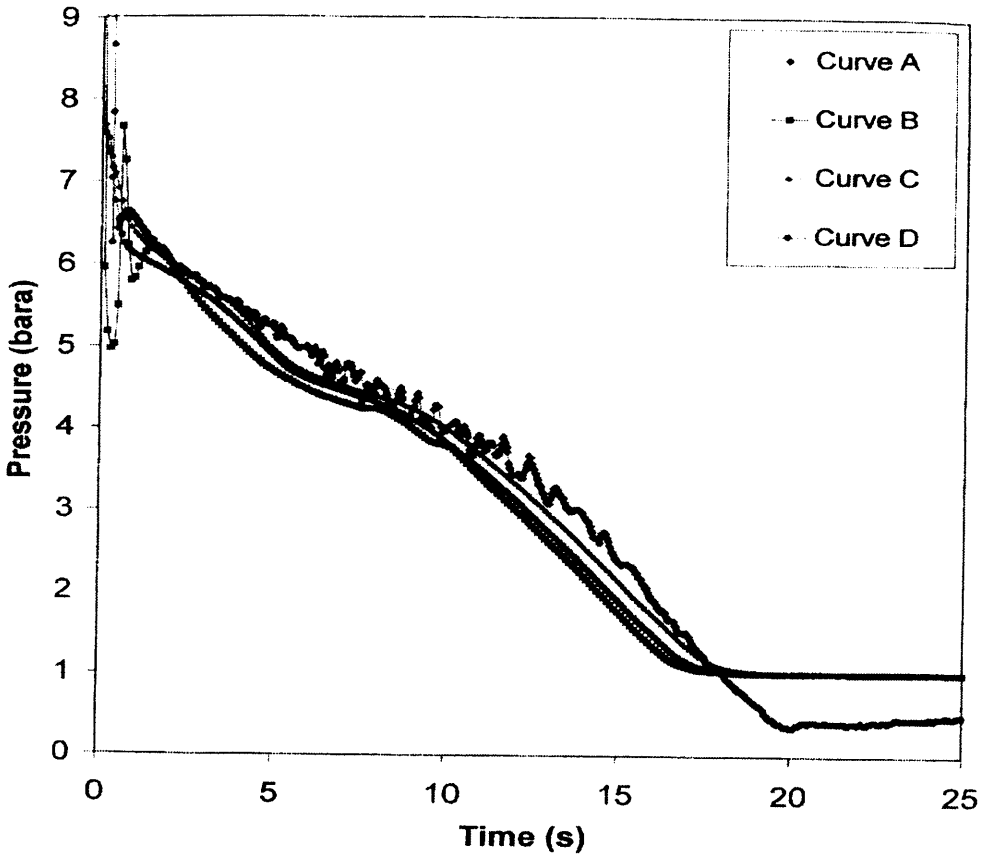

Figure 2.16: FBR pressure-time profiles at open end for test P40 (LPG) showing the effect of primitive variables on simulated results (Oke, 2004).

Curve A: Open end measurement.

Curve B: Open end simulation results using the PDU model.

Curve C: Open end simulation results using the PHU model.

Curve D: Open end simulation results using the PSU model.

Oke's model (2004) was then employed to simulate the blowdown of various configurations of pipeline networks having the same total length of 25 km. The fluid inventories and conditions were the same as those used in the Piper Alpha simulation. From the simulations, it was concluded that that the depressurisation of a pipeline network is strongly influenced by the overall distance travelled by the expansion waves from the rupture plane to the intact end. The shorter the distance travelled, the faster the depressurisation.

The fluid dynamics following the puncture of a hypothetical pipeline was discussed in the model presented by Oke et al. (2003). The pipeline was assumed to be 16 km long, conveying a condensable hydrocarbon mixture with an initial flow rate of 0.3 m^3/s which was sustained for 90 seconds after rupture. The PHU model was used in the simulation with the pipeline assumed to be isolated downstream upon puncture. Figure 2.17 shows a pictorial timeline simulation of the fluid flow pattern following puncture as presented by Oke et al. (2003).

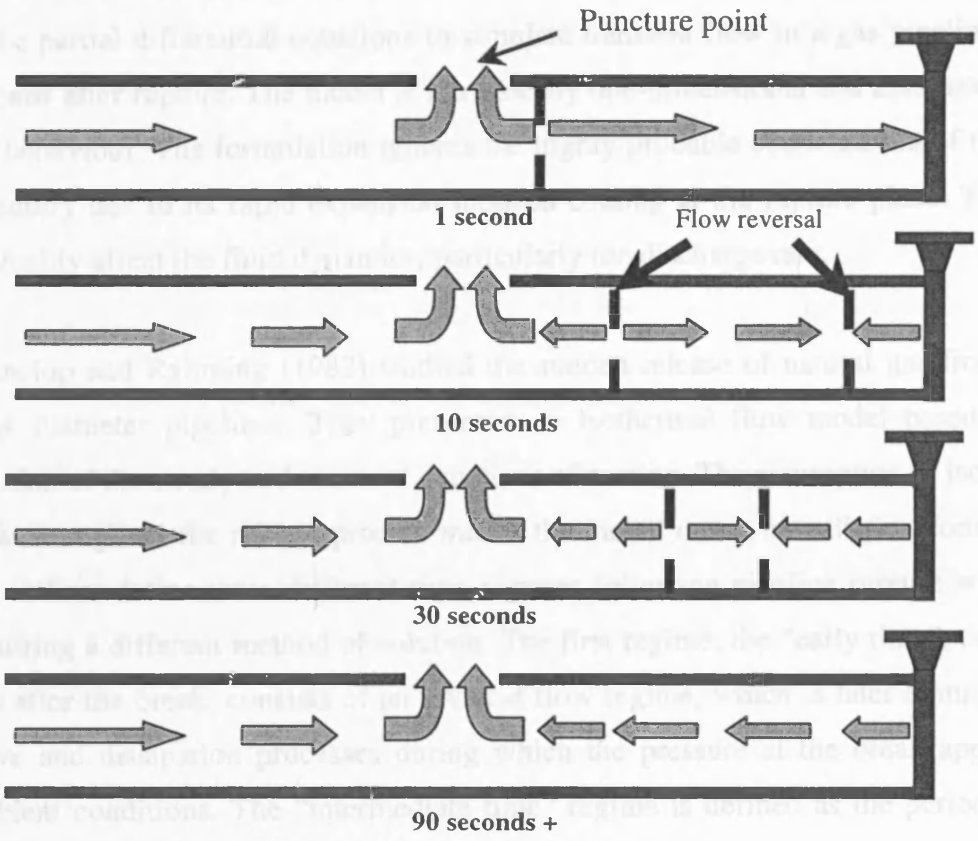

Figure 2.17: Schematic representation of flow patterns in the pipeline following puncture (Oke et al., 2003).

Although the models presented above are in principle capable of simulating outflow from punctures and pipeline networks, the boundary conditions and their solutions as presented by the authors (Oke et al., 2003; Oke, 2004) require modification. It will be shown later (see sections 5.6.2 and 5.7) that the use of the boundary conditions as presented may result in errors.

2.8 Other Models (1970-Date)

Over the past few decades, numerous models have been reported for simulating outflow following pipeline rupture or puncture. Some of the models reported are described briefly below in terms of their formulation strengths and weaknesses.

Sens et al. (1970) used an explicit finite difference method for the numerical solution of the partial differential equations to simulate transient flow in a gas pipeline a few seconds after rupture. The model is intrinsically one-dimensional and assumes perfect gas behaviour. The formulation ignores the highly probable condensation of the fluid inventory due to its rapid expansion induced cooling at the rupture plane. This will inevitably affect the fluid dynamics, particularly the discharge rate.

Fannelop and Ryhming (1982) studied the sudden release of natural gas from long, large diameter pipelines. They presented an isothermal flow model based on the solution of the steady and transient equations of motion. The assumption of isothermal flow throughout the release process makes the model rather unrealistic. Nonetheless, the authors define three different time regimes following pipeline rupture with each requiring a different method of solution. The first regime, the "early time", occurring just after the break, consists of an inviscid flow regime, which is later dominated by wave and dissipation processes during which the pressure at the break approaches ambient conditions. The "intermediate time" regime is defined as the period during which an internal pressure peak- the location of which corresponds approximately with the location of flow reversal initiates, and travels to the closed end of the pipeline. This then gives way to the "late time" regime, which is governed by the balance of such events as wave reflection from the far end and monotonic decrease of pressure towards the open end. The authors then employed a methodology in which they integrated the conservation equations over the length of the pipeline by approximating the fluid property behaviour (pressure and flowrate) along its length with a suitable function. From the foregoing, it can be seen that the choice of an approximate function to describe the fluid property could critically influence the results obtained. Consequently, the authors investigated the effect of using different approximate functions on the results obtained. From their results, they observed that the integral method is relatively insensitive to the type of profile used, and is consistent in predicted trends. In conclusion, the authors recommend the integral method as a tool for the analysis of engineering problems involving pipeline rupture and the resultant release process.

Flatt (1985-1989) studied the use of the method of characteristics for the analysis of unsteady compressible flow in long pipelines following rupture. The author discarded

the simplifying assumptions of isothermal flow often applied in the case of unsteady compressible flow in pipelines. To achieve higher accuracy, higher-order polynomials and an assumption of correspondingly curved characteristic lines were employed. However, the model is one-dimensional and assumes single-phase gas discharge.

Picard and Bishnoi (1988) applied their three models namely the Perfect-gas Isentropic Decompression (PID) model, Real-fluid Isentropic Decompression (RID) model and Real-fluid Non-isentropic Decompression (RND) to investigate the importance of real-fluid behaviour in the modelling of high-pressure gas pipeline ruptures. The models are based on the MOC and assume the flow is one-dimensional. For the RID model, either the Soave-Redlich-Kwong (SRK) or the Peng-Robinson equation of state was employed. The authors observed that the PR-EoS gave better predictions of the fluid rupture data when compared to the SRK-EoS The results also showed that the perfect-gas model (PID) could introduce significant errors as it underestimated the fluid pressure by as much as 20 % when compared with the real fluid model (RID).

As a follow-up to their previous work, Picard and Bishnoi (1989) emphasised the importance of employing real-fluid behaviour in modelling release rates from ruptures in high-pressure pipelines. The authors observed that the previously developed non-isentropic decompression model (RND) was prone to numerical instability at the rupture plane when the selected distance between grid nodes in the region immediately upstream of the rupture plane was too large. To overcome this problem, the authors imposed a short isentropic region at the rupture plane, which was assumed valid if the region was small relative to the total pipe length. Their results showed that the assumption of perfect gas as against real fluid behaviour could underestimate the calculated values of the release rate and total amount of fluid discharged by as much as 45 % and 50 % respectively.

Lang (1991) reported on the computation of gas flow in pipelines following rupture using the spectral method. The governing partial differential equations were converted into a scheme suitable for solution by a computer using a two-step procedure. In the first step, the collocation version of the spectral method was used to calculate the space derivatives. The remaining ordinary differential equations were then integrated

by standard numerical techniques in the second step. The model presented assumes ideal gas behaviour coupled with either isothermal or adiabatic flow conditions. Simulated results obtained using the model showed close agreement with results presented by Battara et al. (1985) and with data from Fannelop and Ryhming (1982). No validation of the model against field or experimental data was presented. The author concludes by recommending the spectral method as a suitable tool for obtaining stable, accurate and efficient solutions to the problem of transient flow following pipeline rupture.

Olorunmaiye and Imide (1993) presented a mathematical model based on perfect gas unsteady isothermal flow theory solved using the MOC. The accuracy of the numerical scheme when using linear characteristics with quadratic interpolation was found to be adequate. It was found that the curvature of the characteristics is not as pronounced in isothermal flow as it is in adiabatic flow. Therefore, it is not necessary to include the effect of curvature of the characteristics in the computation of unsteady isothermal flows. It was concluded that the model is useful in analysing other unsteady flows associated with pipeline operation, such as controlled venting to the atmosphere prior to shutdown or repair, and sudden changes in pressure at either end of the pipeline. The model's formulation makes it unsuitable for modelling accidental pipeline puncture, and limits it to modelling of venting through valves located at the end of the pipeline.

Kunsch et al. (1995) developed a pipeline rupture model by integrating the conservation equations using the two-step MacCormack method. They noted that a precise knowledge of the coefficient of friction and other losses coefficients following pipeline rupture is not necessary in simulating outflow. They demonstrated that the mass flow rates are insensitive to the exact geometric shape and contraction ratio of the break, resulting from an accidental rupture. They also compared their model results with those obtained by Flatt (1985b). They admitted that the results from Flatt's model (which was based on the method of characteristics) were probably more accurate than theirs, for the inertia dominated early time regime. They observed that the ideal gas assumption overestimated the mass flow rate. Other workers (Flatt, 1986; Picard and Bishnoi, 1988) however observed the opposite effect when

employing the perfect gas assumption. The model presented does not account for fluid wave-dynamics following rupture and is only suited to modelling pipeline rupture.

Zhou et al. (1997) tackled the problem of releases from high-pressure pipelines using three-dimensional computational fluid dynamics. This model was designed to incorporate geometric and physical complexities that may exist in the pipe system, and handle the modelling of punctures located and oriented at different angles at any point along the walls of a pipeline. Whilst this model gives an exhaustive description of the fluid mechanical and thermodynamic properties, it nonetheless is based on steady state conditions and assumes steady state discharge.

Fairuzov (1998) proposed a model to simulate the blowdown of long pipelines conveying flashing multi-component fluids at high pressure. The model is based on the homogenous equilibrium assumption and incorporates the effect of pipeline wall thermal capacitance in its energy equation. However, the model assumes that the fluid and pipe wall is in local thermal equilibrium, and heat transfer by conduction in the axial direction is negligible. The solution approach involved breaking the pipeline into a number of control volumes or nodes that are connected by junctions or flow paths. Thereafter, mass and energy conservation equations are written for each node, and an approximate momentum equation is used to calculate flow rates through the flow paths. The model was validated against test P42 from the Isle of Grain experiments, with a reported run time of about 1 hr. However, in order to obtain agreement with test data, the author needed to assume a value of 1 mm for the pipe wall thickness as against the original value of 7.3 mm. This approach therefore casts doubts over the robustness of the model.

Tao and Ti (1998) as well as Ke and Ti (2000) utilised a unique approach in the transient analysis of gas pipeline network. The authors used the electric analogy method for the computation of solutions to the transient gas transmission problem. Instead of having to handle the original partial differential equations, a set of first order ordinary differential equations was solved in their place. However, their models employes the isothermal flow and ideal gas assumptions, both of which limit their applicability to blowdown of simple gasses at relatively low pressures.

Gato and Henriques (2005) presented a numerical solution for the one-dimensional compressible flow system of conservation equations. The equations were solved using the Runge-Kutta discontinuous Galerkin method with a third order approximation in space and time. The model however assumes a constant fluid compressibility, and is suited only to gaseous release.

Due to the complexity involved in modelling pipeline puncture, a large proportion of pipeline puncture models treat the pipeline as a vessel with a hole in its walls. Crowl and Louvar (1990), and Woodward and Mudan (1991) developed models for the estimation of accidental releases from pipelines. These models in principle treat the pipeline as a vessel discharging through an orifice, thereby ignoring the effects of the ensuing pressure and fluid flow transients within the pipeline. Consequently, the accuracy and validity of their prediction is undermined by the assumption of equal and uniform pressure inside the vessel at any given time interval.

Montiel et al. (1998) in trying to tackle the modelling of pipeline puncture developed a simplified model based on steady state adiabatic flow assumption, and ignores real fluid behaviour. Furthermore, the model neglects the initial pressure drop along the pipeline due to frictional effects on fluid flow. These assumptions largely limit the practicality and suitability of the model. Finally, the model fails to account for the transient propagation of pressure waves/disturbances through the fluid contained in the pipeline.

Jo and Ahn (2002) presented a model for calculating the release rate of hazardous gases following puncture. The model is based on steady state isentropic flow. It assumes ideal gas fluid behaviour, one-dimensional flow, and ignores wave propagation or flow reversal effects. The model is at best suited for steady state single-phase gaseous release through a hole at the end of a pipeline.

2.9 Concluding Remarks

Based on the above review, it is clear that there is still significant scope for improving the pipeline failure models reported in the open literature.

Several of these models fail due to the assumption of perfect gas behaviour, or ignoring depressurisation induced wave propagation phenomena. Others suffer from inaccurate posing of boundary conditions, ignoring frictional and heat transfer effects, or treating the pipeline as a vessel discharging through an orifice when simulating puncture. Such shortcomings will inevitability undermine the accuracy of the simulated data.

The homogeneous equilibrium assumption, in which the fluid's constituent phases are assumed to travel at the same velocity is adopted in this work. This is because studies by Chen et al. (1993) have shown the HE model to perform better than the heterogeneous equilibrium model when compared with field data. The failure of other heterogeneous equilibrium models such as PLAC and OLGA to successfully simulate field data, and the associated huge computational expense involved also makes the HE assumption more attractive.

Additionally, in cases where the models have been validated, this task has been carried out against very limited field data. This is understandable considering the practical difficulties and the enormous expense associated with carrying out pipeline rupture field tests especially in the case of long (>100 m) large diameter (>0.2 m) pipelines often encountered in practice. In view of this difficulty, in this work the mass conservation index formulated by Flatt (1986) is used to obtain an indication of the 'accuracy' of the numerical simulation.

Of the models presented, the homogenous equilibrium based models by Mahgerefteh et al. (1999), Chen et al. (1995a, b) and Oke (2004) are the most robust with the latter performing best in terms of accuracy and computational run time. Nonetheless, when simulating the complete blowdown of long pipelines (>100 km), the computational run time associated with all of these models are rather long. Hence, ways of further reducing the computational run time needs to be investigated.

It will be shown later that the models presented by Oke et al. (2003) and Oke (2004) for simulating pipeline puncture and release from pipeline networks require improvement due to the shortcomings associated with the formulation and treatment of the boundary conditions.

A significant drop in the temperature of the escaping fluid following rupture is reported in several of the publications reviewed. This will inevitably affect the mechanical properties of the pipe wall in contact with the escaping fluid. Hence, the hazard associated with such low temperature effects need to be quantitatively modelled.

CHAPTER 3

BASIC EQUATIONS DESCRIBING TRANSIENT FLOW IN PIPELINES

3.1 Introduction

The previous chapter reviewed the mathematical models available for simulating outflow following pipeline failure. In addition, their strengths and weaknesses were analysed, and where available, validation against field/experimental data was presented.

Generally, the development of the outflow fluid dynamics model necessitates accomplishing three main steps. The first involves formulating the basic equations governing flow, thermodynamics and pertinent boundary conditions. The next stage requires the solution of derived equations using an appropriate mathematical technique. Finally from a practical point of view, the results of the model should be validated against available experimental data.

An important precursor to the above is the formulation of the conservation equations relating to mass, momentum and energy in conjunction with a suitable equation of state. Solving the full system of the equations is the ultimate goal of a numerical flow simulation but the numerical discretisation necessary to accomplish this for an entire range of fluid flows is extremely difficult, and requires substantial computer resources. As such, it is necessary to consider if it is indeed always necessary to resolve every term in the Navier-Stokes conservation equations. Dependant on the type of flow, certain terms in the equations will have a negligible effect on the final solution and may therefore effectively be ignored without any serious loss of accuracy.

The final form of these equations, ready for numerical discretisation can be arrived at through many assumptions and simplifications. Accordingly, the equations in general may be linear, quasi-linear or non-linear, parabolic or hyperbolic.

Significant simplifications to the governing equations can greatly reduce computer run times, but this might well be at a cost of reduction in the accuracy of the final solution. For example, Bell (1978) used a simple exponential model that approximated the mass flow rate by the sum of two exponentials. This however did not take into account the type of flow or the length of the pipeline. Fannelop and Ryhming (1982) ignored the frictional force (inertial) terms in the conservation equations, while Crowl and Louvar (1990) did not take account of the heat transport terms between the flowing fluid and its surroundings.

This chapter presents the derivation and formulation of the equations governing the transient flow following pipeline rupture as adopted in this study. This includes:

- Derivation of the mass, momentum and energy conservation equations for transient fluid flow including the important assumptions made.

- Selection of an appropriate equation of state (EoS) and the accompanying hydrodynamic correlations.

- The energy balance model employed for estimating transient ambient-pipe wall-fluid heat transfer.

- The isothermal steady state flow model for determining the fluid flow conditions prior to pipeline rupture.

3.2 General Assumptions Made in Model Development

In this study, the flow within the pipeline is assumed to be one-dimensional, that is, the rate of change of fluid properties normal to the streamline direction is negligible compared with the rate of change along the streamline. However, at the puncture plane where there is fluid flow along and normal to the streamline, a pseudo two-dimensional flow model is employed.

For situations where two-phase flows are encountered, a homogeneous equilibrium model (HEM) is adopted where the two phases are assumed to travel at the same

velocity, and are in thermodynamic and mechanical equilibrium with one another. Studies by others (see for example Chen et al., 1995; Mahgerefteh et al., 1999) validated against experimental data have demonstrated the validity of this assumption in the case of FBR of pipelines (see section 2.6.3). As such, separate conservation for each fluid phase is not considered in this study. In addition, the fluid is assumed to have already attained isothermal steady state flow conditions prior to failure.

The pipeline is also assumed to be inelastic and rigidly anchored; hence vibrations and other associated fluid-structure interaction effects are ignored.

3.2.1 Conservation of Mass

The mass conservation equation can be derived by considering how materials build up within a control volume as fluid passes through the system. Figure 3.1 is a schematic representation of a control volume within a pipe, showing fluid flow across its boundaries.

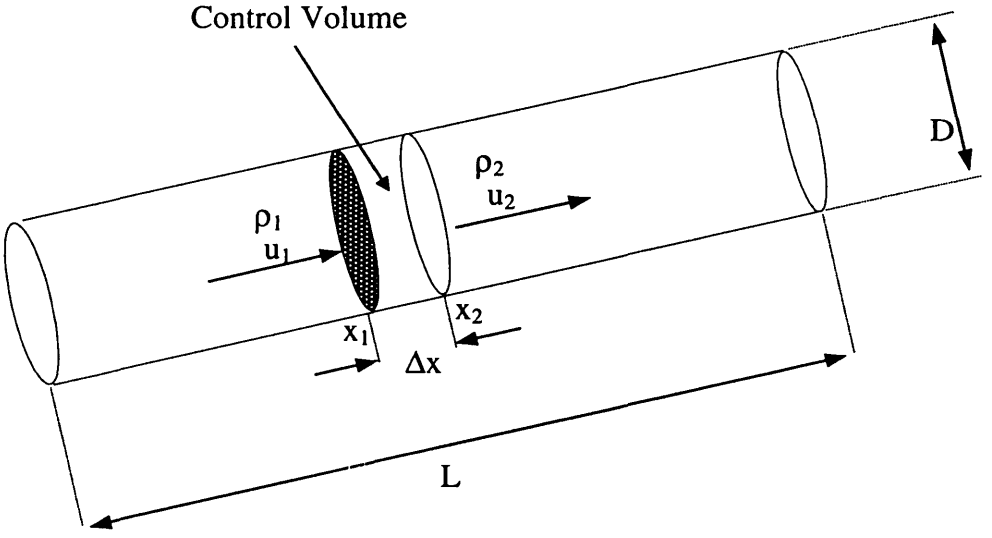

Figure 3.1: Schematic representation of a control volume within a pipe section.

ρ and *u* represent the fluid density and velocity respectively with Δx representing the length of the pipeline section under consideration.

Since the pipeline is impermeable and mass is neither created nor destroyed, then the mass in this section can change only due to fluid flowing across the end points x_1 or x_2. Hence, the rate of accumulation of mass within the control volume equals the net rate of flow in to it.

Given that the mass of fluid within the control volume is $\rho(x,t)Adx$, and the flow rate across x_1 and x_2 is given by $\rho_1 u_1 A$ and $\rho_2 u_2 A$ respectively, the rate of mass change in the control volume can be written as

$$\frac{\partial}{\partial t}\int_{x_1}^{x_2}\rho(x,t)Adx=(\rho uA)_{x_1,t}-(\rho uA)_{x_2,t} \tag{3.1}$$

Dividing (3.1) through by *A* and rearranging gives

$$\int_{x_1}^{x_2}\frac{\partial\rho}{\partial t}dx=-\int_{x_1}^{x_2}\frac{\partial(\rho u)}{\partial x}dx \tag{3.2}$$

Equation (3.2) holds for any section $[x_1, x_2]$ at any time t, and can therefore be written as

$$\frac{\partial\rho}{\partial t}+\frac{\partial(\rho u)}{\partial x}=0 \tag{3.3}$$

Expanding equation (3.3)

$$\frac{\partial\rho}{\partial t}+\frac{u\partial\rho}{\partial x}+\frac{\rho\partial u}{\partial x}=0 \tag{3.4}$$

Equation (3.4) represents the Euler form of the mass conservation equation. For notational purposes, the total or substantive derivative of a function $f(x, t)$, $f = P, \rho, H, h, u,$ is given by:

$$\frac{df}{dt}=\frac{\partial f}{\partial t}+\frac{u\partial f}{\partial x} \tag{3.5}$$

Where P, ρ, H, h, represent the absolute pressure, density, total and specific enthalpies of the fluid respectively.

Applying the above notation to equation (3.4) gives:

$$\frac{d\rho}{dt}+\frac{\rho\partial u}{\partial x}=0 \tag{3.6}$$

As demonstrated by Oke (2004) the total derivative of density with respect to time can be reformulated and expressed in terms of fluid pressure and enthalpy. This reformulation has the benefit of improving the accuracy of simulated results at reduced computational expense as shown in section 2.7.1. Hence, for its obvious advantages the same formulation is employed in this work.

For any fluid, the fluid pressure can be expressed as a function of density (ρ) and entropy (s) i.e., $P = f(\rho, s)$. Thus, in partial differential form, this relationship can be written as:

$$dP=\left(\frac{\partial P}{\partial \rho}\right)_s d\rho+\left(\frac{\partial P}{\partial s}\right)_\rho ds \tag{3.7}$$

Where by definition:

$$\left(\frac{\partial P}{\partial \rho}\right)_s = a^2 \qquad a = \text{speed of sound} \tag{3.8}$$

$$\left(\frac{\partial P}{\partial s}\right)_\rho = \varphi \tag{3.9}$$

Hence, by substituting equations (3.8) and (3.9) into equation (3.7), the substantial derivative of pressure with time can be expressed as:

$$\frac{dP}{dt}=a^2\frac{d\rho}{dt}+\varphi\frac{ds}{dt} \tag{3.10}$$

By rearranging equation (3.10),

$$\frac{d\rho}{dt}=\frac{1}{a^2}\left(\frac{dP}{dt}-\varphi\frac{ds}{dt}\right) \tag{3.11}$$

For any fluid, the total derivative of enthalpy is given by (Walas, 1987):

$$dh = Tds + \frac{1}{\rho} dP \tag{3.12}$$

Thus, from equation (3.12), the total derivative for enthalpy with respect to time becomes:

$$\frac{dh}{dt} = T\frac{ds}{dt} + \frac{1}{\rho}\frac{dP}{dt} \tag{3.13}$$

Rearranging equation (3.13) gives:

$$\frac{1}{T}\left[\frac{dh}{dt} - \frac{1}{\rho}\frac{dP}{dt}\right] = \frac{ds}{dt} \tag{3.14}$$

Substituting equation (3.14) into equation (3.11) by replacing the total derivative of entropy with time results in:

$$\frac{d\rho}{dt} = \frac{1}{a^2}\left[\frac{dP}{dt}\left(1 + \frac{\varphi}{\rho T}\right) - \frac{\varphi}{T}\frac{dh}{dt}\right] \tag{3.15}$$

Substituting equations (3.15) into equation (3.6) and rearranging yields

$$[\rho T + \varphi]\frac{dP}{dt} - \rho\varphi\frac{dh}{dt} + \rho^2 a^2 T\frac{\partial u}{\partial x} = 0 \tag{3.16}$$

The above equation can be expressed as

$$[\rho T + \varphi]\left(\frac{\partial P}{\partial t} + u\frac{\partial P}{\partial x}\right) - \rho\varphi\left(\frac{\partial h}{\partial t} + u\frac{\partial h}{\partial x}\right) + \rho^2 a^2 T\frac{\partial u}{\partial x} = 0 \tag{3.17}$$

Equation (3.17) is the form of the mass conservation equation employed, in which the total derivative of density with time has been expressed in terms of fluid pressure and enthalpy.

3.2.2 Conservation of Momentum

The momentum conservation equation is derived from the application of Newton's second law of motion. This equation relates the sum of the forces acting on a fluid element to its acceleration, or rate of change of momentum in the direction of the resultant force. It can be stated that the rate of change of momentum within a control volume plus the rate of change of momentum due to fluid flow across the boundary is equal to the external and internal forces acting on the control volume.

Sum of forces = Rate of change of momentum within the control volume + net rate of momentum due to fluid flow across the boundary.

(3.18)

This can be mathematically expressed as

$$\sum F_x = \frac{\partial}{dt}(\rho A u)dx + \frac{\partial}{dx}(\rho A u^2)dx \tag{3.19}$$

Figure 3.2 shows the forces acting on the fluid element within the control volume. They include:

1. Gravitational force (F_g)

2. Pressure forces (F_p): This is the force due to the effect of pressure acting on the boundary of the control volume at point x_1 and x_2. At point x_2, the pressure force is negative since it is in the opposite direction of flow.

3. Frictional force (F_f): This is the force that acts in the opposite direction to flow.

Other force terms due to tangential and normal viscous stresses, electromagnetic and electrostatic forces are ignored.

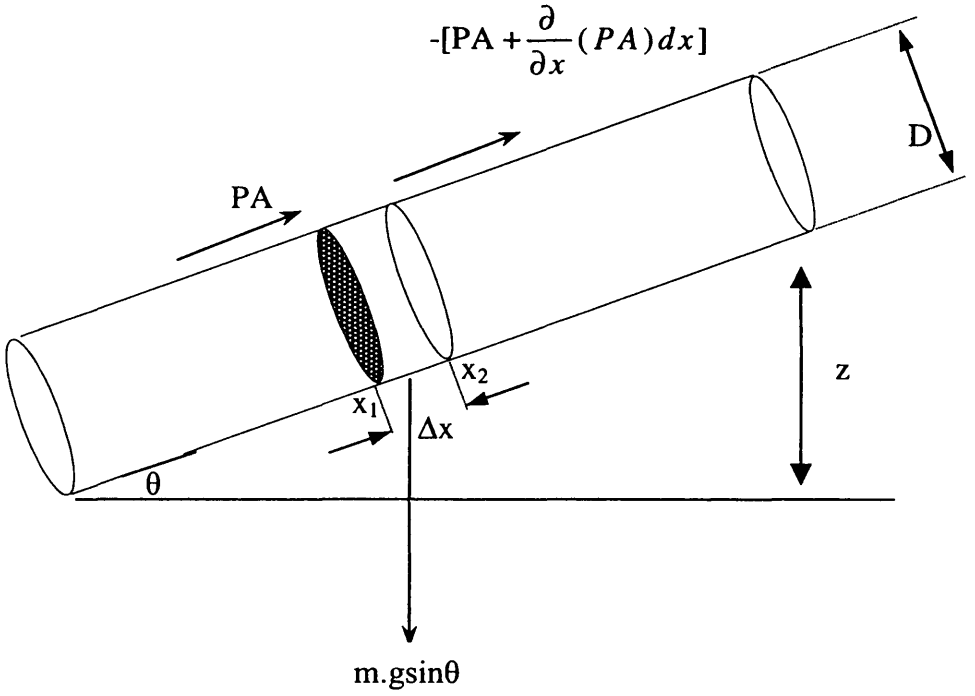

Figure 3.2: Schematic representation of the forces acting on a control volume within a pipeline.

Referring to figure 3.2,

$$F_g = \rho A dx.g\sin\theta \tag{3.20}$$

$$F_p = PA - [\, PA + \frac{\partial}{\partial x}(PA)dx \,] \tag{3.21}$$

$$F_f = -\frac{\rho u^2}{2}.\frac{4f_w}{D}.Adx \tag{3.22}$$

Where f_w is the Fanning friction factor

Substituting equations (3.20-3.22) into equation (3.19) and dividing through by $A\Delta x$ results in

$$-\frac{2\rho u^2 f_w}{D} - \rho g\sin\theta = \frac{\partial(\rho u)}{\partial t} + \frac{\partial(\rho u^2)}{\partial x} + \frac{\partial P}{\partial x} \tag{3.23}$$

Expanding the terms in the brackets, resolving and rearranging equation (3.23) yields

$$-\frac{2\rho u^2 f_w}{D}-\rho\cdot g\cdot\sin\theta=\frac{\partial P}{\partial x}+\rho\frac{\partial u}{\partial t}+\rho u\frac{\partial u}{\partial x}+u(\frac{\partial \rho}{\partial t}+u\frac{\partial \rho}{\partial x}+\rho\frac{\partial u}{\partial x}) \quad (3.24)$$

The expression in the bracket of equation (3.24) is that of the continuity equation i.e. equation (3.6), which equals zero. Hence, (3.24) becomes

$$\rho\frac{\partial u}{\partial t}+\rho u\frac{\partial u}{\partial x}=-\frac{\partial P}{\partial x}-\rho g\sin\theta+\beta_x \quad (3.25)$$

This can also be expressed in terms of the total derivatives as

$$\rho\frac{du}{dt}=-\frac{\partial P}{\partial x}-\rho g\sin\theta+\beta_x \quad (3.26)$$

Where $\beta_x=-\frac{2f_w\rho\cdot u\cdot|u|}{D}$ (3.27)

The modulus of the velocity, $|u|$ is introduced so that the friction force will change sign with change in flow direction.

Equations (3.25) and (3.26) are the differential forms of the momentum equation employed in this study.

3.2.3 Conservation of Energy

The energy conservation equation is derived from the application of the first law of thermodynamics, which states that the change in the total energy of a system is due to the heat transmitted, and the work done on the system. This can be mathematically expressed as

$$\frac{\partial(\rho E)}{\partial t}.Adx+\frac{\partial(\rho Eu)}{\partial x}Adx=W_{shaft}+W_{shear}+W_n+Q_h \quad (3.28)$$

$$Adx=W_{shaft}+W_{shear}+W_n+Q_h$$

Where

E= Total energy per unit mass of the fluid

Q_h = Rate of heat transfer to the fluid

W_n = Net rate of work done by normal forces (i.e. pressure).

W_{shaft} and W_{shear} are the mechanical work and the shear work respectively which are negligible and are assumed to be zero in this study.

Equation (3.28) can be reduced to give

$$\frac{\partial(\rho E)}{\partial t}.Adx+\frac{\partial(\rho Eu)}{\partial x}.Adx=\bar{W}_n+Q_h \tag{3.29}$$

The total energy (E) of the fluid is the sum of its internal (i), kinetic and potential energies per unit mass. It is given by:

$$E=i+\frac{1}{2}u^2+gz \tag{3.30}$$

Where, z is the elevation of the fluid element from the horizontal plane and g is the acceleration due to gravity

On the other hand, the rate of work done by pressure forces on the surface of the control volume is given by $PA.u$.

Figure 3.3 gives a schematic representation of the work done on the control volume.

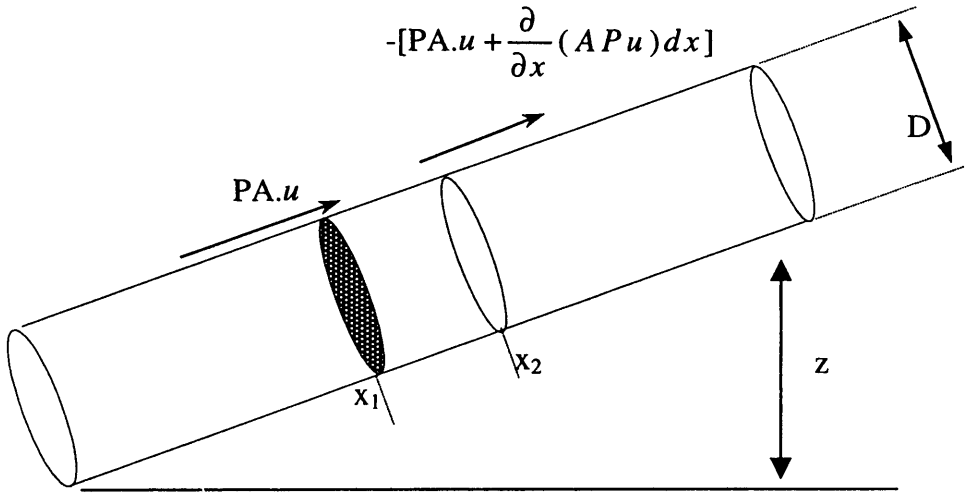

Figure 3.3: Schematic representation showing the work acting on the surfaces of a control volume within a pipeline.

At point x_1:

$$W_{x_1} = A(Pu)_{x_1} \tag{3.31}$$

At point x_2:

$$W_{x_2} = -[A(Pu)_{x_1} + \frac{A\partial(Pu)}{\partial x}dx] \tag{3.32}$$

Hence the net rate of work by pressure forces, W_n acting on the fluid element is

$$W_n = W_{x_2} + W_{x_1} = -A\frac{\partial(Pu)}{\partial x}dx \tag{3.33}$$

Substituting equation (3.33) into equation (3.29), dividing through by $A.dx$, results in

$$\frac{\partial(\rho E)}{\partial t} + \frac{\partial(\rho Eu)}{\partial x} + \frac{\partial(Pu)}{\partial x} = q_h \tag{3.34}$$

Where, q_h is the heat transferred to the fluid element per unit volume.

However, the internal energy of a fluid is related to its specific enthalpy, h, by:

$$i = h - \frac{P}{\rho} \tag{3.35}$$

Thus, substituting for the internal energy term in equation (3.30) and multiplying both sides of the equation by ρ gives:

$$\rho E = \rho H - P + \rho gz \tag{3.36}$$

Where the total enthalpy, H is defined as:

$$H = h + \frac{u^2}{2} \tag{3.37}$$

Substituting equation (3.36) into equation (3.34) gives

$$\frac{\partial(\rho H - P + \rho gz)}{\partial t} + \frac{\partial(\rho H - P + \rho gz + P)u}{\partial x} = q_h \tag{3.38}$$

Expanding the equation above gives:

$$H\frac{\partial \rho}{\partial t}+\rho\frac{\partial H}{\partial t}-\frac{\partial P}{\partial t}+gz\frac{\partial \rho}{\partial t}+\rho g\frac{\partial z}{\partial t}+H\frac{\partial \rho u}{\partial x}+\rho u\frac{\partial H}{\partial x}+gz\frac{\partial \rho u}{\partial x}+g\rho u\frac{\partial z}{\partial x}=q_h \tag{3.39}$$

Collecting like terms and simplifying equation (3.39) becomes:

$$\rho\frac{\partial H}{\partial t}+\rho g\frac{\partial z}{\partial t}+(H+gz)\left(\frac{\partial \rho}{\partial t}+\frac{\partial \rho u}{\partial x}\right)+\rho u\left(\frac{\partial H}{\partial x}+g\frac{\partial z}{\partial x}\right)-\frac{\partial P}{\partial t}=q_h \tag{3.40}$$

It can be observed that the terms in the second bracket of the above equation make up mass conservation equation and hence disappear. Also from figure 3.2 it can be seen that

$$\frac{\partial z}{\partial x}=\sin\theta \tag{3.41}$$

Since the pipeline inclination is time invariant:

$$\frac{\partial z}{\partial t}=0 \tag{3.42}$$

Substituting equations (3.41) and (3.42) into equation (3.40) and rearranging gives:

$$\rho\left(\frac{\partial H}{\partial t}+u\frac{\partial H}{\partial x}\right)+\rho ug\sin\theta-\frac{\partial P}{\partial t}=q_h \tag{3.43}$$

From equation (3.5), the differential equation above can be written as:

$$\rho\frac{dH}{dt}+\rho ug\sin\theta-\frac{\partial P}{\partial t}=q_h \tag{3.44}$$

Substituting equation (3.37) into equation (3.44) results in:

$$\rho\left[\frac{dh}{dt}+\frac{1}{2}\frac{du^2}{dt}\right]+\rho ug\sin\theta-\frac{\partial P}{\partial t}=q_h \tag{3.45}$$

Simplifying equation (3.45) produces

$$\rho\left[\frac{dh}{dt}+u\frac{du}{dt}\right]+\rho ug\sin\theta-\frac{\partial P}{\partial t}=q_h \tag{3.46}$$

Multiplying the momentum conservation equation i.e., equation (3.26) by, u results in

$$\rho u\frac{du}{dt}=-u\frac{\partial P}{\partial x}-\rho ug\sin\theta+u\beta_x \tag{3.47}$$

Rearranging equation (3.47) gives

$$\rho u g \sin\theta = -u\frac{\partial P}{\partial x} - \rho u\frac{du}{dt} + u\beta_x \tag{3.48}$$

Substituting equations (3.48) into (3.46) and expanding the terms in the brackets gives:

$$\rho\frac{dh}{dt} + \rho u\frac{du}{dt} - \rho u\frac{du}{dt} - u\frac{\partial P}{\partial x} - \frac{\partial P}{\partial t} + u\beta_x = q_h \tag{3.49}$$

Resolving equation (3.49) results in

$$\rho\frac{dh}{dt} - \frac{\partial P}{\partial t} - u\frac{\partial P}{\partial x} = q_h - u\beta_x \tag{3.50}$$

By applying the notation expressed in equation (3.5), the differential equation above can be written as:

$$\rho\frac{dh}{dt} - \frac{dP}{dt} = q_h - u\beta_x \tag{3.51}$$

Equations (3.50) and (3.51) are the energy conservation equations expressed in terms of fluid enthalpy.

3.3 Cubic Equation of State (CEoS)

In this study, the Peng-Robinson equation of state (PR-EoS) is used to calculate vapour-liquids thermodynamic data as it has been shown by Walas (1987) to be applicable to high-pressure hydrocarbon mixtures.

The Peng-Robinson equation of state is given by (Walas, 1987):

$$P = \frac{RT}{V - b_V} - \frac{a_V\alpha}{V^2 + 2b_V V - (b_V)^2} \tag{3.52}$$

Where:

$$a_V = \frac{k_1 R^2 T_c^2}{P_c^2} \tag{3.53}$$

$$b_V = \frac{k_2 R T_c}{P_c} \tag{3.54}$$

For mixtures,

$$a_V\alpha = \sum\sum y_i y_j (a_V\alpha)_{ij} \tag{3.55}$$

$$(a_V\alpha)_{ij} = (1-K_{ij})\sqrt{(a_V\alpha)_i (a_V\alpha)_j} \tag{3.56}$$

$$b_{V,i} = \sum y_i b_{V,i} \tag{3.57}$$

Where,

P, P_c	=	The absolute and critical pressures of the fluid respectively (KN/m^2)
T, T_c	=	The absolute and critical temperatures of the fluid respectively (K)
V	=	The fluid's molar volume (m^3/Kmol)
R	=	The universal gas constant (KJ/(Kmol-K))
k_1, k_2	=	Constants specific to the equations of state
α	=	The alpha function
K_{ij}	=	The binary interaction parameter
y_i, y_j	=	Component mole fractions

3.4 Hydrodynamic and Thermodynamic Relations for the HE Model

This section presents the various equations employed for determining two-phase mixture density, the fluid's speed of sound a and other important hydrodynamic properties. The expression for the quantity of heat transferred to the fluid (q_h) is derived.

3.4.1 Two-phase Mixture Density

In the case of the homogeneous equilibrium model assumption, a pseudo-mixture density, (ρ) based on pure liquid and gas densities is calculated using the EoS. This is given by,

$$\rho = \frac{\rho_g \rho_l}{\rho_g(1-\chi)+\rho_l\chi} \tag{3.58}$$

Where the subscripts, g and l denote gas and liquid phase respectively. The term, χ refers to the fluid quality, and is the mass of vapour per unit mass of bulk fluid. The values of the respective phase densities can be calculated according to the following equations:

$$\rho_g = \frac{PM_g}{Z_g RT} \tag{3.59}$$

$$\rho_l = \frac{PM_l}{Z_l RT} \tag{3.60}$$

Where Z is the fluid compressibility

3.4.2 Calculation for a Single and Two-phase Speed of Sound

For single-phase real fluids, the speed of sound through the fluid can be expressed analytically as (Picard and Bishnoi, 1987):

$$a^2 = \frac{\gamma}{k\rho} \tag{3.61}$$

Where γ is the ratio of specific heats, and k is the isothermal coefficient of volumetric expansion.

By definition, γ and k can be expressed respectively as (Walas, 1987):

$$\gamma = \frac{C_P}{C_V} \tag{3.62}$$

$$k = -\rho\left(\frac{\partial V}{\partial P}\right)_T \tag{3.63}$$

Where, C_p and C_v are the specific heats at constant pressure and volume respectively, and V is the specific volume of the fluid.

From equation (3.63), the term $\left(\frac{\partial V}{\partial P}\right)_T$ can be obtained analytically by differentiating the Peng-Robinson equation (equation. (3.52)) to give

$$\left(\frac{\partial V}{\partial P}\right)_T = \left[\frac{-RT}{(V-b_V)^2} - \frac{a_V \alpha.(2V+2b_V)}{[V^2+2b_V V-(b_V)^2]^2}\right]^{-1} \tag{3.64}$$

For two-phase flows, the analytical determination of γ and c_p becomes complex (Mahgerefteh et al., 1999). Hence the speed of sound is evaluated numerically at a given temperature and pressure as (Mahgerefteh et al., 1999):

$$a^2 = \left(\frac{\Delta P}{\rho(T,P) - \rho(T^*, P - \Delta P)} \right)_s \tag{3.65}$$

Where the subscript, s denotes a constant entropy condition and T, P, ΔP and ρ, denote temperature, pressure, infinitesimal change in pressure ($\Delta P = 1x10^{-6}$ bar) and density of the fluid respectively. T* represents the corresponding fluid temperature obtained by performing a $(P-\Delta P)/s$ flash.

3.4.3 Evaluation of the Thermodynamic Function, φ

For single-phase fluids, the isochoric thermodynamic functionφ is given (Picard and Bishnoi, 1988) as

$$\varphi = \left(\frac{\partial P}{\partial s} \right)_\rho = \frac{\rho \cdot \xi \cdot T \cdot a^2}{C_p} \tag{3.66}$$

Where, ξ is the isobaric coefficients of volumetric expansion i.e. $\frac{1}{V}\left(\frac{\partial V}{\partial T} \right)_P$ and C_p, is the specific heat capacity at constant pressure.

For two-phase flows, φ is determined numerically in the following manner.

Given that

$$\varphi = \left(\frac{\partial P}{\partial s} \right)_\rho \equiv \left(\frac{\partial P}{\partial s} \right)_V \tag{3.67}$$

From Maxwell's relations (Walas, 1987):

$$\left(\frac{\partial P}{\partial s} \right)_V = -\left(\frac{\partial T}{\partial V} \right)_s \tag{3.68}$$

Since $V = 1/\rho$, hence $dV = -(1/\rho^2)\, d\rho$), equation (3.68) can expressed as:

$$\left(\frac{\partial T}{\partial V}\right)_s = \rho^2 \left(\frac{\partial T}{\partial \rho}\right)_s \tag{3.69}$$

Therefore from equation (3.67):

$$\varphi = \rho^2 \left(\frac{\partial T}{\partial \rho}\right)_s = \rho^2 \left(\frac{\Delta T}{\Delta \rho}\right)_s \tag{3.70}$$

Hence, by performing an isentropic flash calculation as required by equation (3.65), the above can be solved numerically.

3.4.4 Fanning Friction Factor (f_w) Determination

The Fanning friction factor, f_w is required for calculating the contribution of frictional force to the momentum equation (equation (3.25)). It is a function of the flow Reynolds' number.

Ouyang and Aziz (1996) conducted a study over a wide range of flow conditions ($2000 \leq Re \leq 1 \times 10^8$; $10^{-6} \leq \varepsilon/D_{in} \leq 0.1$), on the performance of 11 major explicit correlations for predicting friction factor. The predictions of these correlations were compared with the highly accurate Colebrook (1939) correlation. From their results, the authors recommend the use of the Chen (1979), Serghides (1984) and the Zigrang and Sylvester (1982) correlations. These three correlations were observed to show a maximum absolute deviation of less than 1 % from the Colebrook correlation.

Although the Colebrook correlation is accepted as the most accurate in terms of predictions, it has the disadvantage of expressing the friction factor in an implicit form with the resultant equation requiring expensive iterations to solve (Ouyang and Aziz, 1996). Thus in this work, for the calculation of the Fanning friction factor, f) for transition and turbulent flows in rough pipes, the Chen (Chen, 1979) correlation is employed. It is given by:

$$\frac{1}{\sqrt{f_w}} = 3.48 - 1.7372 \ln\left(\frac{\varepsilon}{r_{in}} - \frac{16.2446}{\mathrm{Re}} \ln A\right) \tag{3.71}$$

Where:

$$A = \frac{(\varepsilon/r_{in})^{1.0198}}{6.0983} + \left(\frac{7.149}{\mathrm{Re}}\right)^{0.8981} \tag{3.72}$$

ε, is the pipe roughness and r_{in} represents the pipe inner radius

For turbulent flow in smooth pipelines, Rohsenow et al. (1998) recommend the correlation proposed by Techo et al. (1965). The authors assert that the equation gives predictions within ±2 % of extensive experimental measurements (Rohsenow et al., 1998). It is given by

$$\frac{1}{\sqrt{f_w}} = 1.7372 \ln \frac{\mathrm{Re}}{1.964 \ln \mathrm{Re} - 3.8215} \tag{3.73}$$

In the laminar region, the evaluation of the fanning friction factor is independent of the pipe roughness. Thus in general, the fanning friction factor for laminar fully developed flow is given by (Ouyang and Aziz, 1996; Rohsenow et al., 1998):

$$f_w = \frac{16}{\mathrm{Re}} \tag{3.74}$$

3.4.5 Thermal Conductivity and Viscosity Calculations

The vapour thermal conductivity and viscosity used in calculating the Nusselt, Reynolds and Prandtl numbers are determined form the Ely and Hanley's method (Ely and Hanley, 1981, 1983) for non-polar gaseous mixtures. The method is based on the principle of corresponding states with methane as the reference fluid. Assael et al. (1996) claim that Ely and Hanley's (1981) method is one of the few schemes that are able to predict, with reasonable accuracy, the viscosity and thermal conductivity of a large number of non-polar components and their mixtures.

Viscosities and thermal conductivities for liquid mixtures containing alkanes (methane to n-dodecane) are determined from a semi-empirical scheme proposed by

Dymond and Assael (Assael et al., 1996). The scheme generally applies between temperatures ranging from 280 K to 400 K and pressures from saturation up to 990 atm. and has an uncertainty in predictions not greater than 5 per cent (Assael et al., 1996). The authors employed over 2,000 measurements of viscosity and thermal conductivity to optimise the coefficients used in the scheme.

For mixtures containing different classes of compounds, correlations proposed by DIPPR (Design Institute for Physical Property Data) (Daubert and Danner, 1990) are employed due to their accuracy and ease of use.

For two-phase fluids, the mixture thermal conductivity and viscosity is employed as given by:

$$\frac{1}{c_m} = \frac{\chi}{c_g} + \frac{1-\chi}{c} \tag{3.75}$$

Where χ and c respectively represent the fluid quality and the property to be determined.

3.4.6 Fluid/Wall Heat Transfer

Newton's cooling law (Picard and Bishnoi, 1989; Chen et al., 1995b; Fairuzov, 1998; Mahgerefteh et al., 1999) is commonly employed for determining the heat transferred to a fluid flowing in a pipe. It is given by:

$$q_h = \frac{4}{D_{in}} U_h \left(T_{amb} - T_f\right) \tag{3.76}$$

Where U_h, is the overall heat transfer coefficient, D_{in}, the pipeline inner diameter, while T_{amb} and T_f denote the ambient and the fluid temperatures respectively.

Equation (3.76) lumps the pipeline wall and the ambient as a single heat source with a constant heat transfer coefficient. This simplified approach ignores the effect of the pipeline wall both as a heat source/sink, and as a medium for heat conduction between the ambient and the flowing fluid.

Upon pipeline rupture, huge pressure and temperature drops are not uncommon. This leads to phase change and the attendant change in flow and heat transfer properties.

The heat transfer properties of a flowing gas as compared to a flowing liquid/two-phase mixture may differ by orders of magnitude (up to a factor of 2,000 or more (Incropera and De Witt, 1996)). Thus the assumption of a constant heat transfer coefficient for flows with widely varying heat transport properties may introduce errors in simulated results. Furthermore, the use of a constant heat transfer coefficient and the task of picking a "right" value could be daunting and in some cases impossible.

Therefore, in order to properly model the transient heat transfer process occurring at the wall-fluid interface, a transient energy balance across the fluid-wall-ambient surfaces based on a lumped body approach is employed. This method is used to update the wall temperatures after a given time step, thus estimating the heat input to the fluid in the next time interval. Figure 3.4 shows a schematic representation of the important heat transfer parameters.

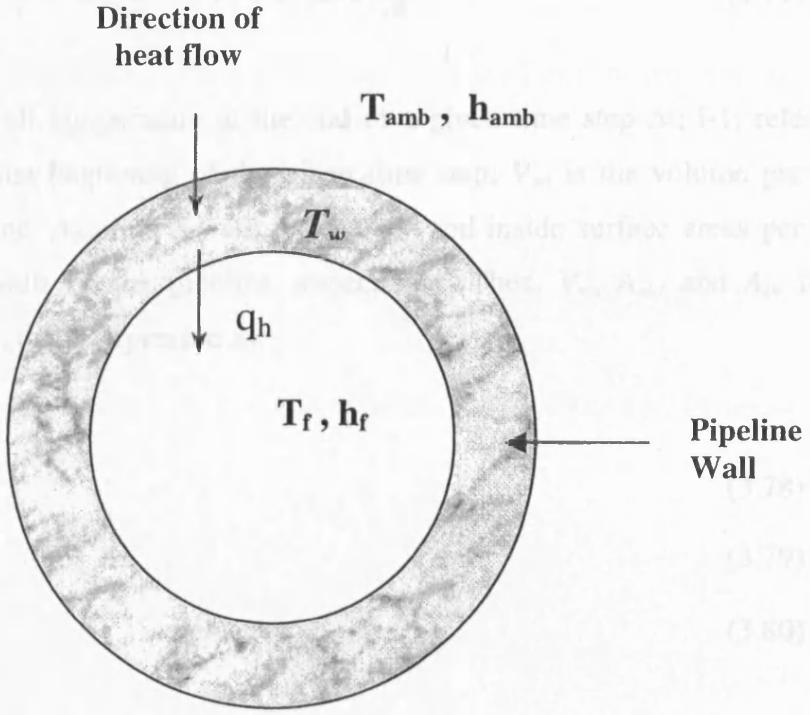

Figure 3.4: Schematic representation of the heat flow across the cross-section of a pipeline wall based on the lumped body approach.

Where T_{amb}, h_{amb} and T_w respectively represent the ambient temperature, heat transfer coefficient of the ambient, and wall temperature. T_f, h_f and q_h respectively represent the fluid's tempereature, fluid heat transfer coefficient, and the quantity of heat transferred to the fluid.

In the lumped body approach, it is assumed that there is no temperature stratification across the pipeline walls. It is also assumed that the wall density ρ_w, specific heat capacity, C_{pw} and thermal conductivity, κ_w are time and space invariant. In addition, the ambient and fluid heat transfer coefficients are assumed to remain constant within a given time step. Finally, heat transfer occurs predominantly in the radial direction across the pipeline wall, with heat flow resulting from longitudinal conduction neglected.

From figure 3.4, the transient energy balance across the pipeline based on the above assumptions can be written as (Myers, 1971):

$$h_{amb}^{i-1}A_{out}\left(T_{amb}-T_w\right)-h_f^{i-1}A_{in}\left(T_w-T_f\right)=\rho_w C_{pw}V_w\frac{dT_w}{dt} \tag{3.77}$$

Where, T_w is the wall temperature at the end of a given time step Δt; i-1, refers to property values at the beginning of the given time step; V_w, is the volume per unit length of the pipeline; A_{out} and A_{in} are the outside and inside surface areas per unit length along the walls of the pipeline respectively. Thus, V_w, A_{out} and A_{in} for a cylindrical pipeline can be expressed as:

$$V_w=\pi\left(\frac{D_{out}^2-D_{in}^2}{4}\right) \tag{3.78}$$

$$A_{out}=\pi D_{out} \tag{3.79}$$

$$A_{in}=\pi D_{in} \tag{3.80}$$

Where, D_{out} and D_{in} are the outer and inner diameter of the pipeline respectively. Rearranging equation (3.81) gives:

$$\frac{dT_w}{dt}+\left(\frac{h_{amb}^{i-1}A_{out}+h_f^{i-1}A_{in}}{\rho_w C_{pw}V_w}\right)T_w=\frac{h_{amb}^{i-1}A_{out}T_{amb}+h_f^{i-1}A_{in}T_f}{\rho_w C_{pw}V_w} \tag{3.81}$$

Alternatively, equation (3.81) can be expressed as:

$$\frac{dT_w}{dt}+AT_w=B \tag{3.82}$$

Where:

$$A=\frac{h_{amb}^{i-1}A_{out}+h_f^{i-1}A_{in}}{\rho_w C_{pw}V_w} \tag{3.83}$$

$$B=\frac{h_{amb}^{i-1}A_{out}T_{amb}+h_f^{i-1}A_{in}T_f}{\rho_w C_{pw}V_w} \tag{3.84}$$

Equation (3.82) is a linear first order differential equation, and has a general solution given by (Stroud, 1995):

$$T_w e^{\int A dt}=\int B e^{\int A dt}dt \tag{3.85}$$

The evaluation of equation (3.85) is subject to the following boundary condition:

$$T_w=T_w^{i-1};\ \text{when}\ \Delta t=0 \tag{3.86}$$

Since A and B contain variables that are assumed to be constants within a given time step (Δt), integrating equation (3.85) gives:

$$T_w e^{A\Delta t}=\frac{B}{A}e^{A\Delta t}+BC \tag{3.87}$$

Where C is a constant of integration.

By applying the boundary condition given in equation (3.86), C can be evaluated as:

$$C=\frac{T_w^{i-1}}{B}-\frac{1}{A} \tag{3.88}$$

Substituting for, C in equation (3.87) gives: $T_w e^{A\Delta t}=\frac{B}{A}e^{A\Delta t}+B\left(\frac{T_w^{i-1}}{B}-\frac{1}{A}\right)$ (3.89)

Equation (3.87) can be rearranged as:

$$T_w = \frac{B}{A} + \left(T_w^{i-1} - \frac{B}{A} \right) e^{-A\Delta t} \tag{3.90}$$

By employing the expressions of A and B given in equation (3.83) and (3.84), the updated wall temperature at the end of a time step Δt can be obtained.

Thus by applying the Newton's cooling law, the rate of heat transferred to the fluid (q_h) in a given time step can be better approximated by:

$$q_h = \frac{4}{D_{in}} h_f^{i-1} \left(T_w - T_f \right) \tag{3.91}$$

3.5 The Steady State Isothermal Flow Model

Prior to pipeline failure, it is assumed that isothermal steady state flow prevails in the pipeline. Several field tests conducted involving steady state fluid flow in pipelines suggest that isothermal flow conditions can be assumed to prevail (Uhl et al., 1965). Consequently, in this section, the isothermal steady state pressure drop equation for one-dimensional flow are derived based on the continuity and momentum equation presented in section 3.2.1 and 3.2.2 respectively.

From equation (3.4), the steady state expression (i.e. when all fluid properties are time invariant) for continuity in one-dimension can be written as:

$$u \frac{d\rho}{dx} + \rho \frac{du}{dx} = 0 \tag{3.92}$$

Separating variables and rearranging equation (3.92), gives

$$\int_{\rho_{i-1}}^{\rho_i} \frac{d\rho}{\rho} = -\int_{u_{i-1}}^{u_i} \frac{du}{u} \tag{3.93}$$

Integrating equation (3.93) gives:

$$\ln\left(\frac{\rho_i}{\rho_{i-1}} \right) = -\ln\left(\frac{u_i}{u_{i-1}} \right) \tag{3.94}$$

Equation (3.94) can be rewritten as:

$$\rho_{i-1} u_{i-1} = \rho_i u_i \text{ (i.e. } \rho u = \text{constant)} \tag{3.95}$$

Where the subscripts i-1 and i respectively represents the penultimate and current grid point under consideration.

Equation (3.95) is the governing equation for mass conservation at steady state for flow in a uni-diameter pipeline.

From equation (3.25), the steady state momentum equation in one-dimension can be expressed as:

$$\rho u\frac{du}{dx} = -\frac{dP}{dx} - \rho g\sin\theta + \beta_x \tag{3.96}$$

Where the steady state frictional force term (β_x) is given by

$$\beta_x = -2\frac{f_w}{D_{in}}\rho u|u| \tag{3.97}$$

The correlations required in calculating the fanning wall friction factor (f_w) have already been discussed in section 3.4.4.

Substituting the expression for β_x in equation (3.96) and rearranging gives

$$\frac{dP}{dx} + \rho u\frac{du}{dx} = -\left(\frac{2f\rho u|u|}{D_{in}} + \rho g\sin\theta\right) \tag{3.98}$$

Multiplying both the above equation by ρdx

$$\rho dP + \rho^2 u du = -\left(\frac{2f(\rho u)^2}{D_{in}} + \rho^2 g\sin\theta\right)dx \tag{3.99}$$

Multiplying equation (3.92) by dx and rearranging

$$du = -\frac{ud\rho}{\rho} \tag{3.100}$$

Substituting the expression for du into equation (3.99) gives

$$\rho dP - (\rho u)^2\frac{d\rho}{\rho} = -\left(\frac{2f(\rho u)^2}{D_{in}} + \rho^2 g\sin\theta\right)dx \tag{3.101}$$

The above equation can be expressed as

$$\rho dP + K_1 \frac{d\rho}{\rho} = (K_2 + \rho^2 K_3) dx \tag{3.102}$$

Where

$$-(\rho u)^2 = K_1 \tag{3.103}$$

$$-\frac{2f(\rho u)^2}{D_{in}} = K_2 \tag{3.104}$$

$$-g \sin\theta = K_3 \tag{3.105}$$

Rearranging equation (3.102) and taking the limits results in

$$\int_{P_{i-1}}^{P_i} \frac{\rho}{(\rho^2 K_3 + K_2)} dP + K_1 \int_{\rho_{i-1}}^{\rho_i} \frac{d\rho}{\rho(\rho^2 K_3 + K_2)} = \int_{x_{i-1}}^{x_i} dx \tag{3.106}$$

The second integral on the LHS of equation (3.106) can be integrated analytically by expressing as partial fractions such that

$$\frac{1}{\rho(\rho^2 K_3 + K_2)} \equiv \frac{A}{\rho} + \frac{B\rho + C}{(\rho^2 K_3 + K_2)} = \frac{A(\rho^2 K_3 + K_2) + B\rho^2 + C\rho}{\rho(\rho^2 K_3 + K_2)} \tag{3.107}$$

Collating like terms and equating results in

$$(AK_3 + B)\rho^2 = 0 \tag{3.108}$$

$$C\rho = 0 \tag{3.109}$$

$$AK_2 = 1 \tag{3.110}$$

The solution of equations (3.108-3.110) gives the values of A, B and C respectively as $1/K_2$, $-\frac{K_3}{K_2}$, and 0

Hence, substituting the values of A, B and C into equation (3.107), and the resultant expression into the second integral on the LHS of equation (3.106) results in

$$\int_{\rho_{i-1}}^{\rho_i} \frac{d\rho}{\rho\left(\rho^2 K_3 + K_2\right)} = \frac{1}{K_2}\int_{\rho_{i-1}}^{\rho_i} \frac{d\rho}{\rho} - \frac{K_3}{K_2}\left(\int_{\rho_{i-1}}^{\rho_i} \frac{\rho d\rho}{\rho^2 K_3 + K_2}\right) \tag{3.111}$$

This can then be expressed analytically as

$$\int_{\rho_{i-1}}^{\rho_i} \frac{d\rho}{\rho\left(\rho^2 K_3 + K_2\right)} = \frac{1}{2K_2}\left[2\ln\left(\frac{\rho_i}{\rho_{i-1}}\right) - \ln\frac{\left(\rho_i^2 K_3 + K_2\right)}{\left(\rho_{i-1}^2 K_3 + K_2\right)}\right] \tag{3.112}$$

The first integral on the LHS of equation (3.106) can be evaluated numerically using the trapezoidal rule (Stroud, 1995) to give

$$\int_{P_{i-1}}^{P_i} \frac{\rho}{\left(\rho^2 K_3 + K_2\right)} dP = \frac{1}{2}\left[\left(\frac{\rho}{\rho^2 K_3 + K_2}\right)_{P_i} + \left(\frac{\rho}{\rho^2 K_3 + K_2}\right)_{P_{i-1}}\right]\left(P_i - P_{i-1}\right) \tag{3.113}$$

Substituting the expression of the integrals in equations (3.112) and (3112) into equation (3.106) results in

$$\frac{1}{2}\left[\left(\frac{\rho}{\rho^2 K_3 + K_2}\right)_{P_i} + \left(\frac{\rho}{\rho^2 K_3 + K_2}\right)_{P_{i-1}}\right]\left(P_i - P_{i-1}\right) + \frac{K_1}{2K_2}\left[2\ln\left(\frac{\rho_i}{\rho_{i-1}}\right) - \ln\frac{\left(\rho_i^2 K_3 + K_2\right)}{\left(\rho_{i-1}^2 K_3 + K_2\right)}\right] = x_i - x_{i-1} \tag{3.114}$$

The expression derived above is used for calculating the isothermal steady state pressure drop along a pipeline. K_1, K_2 and K_3 are constants already defined by equations (3.103-3.105)

The stepwise algorithm below is a summary of the methodology used for calculating the isothermal steady state pressure drop.

1. Collate data at pipeline inlet such as fluid pressure, temperature, velocity, etc.
2. Divide the pipeline into sections (grids) with the distance between the grids being $\Delta_x = x_i - x_{i-1}$.
3. Guess the downstream pressure at the next gird point i.e. P_i.
4. In conjunction with an equation of state, evaluate the expression on the LHS of equation (3.114).
5. If equation (3.114) is satisfied, then the guessed downstream pressure is adopted as the solution. The fluid velocity u_i can then be obtained by applying equation (3.95). If the equation is not satisfied, go back to step 3 and update the guessed P_i.
6. Update the flow properties at this grid point and calculate the pressure drop at the next grid using steps 3-5 until the variables at the final grid point is calculated.

3.6 Hyperbolicity of the Conservation Equations

The partial differential equations pertaining to conservation of mass, momentum and energy together with an equation of state (EoS) constitute a system of equations that are essentially Euler equations with source terms due to the friction term in the momentum equation and the heat transfer term in the energy equation.

In solving these partial differential equations, it is essential to establish their mathematical nature in order to implement the appropriate technique for solving them. It can be shown (see below) that the Euler equations derived on the basis of the inviscid bulk fluid flow assumption can be classified as quasilinear hyperbolic.

A partial differential equation is said to be quasilinear if all the derivatives of the dependent function $f(x, t)$ are linear, while their corresponding coefficients contain at least a term that is either a linear or non-linear function of f (Prasad and Ravindran, 1985). This is illustrated by equation (3.115) below:

$$a(x,t,f)f_t + b(x,t,f)f_x = c(x,t,f) \qquad (3.115)$$

Where f_t, f_x are the partial derivatives of the function f in terms of t and x respectively.

Equation (3.115) is quasilinear because its derivative terms (f_t, f_x) are linear while at least one of their corresponding coefficients [$a(x, t, f)$, $b(x, t, f)$] contain terms that are functions of f. The partial derivatives in the system of conservation equations (equations 3.17, 3.25, and 3.49) can be written as:

$$[\rho T+\varphi](P_t+uP_x)-\rho\varphi(h_t+uh_x)+\rho^2a^2T(u_x)=0 \quad \text{(Continuity)} \tag{3.116}$$

$$\rho(u_t+uu_x)+(P_x)=\alpha \quad \text{(Momentum)} \tag{3.117}$$

$$\rho(h_t+uh_x)-(P_t+uP_x)=\psi \quad \text{(Energy)} \tag{3.118}$$

Where:

$$\alpha=-\rho g\sin\theta+\beta_{wx} \tag{3.119}$$

$$\psi=q_h-u\beta_{wx} \tag{3.120}$$

β_{wx} = β_x (this re-annotation serves to avoid confusing β_x (a non-derivative term) with other derivative terms such as P_x).

From the definition given above for quasilinear equations, the system of conservation equations represented by equations (3.116-3.118) can be seen to be quasilinear. This is because all the partial derivative terms are linear. Furthermore, terms that are coefficients of the partial derivatives, such as density [ρ(P, h)] or flow velocity (u) are functions of some of the dependent functions (P, h, and u). These attributes render the system of equations quasilinear.

In general, the system of equations (i.e., equations (3.116-3.118)) presented above can be broadly expressed as:

$$Am_t+Bm_x=C \tag{3.121}$$

In matrix form, A, m_t, B and m_x, in equation (3.121) are given by:

$$A=\begin{bmatrix}\rho T+\varphi & -\rho\varphi & 0\\ 0 & 0 & \rho\\ -1 & \rho & 0\end{bmatrix}\quad m_t=\begin{bmatrix}P_t\\ h_t\\ u_t\end{bmatrix};\quad B=\begin{bmatrix}(\rho T+\varphi)u & -\rho\varphi u & \rho^2a^2T\\ 1 & 0 & \rho u\\ -u & \rho u & 0\end{bmatrix}\quad m_x=\begin{bmatrix}P_x\\ h_x\\ u_x\end{bmatrix}$$

$$C=\begin{bmatrix}0\\ \alpha\\ \psi\end{bmatrix} \tag{3.122}$$

Hyperbolic Quasilinear Partial Differential Equations

A quasilinear system of partial differential equations as given by equation (3.121) is said to be hyperbolic if the eigenvalue (λ), satisfying equation (3.123) given below, has real and distinct roots (i.e., λ_1, λ_2, λ_3 are real and distinct) (Prasad and Ravindran, 1985):

$$|B-\lambda A|=0 \tag{3.123}$$

Thus, for the conservation equations, equation (3.123) can be expressed as:

$$|B-\lambda A|=\begin{vmatrix}(\rho T+\varphi)(u-\lambda) & \rho\varphi(\lambda-u) & \rho^2a^2T\\ 1 & 0 & \rho(u-\lambda)\\ \lambda-u & \rho(u-\lambda) & 0\end{vmatrix}=0 \tag{3.124}$$

Hence:

$$-(\rho T+\varphi)(u-\lambda)\rho^2(u-\lambda)^2+\rho^2\varphi(\lambda-u)(\lambda-u)(u-\lambda)+\rho^3a^2T(u-\lambda)=0 \tag{3.125}$$

Factorising the above equation results in

$$(u-\lambda)\left[-(\rho T+\varphi)\rho^2(u-\lambda)^2+\rho^2\varphi(u-\lambda)^2+\rho^3a^2T\right]=0 \tag{3.126}$$

Factorising further and resolving yields:

$$(u-\lambda)\left[(-\rho^2(u-\lambda)^2(\rho T)+\rho^3a^2T\right]=0 \tag{3.127}$$

Dividing through by ρ^3T gives:

$$(u-\lambda)\left[a^2-(u-\lambda)^2\right]=0 \tag{3.128}$$

Solving equation (3.128) to obtain the roots of λ gives:

$$\lambda_1 = u \tag{3.129}$$

$$\lambda_2 = u - a \tag{3.130}$$

$$\lambda_3 = u + a \tag{3.131}$$

From equations (3.129-3.131), it can be seen that the eigenvalue (λ) that satisfy equation (3.123) are real and distinct. Thus, the systems of quasilinear partial differential equations for mass, momentum and energy conservation are hyperbolic.

This implies that the behaviour and properties of the physical system described by these equations will be dominated by wave-like phenomena (Prasad and Ravindran, 1985). Indeed the speed of propagation of these waves, known as Mach lines, are given by the eigenvalues *(u+a)* and *(u-a)*, which correspond to the right running and left running characteristic (Mach) lines respectively.

3.7 Numerical Techniques for Resolving Hyperbolic Equations

The conservation equations derived earlier have been shown to be quasi-linear and hyperbolic in nature. Since they posses no closed form, a numerical technique is required to resolve them.

By neglecting or linearising the non-linear terms, various graphical (Parmakian, 1963; Bergeron, 1961) and analytical (Rich, 1963) methods have been developed. These methods are approximate and cannot be used to analyse large systems or systems incorporating complex boundary conditions.

Commonly used techniques, more suitable for computer simulation are the finite-difference (explicit and implicit) method, and the method of characteristics (Lister, 1960; Swaffield, 1972; Boldy, 1975; Wylie and Streeter, 1978).

In summary, finite difference methods involve system discretisation followed by substitution of derivatives appearing in a differential equation with finite approximations to obtain a system of algebraic relations at all grid points. Either the

explicit or the implicit finite difference methods can be employed. The explicit method yields an explicit expression for each value at a new time level t_{n+1} in terms of nearby values at a previous time level t_n. The implicit method couples together values at different grid points at time t_{n+1} leading to an algebraic system of equations, which must be solved simultaneously with the aid of suitable boundary conditions.
Due to problems of convergence, instability and time step limitation commonly associated with explicit methods, implicit methods, which are unconditionally stable and permit the use of large/unrestrained time steps, are commonly employed (Swaffield and Boldy, 1993). However, implicit methods may involve the simultaneous solution of a large number of non-linear equations coupled with complex boundary conditions, thus rendering the implementation complicated. Furthermore, the time step cannot be increased arbitrarily since this will result in a smoothing of the transient pressure peaks. The attributes highlighted above therefore makes the finite difference methods unsuitable for modelling fast transients as encountered in pipeline rupture.

The method of characteristics (MOC) is the natural numerical method for quasi-linear hyperbolic systems with two independent variables. It is essentially an explicit finite difference scheme with a sufficiently different approach to warrant separate treatment. It is based on the principle of the propagation of characteristic waves and is therefore well suited to handling fast transient flow where each disturbance is captured along the propagating Mach lines. However, its primary disadvantage is the need for strict adherence to the time step-distance interval relationship based on the Courant stability criterion in its choice of time steps. This handicap has somewhat been compensated for with the advent of cheap and relatively fast computers.

Based on the work presented by earlier authors (Lister, 1960; Streeter, 1969; Chaudhry, 1987, Swaffield and Boldy, 1993, etc) the MOC has come to be widely accepted as the most appropriate technique for developing computer simulation programs of transient flow in internal fluid flow systems. In fact, for rapid transients in pipeline systems, the method of characteristics is generally considered to be the numerical method by which others may be judged for accuracy and efficiency (Swaffield, 1993).

For the reasons stated above, the MOC has been chosen as the numerical technique of choice employed in this work for resolving the conservative equations.

3.8 Concluding Remarks

In this chapter, the equations describing mass, momentum and energy conservation were derived. Of important note is that the mass conservation equation is formulated in terms of pressure, enthalpy and flow velocity as opposed to pressure, density and velocity. The former formulation has the advantage of significantly reducing the computational runtime and improved model accuracy.

The conservation equations together with the Peng-Robinson equation of state constitute the building blocks for modelling the outflow following the rupture or puncture of pipelines.

The various hydrodynamic and thermodynamic expressions for predicting important parameters including the speed of sound in two-phase media, fluid viscosity as well as fluid flow and phase dependent friction coefficient were presented. In addition, the expression for the quantity of heat transferred to the fluid from the ambient based on the lumped body approach was derived. This approach eliminates the need for assuming a constant overall heat transfer coefficient, and is expected to give predictions that are more reliable.

Furthermore, the steady state isothermal pressure drop model based on a real fluid was derived.

This chapter concluded by showing that the conservation equations derived are quasi-linear and hyperbolic in nature. The MOC was chosen to solve them, as it is well suited to handling the fast transients at the rupture plane.

In Chapter 4, the MOC is used to resolve the conservation equations to yield the corresponding compatibility equations. These equations together with the appropriate boundary conditions are then used to derive expressions for simulating the fluid

dynamics following full bore ruptures and punctures of both single pipelines and pipeline networks.

CHAPTER 4

APPLICATION OF THE METHOD OF CHARACTERISTICS (MOC) FOR MODELLING PIPELINE FAILURE

4.1 Introduction

The MOC involves the definition of an appropriate set of co-ordinates, in terms of the system's independent variables (e.g. distance and time) along which the system of partial differential equations are resolved.

The partial differential equations are converted into a system of ordinary differential equations (compatibility equations), which are only valid along that co-ordinate (characteristic line). The compatibility equations may then be solved by standard single step finite-difference methods for ordinary differential equations. The basic rationale underlying the use of characteristics is that by an appropriate choice of co-ordinates, the original system of hyperbolic equations can be replaced by a system whose co-ordinates are the characteristics.

There are two main grid discretisation methods for the MOC. These are the Characteristic Grid method (CG) which is also known as natural method of characteristics, and the Inverse Marching method or the Method of Specified Time Intervals (ST) (Flat, 1986).

In the Characteristic Grid method, characteristic co-ordinates are applied to two equations in two dependent variables, which is often the case when isothermal flow assumption is made (see for example, Wylie and Streeter, 1993). Applying the method of characteristic in this way makes it particularly simple. However Chen et al. (1993) extended this method to the three characteristic model necessary to describe non-isothermal transient fluid flow and this is referred to as the Wave Tracing method.

In any characteristic grid method, the position of the new solution point is not specified *a priori* , but is determined from the intersection of left and right running characteristics with origins located at known solution points or initial data. Hence, a free-floating grid is developed in the *x-t* plane as shown in figure 4.1. This method of characteristics is particularly accurate since the solution progresses naturally along the characteristic lines. However, when more than two characteristic lines are present, i.e. when an energy equation is solved, in addition to the mass and momentum conservation equations, interpolation is required to locate the path line intersection between known initial points.

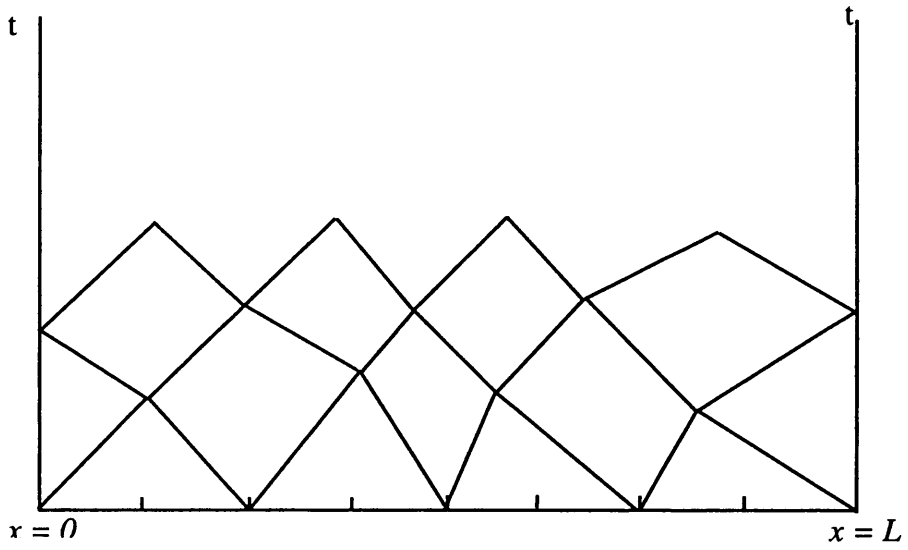

Figure 4.1: The Characteristic Grid method.

In the method of specified time intervals, the location of the solution points in the space-time grid is specified *a priori* and the characteristic lines are extended backwards in time to intersect a time line on which initial-data points lie. This necessitates interpolation to locate the intersection of all three characteristic lines on the previous time line.

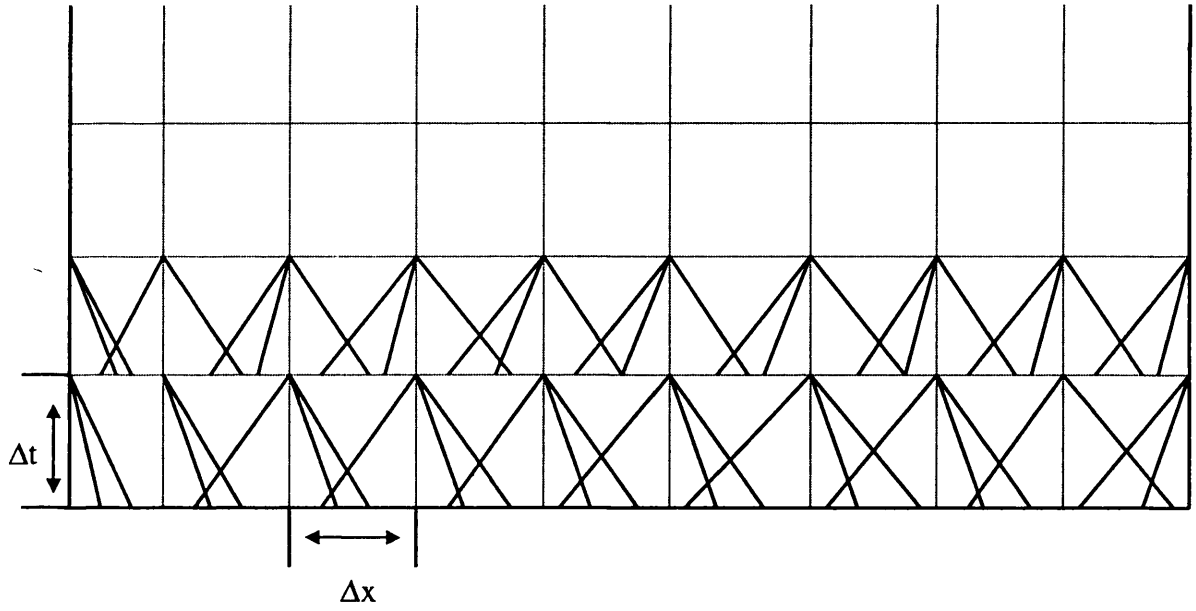

Figure 4.2: The method of Specified Time Intervals.

Although the CG method may be more accurate than the ST method, its main draw back is that there is no direct control on the time of input variables at boundaries. This is in contrast to the ST approach in which boundary conditions may be introduced at predefined times. This feature makes the CG method quite cumbersome in modelling systems that commonly prevail in reality such as valve closure, or pump shutdown. For this reason, the ST method of discretisation is used throughout this work.

4.2 Compatibility and Characteristic Equations

In chapter 3, the Euler equations for unsteady real fluid flow were derived in the following final form,

$$[\rho T+\varphi](P_t+uP_x)-\rho\varphi(h_t+uh_x)+\rho^2a^2T(u_x)=0 \quad \text{(Continuity)} \qquad (3.118)$$

$$\rho(u_t+uu_x)+(P_x)=\alpha \quad \text{(Momentum)} \qquad (3.119)$$

$$\rho(h_t+uh_x)-(P_t+uP_x)=\psi \quad \text{(Energy)} \qquad (3.120)$$

Where:

$$\alpha = -\rho g \sin\theta + \beta_x \tag{3.121}$$

$$\psi = q_h - u\beta_x \tag{3.122}$$

$$\beta_x = -\frac{2f_w \rho \cdot u \cdot |u|}{D} \tag{3.26}$$

The first step for MOC solution involves the conversion of the basic partial differential equations of flow into ordinary differential equations (compatibility equations). The second step involves solution of the compatibility equations based on the ST method and employing the Euler predictor-corrector technique (Zucrow and Hoffman, 1976) to enhance accuracy of the numerical results.

The two most common methods of converting the PDEs to ODEs (i.e. the first step) are the matrix transformation method (see Tiley, 1989) and that of multiplying the basic equations by an unknown parameter and subsequent summation. Wylie and Streeter (1978, 1993) employed the latter method for isothermal flow, while Zucrow and Hoffman (1976) also employed the same method for non-isothermal flow. Due to its simplicity and mathematical rigour, the method employed by Zucrow and Hoffman (1976) is adapted for use in this study.

Following Oke (2004), and introducing $1/\lambda$ to represent the slope of the characteristic lines, the conservation equations may be replaced by 3 compatibility equations, which are valid along 3 characteristic equations given below:

$$\rho d_0 h - d_0 P = \psi d_0 t \quad \text{along} \quad \frac{d_0 t}{d_0 x} = \frac{1}{u} = \frac{1}{\lambda_o} \tag{4.1}$$

(Path line compatibility equation along the Path line characteristic)

$$d_+ P + [\rho a] d_+ u = \left[\frac{\varphi\psi}{\rho T} + a\alpha\right] d_+ t \quad \text{along} \quad \frac{d_+ t}{d_+ x} = \frac{1}{u+a} = \frac{1}{\lambda_+} \tag{4.2}$$

(Positive Mach line compatibility equation along the Positive Mach line characteristic)

$$d\_P+[\rho a]d\_u=\left[\frac{\varphi\psi}{\rho T}-a\alpha\right]d\_t \quad \text{along} \quad \frac{d\_t}{d\_x}=\frac{1}{u-a}=\frac{1}{\lambda\_} \tag{4.3}$$

(Negative Mach line compatibility equation along the Negative Mach line characteristic)

The positive (C_+) and negative (C_-) mach lines respectively govern the speed at which expansion and compression waves propagate from the low and high-pressure ends of the pipeline respectively, while the path line (C_0) dictates the rate of flow through any given point along the pipeline.

To apply the characteristic and compatibility equations, a characteristic grid such as that shown in figure 4.2 needs to be devised. Figure 4.3 is a schematic representation of the characteristic lines at a grid point along the space (x) and time (t) independent co-ordinates.

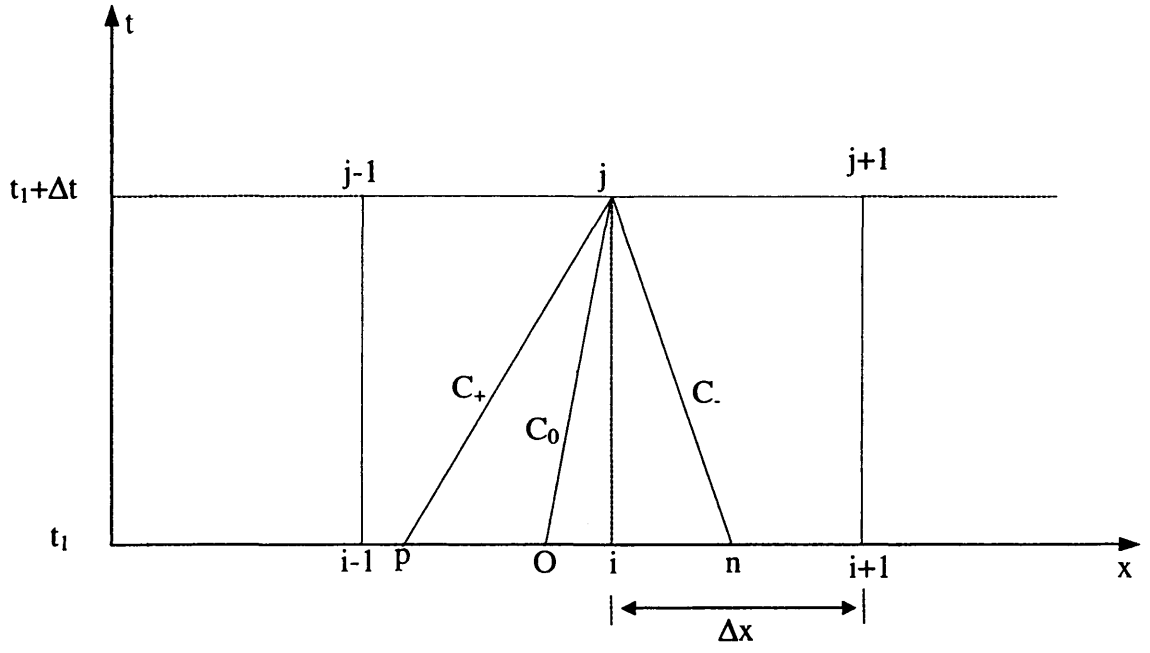

Figure 4.3: A schematic representation of Path line (C_0) and Mach lines (C_+, C_-) characteristics at a grid point along the time (t) and space (x) axes.

In order to apply the compatibility equations along the grid scheme, it is necessary to determine the conditions at points p, o and n at time t_1. This can be achieved by interpolating linearly (see section 4.3.1) between points i-1, i and i+1 whose conditions are known at time t_1. Once the conditions at p, o and n are determined, the compatibility equations are solved by the finite difference method to obtain the flow properties (P, h, u) at the intersection point *j*. Since the characteristics lines are by nature not straight, but rather curved, it is necessary to minimise errors introduced by the first order (linear) approximation. This is achieved by employing the corrector step (the Euler -corrector technique) to update the first order solution (see section 4.3.2).

The time steps (Δt) employed are pre-specified and are calculated subject to the Courant-Friedrichs-Lewy criterion (Courant et al.,1926; Zucrow and Hoffman, 1976). This criterion ensures the stability of the numerical scheme employed, and the solution obtained, for the entire system under consideration. It is given by:

$$\Delta t \leq \frac{\Delta x}{\left(|u+a|_{max}\right)} \tag{4.4}$$

As flow properties (u and a) may vary in each time step, it is important to maintain the numerical stability of solutions obtained in subsequent time steps.

4.3 Finite Difference Solution of the Compatibility and Characteristic Equations

The compatibility and characteristic equations (4.1-4.3) are total differentials, which are solved numerically by finite difference method using the Euler predictor-corrector algorithm. As the name implies, it comprises of a predictor step (first order approximation), which is used to estimate the approximate value of the flow properties at the solution point. On the other hand, the corrector step, based on second order approximation improves on the initial approximation of the predictor step.

4.3.1 First Order Approximation: Predictor Step

The compatibility equations given by equations (4.1) to (4.3) can be expressed in finite difference form as

$$(\rho)_0(h_j - h_0) - (P_j - P_0) = \psi_0(t_j - t_0) \tag{4.5}$$

$$(P_j - P_p) + (\rho a)_p (u_j - u_p) = \left(\frac{\varphi\psi}{\rho T} + a\alpha\right)_p (t_j - t_p) \tag{4.6}$$

$$(P_j - P_n) - (\rho a)_n (u_j - u_n) = \left(\frac{\varphi\psi}{\rho T} - a\alpha\right)_n (t_j - t_n) \tag{4.7}$$

The subscripts assigned to the various properties in equations (4.5) to (4.7) denote the location in space and time, as shown in figure 4.3

In order to calculate the flow properties (P, h, u, ρ, etc) at the solution point *j*, it is necessary that the positions (x_p , x_o and x_n) and fluid properties at the intersection of the characteristic lines at the previous time level (t_1) be determined. This can be determined from the knowledge of the slope of the characteristics lines and by linear interpolation between points i-1, i and i+1 whose conditions are known at time t_1.

By expressing the characteristic lines in finite difference form, the path line, positive Mach line and negative Mach line can be expressed respectively as

$$\lambda_0 = u_o = \frac{x_i - x_o}{\Delta t} \Rightarrow x_o = x_i - u_o \Delta t \tag{4.8}$$

$$\lambda_+ = u_p + a_p = \frac{x_i - x_p}{\Delta t} \Rightarrow x_p = x_i - (u_p + a_p)\Delta t \tag{4.9}$$

$$\lambda_- = u_n - a_n = \frac{x_i - x_n}{\Delta t} \Rightarrow x_n = x_i - (u_n - a_n)\Delta t \tag{4.10}$$

Also, assuming that flow properties (Z) at the lower time level (t_1) vary linearly in space, linear interpolation formulas that estimate unknown flow variables at points p,

o, and n from known variables at points (i), (i-1), and (i+1) can be expressed respectively as:

$$Z_p = Z_{i-1} + \frac{Z_i - Z_{i-1}}{x_i - x_{i-1}}\left(x_p - x_{i-1}\right) \tag{4.11}$$

$$Z_o = \begin{cases} Z_{i-1} + \dfrac{Z_i - Z_{i-1}}{x_i - x_{i-1}}\left(x_o - x_{i-1}\right) & \text{if } \lambda_o > 0 \\ Z_i + \dfrac{Z_{i+1} - Z_i}{x_{i+1} - x_i}\left(x_o - x_i\right) & \text{if } \lambda_o < 0 \end{cases} \tag{4.12}$$

$$Z_n = Z_i + \frac{Z_{i+1} - Z_i}{x_{i+1} - x_i}\left(x_n - x_i\right) \tag{4.13}$$

Where $Z = P, h, u,$ *and* a

Thus the expressions for the velocity (u) and speed of sound (a) in equations (4.8) - (4.10) can be obtained from linear interpolation formulas. These expressions can then be substituted back into the characteristic equations, (4.8) to (4.10) to give:

$$u_p = u_{i-1} + \frac{u_i - u_{i-1}}{x_i - x_{i-1}}\left[x_i - x_{i-1} - \Delta t\left(u_p + a_p\right)\right] = u_i - \frac{u_i - u_{i-1}}{x_i - x_{i-1}}\Delta t\left(u_p + a_p\right) \tag{4.14}$$

Rearranging equation (4.14) results in:

$$u_p\left(1 + \frac{u_i - u_{i-1}}{x_i - x_{i-1}}\Delta t\right) + \frac{u_i - u_{i-1}}{x_i - x_{i-1}}\Delta t a_p = u_i \tag{4.15}$$

Conducting the same manipulation for a_p, gives:

$$a_p\left(1 + \frac{a_i - a_{i-1}}{x_i - x_{i-1}}\Delta t\right) + \frac{a_i - a_{i-1}}{x_i - x_{i-1}}\Delta t u_p = a_i \tag{4.16}$$

Equations (4.15) and (4.16) can be solved simultaneously for u_p and a_p.

Similarly a 2×2 system of equations can be set up for u_n and a_n by applying the same mathematical manipulation described above.

For u_o, the solution depends on whether the slope of the path line characteristic is positive or negative. The nature of the sign determines which way the fluid is flowing. If it is positive the, flow is travelling towards (i+1), while the converse is true if the sign is negative.

Thus from equations (4.8) and (4.12),

When $\lambda_o > 0$ then,

$$\lambda_0 = u_o = u_{i-1} + \frac{u_i - u_{i-1}}{x_i - x_{i-1}}\left(x_i - \Delta t u_o - x_{i-1}\right) = u_{i-1} + u_i - u_{i-1} - \frac{u_i - u_{i-1}}{x_i - x_{i-1}}\Delta t u_o \qquad (4.17)$$

Equation (4.17) on simplifying becomes:

$$u_o = \frac{u_i}{\left(1 + \frac{u_i - u_{i-1}}{x_i - x_{i-1}}\Delta t\right)} \qquad (4.18)$$

However, when $\lambda_o < 0$, from equations (4.8) and (4.12), u_o can be similarly derived as:

$$u_o = \frac{u_i}{\left(1 + \frac{u_{i+1} - u_i}{x_{i+1} - x_i}\Delta t\right)} \qquad (4.19)$$

Thus, the locations of x_p, x_n, and x_o can be obtained directly from equations (4.8) to (4.10) by substituting the calculated values for u_p, a_p, u_n, a_n, and u_o into their corresponding equations.

Thereafter, the values of P and h at the initial points p, o, and n are calculated from relevant linear interpolation formulas (i.e., equations (4.11), (4.12) and (4.13)). With the aid of these calculated values, other corresponding thermodynamic properties at the initial points such as ρ, T, and φ are determined by performing a *P-h* flash calculation.

Hence, at this stage all the initial point flow variables are available to compute the flow conditions at the solution point (j) in the predictor step.

Manipulating equations (4.6) and (4.7) respectively to solve for P_j gives:

$$P_j = K_1 - (\rho a)_p (u_j - u_p) + P_p \tag{4.20}$$

$$P_j = K_2 + (\rho a)_n (u_j - u_n) + P_n \tag{4.21}$$

Where K_1 and K_2 are given by:

$$K_1 = \left(\frac{\varphi \psi}{\rho T} + a\alpha \right)_p \Delta t \tag{4.22}$$

$$K_2 = \left(\frac{\varphi \psi}{\rho T} - a\alpha \right)_n \Delta t \tag{4.23}$$

Solving the equations (4.20) and (4.21) simultaneously for u_j gives:

$$u_j = \frac{K_1 - K_2 + (\rho a)_p u_p + (\rho a)_n u_n + P_p + P_n}{(\rho a)_n + (\rho a)_p} \tag{4.24}$$

Hence, the pressure at the solution point, P_j can be calculated by the direct substitution of u_j into either equations (4.20) or (4.21).

The enthalpy at the solution point can subsequently be obtained from the path line compatibility (i.e., equation (4.5)) as:

$$h_j = \frac{\psi_0 \Delta t + (P_j - P_0) + \rho_0 h_0}{\rho_0} \tag{4.25}$$

Once the pressure and enthalpy are determined, other thermodynamic properties at the solution point (e.g. ρ, φ, and T) are obtained from a pressure-enthalpy flash calculation.

The procedure in which the tentative values are obtained at the solution point "j" constitutes the predictor step.

4.3.2 Second Order Approximation: Corrector Step

To improve on the first order solution, a second order approximation to the compatibility and characteristic is required. The procedure is given below.

The second order finite difference form of the compatibility equations (equations 4.1-4.3) can be expressed as

Path line compatibility;

$$\frac{1}{2}\left[(\rho)_0+(\rho)_j\right](h_j-h_0)-(P_j-P_0)=\frac{1}{2}\left[\psi_0+\psi_j\right](t_j-t_0) \tag{4.26}$$

Positive Mach line compatibility;

$$(P_j-P_p)+\frac{1}{2}\left[(\rho a)_p+(\rho a)_j\right](u_j-u_p)=\frac{1}{2}\left[\left(\frac{\varphi\psi}{\rho T}+a\alpha\right)_p+\left(\frac{\varphi\psi}{\rho T}+a\alpha\right)_j\right](t_j-t_p) \tag{4.27}$$

Negative Mach line compatibility;

$$(P_j-P_n)-\frac{1}{2}\left[(\rho a)_n+(\rho a)_j\right](u_j-u_n)=\frac{1}{2}\left[\left(\frac{\varphi\psi}{\rho T}-a\alpha\right)_n+\left(\frac{\varphi\psi}{\rho T}-a\alpha\right)_j\right](t_j-t_n) \tag{4.28}$$

As with the predictor step, the positions x_p, x_o and x_n, and fluid properties at these corresponding locations need to be determined. This is achieved by expressing the characteristic equations (equations 4.1-4.3) in second order form and interpolating between points i-1, i and i+1.

The second order approximations to characteristic equation are given by:

Path line characteristic;

$$x_j-x_o=\frac{1}{2}(\lambda_0+\lambda_j)(t_j-t_o) \tag{4.29}$$

Positive Mach line or right running characteristic;

$$x_j - x_p = \frac{1}{2}(\lambda_p + \lambda_j)(t_j - t_p) \tag{4.30}$$

Negative Mach line or left running characteristic;

$$x_j - x_n = \frac{1}{2}(\lambda_n + \lambda_j)(t_j - t_n) \tag{4.31}$$

From equations (4.29), (4.30) and (4.31), the corrector step can be expressed as:

$$\frac{1}{2}(\lambda_0 + \lambda_j) = \frac{1}{2}(u_o + u_j^r) = \frac{x_i - x_o}{\Delta t} \Rightarrow x_o = x_i - \frac{\Delta t}{2}(u_o + u_j^r) \tag{4.32}$$

$$\frac{1}{2}(\lambda_+ + \lambda_j) = \frac{1}{2}(u_p + u_j^r) + \frac{1}{2}(a_p + a_j^r) = \frac{x_i - x_p}{\Delta t} \Rightarrow x_p = x_i - \frac{\Delta t}{2}(u_p + a_p + u_j^r + a_j^r) \tag{4.33}$$

$$\frac{1}{2}(\lambda_- + \lambda_j) = \frac{1}{2}(u_n + u_j^r) - \frac{1}{2}(a_n + a_j^r) = \frac{x_i - x_n}{\Delta t} \Rightarrow x_n = x_i - \frac{\Delta t}{2}(u_n - a_n + u_j^r - a_j^r) \tag{4.34}$$

The subscript j together with superscript r refer to the solution condition at the previous iteration step, r.

From equations (4.32) and (4.12), and following the same approach employed for the predictor step:

If $\lambda_o > 0$ then,

$$u_o = u_{i-1} + \frac{u_i - u_{i-1}}{x_i - x_{i-1}}\left(x_i - \frac{\Delta t}{2}(u_o + u_j^r) - x_{i-1} \right) \tag{4.35}$$

Rearranging (4.35) yields

$$u_o = \frac{u_i - \frac{u_i - u_{i-1}}{x_i - x_{i-1}}\frac{\Delta t}{2}u_j^r}{\left(1 + \frac{u_i - u_{i-1}}{x_i - x_{i-1}}\frac{\Delta t}{2}\right)} \tag{4.36}$$

If $\lambda_o < 0$, u_o can be obtained from equation (4.32) and (4.12) as:

$$u_o = \frac{u_i - \frac{u_{i+1}-u_i}{x_{i+1}-x_i}\frac{\Delta t}{2}u_j^r}{\left(1+\frac{u_{i+1}-u_i}{x_{i+1}-x_i}\frac{\Delta t}{2}\right)} \tag{4.37}$$

Thereafter, x_o is obtained by substituting u_o into equation (4.32)

From linear interpolation (equation (4.11)) and equation (4.33) gives:

$$u_p = u_{i-1} + \frac{u_i - u_{i-1}}{x_i - x_{i-1}}\left[x_i - x_{i-1} - \frac{\Delta t}{2}\left(u_p + a_p + u_j^r + a_j^r\right)\right] \tag{4.38}$$

Rearranging equation (4.38) yields:

$$u_p\left(1+\frac{u_i-u_{i-1}}{x_i-x_{i-1}}\frac{\Delta t}{2}\right)+\frac{u_i-u_{i-1}}{x_i-x_{i-1}}\frac{\Delta t}{2}a_p = u_i - \frac{u_i-u_{i-1}}{x_i-x_{i-1}}\frac{\Delta t}{2}\left(u_j^r + a_j^r\right) \tag{4.39}$$

Performing the same manipulation for a_p, using linear interpolation in conjunction with equation (4.33) yields:

$$a_p\left(1+\frac{a_i-a_{i-1}}{x_i-x_{i-1}}\frac{\Delta t}{2}\right)+\frac{a_i-a_{i-1}}{x_i-x_{i-1}}\frac{\Delta t}{2}u_p = a_i - \frac{a_i-a_{i-1}}{x_i-x_{i-1}}\frac{\Delta t}{2}\left(u_j^r + a_j^r\right) \tag{4.40}$$

As with the predictor step, equations (4.39) and (4.40) can be solved simultaneously for u_p and a_p, and by substituting these values into equation (4.33), x_p is obtained.

A 2×2 system of equations can also be set up for u_n and a_n in the corrector step, and x_n is obtained via equation (4.34).

The dependent flow variables at the solution point can now be calculated at the next iteration (r+1) step.

Manipulating equations (4.27) and (4.28) respectively to solve for P_j gives:

$$P_j^{r+1} = K_1 - \frac{1}{2}\left[(\rho a)_p + (\rho a)_j^r\right]\left(u_j^{r+1} - u_p\right) + P_p \tag{4.41}$$

$$P_j^{r+1} = K_2 + \frac{1}{2}\left[(\rho a)_n + (\rho a)_j^r\right]\left(u_j^{r+1} - u_n\right) + P_n \tag{4.42}$$

Where K_1 and K_2 are given by:

$$K_1 = \frac{1}{2}\left[\left(\frac{\varphi\psi}{\rho T} + a\alpha\right)_p + \left(\frac{\varphi\psi}{\rho T} + a\alpha\right)_j^r\right]\Delta t \tag{4.43}$$

$$K_2 = \frac{1}{2}\left[\left(\frac{\varphi\psi}{\rho T} - a\alpha\right)_n + \left(\frac{\varphi\psi}{\rho T} - a\alpha\right)_j^r\right]\Delta t \tag{4.44}$$

Solving the equations (4.41) and (4.42) simultaneously yields P_j^{r+1} and u_j^{r+1}

$$u_j^{r+1} = \frac{K_1 - K_2 + \frac{1}{2}\left[(\rho a)_p + (\rho a)_j^r\right]u_p + \frac{1}{2}\left[(\rho a)_n + (\rho a)_j^r\right]u_n + P_p - P_n}{\frac{1}{2}\left[(\rho a)_p + (\rho a)_j^r\right] + \frac{1}{2}\left[(\rho a)_n + (\rho a)_j^r\right]} \tag{4.45}$$

P_j^{r+1} is then obtained from equation (4.41), and the enthalpy at the solution point is obtained from the path line compatibility (i.e., equation (4.26)) as:

$$h_j^{r+1} = \frac{\left[\psi_0 + \psi_j^r\right]\Delta t + 2\left(P_j^{r+1} - P_0\right)}{\rho_o + \rho_j^r} + h_o \tag{4.46}$$

The above second order calculation procedure is repeated until a certain tolerance (*ca.* 10^{-5}) is satisfied for the three dependent variables, i.e. *P*, *h* and *u*. Figure 4.4 is the calculation flow chart for the solution of the flow variables at the next time step based on the predictor-corrector procedure, and is given below.

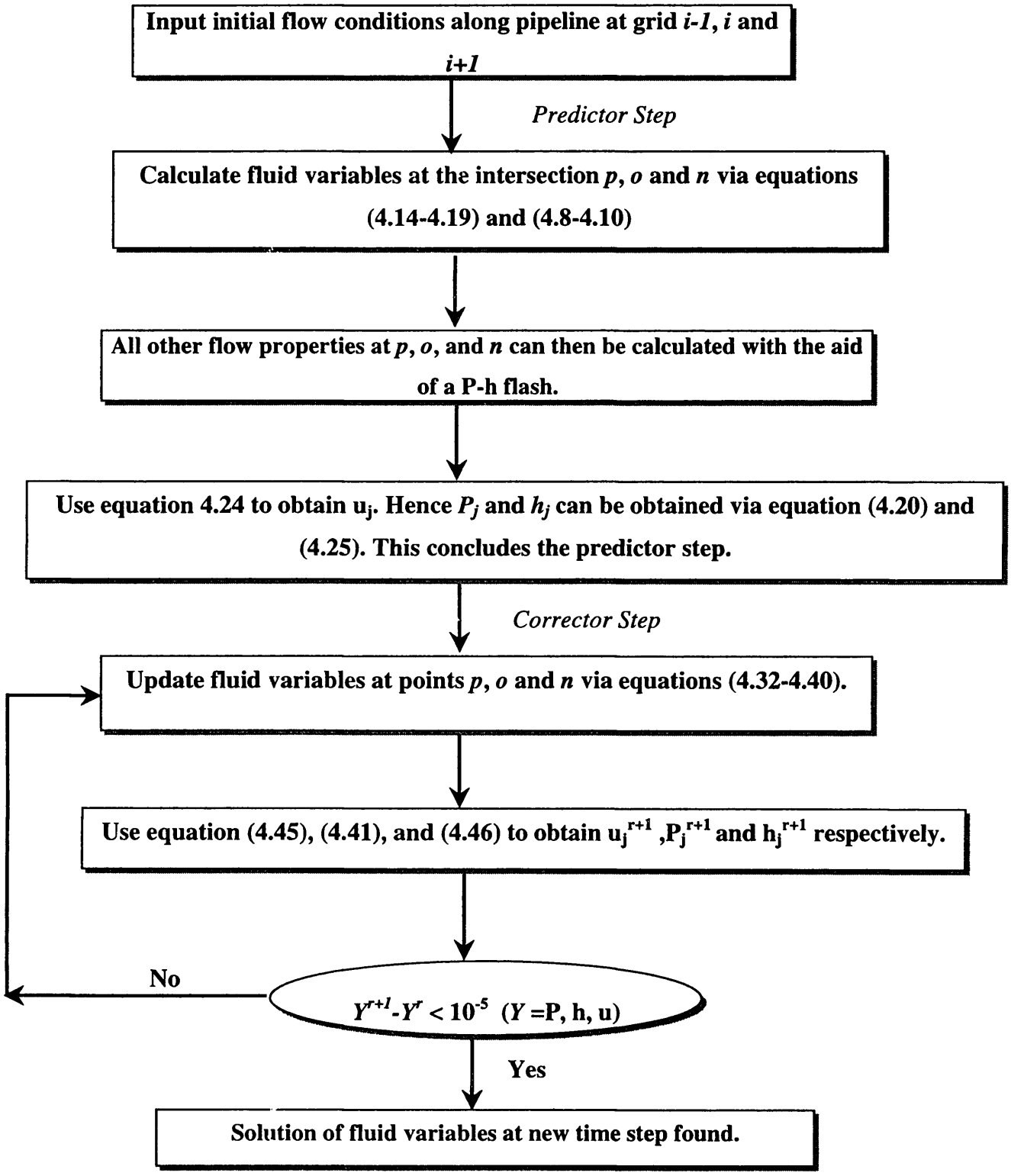

Figure 4.4: Calculation algorithm incorporating the Euler predictor-corrector technique in calculating the flow variables at the next time step.

4.3.3 Fluid Interface Modelling

A boundary between a gas and two-phase can be termed as a condensation boundary whereas that between liquid and two-phase can be termed as a boiling/condensation boundary.

The presence of an interface between a single-phase and a two-phase mixture poses problems from a computational viewpoint for two reasons.

Firstly, fluid properties may change significantly across an interface so the compatibility equations have to account for the presence of an interface (Nakamura et. al., 1975). In addition, if the characteristic lines were to cross such an interface, the assumption that the fluid properties vary linearly in space may lead to significant errors. Figure 4.5 shows the variation in acoustic velocity of a fluid comprising of 95% propane and 5 % methane with pressure at a constant temperature of 280 K.

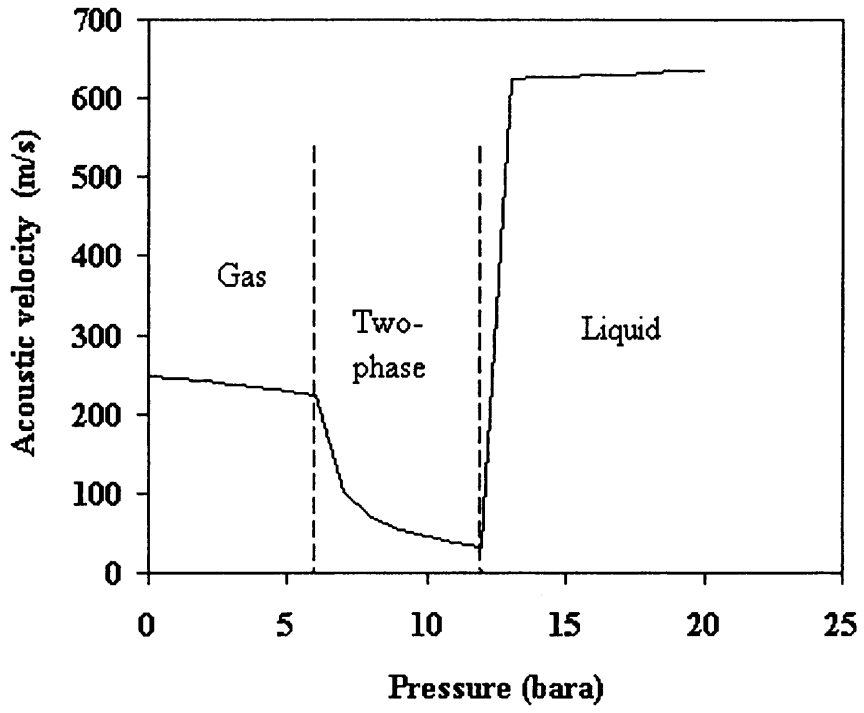

Figure 4.5: Variation of the acoustic velocity with pressure at 280K for a mixture of 95% Propane and 5% n-butane.

The sudden drop in the speed of sound at ca 6 bar and 13 bar coincides with the onset of condensation and boiling respectively in the mixture. As can be observed from figure 4.5, a greater drop in sound velocity is observed across the boiling boundary. Hence, if the characteristic line crosses either boundary (especially the liquid/two-phase), significant errors could be introduced in the simulated results by using interpolation.

Secondly, the substantial difference in acoustic velocities across the interface means that significant refraction would occur as schematically represented in figure 4.6 for a left travelling interface.

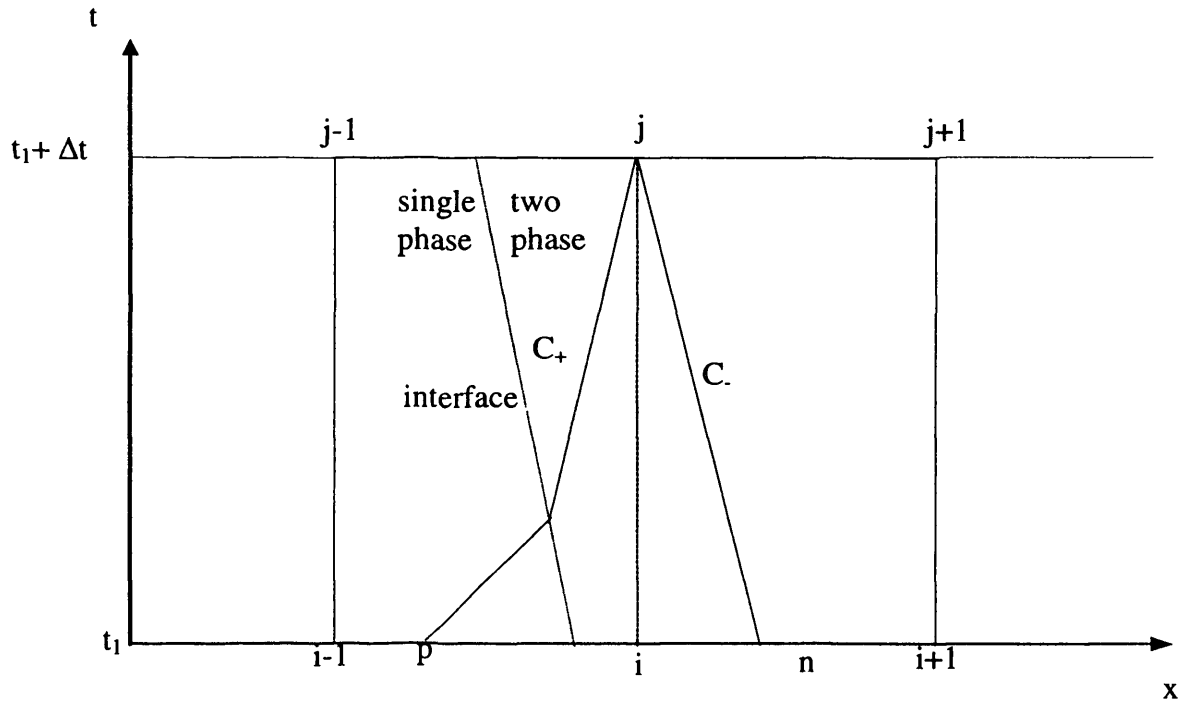

Figure 4.6: Refraction of the characteristic lines at a fluid interface.

The propagation velocity of the positive Mach line is greater in a single-phase than in a two-phase mixture hence the gradient ($\Delta t/\Delta x$) will be steeper in two-phase mixture than in single-phase.

The added complexity of the mathematical modelling that is necessary to fully account for this interface phenomenon is avoided in this study by using a sufficiently small Δt. This effectively forces the characteristic lines closer to grid *i* (see figure 4.6), hence minimising the overall error caused by interpolation and the possible refraction of characteristic lines. The effect of refraction across the fluid interface on simulated results is investigated in section 5.4.

4.3.4 Nested Grid System

In the nested grid system, the grids close to the rupture plane are subdivided into smaller meshes. Hence, the fast transients close to the rupture plane are modelled with a smaller meshes as compared to the rest of the pipeline. Clearly the longer the pipeline, the slower the transient within the pipeline, and therefore a comparatively large Δx (fewer grids) may be used to model the flow conditions in this region. The use of fewer grids results in fewer calculations being performed, which in turn reduces CPU run time.

The nested discritisation grid adopted in this study involves dividing 2 normal time-space meshes at the pipe exit into 5×5 cells such that the space-step is Δx_2. Further refinement is also possible by subdividing the last 2 finer meshes into 5×5 cells, with Δx_1 being the space-step is.

Figure 4.7 gives a schematic representation of the nested grid system

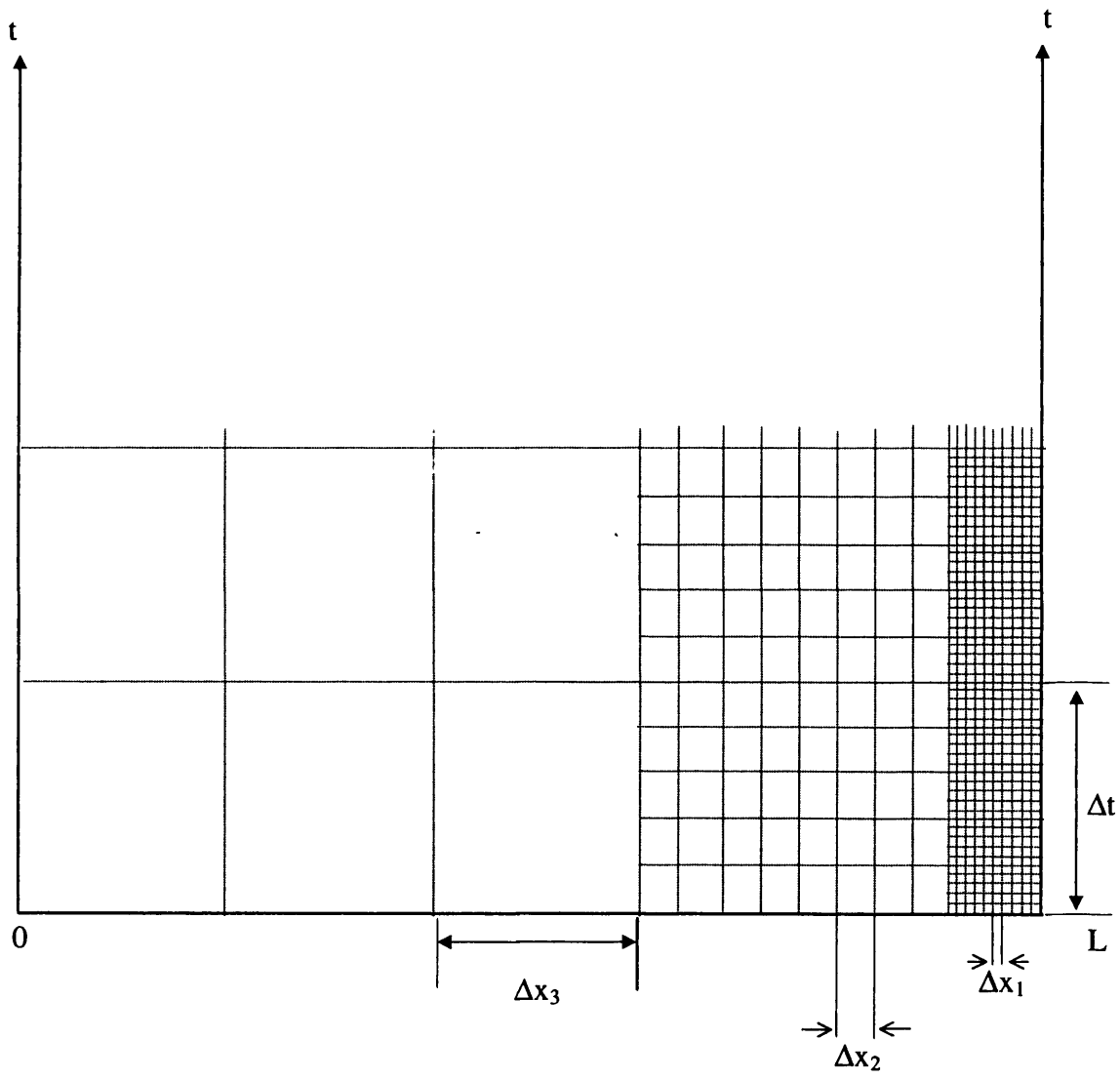

Figure 4.7: Schematic representation of the mesh arrangement in the nested grid system.

Since the smaller cells are geometrically similar, and contained within the large normal mesh (space-step = Δx_3), a consistent Courant number is maintained throughout the discharge process and numerical instability is avoided. Therefore accuracy in the fast transient region near the open end is assured, whilst speeding up the rest of the calculations along the coarser grid where Δx_3 is large.

For the purposes of terminology, a single refinement to the uniform, simple grid system (SGS) (i.e., just one 5×5 division over the two Δx's next to the rupture plane) is referred to as 'Nested Grid Scheme (NGS)', whereas the double refinement (say two 5×5 divisions) is denoted as 'Compound Nested Grid Scheme (CNGS)'.

At the junctions of different size meshes, slight modifications to the finite difference form of the compatibility equations presented in section 4.3.1 are required.

Methodology

The calculation at solution point j+4 at the boundary between the coarse and fine meshes as shown in figure 4.8 is given as an example.

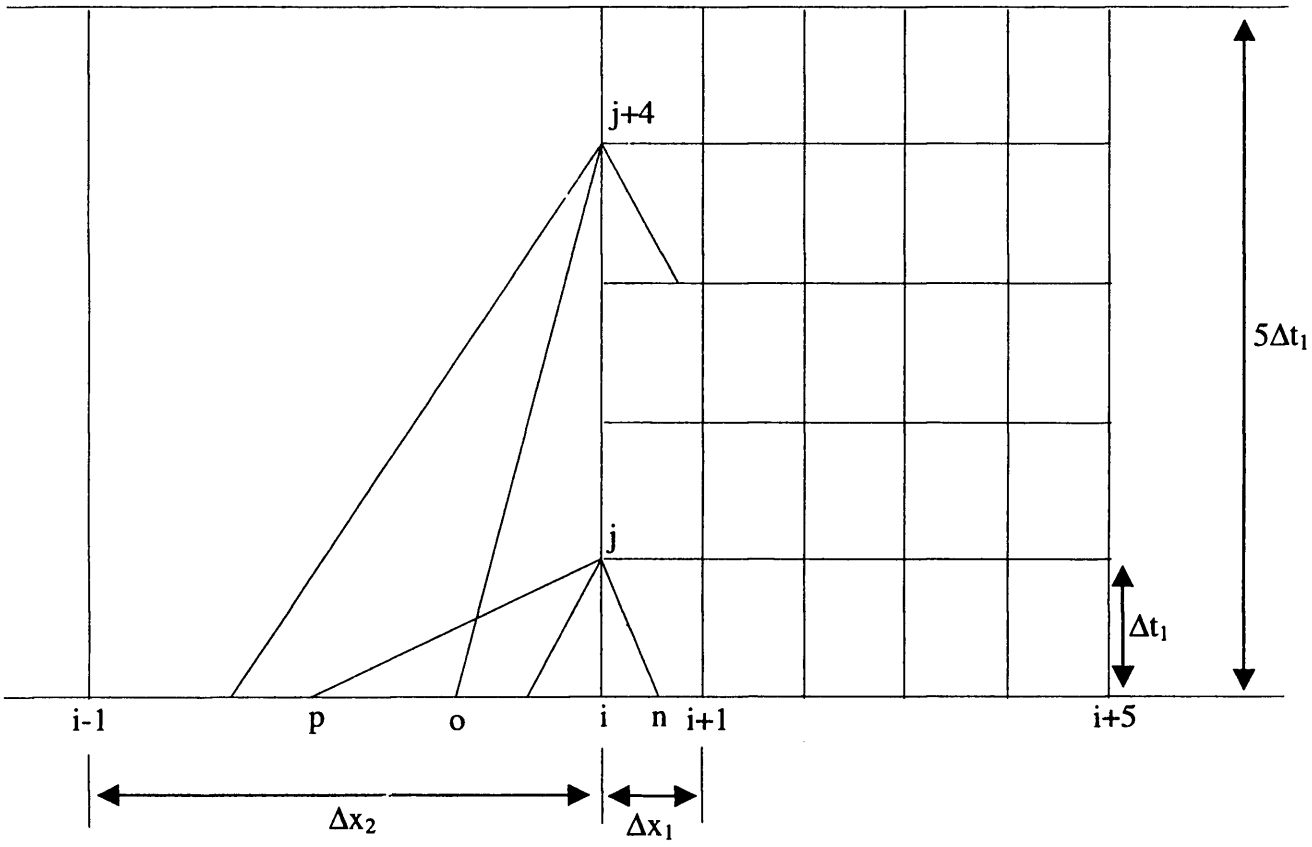

Figure 4.8: Boundary between coarse and fine mesh.

For the predictor step,

$$\lambda_0 = u_o = \frac{x_i - x_o}{4\Delta t_1} \Rightarrow x_o = x_i - 4\Delta t_1 u_o \tag{4.47}$$

$$\lambda_p = u_p + a_p = \frac{x_i - x_p}{4\Delta t_1} \Rightarrow x_p = x_i - \left(u_p + a_p\right)4\Delta t_1 \tag{4.48}$$

$$\lambda_n = u_n - a_n = \frac{x_i - x_n}{\Delta t_1} \Rightarrow x_n = x_i - \left(u_n - a_n\right)\Delta t_1 \tag{4.49}$$

Following the same mathematical manipulation as that performed in section 4.3.1, the simultaneous equations obtained for the solution of points u_p and a_p are:

$$u_p\left(1 + \frac{u_i - u_{i-1}}{\Delta x_2}4\Delta t_1\right) + \frac{u_i - u_{i-1}}{\Delta x_2}4\Delta t_1 a_p = u_i \tag{4.50}$$

$$a_p\left(1 + \frac{a_i - a_{i-1}}{\Delta x_2}4\Delta t_1\right) + \frac{a_i - a_{i-1}}{\Delta x_2}4\Delta t_1 u_p = a_i \tag{4.51}$$

Similarly a 2×2 system of equations can be set up for u_n and a_n based on the same mathematical manipulation to yield,

$$u_n\left(1 + \frac{u_{i+1} - u_i}{\Delta x_1}\Delta t_1\right) - \frac{u_{i+1} - u_i}{\Delta x_1}\Delta t_1 a_n = u_i \tag{4.52}$$

$$a_n\left(1 + \frac{a_{i+1} - a_i}{\Delta x_1}\Delta t_1\right) - \frac{a_{i+1} - a_i}{\Delta x_1}\Delta t_1 u_n = a_i \tag{4.53}$$

The solution for u_o depends on the direction of fluid flow.

If $\lambda_o > 0$ then,

$$u_o = \frac{u_i}{\left(1 + \frac{u_i - u_{i-1}}{\Delta x_2}4\Delta t_1\right)} \tag{4.54}$$

If $\lambda_o < 0$,

$$u_o = \frac{u_i}{\left(1 + \frac{u_{i+1} - u_i}{\Delta x_1} \Delta t_1\right)} \tag{4.55}$$

The locations of x_p, x_n, and x_o can now be calculated directly from equations (4.47) to (4.49) by substituting the calculated values for u_p, a_p, u_n, a_n, and u_o from the above equations. The pressure *(P)* and enthalpy *(h)* at the initial points p, o, and n are calculated from relevant linear interpolation formulas (equations (4.11), (4.12) or (4.13)).

All the initial point flow variables are now available to compute the flow conditions at the solution point *j* by employing the predictor-corrector algorithm.

The procedure for calculating the flow variables as summarised by the flow sheet in figure 4.4 is only applicable when the 3 characteristic equations are active, i.e. within the interior of the pipeline only. At the closed end of the pipeline (where only 2 characteristics are active), and at the rupture plane, special treatment and the imposition of suitable boundary conditions are required.

The section below deals with modelling the fluid dynamics at the closed end or upstream section, and the rupture plane (downstream) of the pipeline.

4.3.5 The Intact End Point Calculation

In modelling the intact end flow properties, the C_+ is non-existent, and the slope of the path line characteristic (C_o) is infinity since the velocity at all times (u_j) is zero. Figure 4.9 shows the grid scheme for the intact end point.

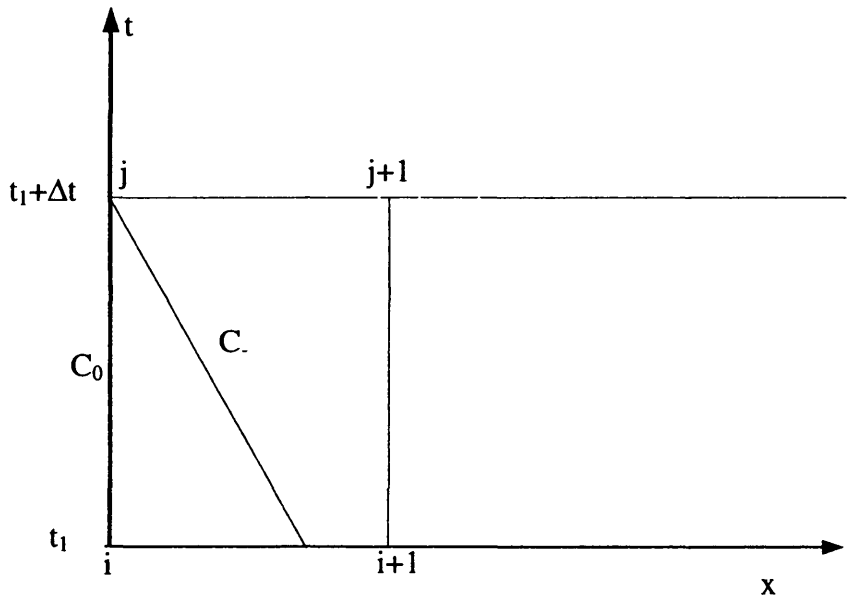

Figure 4.9: Grid scheme showing the active characteristic lines (C_0 and C_-) at the intact end point.

As can be seen from the figure 4.9 above, only the path line and negative characteristics are active. Based on equation (4.21), and noting that $u_j = 0$, the negative characteristic can be written as

$$P_j = K_2 + (\rho a)_n (0 - u_n) + P_n \tag{4.56}$$

Solving equation (4.56) yields the pressure at the intact end for the next time step, and is given as

$$P_j = K_2 - (\rho a u)_n + P_n \tag{4.57}$$

Where K_2 is defined by equation (4.23) as

$$K_2 = \left(\frac{\varphi \psi}{\rho T} - a\alpha \right)_n \Delta t \tag{4.23}$$

The upstream enthalpy (h_j) is obtained via the solution of the path line characteristic (equation (4.5)) and is given as

$$h_j = \frac{\psi_0 \Delta t + (P_j - P_0) + \rho_0 h_0}{\rho_0} \tag{4.58}$$

(Where P_j is obtained from equation (4.57))

The corrector step as described in section 4.32 is then subsequently employed to yield the flow variables at the intact end.

For scenarios where a pump or reservoir is present upstream, specifying the characteristics of the upstream source, for example pressure or flow rate, allows for the closure of the characteristic equations.

4.3.6 Rupture Plane Calculation

There are two time domains for discharge at the failure/release plane. The first is the choked/critical flow time domain. Its duration depends on how quickly the pressure at the failure plane drops down to the external pressure. Under this flow regime, the fluid expands and discharges at a critical pressure, which is higher than the ambient pressure, and at which the release rate is maximum. The release velocity corresponds to the sonic velocity at the prevailing release pressure, and conditions downstream of the release plane have no influence on the discharge process. Thus, during critical flow, no disturbance downstream of the release plane can propagate upstream. However, once the external pressure is reached at the release plane, the second time domain is initiated, and in this period the outflow is subsonic.

For both full-bore rupture and orifice at pipeline end, the fluid approaching the rupture plane (i.e., the solution point fluid with properties P_j, h_j, s_j,ρ_j, u_j) is assumed to undergo an isentropic expansion on exposure to ambient conditions.

In modelling the rupture plane conditions only the C_+ and C_0 characteristics are applicable. However, the absence of a simple algebraic relationship expressing the expansion process across the release plane as a function of one or more of the flow variables renders the simultaneous solution of the positive and path line compatibility

equations impossible. This necessitates the introduction of a "ghost" cell adjacent to the boundary cell as depicted in figure 4.10 within which expressions for the negative compatibility can be formulated. The ghost cell is a form of fictitious node with the node (i+1) lying on node (i) as illustrated in figure 4.10 below.

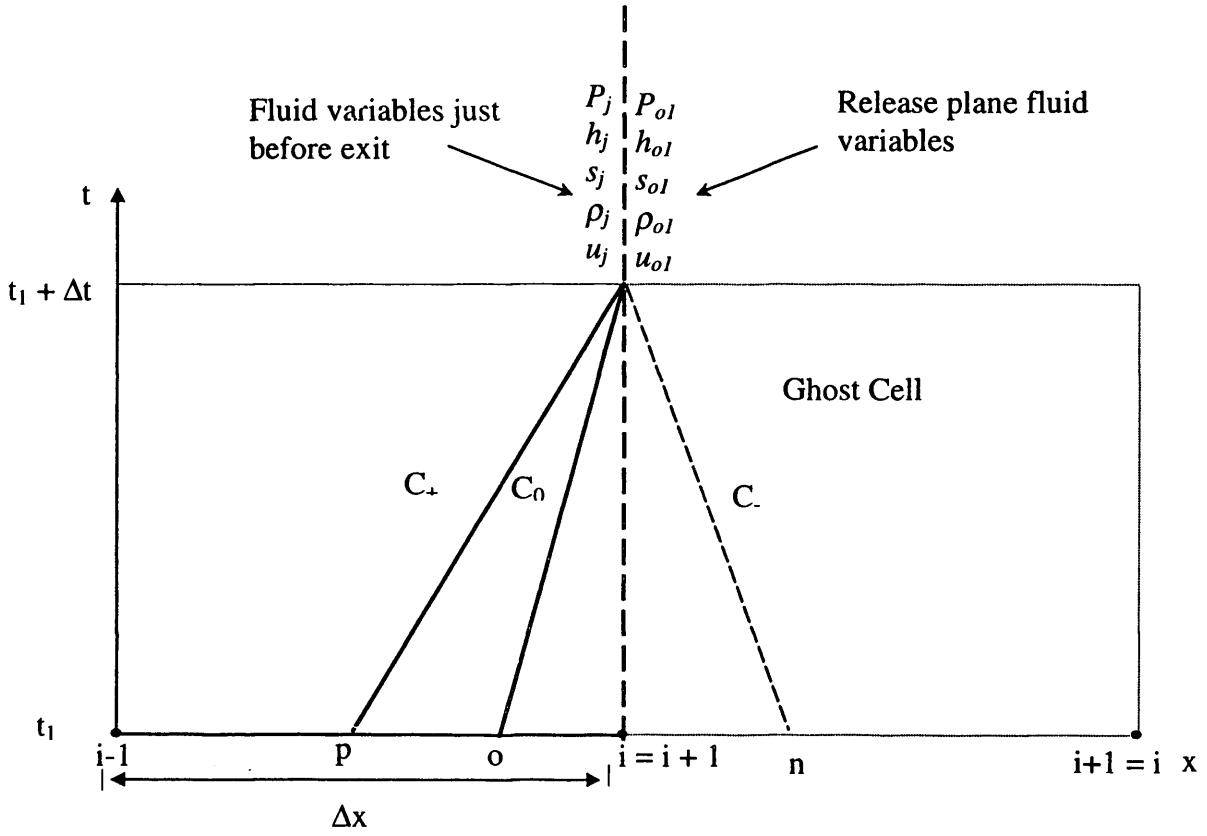

Figure 4.10: Diagram illustrating characteristic lines at the rupture plane based on the concept of a ghost cell.

With the introduction of the negative characteristics, the flow properties at point *j* can be obtained just as it is done for the interior point calculation i.e. with the aid of equations (4.21),(4.24) and (4.25). It should be noted that interpolation is not required within the ghost cell as all the properties within it are space invariant.

The flow variables at the release plane (P_{o1}, h_{o1}, u_{o1}) are calculated using a discharge rate algorithm described later (see section 4.37).

For discharge across the release plane, there is no accumulation of mass; thus the mass flow rate across the release plane is conserved. Furthermore, although the expansion process across the release plane is assumed to be isentropic, resistance posed by the release plane to the exiting fluid (as is the case with a puncture at the end of a pipeline) introduces irreversibility and hence non-isentropic conditions.

Accordingly, the actual flow rate of the exiting fluid at the release plane is smaller than the isentropic flow rate and the ratio between both flow rates is given by the discharge coefficient, C_d. Thus, the relationship between the mass flow rate approaching and that leaving the release plane can be expressed as:

$$u_j \times \rho_j \times A_{pipe} = C_d \times \rho_{o1} \times u_{o1} \times A_{o1} \qquad (4.59)$$

Where ρ_{o1}, u_{o1}, A_{o1} and A_{pipe} are the fluid density, fluid velocity, orifice area, and pipe area respectively.

The values of ρ_{o1} and u_{o1} (and all other fluid properties at the release plane) are obtained from the discharge rate calculation algorithm described below.

4.3.7 Discharge Rate Calculation Algorithm

Figure 4.11 is a schematic representation of the pertinent pressures at the release plane governing the discharge process. P_d is the downstream or ambient pressure. For critical/choked release, the discharge pressure, P_{o1} is higher than the downstream

pressure P_d. Under such condition, the discharge rate through the release plane is maximum, and no disturbance can be propagated upstream of the failure plane.

However, under non-critical or no choking conditions, the fluid discharge pressure, P_{ol} is equal to the downstream pressure, P_d and the release rate is calculated accordingly.

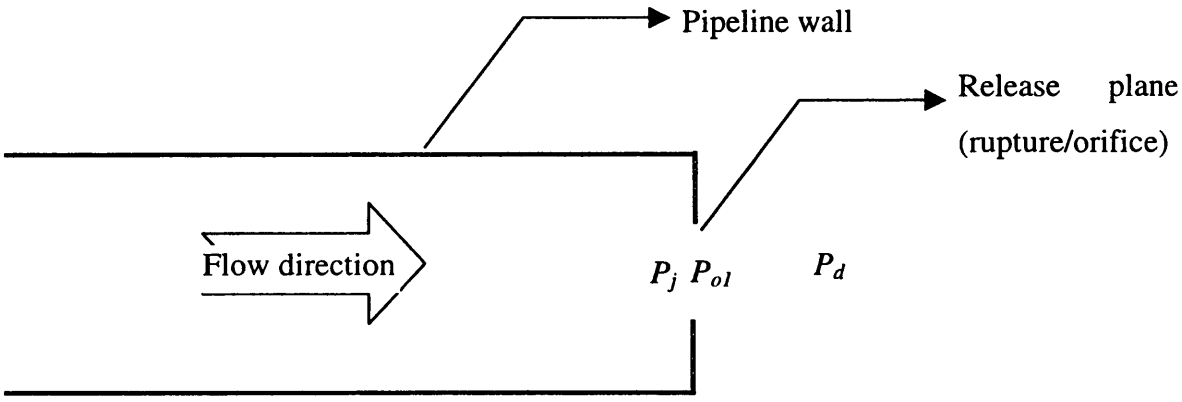

Figure 4.11: A Schematic representation of pertinent pressures at the failure plane governing the discharge rate.

The calculations of the choked and non-choked velocities and hence the subsequent discharge rate requires the application of an energy balance across the release plane. As earlier mentioned, the expansion process and hence the energy balance written across the release plane is based on isentropic flow assumption. Non-isentropic effects are accounted for with the aid of equation (4.59). Furthermore, for two-phase release, both phases are assumed to be in thermodynamic equilibrium, and travel at the same velocity.

Thus, at any time (t_i), and ignoring changes in potential energies between the flow approaching and the flow exiting the release plane, the corresponding energy balance across the release plane is given by:

$$H_j = h_{o1} + \frac{1}{2}u_{o1}^2 \tag{4.60}$$

Where:

$$H_j = h_j + \frac{1}{2}u_j^2 \tag{4.61}$$

In the case of choked/critical flow, equation (4.60) is solved iteratively using the Brent iteration method (Press et al., 1992), and the velocity, u_{o1} replaced by the local single/two-phase speed of sound, a_{o1}. The iterative solution of equation (4.60) involves guessing and updating guessed discharge pressures (P_{o1}) in conjunction with pressure-entropy (isentropic) flash calculations until equation (4.60) is satisfied. Once a solution is obtained, other flow variables at the release plane (ρ_{o1}, T_{o1}, h_{o1}) are determined from a corresponding pressure-entropy (P_{o1}-s_j) flash calculation.

On the other hand, for non-critical flow, the release pressure (P_{o1}) is equal to the ambient pressure (P_d). Thus, from a pressure-entropy (P_{o1}-s_j) flash calculation, the release enthalpy (h_{o1}) is determined and substituted in equation (4.60) to obtain the release velocity (u_{o1}). Unlike critical discharge, no iteration is required in determining flow conditions at the release plane.

Following the solution of equation (4.60), u_j is updated using equation (4.59) and employed in the corrector steps (see section 4.3.2) until convergence is observed. The calculation flow logic for the end point calculation is given below.

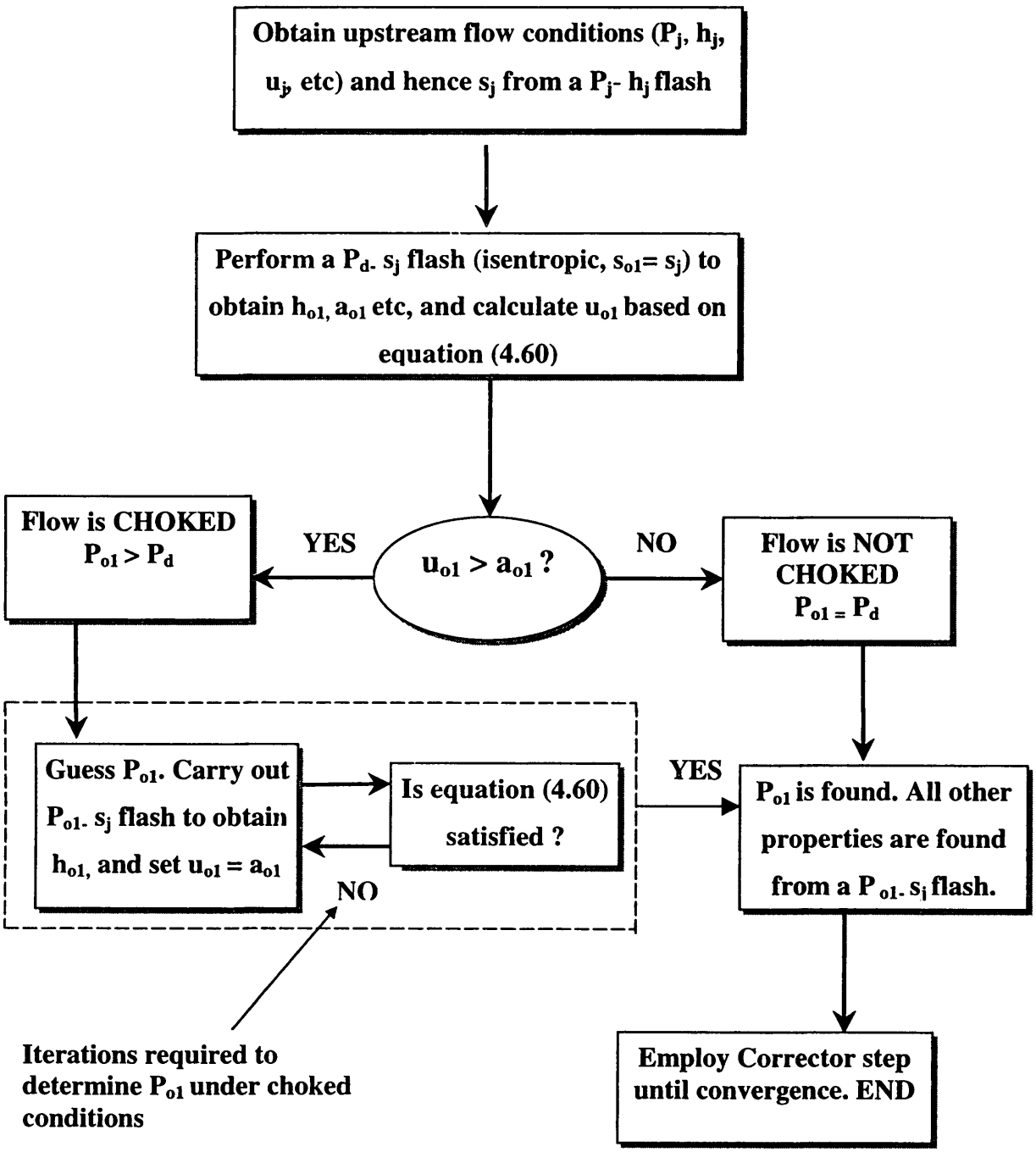

Figure 4.12: Calculation algorithm for obtaining flow variables at the discharge plane.

4.4 Modelling Pipeline Puncture

Puncture is by far the most common form of pipeline failure. Research sponsored by The Swedish Nuclear Power Inspectorate (SKI) shows that of the 3,751 pipe failure events recorded between 1994 and 1999, about two-thirds were in the form of leaks or punctures (Lydell, 2000).

The shortcomings of existing models in describing the outflow characteristics following pipeline puncture have been highlighted earlier in chapter 2. Although the model proposed by Oke et al. (2003) is in principle capable of modelling pipeline puncture, the continuity around the puncture region assumes a constant fluid density across the puncture plane boundaries (see figure 4.13). This is clearly not the case especially when dealing with compressible fluids. Hence, the boundary condition requires modification, as its use, as proposed by Oke et al. (2003), may yield inaccurate results (see section 5.6).

The updated puncture model based on the MOC is thus presented.

Figure 4.13 is a schematic representation of the fluid flow process and the active characteristic lines at the boundary following a puncture on the walls of a pipeline.

The notations j_1 and j_2 refer to the flow transport properties at the end of a calculation time step, Δt at flow boundaries B_1 and B_2 respectively, while j_{o1} refer to the orifice conditions at boundary, B_3. For ease of analysis, the puncture depicted in figure 4.13 is assumed to split the pipeline under consideration into two (i.e., upstream pipe section 1 and downstream pipe section 2) with the puncture region acting as a common junction between the two pipeline sections. Pipeline sections 1 and 2 terminate and emanate from the puncture junction respectively. Consequently, there are three flow boundaries (B_1, B_2, and B_3) at the common junction, each requiring the imposition of appropriate boundary conditions.

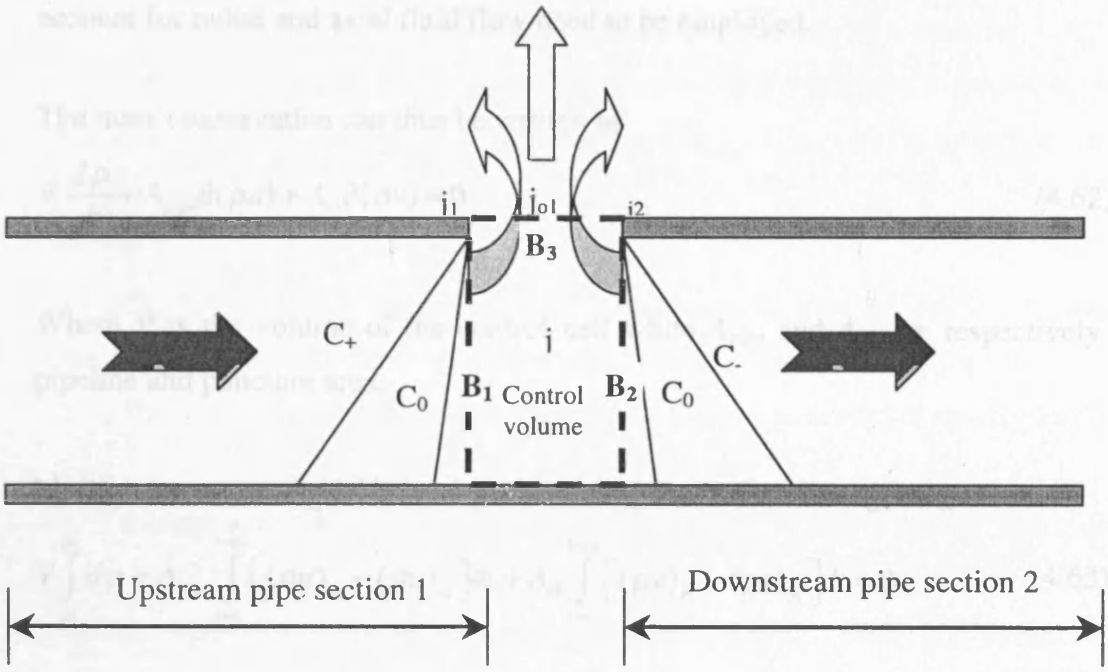

Figure 4.13: Schematic representation of fluid flow analysis following pipeline puncture.

Upstream of the common junction (pipeline section 1, i.e., plane B_1), only the positive and path line compatibility equations are active, while downstream (plane B_2), only the path line and the negative compatibility equations are applicable. A control volume, which bounds boundaries B_1-B_3, and is fixed in space, is employed in the modelling.

The boundary condition employed at the common junction stipulates the solution point pressures, P_{j1} (pipeline section 1 downstream pressure), P_{j2} (pipeline section 2 upstream pressure) and the junction pressure, P_j to be equal. The fluid properties within the control volume are defined at the centre of the cell such that $s_j = (s_{j1+} s_{j2})/2$, and the flow through the puncture plane (B_3) is assumed to be isentropic, hence $s_{o1} = s_j$.

In order to account for the non- isentropic effects encountered in reality, a discharge coefficient is employed in calculating the mass released from the puncture.

Since the flow at the puncture region is two dimensional, conservation equations to account for radial and axial fluid flow need to be employed.

The mass conservation can thus be written as

$$V\frac{d\rho}{dt}+A_{pipe}\partial(\rho u)+A_{o1}\partial(\rho v)=0 \tag{4.62}$$

Where V is the volume of the control cell while A_{pipe} and A_{o1} are respectively the pipeline and puncture area.

Multiplying equation (4.62) by dt and inserting the limits of integrating results in

$$V\int_{\rho_1}^{\rho_2} d\rho + A_{pipe}\int_{t=t_1}^{t=t_2}\left[(\rho u)_{x_2}-(\rho u)_{x_1}\right]dt + A_{o1}\int_{t=t_1}^{t=t_2}\left[(\rho v)_{y_2}-(\rho v)_{y_1}\right]dt=0 \tag{4.63}$$

Integrating numerically using the trapezoidal rule and noting that $(\rho v)_{y1}=0$ gives

$$V\left(\rho_{j_{|t=t_2}}-\rho_{j_{|t=t_1}}\right)+\left\{A_{pipe}\left[(\rho u)_{j_{|x=x_2}}-(\rho u)_{j_{|x=x_1}}\right]_{ave}+A_{o1}\left(v_{j_{|y=y2}}\right)_{ave}\right\}\Delta t=0 \tag{4.64}$$

Where the subscript, *ave* represents the average of the value in the brackets between time, $t = t_1$ and $t = t_2$, such that $t_2 - t_1 = \Delta t$. x_2 and x_1, respectively represent the upper (B_2) and lower (B_1) boundaries along the x-axis of the control volume, V.

To account for non-isentropic effects across the release plane, the release through the orifice is multiplied by a discharge coefficient, C_d. Hence equation (4.64) becomes

$$V\left(\rho_{j_{|t=t_2}}-\rho_{j_{|t=t_1}}\right)+\left\{A_{pipe}\left[(\rho u)_{j_{|x=x_2}}-(\rho u)_{j_{|x=x_1}}\right]_{ave}+C_dA_{o1}\left(v_{j_{|y=y2}}\right)_{ave}\right\}\Delta t=0 \tag{4.65}$$

Equation (4.65) represents the boundary equation based on a 2-D continuity balance, which couples together the flow behaviour at planes B_1-B_3. Hence, the solution at the common junction must satisfy the above equation.

The corresponding algorithm employed involves guessing a junction pressure P_j = P_{j1}= P_{j2}, and using the Euler predictor-corrector algorithm (see sections 4.3.1 and 4.3.2) to obtain u_{j1}, and h_{j1} from active compatibility equations at plane B_1 (i.e., equations (4.20) and (4.25)). From a pressure-enthalpy (P_{j1} - h_{j1}) flash calculation, s_{j1}, the fluid entropy at $B_1$is determined.

Similarly, by employing equations (4.21) and (4.25), u_{j2}, and h_{j2} can be obtained at plane B_2 with a P_{j2} - h_{j2} flash calculation, yielding s_{j2}. The representative fluid entropy within the control volume is then taken as the average entropies at plane B_1 and B_2.

The discharge rate algorithm described in section 4.3.7 is employed for determining flow conditions at the puncture plane with h_{j1} replacing H_j in equation (4.60) while u_{o1} becomes v_{o1}. The flow transport properties obtained from the solution of characteristic/boundary equations at planes B_1, B_2, and B_3, are substituted in equation (4.65). If equation (4.65) is satisfied, the flow transport properties obtained at the corresponding iteration step are adopted as the required solution. Otherwise, a new junction pressure is guessed and the iteration process repeated until a satisfactory solution is found. The Brent iteration algorithm (Press et al., 1992) is employed in updating guessed junction pressures until equation (4.65) is satisfied.

Figure 4.14 is the calculation algorithm for determining fluid flow transport properties at the puncture plane during the release process.

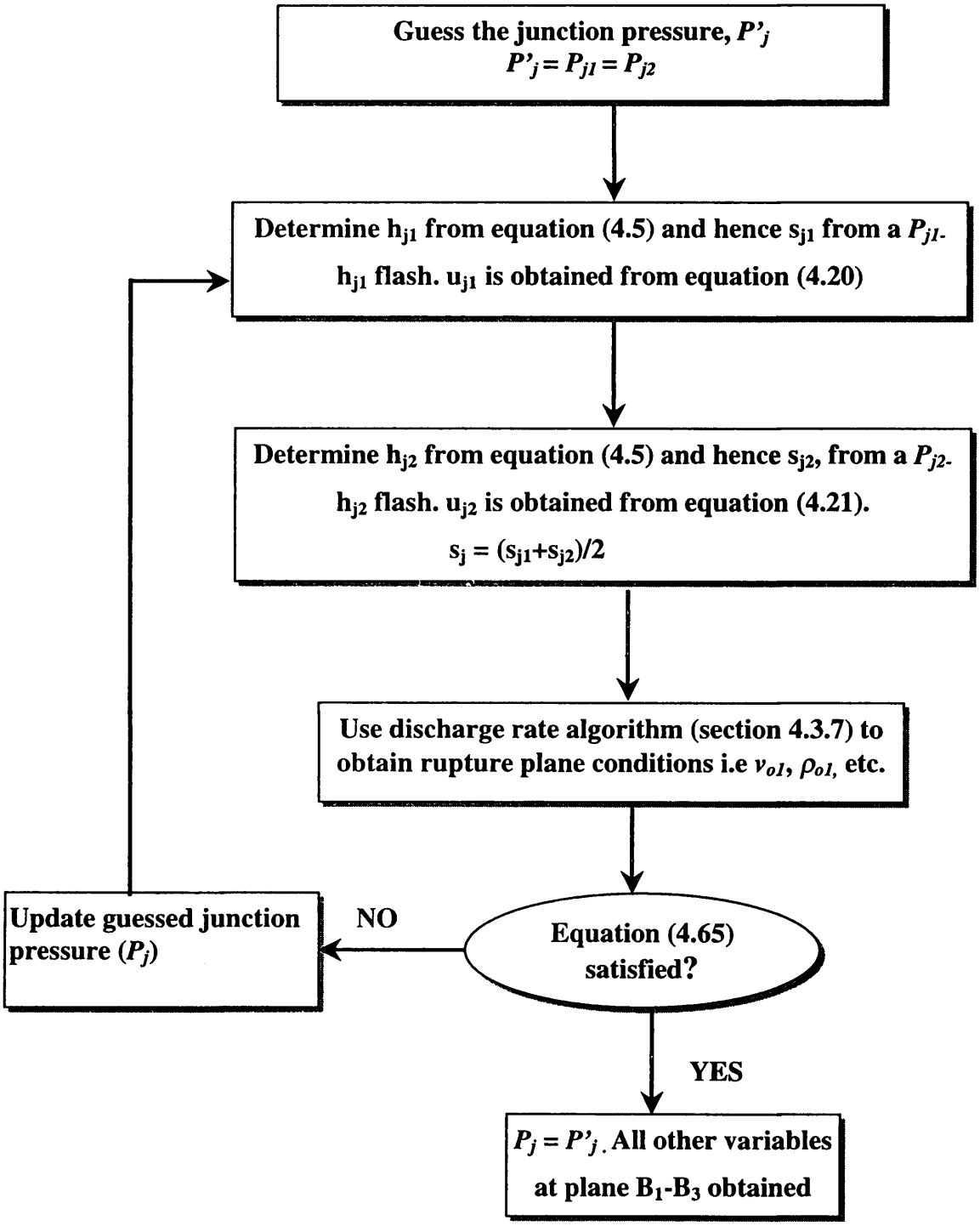

Figure 4.14: Calculation algorithm for obtaining flow variables at a puncture located on the major axis of a pipeline.

4.5 Modelling Outflow from Pipeline Networks

Publications dealing with the problem of pipeline rupture have been almost entirely limited to those involving straight pipelines. In practice however, pipelines conveying hydrocarbons usually consist of a network of pipelines. Elbows, tees and connectors are employed in building a network of pipelines, and can be used to change the direction of flow or inclination of pipelines. Such fittings are capable of inducing losses due to friction or change in direction and need to be accounted for in modelling pipeline failure.

Oke (2004) presented a MOC based model to simulate outflow following the rupture of pipeline networks. However, the solution methodology at pipeline junctions may result in errors (see section 5.7 for details) and therefore requires modification.

The updated approach, capable of simulating flow across an n-junction pipeline network is thus presented below. Figure 4.15 is a schematic representation of characteristic lines at a typical bend or connector. B_1 and B_2 represent the flow boundaries at the common junction associated with pipeline 1 and 2 respectively.

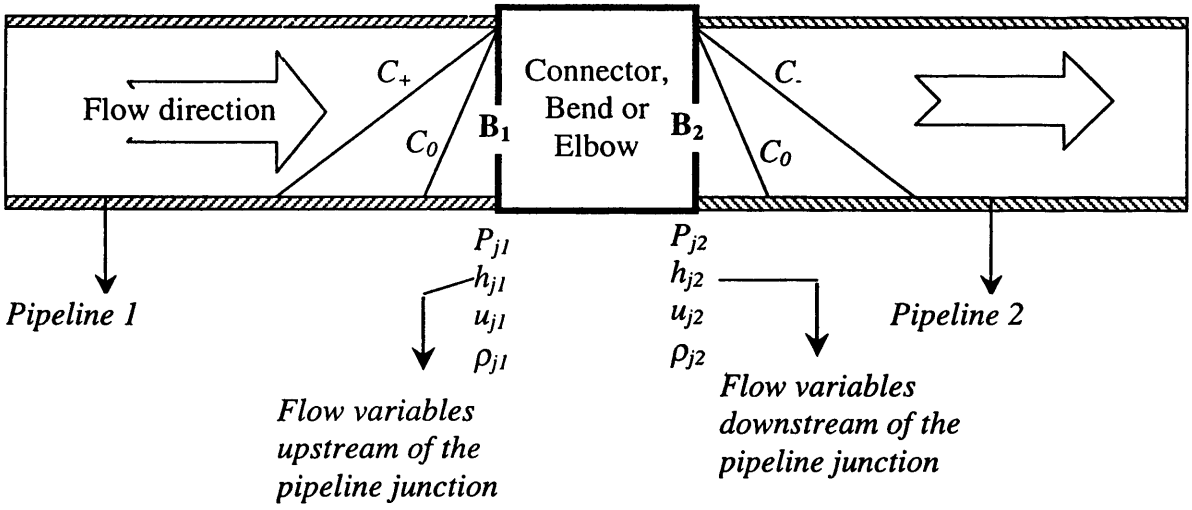

Figure 4.15: Schematic representation of characteristic lines upstream and downstream of a 2-way junction.

For the pipeline terminating at the junction (pipeline 1), only the positive and path line compatibility equations are active, while for pipeline 2, only the negative and path line compatibility equations are applicable. In modelling the boundary variables resulting from the junction of two pipelines, losses due to friction or changes in flow direction across a fitting are accounted for using a loss coefficient (K_{loss}) (Swaffield and Boldy, 1993). This coefficient is determined empirically for different types of fittings, and is employed in calculating the pressure drop resulting from flow across a given fitting (Perry and Green, 1997).

Apart from the compatibility equations mentioned above, two other boundary equations are employed in defining flow behaviour through a pipeline junction (Swaffield and Boldy, 1993). The first represents the effect of separation losses, K_{pl} due to flow across the junction as given by

$$P_{j2} = P_{j1} + K_{pl} \tag{4.66}$$

Where

$$K_{pl} = 0.5\left(\rho_{j1} u_{j1} \left|u_{j1}\right| - \rho_{j2} (1 + K_{loss}) u_{j2} \left|u_{j2}\right|\right) \tag{4.67}$$

The subscript j_1 and j_2 represents the solution variables at boundary planes B_1 and B_2 for pipelines 1 and 2 respectively

The loss coefficient, K_{loss} accounts for the pressure drop due to friction or changes in flow direction across a fitting at the pipeline junction, and its values are obtained from the literature (Perry and Green, 1997). Experimental data (Perry and Green, 1997) indicate that these loss-coefficients are Reynolds number (Re) insensitive for Re $\geq$ 500. During pipeline rupture, turbulent flow (Re $\geq$ 20,000) will most likely prevail at pipeline junctions during the depressurisation process. Hence, constant loss coefficients are employed in this study.

The second, boundary equation ensures flow continuity between the two pipeline sections. Taking the junction as a control volume with no accumulation such that

flows into it are positive, and flows away are negative; the continuity equation is given by:

$$\rho_{j1} u_{j1} A_{j1} + \rho_{j2} u_{j2} A_{j2} = 0 \qquad (4.68)$$

Where A_j is the cross section area of the pipeline.

The procedure involved in obtaining the flow variables at boundaries B1 and B_2 requires guessing the upstream pressure, P_{j1}, and employing equations (4.5) and (4.6) to obtain h_{j1} and u_{j1} .The Euler predictor-corrector technique is then invoked, until convergence is achieved. P_{j2} is obtained from equation (4.66) and u_{j2} and h_{j2} obtained using the Euler predictor-corrector technique, with a P_{j2} - h_{j2} flash calculation, yielding ρ_{j2}.

If continuity (equation (4.68)) is satisfied across the boundaries, the flow transport properties obtained at the corresponding iteration step are adopted as the required solution. Otherwise, a new upstream pressure (P_{j1}) is guessed and the iteration process repeated until a satisfactory solution is found.

The analysis of transient flow across a junction of three pipelines is quite similar to that described above for a 2-way junction. Figure 4.16 is a schematic representation of characteristic lines at a tee joint or branch. B_1, B_2, and B_3 represent the flow boundaries at the common junction associated with pipelines 1, 2 and 3 respectively.

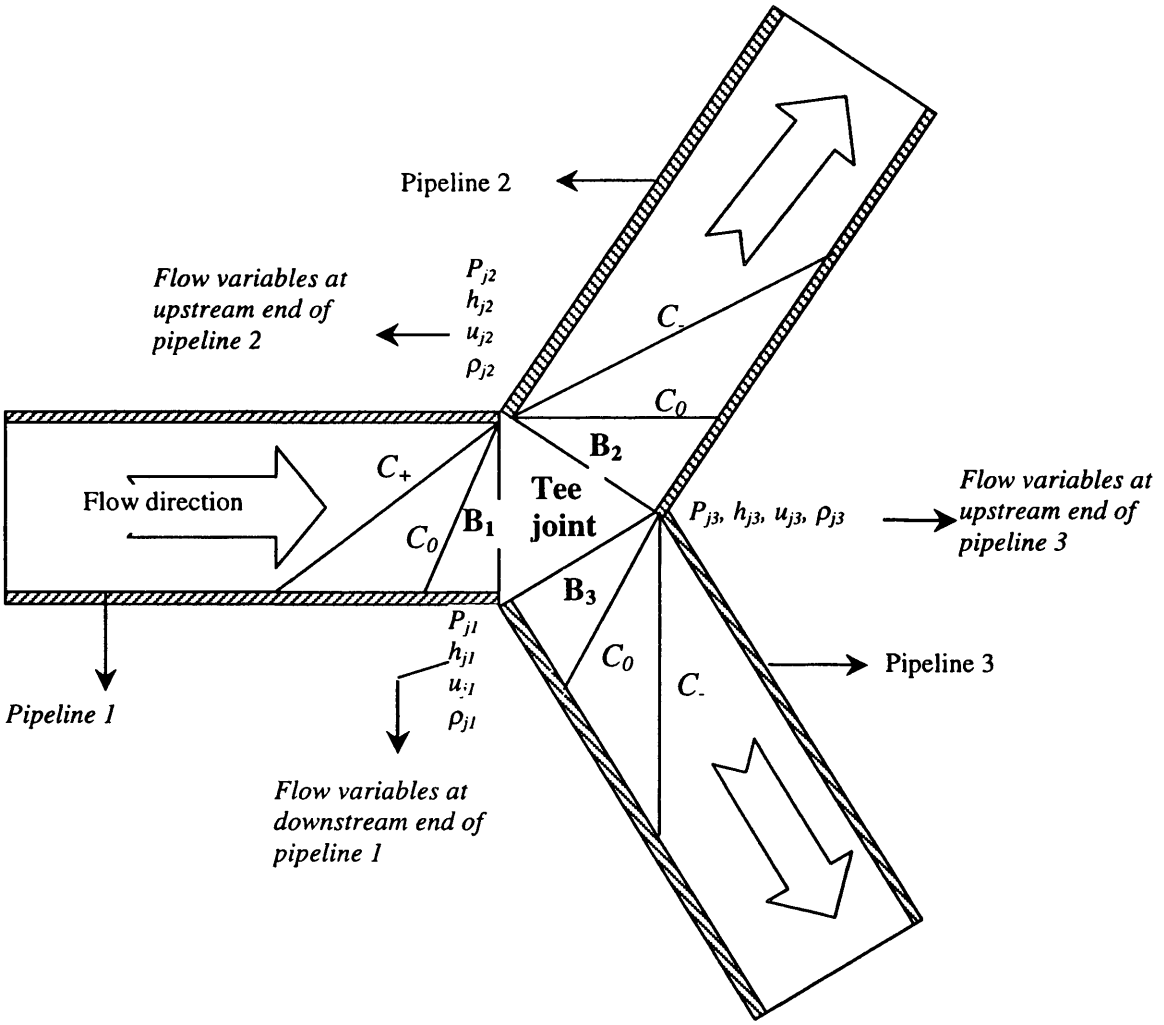

Figure 4.16: Schematic representation of the characteristic lines upstream and downstream of a 3-wayjunction.

Pipeline 1 is the only pipeline in which the positive Mach and path line compatibility equations are active. At the boundaries B_2 and B_3 (i.e., inlet points into pipelines 2 and 3 respectively), only the negative Mach and path line compatibility equations are applicable. Apart from the compatibility equations mentioned above, three other boundary equations are employed in defining flow behaviour through a three-pipeline junction. These are:

i) The equation representing the effect of separation losses due to flow across the junction between pipeline 1 and 2:

$$P_{j2} = P_{j1} + K_{pl12} \tag{4.69}$$

ii) The equation representing the effect of separation losses due to flow across the junction between pipeline 1 and 3:

$$P_{j3} = P_{j1} + K_{pl13} \tag{4.70}$$

iii) The equation ensuring that continuity of flow exists between the three pipelines.

$$\rho_{j1} u_{j1} A_{j1} + \rho_{j2} u_{j2} A_{j2} + \rho_{j3} u_{j3} A_{j3} = 0 \tag{4.71}$$

Where K_{pl12} and K_{pl13} are the separation losses due to friction and/or change in flow direction across the junction. They are respectively given by:

$$K_{pl12} = 0.5\left(\rho_{j1} u_{j1} \left|u_{j1}\right| - \rho_{j2}\left(1 + K_{loss12}\right) u_{j2} \left|u_{j2}\right|\right) \tag{4.72}$$

$$K_{pl13} = 0.5\left(\rho_{j1} u_{j1} \left|u_{j1}\right| - \rho_{j3}\left(1 + K_{loss13}\right) u_{j3} \left|u_{j3}\right|\right) \tag{4.73}$$

The subscript j_1, j_2 and j_3 represent the solution variables at boundary planes B_1, B_2 and B_3. K_{loss12} and K_{loss13} are the loss coefficients accounting for frictional and/or secondary losses due to flow between pipelines 1 and 2, and pipelines 1 and 3 respectively.

In general, this model can be used to simulate the fluid properties at the boundary of an n-junction pipeline network (with uniform or non-uniform diameters) where n refers to the total number of pipelines terminating and emanation from the junction. This requires the imposition of n boundary equations at the junction of which n-1 would relate to separation losses between pipelines, with the last one ensuring continuity of flow between pipelines. Figure 4.17 shows the calculation algorithm in determining the fluid condition at the junction of an n-junction pipeline network.

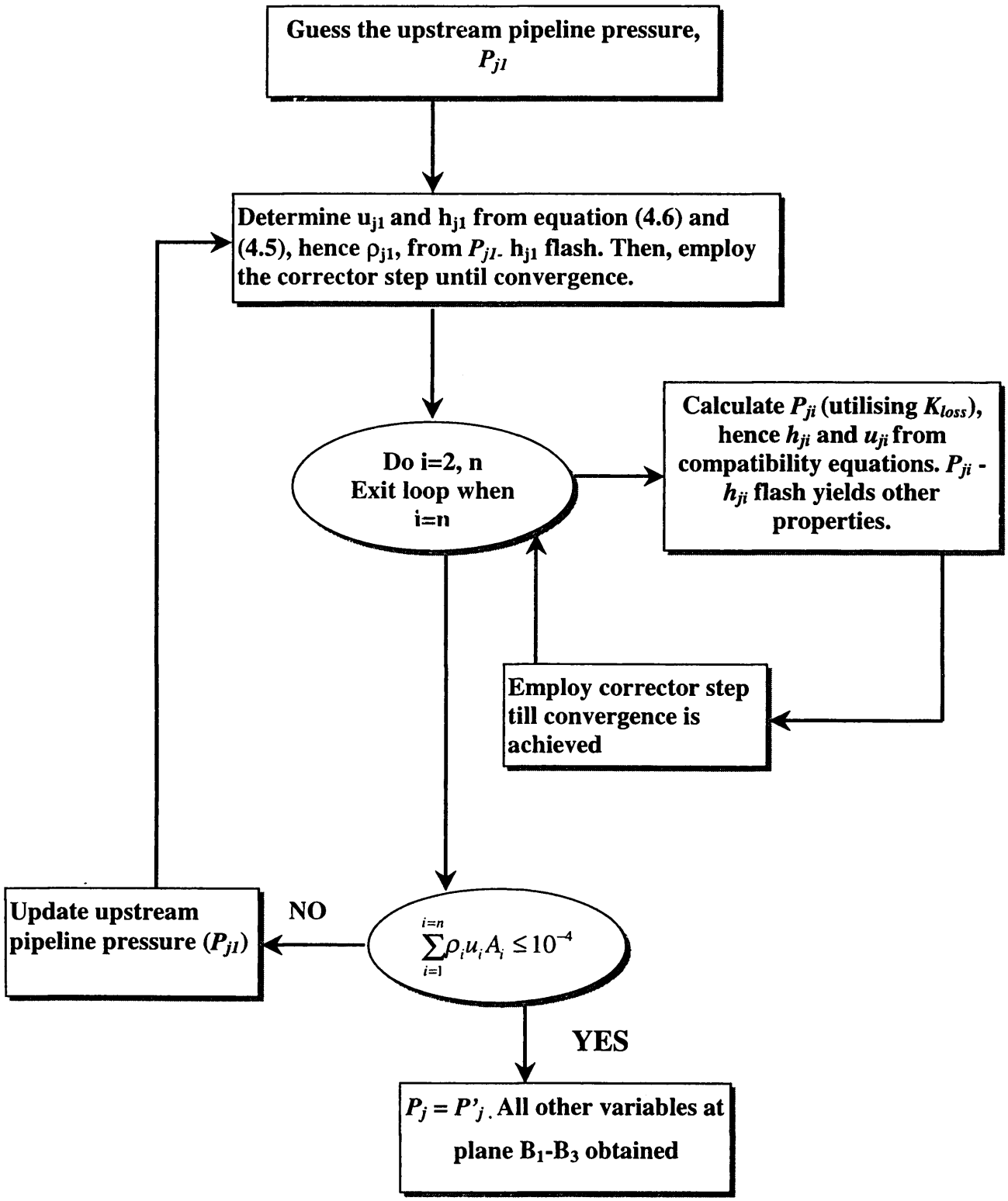

Figure 4.17: Calculation algorithm for obtaining flow variables at the boundaries of an n-junction pipeline network.

4.7 Scheme for Reducing Computational Run Time

In the preceding sections, a MOC based model for simulating the transient fluid dynamics following rupture or puncture of a straight or network of pipelines was presented. Although the MOC has been shown to be successful in simulating real data (see for example, Mahgerefteh et al., 1999; Oke et al., 2003) it is often criticised for the small time step required in its implementation, which invariably increases the CPU run time.

This small time step restriction is required in order to ensure stability. It is given by the well-known Courant-Fredrich- Lewy (CFL) stability criterion given in equation (4.4).

The use of implicit schemes, which are unconditionally stable and allow the use of large time steps have been commonly employed as a way to avoid the small time step restriction. This however involves the simultaneous solutions of a large number of non linear equations, and can quickly become complicated when complex boundary conditions that require an iterative solution are imposed. In addition, where the identification of pressure peaks is important, time steps cannot be arbitrarily increased as this will result in a smoothing of predicted pressure profiles (Faille and Heintze, 1999). Nonetheless, the implicit method has been found to be applicable when analysing slow transients.

However, when dealing with fast transients as encountered in pipeline failure, strict adherence to the CFL stability criterion becomes important (Nakaruma et al., 1975).

Since computations using the MOC for simulating pipeline transients are expensive, and therefore undesirable, it is necessary to investigate ways of reducing the CPU run time while still maintaining model robustness and accuracy.

The use of the method of characteristics in resolving the compatibility equations requires the determination of the fluid properties at point p, o and n (see figure 4.3) on the lower time level for all grid points. This is done via a real fluid equation of state (Peng-Robinson EoS), and various property prediction correlations (see section 3.5).

The use of the corrector step in which the compatibility equations are repeatedly solved (per grid) until convergence is achieved further requires thermodynamic flash calculations at each iteration step.

For example, in order to accurately simulate the complete blowdown of the Piper Alpha pipeline (see section 5.3), approximately 2 billion flash calculations are required. This is responsible for a significant percentage of the total computational run time. In fact, simulation time profiling of the present pipeline rupture computer code has shown that up to 90 % of the total run time is spent performing flash calculations.

The following describes the development of an interpolation technique, which drastically reduces the number of actual flash calculations, thus leading to a significant reduction in the computational run time. This involves *a priori* generation of a database containing the relevant thermodynamic properties at set intervals within a predefined range and determining intermediate values using interpolation.

Methodology

The interpolation domain is developed by first determining the likely range of fluid enthalpies (h_{max}, h_{min}) at the likely maximum and minimum pipeline pressures (P_{max}, P_{min}) and temperatures (T_{max}, T_{min}).

P_{max} and P_{min} are taken as the inlet and ambient pressures respectively. T_{max} on the other hand is the greater of the feed and the ambient temperatures. The minimum fluid temperature, T_{min} is determined by performing an isentropic flash from P_{max} and T_{max} to P_{min}.

Allowance for pressure surges such as those due to the rapid closure of emergency shutdown valves may be made for equating P_{max} to the inlet pressure multiplied by a predetermined factor.

Figure 4.21 shows the corresponding interpolation domain.

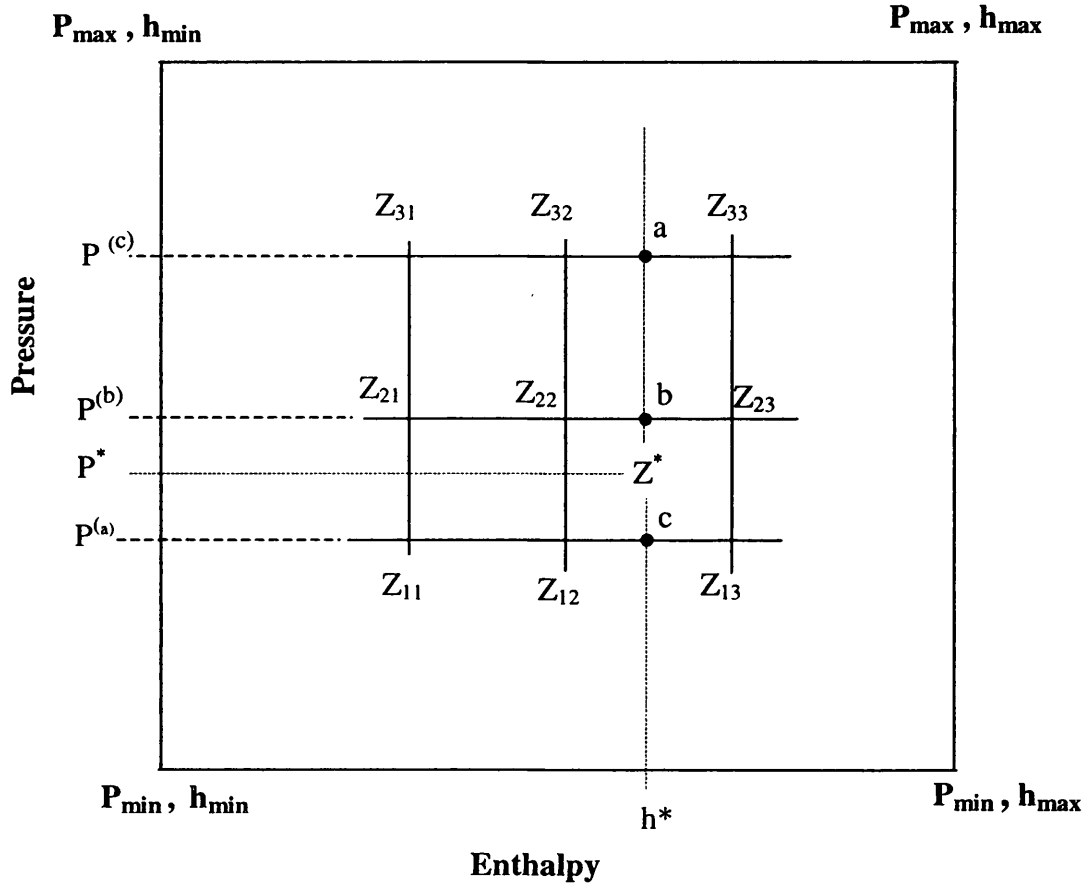

Figure 4.21: Schematic representation of the pressure/enthalpy interpolation domain.

Once the interpolating space domain is defined using the procedure described above, it is discretised along the pressure and enthalpy axes. Pressure and enthalpy have been chosen as the independent axes since the conservation equation are formulated in terms of *P* and *h*.

The pertinent fluid thermo physical properties, Z (= *f* (*P*, *h*, composition) at each node are then determined by performing P-h flash. This leads to a 3 dimensional array comprising pressure, enthalpy and fluid properties.

The fluid properties, Z required at any intermediate pressure and enthalpy values may then be directly determined using interpolation as opposed to time consuming flash calculations that would require the solution of the equation of state.

Z_{11}-Z_{33} represents the predetermined nodal fluid properties based on P-h flash calculations. Z* (the fluid property to be obtained at a specific P and h) on the other hand is evaluated at P*- h* using a Double Sweep Quadratic Interpolation Scheme.

The Lagrange polynomial is employed for the quadratic interpolation due to its higher accuracy and ease of implementation as compared to Newton's method and divided difference method (Hoffmann, 1992). In addition, and in contrast to the direct fit polynomial method, no sets of equations are required to be solved, hence resulting in computational run time savings.

Returning to figure 4.21, the interpolation is performed in two stages. The first sweep involves determining the intermediate values of Z at points a, b and c corresponding to the enthalpy, h* by interpolating between points Z_{11}-Z_{13} , Z_{21}-Z_{23}, and Z_{31}-Z_{33} respectively using the following interpolation formulas (Hoffmann, 1992).

$$Z^{(a)} = \frac{(h^*-h_{12})(h^*-h_{13})}{(h_{11}-h_{12})(h_{11}-h_{13})}Z_{11} + \frac{(h^*-h_{11})(h^*-h_{13})}{(h_{12}-h_{11})(h_{12}-h_{13})}Z_{12} + \frac{(h^*-h_{11})(h^*-h_{12})}{(h_{13}-h_{11})(h_{13}-h_{12})}Z_{13} \tag{4.74}$$

$$Z^{(b)} = \frac{(h^*-h_{22})(h^*-h_{23})}{(h_{21}-h_{22})(h_{21}-h_{23})}Z_{21} + \frac{(h^*-h_{21})(h^*-h_{23})}{(h_{22}-h_{21})(h_{22}-h_{23})}Z_{22} + \frac{(h^*-h_{21})(h^*-h_{22})}{(h_{23}-h_{21})(h_{23}-h_{22})}Z_{23} \tag{4.75}$$

$$Z^{(c)} = \frac{(h^*-h_{32})(h^*-h_{33})}{(h_{31}-h_{32})(h_{31}-h_{33})}Z_{31} + \frac{(h^*-h_{31})(h^*-h_{33})}{(h_{32}-h_{31})(h_{32}-h_{33})}Z_{32} + \frac{(h^*-h_{31})(h^*-h_{33})}{(h_{33}-h_{31})(h_{33}-h_{33})}Z_{33} \tag{4.76}$$

Finally Z* is obtained in the second sweep by interpolating between $Z^{(a)}$, $Z^{(b)}$ and $Z^{(c)}$ along the pressure axis using

$$Z^{(*)} = \frac{(P^{(*)} - P^{(b)})(P^{(*)} - P^{(c)})}{(P^{(a)} - P^{(b)})(P^{(a)} - P^{(c)})} Z^{(a)} + \frac{(P^{(*)} - P^{(a)})(P^{(*)} - P^{(c)})}{(P^{(b)} - P^{(a)})(P^{(b)} - P^{(c)})} Z^{(b)} + \frac{(P^{(*)} - P^{(a)})(P^{(*)} - P^{(b)})}{(P^{(c)} - P^{(a)})(P^{(c)} - P^{(b)})} Z^{(c)} \tag{4.77}$$

The above methodology ensures that fluid properties can be determined via this relatively efficient interpolation scheme at a given pressure and enthalpy as opposed to the more computationally expensive flash calculations.

The flash routine however is still employed in the unlikely event that an input pressure or enthalpy falls outside the interpolation domain, or perhaps when a pressure-entropy flash is required.

4.8 Concluding Remarks

In this chapter, the compatibility equations obtained from the resolution of conservation equations were discretised using the Euler predictor-corrector technique (a finite difference scheme). By assuming that the fluid properties varied linearly with distance, algebraic expressions for the fluid variables at the next time step along the pipeline length were obtained.

These expressions in conjunction with suitable boundary conditions and solution methodologies were applied to model the fluid dynamics following failure of pipelines or pipeline networks.

In particular, the boundary conditions for the puncture model have been modified to properly account for continuity at the puncture plane. Likewise, new boundary conditions at the junction of pipelines in the network model have been implemented, capable of simulating outflow from an n-junction pipe network. These modifications are expected to address the shortcomings of the Oke (2004) outflow model.

Two schemes for reducing computational run time were also presented. The first was the nested grid system, which employs finer grid discritisation only near the rupture plane, thus enabling simulation with relatively fewer overall number of grids. The methodology for treating the boundary between the coarse and fine mesh was also presented. The second scheme involves generating a database of fluid properties at set intervals prior to the MOC calculations, and then employing a quadratic interpolation technique for determining intermediate values. This drastically reduces the amount of flash calculations required, which in turn reduces the computational run time.

In chapter 5, results from the models presented in chapter 4 are validated against available field data where available. In particular, the effectiveness of the interpolation scheme for reducing simulation run time and its effect on model accuracy are evaluated.

In addition, the outflow characteristics such as variations of discharge rate, pressure and temperature following pipeline failure are presented and discussed. In all cases, a mass conservation index is used to judge the accuracy of results. This is particularly useful for cases where experimental data are unavailable.

CHAPTER 5

MODEL VALIDATION AND CASE STUDIES

5.1 Introduction

In chapters 3 and 4, the governing theory, solution methodology, and relevant boundary conditions that describe a numerical model for the simulation of pipeline failure were described. In this chapter, the models developed are validated against real data. In addition, the mass conservation index, described in section 5.2, is used to ascertain the validity of the simulated results. This is particularly useful in cases where real data are unavailable.

Important features of the model, such as the choice of wall heat transfer model, the use of smaller time steps when a fluid interface is encountered, and the model's sensitivity to various pipeline discretisation schemes are discussed. These parameters are expected to have a direct influence on the model's predictions.

In addition, the benefit of using the interpolation scheme (see section 4.7) as a means of significantly reducing computational runtime without loss of accuracy is demonstrated. Finally, the effects of couplers, branches and pipeline inclination on the fluid transients and outflow following pipeline failure are presented, and the results discussed.

5.2 The Mass Conservation Index

In developing pipeline rupture mathematical models, it is always desirable to validate the simulated results against experimental data in order to ascertain the robustness and accuracy of their predictions. However, it is impracticable to conduct experiments or field tests to validate the model predictions under a full range of conditions due to economic and/or safety implications. As such, only a handful of published experimental data for pipeline rupture are available.

In view of the above, it is therefore essential that some methodology be available to check the degree of accuracy of results. In this study, a 'measure' of the robustness of the simulated data is obtained by evaluating the mass conservation index as proposed by Flatt (1986). This in essence checks how well the global conservation of mass is satisfied.

Following Lang and Fannelop (1987), the mass conservation index (MCI) ε, is defined as:

$$\varepsilon = \frac{\int_0^l \rho_{(t_0)} - \rho_{(t)} dx}{\int_{t_0}^{t} \rho_{(t)} u_{(t)} dt} \tag{5.1}$$

The above equation calculates the ratio of the total inventory lost, computed by integrating the density-distance profile at time t along the length of the pipeline, to that evaluated by integrating the discharge rate-time profile. Ideally, this ratio should be 1, and hence the error in mass conservation, e may be given as

$$e = |(1-\varepsilon)| \tag{5.2}$$

In this study, the integrals in equation (5.1) are evaluated using the trapezoidal rule:

$$\int_0^l \rho_{(t_0)} - \rho_{(t)} dx = \sum_{i=0}^{i=k-1} 0.5(\rho_i + \rho_{i+1})_{t=0} \Delta x - \sum_{i=0}^{i=k-1} 0.5(\rho_i + \rho_{i+1})_{t=t} \Delta x \tag{5.3}$$

$$\int_{t_0}^{t} \rho_{(t)} u_{(t)} dt = \sum_{n=1}^{n=n} 0.5\left[(\rho u)_{n-1} + (\rho u)_n\right] \Delta t \tag{5.4}$$

Where k, n, Δx and Δt are the number of grids, number of time steps, the grids spacing and the time step respectively.

5.3 FBR Model Validation and the Application of the Interpolation Scheme for Reducing Computational Run Time

The following describes the results of the validation of the model developed in chapters 3, and 4. In addition, the effectiveness of the interpolation scheme described in section 4.7 as a means of reducing simulation run time is evaluated.

Two sets of data set are chosen for this purpose, as they are found suitable for modelling the FBR of long pipelines. The first set are the results of the P40 and P42 experiments carried out by Shell and BP on the Isle of Grain (Chen, 1993) while the second is obtained from the Piper-Alpha tragedy (Richardson and Saville, 1991).

All simulations presented in this work were conducted on a Dell 2.4 GHz Intel Pentium IV PC. The wall friction factor is evaluated using the Chen correlation (Chen, 1979, also see equations (3.71)).

For the Isle of Grain depressurisation tests, two 100 m instrumented parallel carbon steel pipelines were used. The pipelines were of 154 mm nominal diameter with a wall thickness of 7.3 mm. Pressure transducers and thermocouples measuring fluid temperature were attached along each line. Inventory and hold-up were measured using load-cells and neutron back scattering.

The pipelines contained commercial propane or LPG. This usually comprises a mixture of propane and other low molecular weight hydrocarbons, such as butane and ethane. The exact fluid composition is not given, but Chen (1993) assumes a mixture of 95-mole % propane and 5-mole % butane.

Transient tests conducted were initiated by rupture of a disc at the downstream end of the pipeline. Table 5.1 is a summary of the prevailing conditions in both tests prior to rupture.

For heat transfer calculations requiring pipeline wall thermophysical properties, respective values of 7854 kg/m^3, 434 J/kg/K, and 54 W/m/K for carbon steel are

assumed for the wall density (ρ_w), specific heat capacity at constant pressure (C_p), and thermal conductivity (κ) (Perry and Green, 1997).

Parameter	Test P40	Test P42
Initial pressure (bara)	21.6	11.3
Initial temperature (°C)	20.0	20.0
Ambient temperature (°C)	19.1	18.6
Pipeline roughness (m)	0.00005	0.00005
Rupture diameter (m)	0.154	0.154
Discharge coefficient	1.0	1.0
Wall thickness (m)	0.0073	0.0073

Table 5.1: Prevailing conditions in tests P40 and P42 prior to rupture.

5.3.1 P40 Simulation (FBR)

For this simulation, the pipeline is discretised into 40 grids of equal spacing (simple grid discretisation) since the use of the nested grid discretisation would in fact take longer to execute. The conditions under which the nested grid scheme offers advantages in terms of reducing CPU run time are discussed in section 5.4.

Figure 5.1 shows the results for prediction of open end pressure-time histories for the LPG mixture. Curve A shows the measured data, while curves B and C respectively represent the predicted data based on the model without interpolation (i.e purely flash calculations) and that incorporating the interpolation scheme.

The interpolation space for obtaining the fluid properties is discretised by increments of (80 ÷ molecular weight) $kJkg^{-1}$ along the enthalpy axis, and 1.5 % along the pressure (bara) axes. The application of the above scheme to a range of representative fluids such as permanent gases, two-phase mixtures, and permanent liquids reveals a maximum of 0.1 % difference between the predicted fluid properties based on

interpolation as compared to direct flash calculations. This finite difference is found to have a negligible effect on the predicted fluid flow profiles such as pressure, discharge velocity, and mass flow rate and discharge temperature following pipeline rupture.

A typical computational run time for the generation of an interpolation table is *ca.* 30 s depending on the interpolation space. As such its effect on the total computational run time for the simulation of the entire pipeline rupture outflow data is generally insignificant.

Returning to figure 5.1, the transition of the compressed liquid to saturation conditions upon rupture is marked by a rapid, almost instantaneous drop in the discharge pressure to *ca.* 7 bara. A slight undershoot can be noticed in the open end pressure measurements (curve A) at the early stage of depressurisation. This can most probably be attributed to non-equilibrium effects such as delayed bubble nucleation arising from the rapidity of the pressure decrease. This is followed by a relatively slow pressure transient corresponding to the evaporation of the two-phase mixture to pure vapour at about 20 s following rupture.

From figure 5.1, it can be observed that the simulated data (curves B and C) are in excellent accord with one another, and in good agreement with the test data.

It is interesting to note that the measured open-end pressure falls below 1 bara towards the end of the blowdown. This is however within the pressure measurement uncertainty range of +/-0.5 bara.

The mass conservation index obtained for the P40 simulation is 1.04. The computational run time expended in obtaining the data without the use of the interpolation scheme (curve B) is 15 minutes compared to 3.5 minutes required when the interpolation scheme is implemented. This represents an 80 % reduction in the computational run time without loss of accuracy.

Figure 5.2 shows the corresponding closed end data as in figure 5.1. Curve A represents measured data, while curves B and C respectively represent the predicted data without, and with the interpolation scheme.

As with the open end data, a rapid drop in pressure to saturated conditions occurs. Once the transition to saturated liquid is reached, the pressure at the closed end remains approximately at the saturation pressure for a further 12 s, gradually dropping to ambient pressure.

It may be observed that the predicted pressure profiles at the closed end (curves B and C) closely match the measurements (curves A).

Figure 5.3 shows the predicted (curves B and C) and the measured temperature-time profile (curve A) at the rupture plane for test P40. The rapid expansion of the inventory at the rupture plane results in a significant and almost monotonous decrease in its temperature to *ca.* 238 K at 20 s following rupture. The subsequent rapid recovery in the fluid temperature is due to the cessation of two-phase flow, with the onset of gas phase flow at the rupture plane. This effect is however not observed by other workers (Chen, 1993; Fairuzov, 1998) using a constant heat transfer coefficient. Again, both sets of simulated data are in good agreement with measurements.

Figure 5.4 shows the closed end temperature data for test P40. Curve A represents measured data, whilst curves B and C respectively represent the predicted data obtained without, and with the interpolation scheme. Good agreement between measured and simulated data may also be observed.

Figure 5.5 shows the measured discharge rate–time profile for test P40 (curve A) in comparison to the model predictions (curves B (no interpolation) and C (interpolation)). Although the two sets of simulated data (curves B and C) are in excellent accord, some discrepancy with the experimental data may be observed (curve A).

This may be due to the inaccuracy of the load cells inventory measurement manifested in the large amount of scatter in the measured data. The uncertainty in the load cell data was estimated as ± 5 % (Richardson and Saville, 1996a). It is interesting to note from the measured data (curve A) that post 18 s, negative mass is being discharged

(i.e. pipeline inventory increased with time). This is clearly physically unrealistic and may be attributed to measurement error.

5.3.2 P42 Simulation (FBR)

The model parameters for test P42 are given in table 5.1. Figure 5.6 and 5.7 respectively show the FBR data for the open end and closed end pressure-time predictions for the LPG mixture as compared to measured test P42 data.

Curves A show the measured data, whilst curves B and C respectively represent the predicted data obtained without, and with the interpolation scheme. As with test P40 simulations, 40 simple grids are employed for the pipeline discretisation.

As it may be observed in all cases, the model predictions are in agreement with experimental data.

Figures 5.8 and 5.9 respectively show the corresponding variations of rupture plane temperature and total line inventory with time. In both figures, curve A represents the measured data, while curves B and C respectively represent the predicted data without, and with the interpolation scheme. Again, good agreement between the measured and experimental data is observed.

In terms of computational runtime, the model incorporating the interpolation scheme was executed in 12 minutes as compared to 3 minutes using the interpolation scheme. This represents *ca.* 77 % saving in CPU run time. The mass conservation index associated with the P42 simulation is 1.05.

5.3.3 Piper Alpha (FBR) Simulation

The data used in this validation is the closed end pressure data logged following the FBR of the sub-sea line from Piper Alpha to MCP-01 during the Piper-Alpha tragedy (Richardson and Saville, 1991). The fluid composition and initial conditions prior to rupture are given in tables 5.2 and 5.3 respectively.

Component	mole %
CH_4	73.6
C_2H_6	13.4
C_3H_8	7.4
i-C_4H_{10}	0.4
n-C_4H_{10}	1.0
i-C_5H_{12}	0.08
n-C_5H_{12}	0.07
n-C_6H_{14}	0.02
N_2	4.03

Table 5.2: Composition of mixture in sub-sea line from Piper-Alpha to MCP-01 platforms (Richardson and Saville, 1991).

Initial condition	Data
Pipeline length, (km)	54
Inner diameter, (m)	0.4191
Pipeline thickness (m)	0.019
Pipe roughness (m)	0.00026
Initial pressure, (bara)	117
Initial temperature, (K)	283
Ambient temperature, T (K)	283
Heat transfer coefficient, ($W/(m^2K)$)	1.136

Table 5.3: Initial conditions prior to FBR of the sub-sea gas line between the Piper Alpha and MCP-01 platforms.

In simulating the blowdown of the Piper Alpha pipeline, a compound nested grid scheme (Δx_3 = 500 m, Δx_2 = 100 m and Δx_1 = 20 m) is employed in order to reduce computational run time without compromising accuracy. The use of the simple grid

scheme for such a long pipeline would be impracticable, as it may require up to 2,000 grids to achieve the same level of accuracy, resulting in huge computational expense.

Figure 5.10 shows the simulation of intact end pressure data logged during the Piper Alpha tragedy (Richardson and Saville, 1991) obtained without (curve B) and with the interpolation scheme (curve C). Curve A on the other hand represents the measured data.

Details of the network configuration, such as the number of pipelines making up the network and surface topography are not readily obtainable. As such the 54 km pipeline is assumed to be straight and horizontal (Chen, 1993; Saha, 1997; Mahgerefteh et al., 1999).

Referring to the simulated data, 3 flow regimes corresponding to points of phase-transition at the intact end exist.

During the first regime (*ca.* $\leq$ 1,300 s), the sub-cooled fluid at the intact end of the pipeline experiences a rapid drop in pressure until it crosses into the two-phase region.

The second flow regime, lasting between *ca.* 1,300 s - 16,400 s following rupture, represents the period during which two-phase conditions prevail at the intact end. During this period, the rate of depressurisation along the pipeline is generally slower in comparison to the first regime. This is because the fluid speed of sound, which determines the rate at which expansion waves travel, is lower (Picard and Bishnoi, 1987).

The third regime represents the period during which the fluid over the entire length of the pipeline exists in the gaseous state.

It can be observed from the figure (5.10) that the predicted data (curves B and C) are in very good agreement with experimental results. The interpolation scheme also results in an 80 % saving in terms of computational run time (c.f. 28 hrs (curve B) with 5 hrs (curve C).

The mass conservation index associated with the Piper Alpha simulation is 0.91.This can be however be improved if more grids are used.

From the above cases presented in sections 5.3.1 - 5.3.3, it is clear that the interpolation scheme is capable of reducing the simulation runtimes by up to 80 % without any loss in accuracy. Hence, the proceeding simulations and the corresponding computational run times reported will be based on data obtained using the interpolation scheme.

5.4 The Effect of Using of Smaller Time Steps at the Fluid Interface

The maximum time step, Δt_{max} for numerical stability is given by the Courant stability criterion (see chapter 4, equation (4.4)). In this study, 90 % of the maximum allowable time step is used throughout when no fluid interface is encountered.

As described in section 4.3.3, if a fluid interface exists within the pipeline, significant refraction of the acoustic wave may occur and the assumption that the fluid properties vary linearly with distance may lead to significant errors.

In this section the effect of using a smaller time step (10 % of the maximum allowable; $0.1\Delta t_{max}$) when a fluid interface is present as opposed to the standard time step (90 % of the maximum allowable; $0.9\Delta t_{max}$) is investigated.

The Isle of grain depressurisation test (test P40) lends itself to this exercise, as two different fluid phases co-exist within the pipeline during the depressurisation process. Between the time of rupture and 0.3 s after rupture, the pipeline contains both a liquid phase and a two-phase fluid, thus giving rise to refraction of the characteristic lines across the interface.

For this simulation, the pipeline is discretised into 40 grids of equal spacing (simple grid discretisation).

Figures 5.11 and 5.12 respectively show the effect of using the standard time step of $0.9\Delta t_{max}$ (curves B), and that using $0.1\Delta t_{max}$ (curves C) on the predicted rupture plane fluid temperature and pressure data. Curves A show the corresponding measured data.

Although liquid and two-phase fluid coexisted within the pipeline for only a short duration (*ca.* 0.3 s), it may be observed from figures 5.11 and 5.12 that the predicted data, based on using $0.1\Delta t_{max}$, is in better agreement with measurement.

Figure 5.13 shows the corresponding discharge rate variation with time. Curve A shows the measured data while curves B and C represent the simulated data based on employing $0.9\Delta t_{max}$ and $0.1\Delta t_{max}$ respectively. Taking account of the uncertainties associated with the measured data, the differences between the simulated data based on employing $0.9\Delta t_{max}$ and $0.1\Delta t_{max}$ (curves B and C) are not substantial. However, the mass conservation index using $0.9\Delta t_{max}$ is 1.1 as compared to 1.04 when $0.1\Delta t_{max}$ is used.

The simulations using $0.9\Delta t_{max}$ required 3 minutes to execute as compared to 3.5 minutes using $0.1\Delta t_{max}$.

5.5 Analysis of the Simple and Nested Grid Discretisation System

The following investigates the effect of pipeline discretisation based on the simple and nested grid schemes on the simulated results.

The simple grid system employs uniform space–time discretisation throughout the pipeline. For the nested grid system however, the last two uniform grids are further subdivided into 5x5 space-time meshes as shown in chapter 4, figure 4.7.

In general, the finer the discretisation, the more numerically accurate the results are expected to be, with the results approaching convergence as the number of grids increases. However, by increasing the number of grids, the number of calculations, and hence the computational run time is invariably increased. It is therefore important that a reasonable compromise is made between accuracy and computational run time.

In this study, the parameter evaluated for determining convergence is the variation of cumulative mass discharged with time. This is chosen as the basis of convergence as it is considered to be the most important data in the risk analysis of ruptured pipelines. The mass conservation index for each simulation is also reported.

The following simulations demonstrate the effect of the simple and nested grid schemes on convergence and computational run time.

The simulations performed include gas and two-phase mixtures in both short and long pipelines. The pipeline dimensions and the feed conditions for the short and long pipelines prior to rupture are given in table 5.4.

Input Data	**Short pipeline**	**Long pipeline**
Pipeline length, (km)	0.2	20
Inner diameter, (m)	0.154	0.914
Pipeline thickness (mm)	7.3	9.5
Feed Initial pressure, (bara)	40	40
Feed Initial temperature, (K)	292	292
Ambient temperature, T (K)	293	293
Pipe roughness, (m)	0.00005	0.00005

Table 5.4: Input parameters employed in studying the effect of pipeline discretisation on simulated results.

The composition of the gas and two phase feeds are given below:

Gas composition (mole %): Methane (100).

Two-phase composition (mole %): Methane (2), Ethane (10), Propane (20), n-Butane (20), Heptane (18), C11 (15), C20 (15).

Short pipeline results

Figure 5.14a shows the cumulative mass discharged for the gas inventory using varying numbers of simple grids, while figure 5.14b shows the corresponding data using nested grids. Figure 5.14c, on the other hand, shows the converged cumulative mass discharged profiles for the simple and nested grids as extracted from figures 5.14a-b.

As it may be observed from figures 5.14a and 5.14b, convergence is achieved in both cases, although this is reached using fewer number of nested grids. In addition, the mass discharged during the early stages of depressurisation is insensitive to pipeline discretisation when the nested grid scheme is employed.

The use of the nested grid does not seem to offer any significant advantages in reducing the computational run time. The mass conservation indices obtained for the simulations that ensure a balance between accuracy and run time (i.e. 50 simple grids and 20 nested grids) are 0.98 and 1.04 respectively.

It is clear from figure 5.14c that the results obtained from the simple and nested grids are similar, with a maximum difference of *ca.* 3 %. This difference is expected to reduce as the number of grids is increased further.

Figures 5.15a-5.15c show the corresponding data as those in figures 5.14a-5.14c obtained using the two-phase inventory. In this case, the same observations as for figures 5.14a-5.14c are made with the exception that the nested grid system is in fact computationally more expensive.

The use of 20 nested, and 20 simple grids gives a reasonable compromise between run time and accuracy. For 20 nested grids, the simulation required 11 minutes to execute. This compares with 3 minutes when 20 simple grids were used. The respective mass conservation indices were 0.97 and 1.01.

Long pipeline results

Figure 5.16a shows the cumulative mass discharged for the gas inventory using varying numbers of simple grids for the long pipeline. Figure 5.16b shows the corresponding data using nested grids. Figure 5.16c on the other hand, shows the converged cumulative mass discharged profiles using the simple and nested grids as extracted from figures 5.14a-b.

From figure 5.16a, it may be observed that convergence is reached using 1,000 simple grids. This is in contrast to the nested grid results shown in figure 5.16b, in which convergence is obtained when only 100 nested grids are used. In this case, the use of the nested grid system offers significant savings (*ca.* 80 %) in computational run time.

As it may be observed from figure 5.16c, the differences between the results obtained using the simple and nested grid system are insignificant.

The mass conservation indices using the 1,000 simple grids and 100 nested grids are 0.98 and 1.04 respectively.

Figures 5.17a-5.17c show the corresponding data as those in figures 5.16a-5.16c but using the two-phase inventory.

As may be observed from the figures (5.17a and 5.17b) convergence is achieved with both the simple and nested grid schemes. However, the nested grid scheme is computationally more expensive (57 minutes; 250 nested grids compared with 46 minutes; 1,000 simple grids). The converged mass discharge-time profiles for the simple and nested grid scheme, as shown in figure 5.17c, are similar.

It should be noted that the uncertainty associated with calculating the mass conservation index might be substantial during the early stages of blowdown. This is especially true if the depressurising fluid is a liquid or a two-phase mixture. Figure 5.18 shows the variation of the mass conservation index with time during the depressurisation of the 20 km two-phase pipeline when 500 simple grids are used. Curve A represents the data for a -1 % error in evaluating the mass conservation index

from equation (5.1). Curve B represents the actual data obtained, while curve C represents the data for a +1 % error in evaluating the mass conservation index.

As it may be observed from figure 5.18, even small errors (e.g. ±1 %) in computing the mass conservation index (MCI) produces significant deviations from unity in the early stages of depressurisation. This however quickly diminishes during the course of the depressurisation.

Based on all the above observations, the following may be summarised:

1) Convergence is achieved for both the simple and nested grid schemes if sufficient numbers of grids are used. This observation demonstrates the consistency and stability of the solution methodology employed

2) Convergence occurs with fewer grids when the nested grid scheme is used in comparison to the simple grid. The converged results for the simple and nested grid schemes are quite similar, with the maximum difference being <3 %.

3) In contrast to the simple grid scheme, the mass discharged during the early stages of blowdown is insensitive to the number of grids used when nested grids are employed.

4) In achieving a reasonable compromise between accuracy and computational run time, the nested grid system has been found to be suitable for simulating the blowdown of long gas pipelines. For other systems (short pipelines or two-phase mixtures), the nested grid system does not seem to offer any advantages and in fact, may be more computationally expensive than the simple grid system.

5) The mass conservation index can be used as a tool in evaluating 'the numerical accuracy' of the predicted results. However, care should be taken in relying on its credibility during the early stages of blowdown due to its large sensitivity to errors associated with its evaluation.

5.6 Puncture Model Validation

The following describes the results of validation of the puncture model described in sections 4.3.7 and 4.4 against experimental data.

In addition, the model developed by Oke et al. (2003) is employed to simulate a hypothetical puncture scenario and the results are compared to those obtained using the present model. The performance of the two models based on the mass conservation index is also reported. Other salient characteristics of the discharge process are highlighted and discussed.

The experimental data used to validate the puncture model is that of the Isle of Grain depressurisation test P45 (Richardson and Saville, 1996a). The depressurisation was initiated following the rupture of a 75 mm disc at the end of the pipeline.

Table 5.5 below gives the experimental conditions, as well as the data for the hypothetical pipeline puncture, referred herewith as 'Case study'.

Input	Test P45	Case study
Pipeline Length (m)	100	10000
Pipeline inner diameter (m)	0.154	0.5
Initial pressure (bara)	11.4	100
Initial temperature (°C)	15.9	20.0
Wall thickness (m)	7.3	10
Rupture location	Pipeline end, normal to major axis	2,500 m from high pressure end
Discharge coefficient	0.8	0.8
Feed flowrate prior to rupture and isolation (kg/s)	0	100
Orifice diameter (mm)	75	100
Inventory (mole %)	Propane (95), n-butane (5)	Methane (96), Ethane (2), Propane (1)

Table 5.5: Initial conditions prior to puncture in test P45 and those employed for the case study.

5.6.1 P45 (Puncture) Simulation

There appears to be some uncertainty between the reported nominal and effective orifice diameters for test P45. Experimental evidence (Haque et al., 1992b) suggests that a discharge coefficient of 0.8 is appropriate for flow of a gas or two-phase mixture through an orifice. Accordingly, Richardson and Saville (1996a), using a discharge coefficient of 0.8 determined the equivalent orifice diameter of 95 mm that produced efflux rates that matched the measured data for the test pipeline. Preliminary investigations carried out using the current model (PipeTech) also indicated that an orifice diameter of 95 mm together with a discharge coefficient of 0.8 provide the best agreement with experimental data.

In this work therefore, an equivalent orifice diameter of 95 mm is adopted, and for the simulations, the pipeline is discretised into 40 simple grids. The heat transfer model described in section 3.4.6 is used to determine the quantity of heat transferred across the pipe wall, whilst the interpolation scheme is used in the MOC computations.

Figures 5.19-5.23 show the simulated open and close end pressure, (figures 5.19 and 5.20), temperature (figures 5.21 and 5.22) and inventory variations (figure 5.23) with time as compared to field data. Curves A represent the field data whilst curves B represent the corresponding simulated data. The computational run time for the simulation is *ca.* 16 mins., and the computed mass conservation index is 0.99.

As it may be observed from figures 5.19-5.23 in general, the simulated pressure, temperature and the inventory data are in reasonably good agreement with field data.

The open and closed end pressure profiles (figures 5.19 and 5.20) indicate an almost instantaneous drop in pressure to *ca.* 6.8 bara at the onset of blowdown followed by a steady decline to ambient conditions.

The open and closed end pressure profiles in test P45 look quite similar. This is probably due to the smaller discharge area employed, resulting in a more uniform pressure profile along the pipeline length. This observation is in contrast to the pressure profiles of tests P40 and P42, which are full-bore.

As may be observed from figure 5.21, a rise in the open-end temperature from *ca.* 236 K to 240 K at the tail end of blowdown (> 55 s) is predicted by the model. However, the reported temperature-time data does not show this rise at this stage of the blowdown. It is however expected that such a temperature rise would eventually be observed (as with test P40 and P42 measured data) if the measured data were logged for a longer period. This rise in temperature is expected due to the warming of the pipe wall by the surrounding ambient.

From figure 5.23, it may be observed that there is a fair agreement between the predicted pipeline inventory (curve B) and measured load cell data. It may also be observed that the predicted and measured inventories at the end of blowdown are approximately 8 kg and 33 kg respectively.

The discrepancy in the inventory-time profile data may be as a result of the orifice plate at the punctured end of the pipeline acting as a dam, which holds back liquid and entrained droplets, thus resulting in non-homogeneous flow. This will undermine the applicability of the present model predictions, as is it is based on the assumption of homogenous equilibrium. This assumption is likely to be invalid in the case of a small puncture of the walls of a pipeline carrying a flashing liquid. Under this condition, the flow is expected to be stratified (gas on top, liquid at the bottom) and thus gives rise to different outflow during top and bottom blowdown. Experimental evidence (Richardson et al., 2006) also indicate that for flows through small orifices, the HEM becomes invalid when the liquid fraction is greater than *ca.* 0.8

Other sources of error may be due to inaccuracies in the vapour-liquid equilibrium (VLE) calculations or in the measurement data. For example based on the fluid density of 2.6 kg/m^3 within the pipeline at the prevailing measured line temperature and pressure of 240 K and 1.4 bar respectively, the calculated amount of inventory left in the pipeline following the depressurisation should be *ca.* 10 kg. This is different from the 33 kg obtained from measurement, and is, in fact, closer to the 8 kg predicted based on the numerical simulation.

5.6.2 Case Study (Puncture) Simulation

In this section, the puncture model developed in section 4.4 is used to simulate the fluid dynamics following the hypothetical puncture of a pipeline along its length conveying natural gas, highlighting the salient features of the discharge process. The results are also compared against those obtained based on the implementation of the Oke et al. (2003) puncture model.

Table 5.5 above shows the prevailing conditions for the puncture of the 10 km pipeline. The initial feed flow rate is 100 kg/s and is assumed to terminate upon a 0.1 m puncture located 2.5 km along the length of the pipeline.

Figures 5.24 and 5.25 respectively show the velocity and pressures data along the pipeline length at different times following puncture. Figure 5.26 on the other hand shows the variation of discharge rate with time for the first 100 s obtained using the current model (curve A) and that obtained using Oke et al.'s (2003) model (curve B).

Velocity and pressure profile data

The velocity and pressure profiles (figures 5.24 and 5.25) obtained from the simulation are herein discussed in chronological order starting from t=0 s to t=100 s. Flow velocities from left to right are positive, while flows from right to left are negative.

- t=0 s: Prior to puncture, the fluid flow within the pipeline is at steady state and the velocity across the length of the pipeline is nearly uniform at *ca.* 6 m/s. Due to frictional effects, there is a 4 bar pressure drop across the length of the pipeline (100 bar to 96 bar).

- t=2 s: The pipeline is isolated upon puncture (i.e. no fluid flows in or out of the pipeline except through the puncture), hence the velocities at both ends of the pipeline drop to 0 m/s. There is flow towards the puncture plane upstream of the failure point, and although the fluid is flowing away from it downstream, its velocity drops from 6 m/s to 2 m/s. It is noteworthy that the effect of the puncture

and subsequent isolation has not been detected between the 1–1.5 km and the 3.5-9 km sections of the pipeline.

As it may be observed from the pressure data in figure 5.25, the instantaneous termination of fluid flow results in a pressure surge of 3 bar, (96 bar to 99 bar) at the down stream end of the pipeline. Pressure surges are detrimental to pipeline installations, and its magnitude may be estimated as the product of the fluid's flow rate and its speed of sound (i.e. equation (4.57)). Hence, two fluids with the same flow rate approaching a valve will produce different surge levels depending on the local speed of sound. This implies that in general, a gas with the same flow rate as a two-phase fluid will produce a larger pressure surge due to its higher speed of sound.

A 3 bar drop in pressure from 100 bar to 97 bar is also observed at x=0 km due to fluid flowing away without it being refreshed by incoming inventory.

- t=6 s: From the velocity data it can be seen that at the upstream pipe section, flow is maintained towards the rupture plane. Likewise, at the downstream section, there is now fluid flow towards the failure point due to flow reversal. However, beyond *ca.* 5 km, fluid is still flowing away from the rupture point, with the 5.5 -7 km section of the pipeline oblivious to pipeline puncture or isolation. The pressure data at t=6 s indicates that the depressurisation wave has travelled the entire upstream section, but not the entire downstream section. A line pack due to fluid flow towards the downstream end of the pipeline and the reflected pressure wave at 10km, results in a rise in pressure at 7.5-10 km

- t=12 s: The effect of pipeline depressurisation and the subsequent isolation is now felt across the entire length of the pipeline. Flow reversal occurs at *ca.* 7 km (see fig. 5.24) , with fluid flowing away from the rupture plane beyond this point.

- t=50 s: It may be observed from figure 5.24 that complete flow reversal downstream of the puncture plane is achieved, and all surges and rapid transients within the pipeline have dissipated. From figure 5.25 (t=50 s), it is clear that the

fluid pressure along the entire length of the pipeline has equilibrated to a uniform value (*ca.* 92 bar). From this stage onwards, the pipeline may be treated as a vessel discharging through an orifice.

- t=100 s: Velocity profile is much the same as that obtained at t=50 s, confirming the dissipation of all rapid transients. The pressure within the pipeline remains practically uniform across the entire length. However, due to loss of inventory the pressure within the pipeline has dropped to *ca.* 89 bar.

Discharge rate data

Figure 5.26 shows the variation of discharge rate through the puncture with time. Curve A shows data obtained using the current model, whilst curve B is generated using the model developed by Oke et al. (2003).

As it may be observed, the discharge rates obtained by both models start at a peak value of *ca.* 126 kg/s and follow the same trend throughout the depressurisation process. However, the discharge rate from Oke et al. (2003) (curve B) drops at a much faster rate than the current model (curve A). The oscillatory nature of the discharge rate profiles during the early stages of blowdown (< 40s) predicted by both models is due to the transients, as shown by figures 5.24 and 5.25 occurring within the pipeline. However, once these transients have ceased, the discharge rate –time profile becomes relatively smooth with the discharge rate decreasing monotonically with time.

The mass conservation index from the present puncture model is 0.99 as compared to 1.61 obtained from Oke et al. (2003). This shows that the predictions obtained from the current model are more reliable than those obtained using Oke et al.'s (2003) model. The inaccuracies in the Oke et al. (2003) model are due to the incorrect puncture plane boundary condition, as described in section 4.4.

5.7 The Effect of Connectors and Branches on the Depressurisation Process Following Full-bore Rupture

In this section, the simulated results based on of the pipeline network model presented in section 4.5 are compared against those generated by the model of Oke (2004). As with the puncture scenario, both models are evaluated based on the mass conservation index, and expected trends. This is then followed by a more detailed analysis of the effect of bends and branches on the depressurisation process following the full bore rupture of a pipeline network.

In the first instance, both models are employed for simulating the rupture of two pipelines containing methane joined via a butt-welded connector as shown in figure 5.27. Table 5.6 below shows the conditions prior to rupture.

Initial condition	**Data**
Overall Pipeline Length (m)	1000
Pipeline inner diameter (m)	0.154
Initial pressure (bara)	21.6
Initial temperature (°C)	20
Ambient temperature (°C)	20
Pipeline roughness (m)	0.00005
Wall thickness (m)	7.3
Rupture location(m)	420
Number of pipelines	2 (400 m and 600 m)
Angle between pipelines (°)	0
Loss coefficient across connector	0.04
Inventory (mole %)	Methane (100)

Table 5.6: Initial conditions prior to rupture of a simple pipeline network.

For the simulations, the pipeline is discretised into 100 simple grids, incorporating the interpolation scheme.

Figure 5.28 shows the variation of the fluid temperature upstream and downstream of the connector for both models. Curves A1 and A2 respectively represent the temperatures upstream and downstream of the connector obtained using the current model. Curves B1 and B2 on the other hand represent the connector upstream and downstream temperatures obtained using the Oke (2004) model.

Referring to figure 5.28, the temperatures upstream and downstream of the connector as predicted by the current model (curves A1 and A2) indicate a small temperature drop of about 0.5 K.

Contrary to the above, the data generated from the Oke (2004) model indicates a 50 K rise in temperature across the connector, which is clearly unrealistic. It should be noted however that the temperatures upstream of the connector predicted from both models (curves A1 and B1) are quite similar.

The corresponding mass conservation indices based on the present model and that for Oke (2004) are 0.97 and 0.89 respectively.

The main source of discrepancy between both models is the manner in which the corrector step (see section 4.3.2.) at the pipeline junction boundary is implemented.

Oke (2004) reformulates the compatibility equations at the boundary in terms of pressure density and velocity (P-ρ-u). By coupling the resulting equations with the continuity and separation loss equations (i.e. (4.68) and (4.66)), all the variables at the pipeline junction were determined in a single step. The corrector step was then invoked with the aim of achieving convergence for all the variables at the boundary at each iteration step.

However, examination of the output data from the model of Oke (2004), indicated that in some cases, convergence was not achieved, leading to spurious results.

In this current model however (see figure 4.17 for the calculation algorithm), the pressure- enthalpy -velocity formulation (P-h-u) of the compatibility equations are retained (see equations (4.5-4.7)). By guessing the upstream pressure of the first pipeline, all the variables at the first pipeline can be determined. The corrector procedure is then invoked until convergence is achieved. The separator and compatibility equations are then solved to yield the variables at the boundary of the second pipeline, after which, the corrector step is implemented. If the continuity between the pipes are satisfied, then the guessed pressure is taken as the upstream pressure at pipeline 1; else, the guessed pressure is updated until continuity is satisfied.

Although the current procedure invokes the corrector step at the boundary of each pipeline section, thus requiring more iterations, it produces more accurate results in comparison to Oke's (2004) model.

The following presents and discusses the results of the application of the network model to the hypothetical rupture of 3 equal length pipeline configurations as depicted in figures 5.29a-c. The pipelines are assumed to contain a natural gas mixture (90 mole % methane and 10 mole % ethane) at 117 bara and 9.85 ^{o}C with zero initial flow rate. For comparison purposes, all three mild steel pipeline configurations (density 7854 kg/m^3, specific heat capacity 434 J/kg/K and thermal conductivity of 53.60 W/m/K; Perry and Green, 1997) are assumed to have the same overall total length, internal diameter and thickness of 25 km, 0.419 m and 0.019 m respectively.

As shown in figure 5.29, configuration A comprises a single 25 km straight pipeline, whilst configuration B consists of 5 pipeline sections, each 5 km in length connected via couplers to form a 25 km long straight chain. Configuration C consists of 5 pipelines, each 5 km in length, but with a Y-splitter at the 3rd section as shown in the figure. For reference purposes, for configurations B and C, each pipeline section is numbered consecutively from 1–5.

Respective loss coefficients of 0.04 and 1.0 (Perry and Green, 1997) are assumed for the butt-welded connectors and Y-splitter. For all the simulations, 250 nested grids are

employed whilst satisfying the Courant-Friedrich-Lewy stability criterion regarding the maximum allowable time step.

Returning to figures 5.29a-c, for configurations A and B, full-bore rupture is assumed to take place at one end of the pipelines. In the case of configuration C, FBR is assumed to occur at the end of pipeline 5.

Figure 5.30 shows the simulated pressure-time profile at the intact end (curves A1-C1) and the rupture plane (curves A2-C2) for the three pipeline configurations A, B and C. As it may be observed, configuration C (the branched pipeline) exhibits the fastest rate of depressurisation at the intact end. This is because the expansion waves, which determine the rate of depressurisation, (Mahgerefteh et al., 1997) have a shorter distance of 20 km to travel to the intact end in the branched pipeline as compared with 25 km in the two straight pipelines. The straight pipelines on the other hand show practically the same rate of depressurisation at the intact end throughout the discharge process.

From the rupture plane pressure data (figure 5.30), it may be observed that the release pressure profiles of the three pipeline configurations (curves A2, B2 and C2) are generally similar exhibiting a rapid decay to near ambient pressure *ca.* 2,000 s following FBR. A close examination of the data indicate that between *ca.* 100 s and 1,000 s, configuration C discharges at a slightly higher pressure in comparison to configurations A and B. As with the intact end data, the release pressure for configurations A and B remain more or less the same.

The very similar intact and open end pressure-time profiles obtained for configurations A and B suggests that at the effect of couplers on the data is not appreciable during FBR.

Figure 5.31 shows the velocity versus time variations for the fluid velocity entering and leaving the branch junction in configuration C for pipe sections 3 (curve A), 4 (curve B) and 5 (curve C) following full bore rupture. Positive flow velocity indicates flow into the junction whilst negative velocity indicates the opposite.

Following an initial *ca.* 11 seconds delay, rupture results in flow towards the junction point from pipelines 3 and 4 and discharge into pipeline 5. The observed period of quiescence during which no flow occurs is due to the time taken for the propagation of the depressurisation front to travel from the rupture plane towards the junction. Such delays would have a profound effect on the dynamic response of non-return valves used as a means of isolating flow following pipeline rupture. For example, a valve placed at the junction will remain oblivious to pipeline failure for the first 11 s following rupture. Given the hyperbolic variation of discharge rate with time, the above will result in a significant escape of inventory prior to emergency isolation.

Returning to figure 5.31, the fluid discharge velocities from pipelines 3 and 4 into the junction plane remain the same for the first 33 s following rupture. The discharge velocity from pipeline 4 then begins to drop, much earlier than that for pipeline 3, due to its shorter length.

Figures 5.32 and 5.33 respectively show the variations of discharge rate and velocity with time for the three pipeline configurations A, B and C. This data is especially important if the release ignites, as the rate of release determines the size and heat intensity of the jet flame, which in turn determines the time available for persons to find shelter, a factor that is crucial to their survival.

Referring to figure 5.32, the data indicates a rapid drop in the discharge rate from a peak value of *ca.* 3,700 kg/s to 400 kg/s in 100 s. This is followed by a gradual reduction in the release rate until depressurisation of the pipeline *ca.* 3,000 s following rupture. Remarkably, in the case of all three pipelines, much the same as the rupture plane pressure data (figure 5.30), mass outflow rate remains practically the same despite the differences in the pipeline configurations.

This is in contrast to the velocity data; figure 5.33. Here following an initial rapid drop, the discharge velocities for the three configurations remain substantially the same, gradually increasing from *ca.* 240 – 290 m/s at 2,200 s following rupture. This is then followed by a rapid drop in discharge velocity with the branched pipeline exhibiting the fastest rate of drop as compared to the straight pipelines, which follow the same velocity trends.

5.8 The Effect of Multiple Pipeline Inclination on the Depressurisation Process Following Full-bore Rupture

In this section, the results of the application of the pipeline rupture model to the hypothetical rupture of two equal length pipeline configurations as depicted in figures 5.34a-b is described. The aim is to determine if a multi-inclined pipeline network can be modelled as a uniformly (singly) inclined pipeline.

To demonstrate this, the depressurisation of two different pipeline configurations, as shown in figure 5.34 is simulated. The first pipeline configuration consists of 5 pipeline sections with an overall length of 7 km, in which the first pipeline connects to the remaining four sections via a 90° elbow. This sort of configuration is not uncommon in situations where a hydrocarbon source is below the seabed and it needs to be transported through various terrains to a processing facility. The second pipeline configuration also consists of a single 7 km long pipeline, and inclined at an angle to match its steady state outlet pressure to that of configuration A.

The pipelines are assumed to contain a LPG mixture (96 mole % propane, 3 mole % ethane, and 1 mole % n-butane) at 150 bara and 10°C with an initial flow rate of 150 kg/s. The internal diameter and thickness of 0.419 m and 0.019 m respectively are assumed for both of the pipelines configurations shown in figure 5.34 a-b.

The simulations are carried out using the interpolation scheme for fluid property determination, and 700 uniform grids in discretising both pipeline configurations.

Figures 5.35 and 5.36 show respectively the simulated pressure-time profiles at the rupture plane and the pressure-distance profile at 500 s following rupture. In each of the figures, curve A represents the data corresponding to pipeline configuration A while curve B represents the data corresponding to pipeline configuration B.

From figure 5.35 it may be observed that following rupture, there is an instantaneous drop from the steady state pressure of 36 bar to 6.6 bar at the rupture plane for both pipeline configurations. Although the release pressure data for both pipelines are

practically the same for *ca.* 8 s following rupture, the fluid pressure in configuration B starts to drop at a faster rate in comparison to configuration A. This is because a smaller amount of inventory per unit time flows upward towards the rupture plane in configuration B, and hence high pressures cannot be sustained.

Returning to figure 5.36, the pressure-distance profile for configuration A indicates a large pressure drop (120 bar to 10 bar) over the first 2 km pipeline section (i.e. pipeline 1), and a more uniform pressure of *ca.* 3 bar over the remaining 5 km section. However, the pressure-distance profile for configuration B shows a relatively constant rate of pressure drop from *ca.* 100 bar to 2 bar over the entire pipeline length.

The pipeline portions exhibiting the observed pressure drops (0-2 km section of configuration A, and the 0-7 km section of configuration B), are those which are inclined at a relatively large angle (90^{o} and 17^{o} respectively).

Figure 5.37 shows the rupture plane fluid velocity as a function of time for configuration A (curve A) and configuration B (curve B). It may be observed that the exit velocities for both configurations are the same for about 8 seconds into the depressurisation process. The discharge velocity from configuration B then begins to increase at a faster rate than that for configuration A. This is so because the speed of sound of the fluid mixture, which governs the release velocity under chocking conditions, is higher in configuration B.

Finally, figure 5.38 shows the cumulative mass discharged as a function of time for both configurations (A and B). From the figure, it can be observed that at the end of the simulation period (500 s), configuration A has discharged 65 % more inventory than configuration B (137 tons compared to 83 tons).

The computational run times expended in simulating the blowdown of pipeline configurations A and B are *ca.* 16 and 15 hours respectively. The mass conservation index associated with computations is *ca.* 1.08 for both configurations.

The relatively large difference in the results for both configuration indicate that a multi-inclined pipeline cannot be modelled as a single pipeline inclined at an 'equivalent' angle.

5.9 Concluding Remarks

In this chapter the full bore rupture and puncture models described in chapter 4 were validated. This exercise involved investigating the effects of the interpolation and the nested grid schemes on the simulation accuracy as compared to real data and the computational run time. A mass conservation index was used as a means of determining the numerical solution accuracy of the models developed in cases where real data were not available. For the full bore rupture validations, tests P40 and P42 from the Isle of Grain experiments were used as well as the pressure data logged during the Piper Alpha tragedy. For the puncture simulation, the Isle of Grain test P45 data was employed.

In general, good agreement between the field and simulated data were observed, with the finite discrepancies between them attributed to errors in VLE calculations, measurements uncertainties or errors, as well as the homogenous flow assumption.

The application of the interpolation scheme was shown to reduce the computational runtime by up to 80 % without loss in accuracy.

However the use of the nested grid system showed that reduction in the computational run time was confined to long pipelines containing gases. Surprisingly the nested grid system was found to be more computationally expensive as compared to the simple grid system for other cases such as short pipelines and two-phase fluids.

These investigations showed that discretisation errors (based on the mass conservation index) lower than 5 % can be obtained in reasonable time scales using interpolation coupled with the appropriate numerical discretisation scheme.

Rigorous modelling of the heat transfer across the pipeline and the presence of a single/two-phase interface during blowdown resulted in improved accuracy of the model predictions.

The limitations of the homogenous equilibrium model with respect to the blowdown of pipelines conveying flashing/ two-phase fluids discharging through a small orifice were highlighted. Under these conditions, the flow becomes highly stratified, and hence non-homogenous. As such different outflow characteristics may be expected during top and bottom blowdown.

Different hypothetical case studies demonstrating the fluid transients following pipeline puncture and rupture of pipeline networks were presented and the results discussed.

The puncture simulations case study indicated that under the same operating conditions, a gas approaching a closed valve might produce a greater pressure surge than a two-phase flow due to its higher speed of sound. In addition, the results show that the new boundary conditions presented in this study gave better predictions in comparison to Oke et al.'s (2003) model. Likewise, the modified boundary condition in the network model addressed the errors associated with Oke's (2004) model.

Studies of the outflow characteristics in a horizontal pipeline network indicated that the depressurisation process during FBR is strongly influenced by the distance the depressurisation wave travels from the open to the closed end of the pipeline. For the same overall length, the more branches a pipeline may have, the faster the depressurisation. However, the flow rate through the open end does not seem to be a function of the number of couplers or branches. The study also highlighted the importance of accounting for the depressurisation induced wave propagation as it has a direct influence on valve response.

Application of the network model to outflow in inclined pipelines highlighted the importance of taking into account the topography. The simulation results indicated that a multi-inclined pipeline cannot be modelled as a straight pipeline inclined at an 'equivalent' angle.

Chapter 6 investigates whether the observed relatively large drop in the temperature of the escaping fluid, and the associated cooling of the pipe wall may result in the transformation of an initial defect into a propagating fracture.

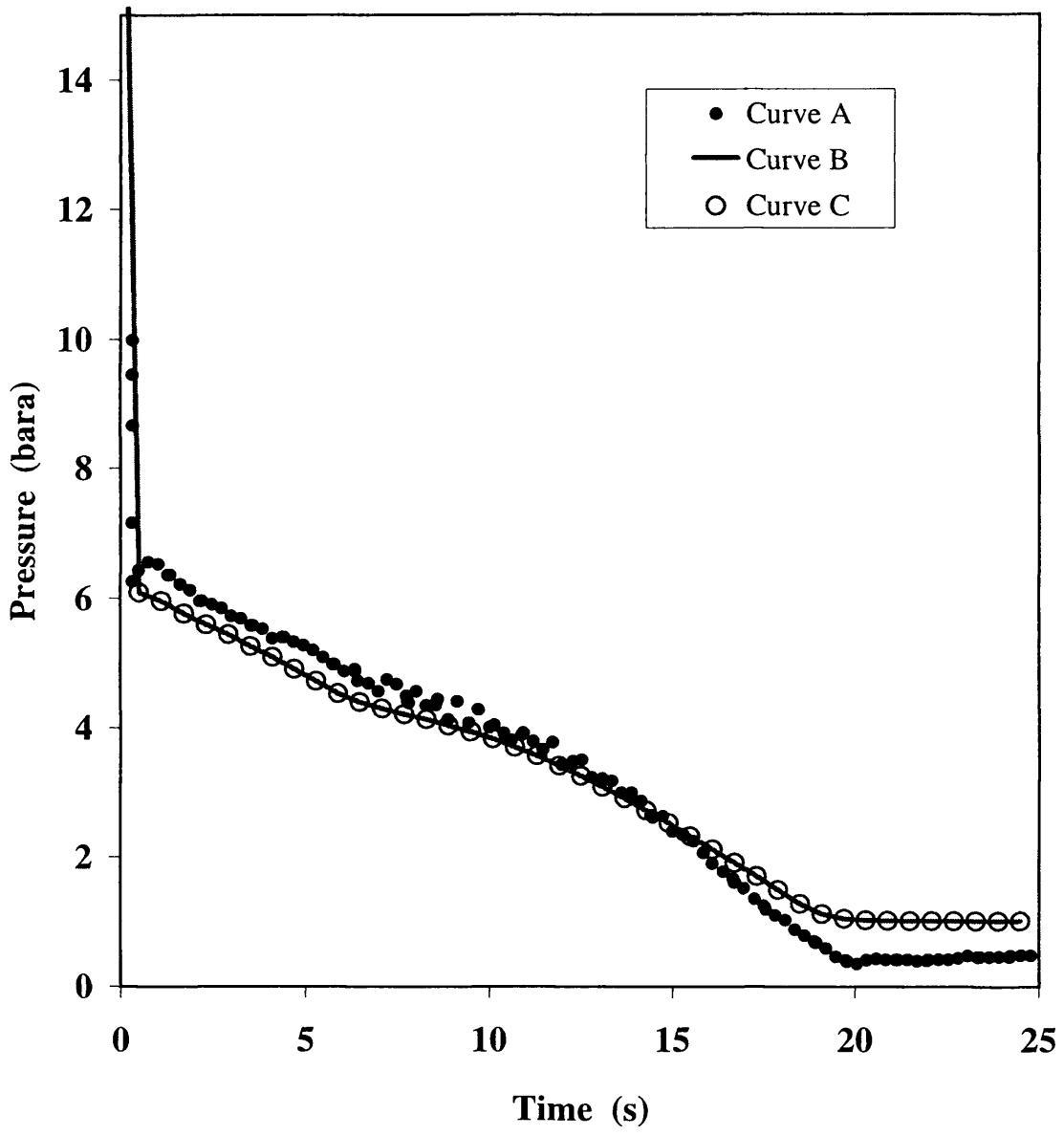

Figure 5.1: FBR open end pressure-time profiles for test P40 (LPG) showing the effect of the interpolation scheme on simulated results. Simulation data are obtained using 40 simple grids.

Curve A: Measurement (Richardson and Saville, 1996a,b).
Curve B: Simulated results without interpolation scheme. Run time, 15 mins.
Curve C: Simulated results using the interpolation scheme. Run time, 3.5 mins.

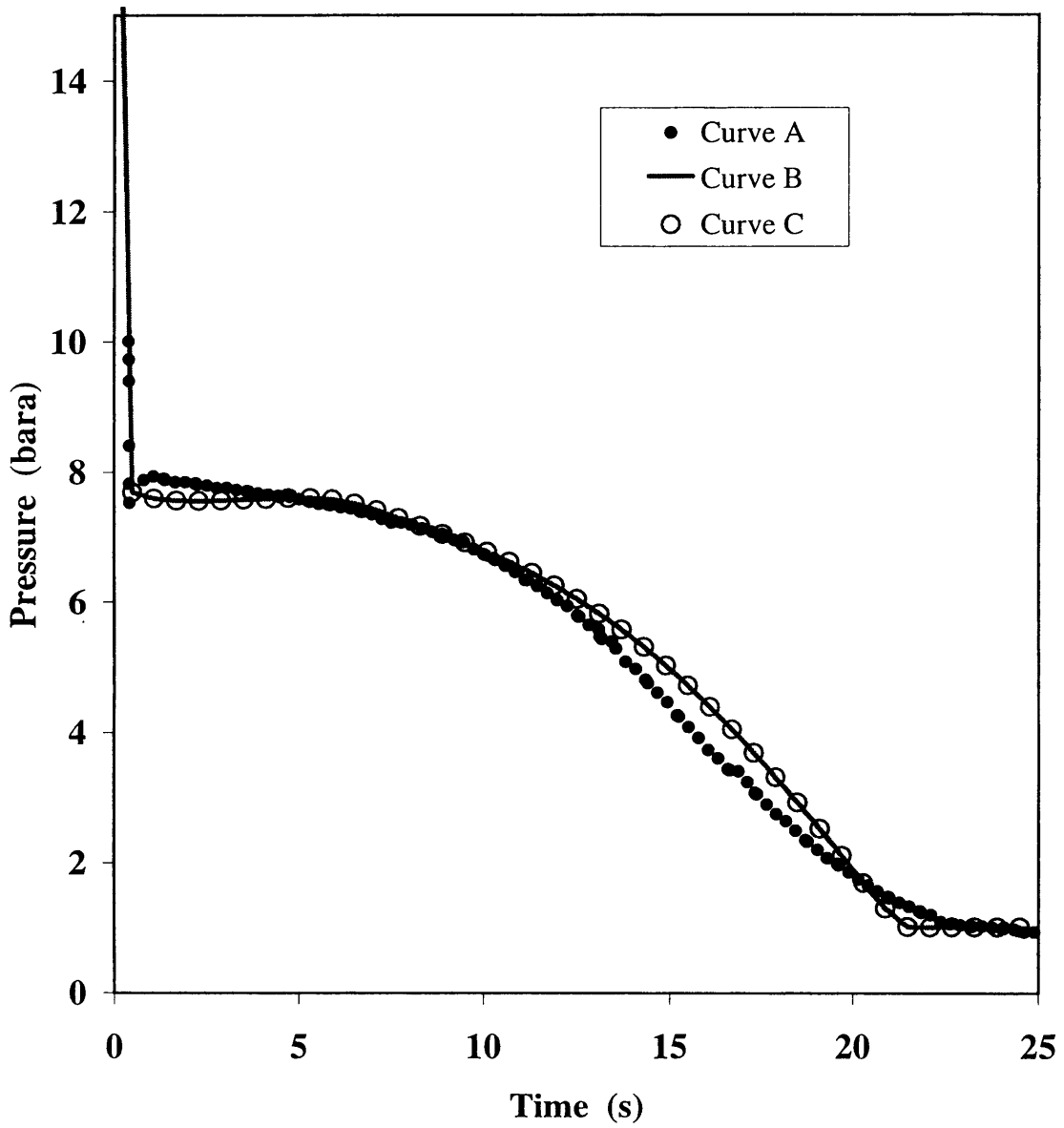

Figure 5.2: FBR closed end pressure -time profiles for test P40 (LPG) showing the effect of the interpolation scheme on simulated results. Simulation data are obtained using 40 simple grids.

Curve A: Measurement (Richardson and Saville, 1996a,b).
Curve B: Simulated results without interpolation scheme. Run time, 15 mins.
Curve C: Simulated results using the interpolation scheme. Run time, 3.5 mins.

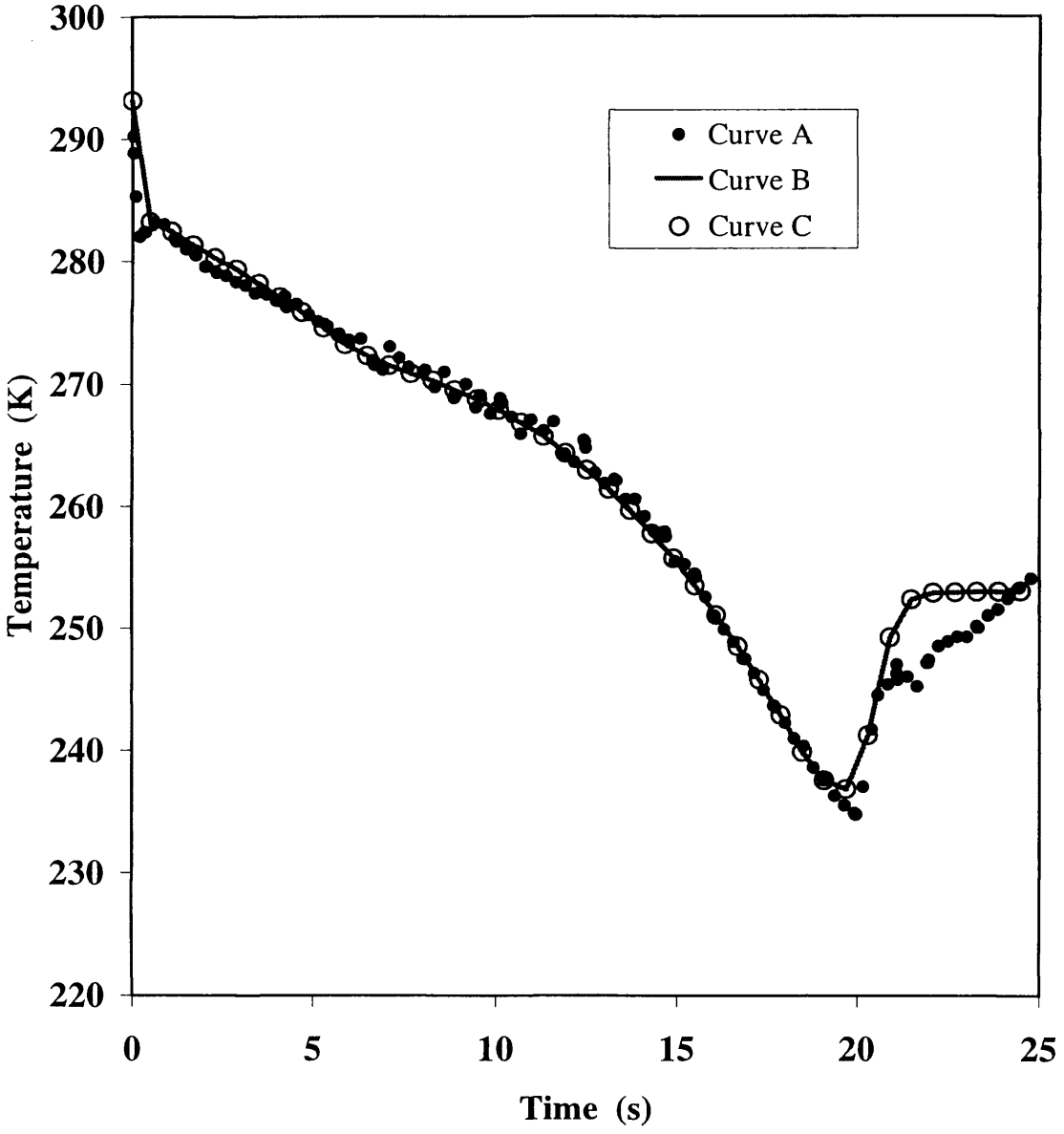

Figure 5.3: FBR open end temperature -time profiles for test P40 (LPG) showing the effect of the interpolation scheme on simulated results. Simulation data are obtained using 40 simple grids.

Curve A: Measurement (Richardson and Saville, 1996a,b).
Curve B: Simulated results without interpolation scheme. Run time, 15 mins.
Curve C: Simulated results using the interpolation scheme. Run time, 3.5 mins.

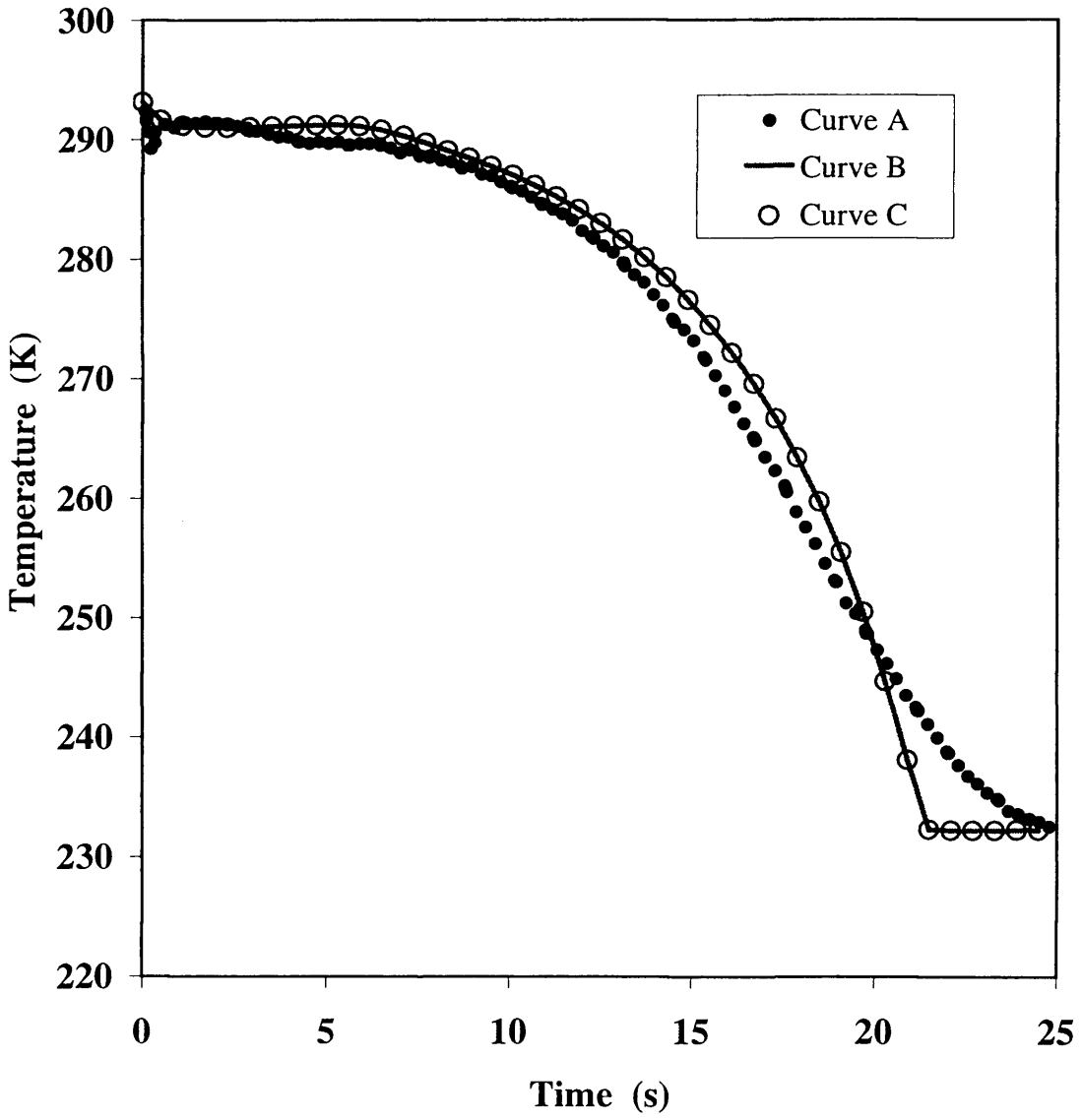

Figure 5.4: FBR closed end temperature -time profiles for test P40 (LPG) showing the effect of the interpolation scheme on simulated results. Simulation data are obtained using 40 simple grids.

Curve A: Measurement (Richardson and Saville, 1996a,b).
Curve B: Simulated results without interpolation scheme. Run time, 15 mins.
Curve C: Simulated results using the interpolation scheme. Run time, 3.5 mins.

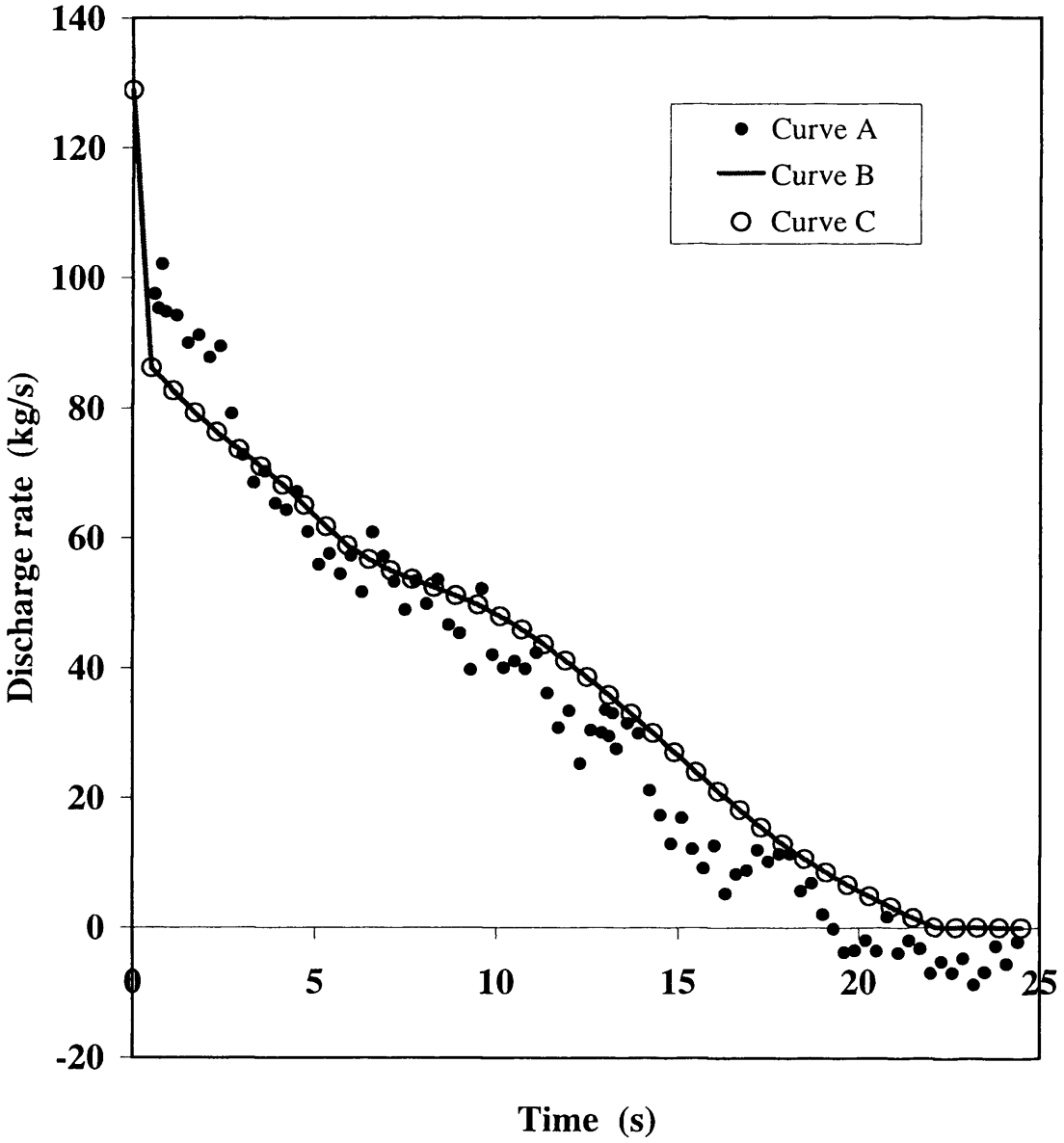

Figure 5.5: FBR discharge rate-time profiles for test P40 (LPG) showing the effect of the interpolation scheme on simulated results. Simulation data are obtained using 40 simple grids.

Curve A: Measurement (Richardson and Saville, 1996a,b).
Curve B: Simulated results without interpolation scheme. Run time, 15 mins.
Curve C: Simulated results using the interpolation scheme. Run time, 3.5 mins.

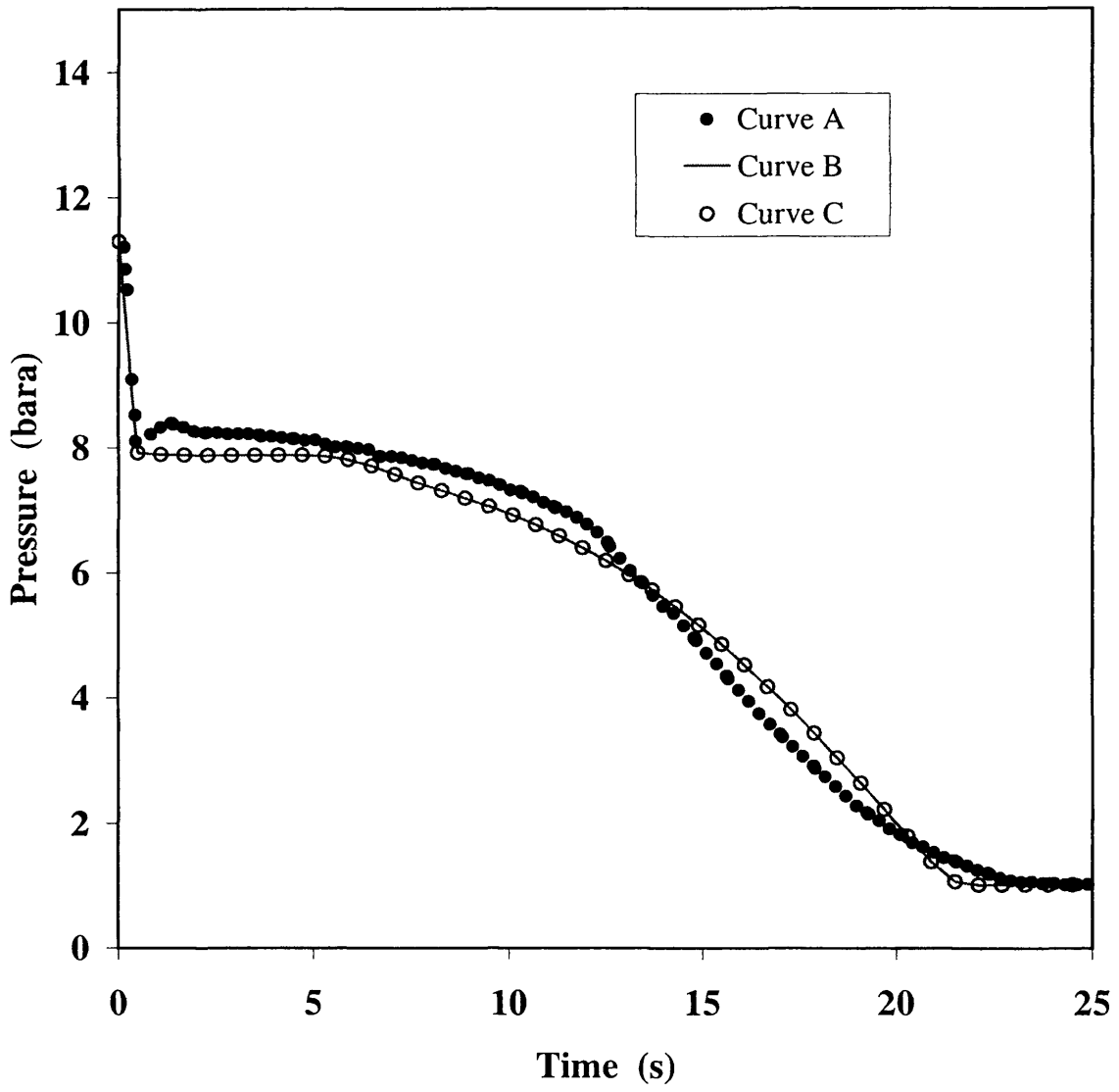

Figure 5.6: FBR open end pressure-time profiles for test P42 (LPG) showing the effect of the interpolation scheme on simulated results. Simulation data are obtained using 40 simple grids.

Curve A: Measurement (Richardson and Saville, 1996a,b).
Curve B: Simulated results without interpolation scheme. Run time, 12 mins.
Curve C: Simulated results using the interpolation scheme. Run time, 3 mins.

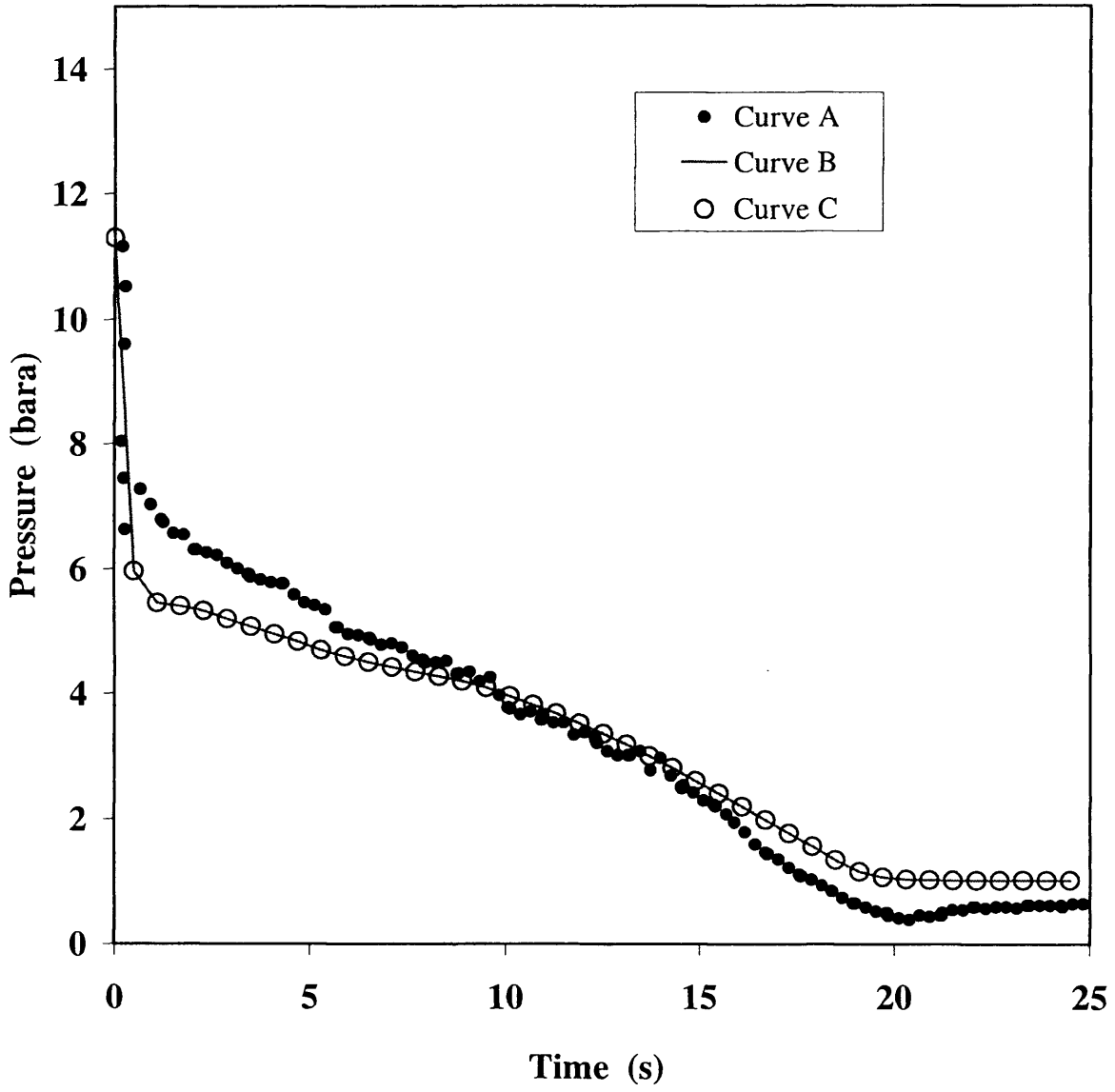

Figure 5.7: FBR closed end pressure -time profiles for test P42 (LPG) showing the effect of the interpolation scheme on simulated results. Simulation data are obtained using 40 simple grids.

Curve A: Measurement (Richardson and Saville, 1996a,b).
Curve B: Simulated results without interpolation scheme. Run time, 12 mins.
Curve C: Simulated results using the interpolation scheme. Run time, 3 mins.

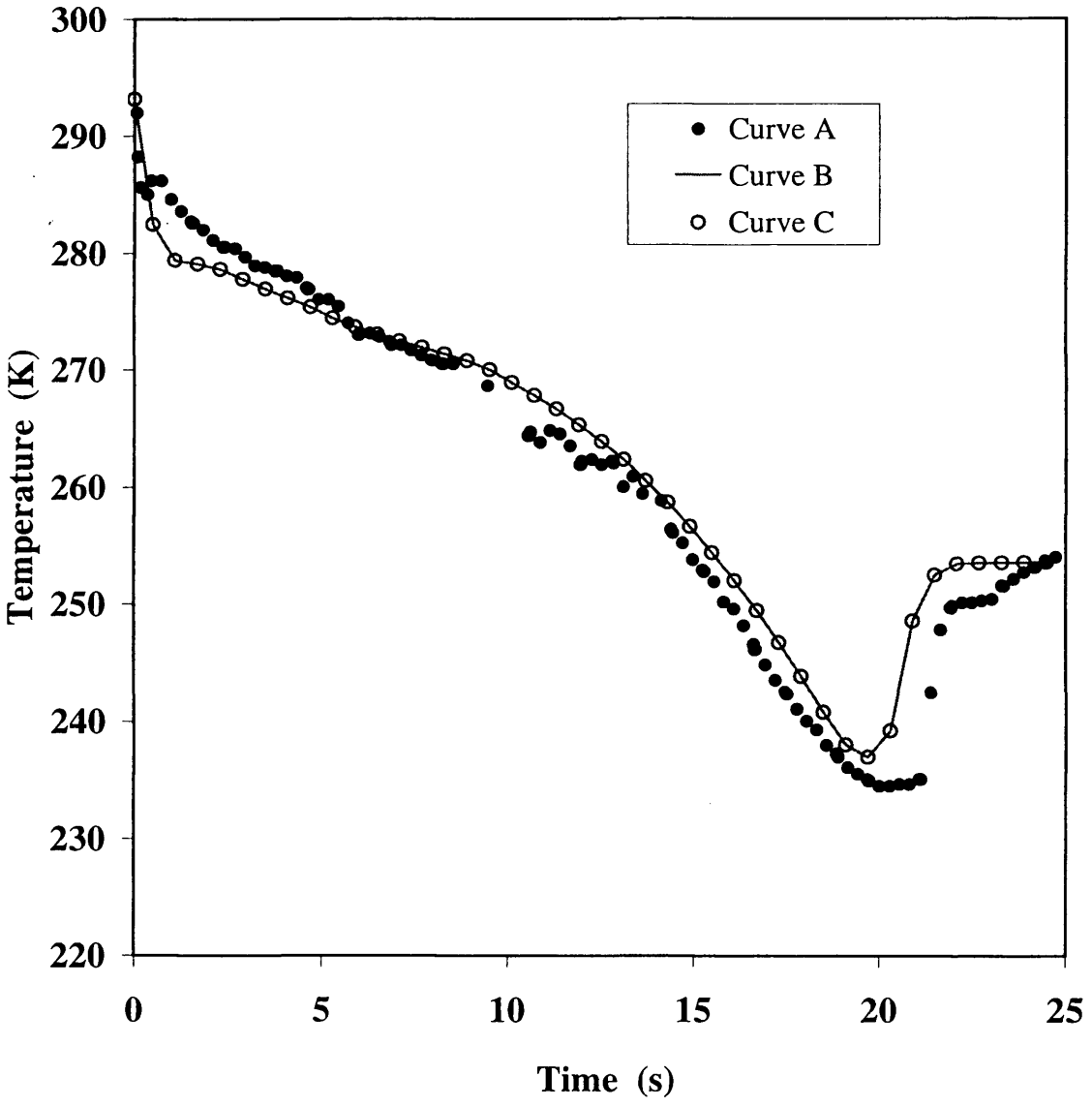

Figure 5.8: FBR open end temperature -time profiles for test P42 (LPG) showing the effect of the interpolation scheme on simulated results. Simulation data are obtained using 40 simple grids.

Curve A: Measurement (Richardson and Saville, 1996a,b).
Curve B: Simulated results without interpolation scheme. Run time, 12 mins.
Curve C: Simulated results using the interpolation scheme. Run time, 3 mins.

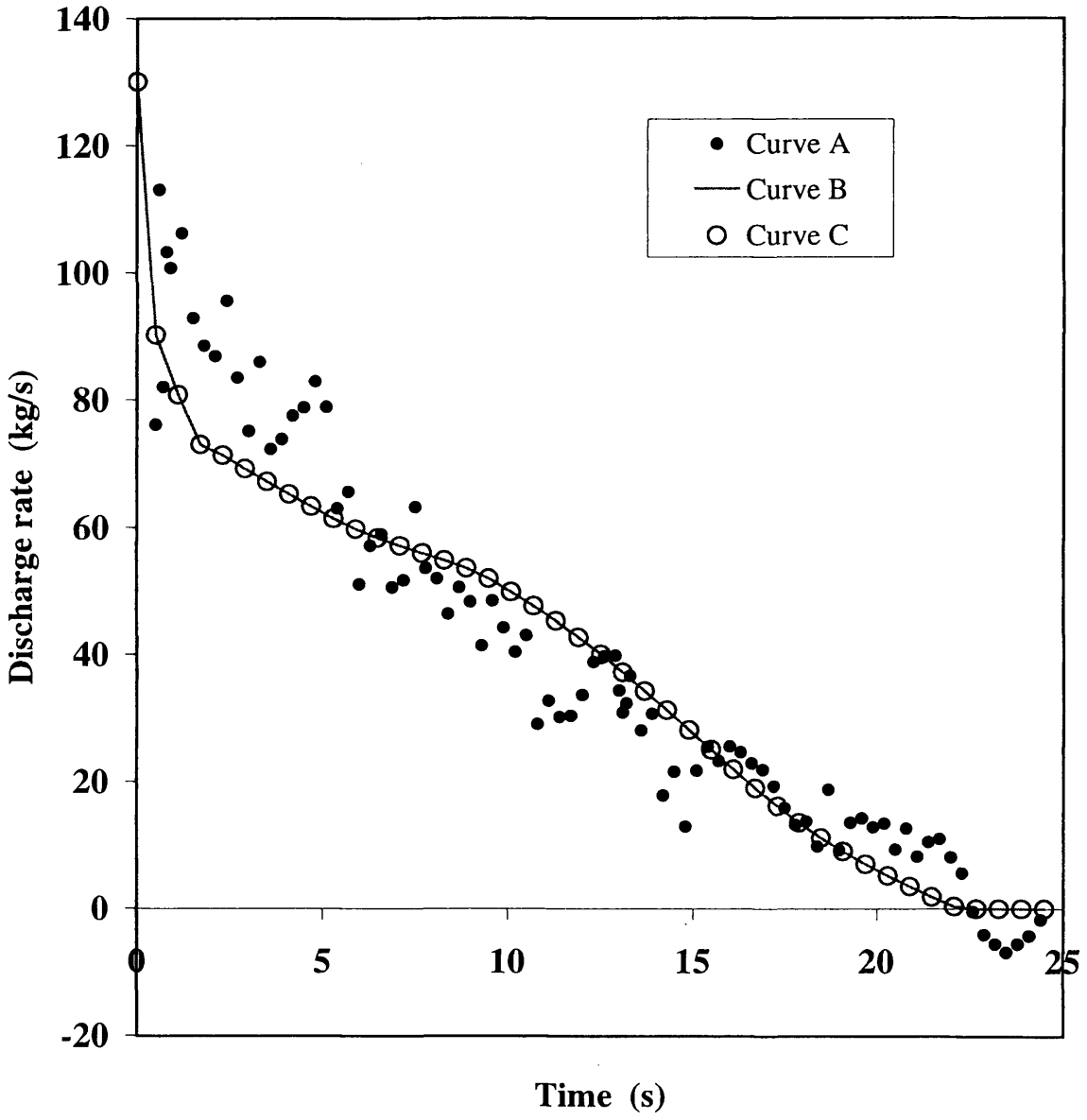

Figure 5.9: FBR discharge rate-time profiles for test P42 (LPG) showing the effect of the interpolation scheme on simulated results. Simulation data are obtained using 40 simple grids.

Curve A: Measurement (Richardson and Saville, 1996a,b).
Curve B: Simulated results without interpolation scheme. Run time, 12 mins.
Curve C: Simulated results using the interpolation scheme. Run time, 3 mins.

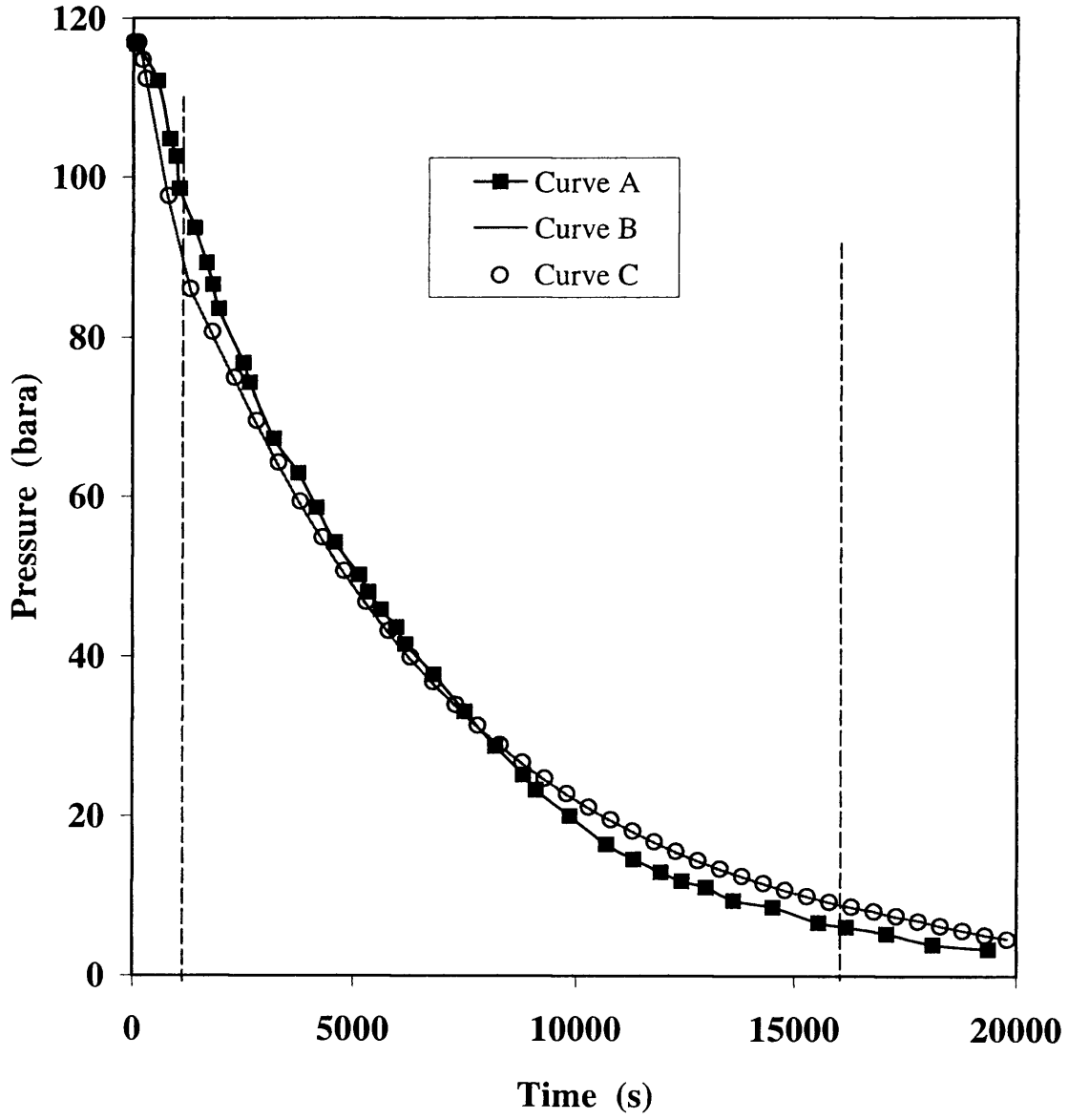

Figure 5.10: Variation of intact end pressure with time following FBR of the subsea line from Piper Alpha to MCP-01 during the Piper Alpha disaster. Simulation data are obtained using 108 compound nested grids.

Curve A: Measurement (Richardson and Saville, 1991).
Curve B: Simulated results without interpolation scheme. Run time, 28 hrs.
Curve C: Simulated results using the interpolation scheme. Run time, 5.5 hrs.

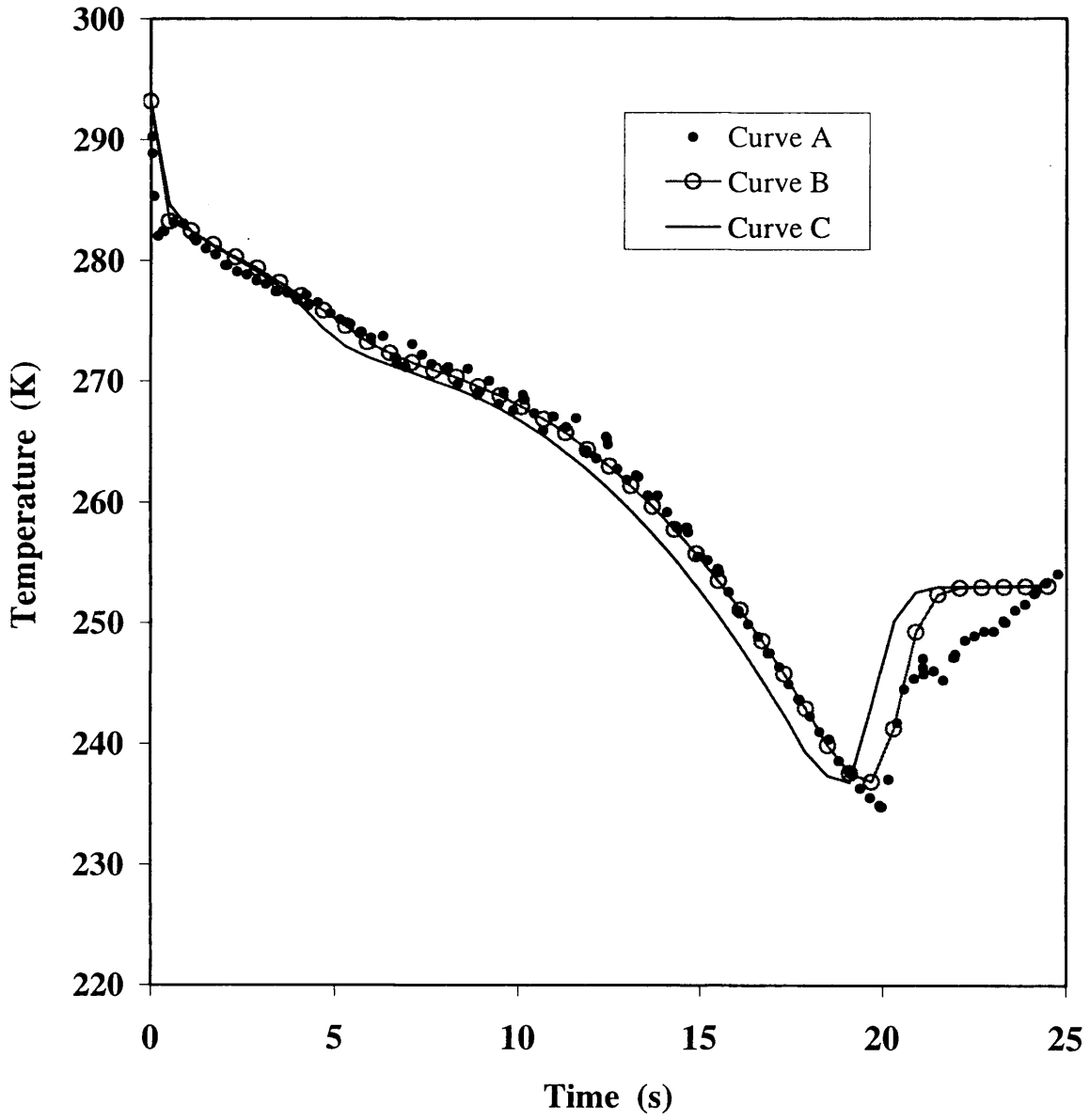

Figure 5.11: FBR open end temperature -time profiles for test P40 (LPG) showing the effect using a smaller time-step in modelling the fluid interface. Simulation data are obtained using 40 simple grids.

Curve A: Measurement (Richardson and Saville, 1996a,b).
Curve B: Simulated data; $0.1\Delta t_{max}$. Run time, 3.5 mins.
Curve C: Simulated data; $0.9\Delta t_{max}$. Run time, 3 mins.

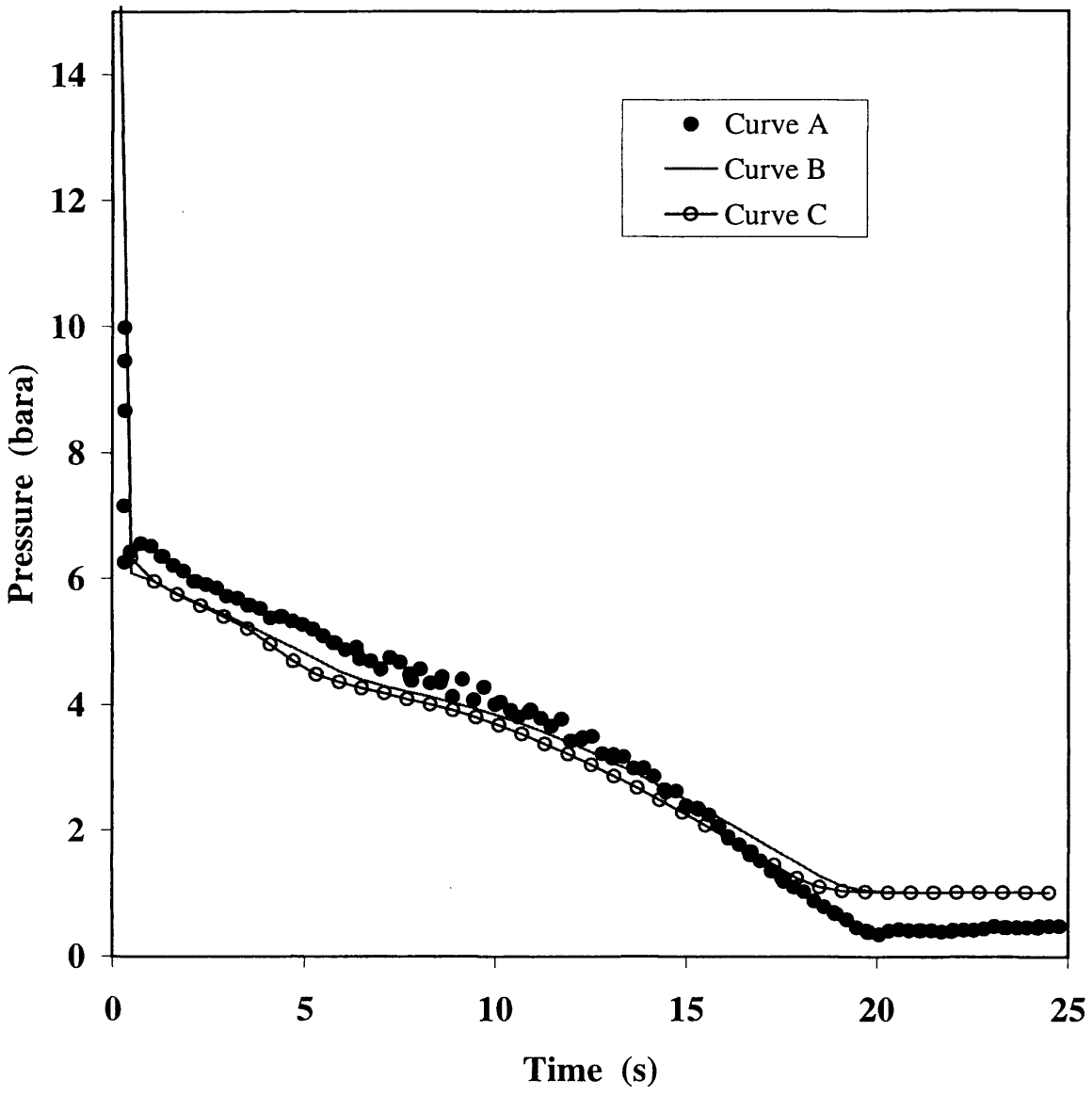

Figure 5.12: FBR pressure-time profiles for test P40 (LPG) showing the effect using a smaller time-step in modelling the fluid interface. Simulation data are obtained using 40 simple grids.

Curve A: Measurement (Richardson and Saville, 1996a,b).
Curve B: Simulated data; $0.1\Delta t_{max}$. Run time, 3.5 mins.
Curve C: Simulated data; $0.9\Delta t_{max}$. Run time, 3 mins.

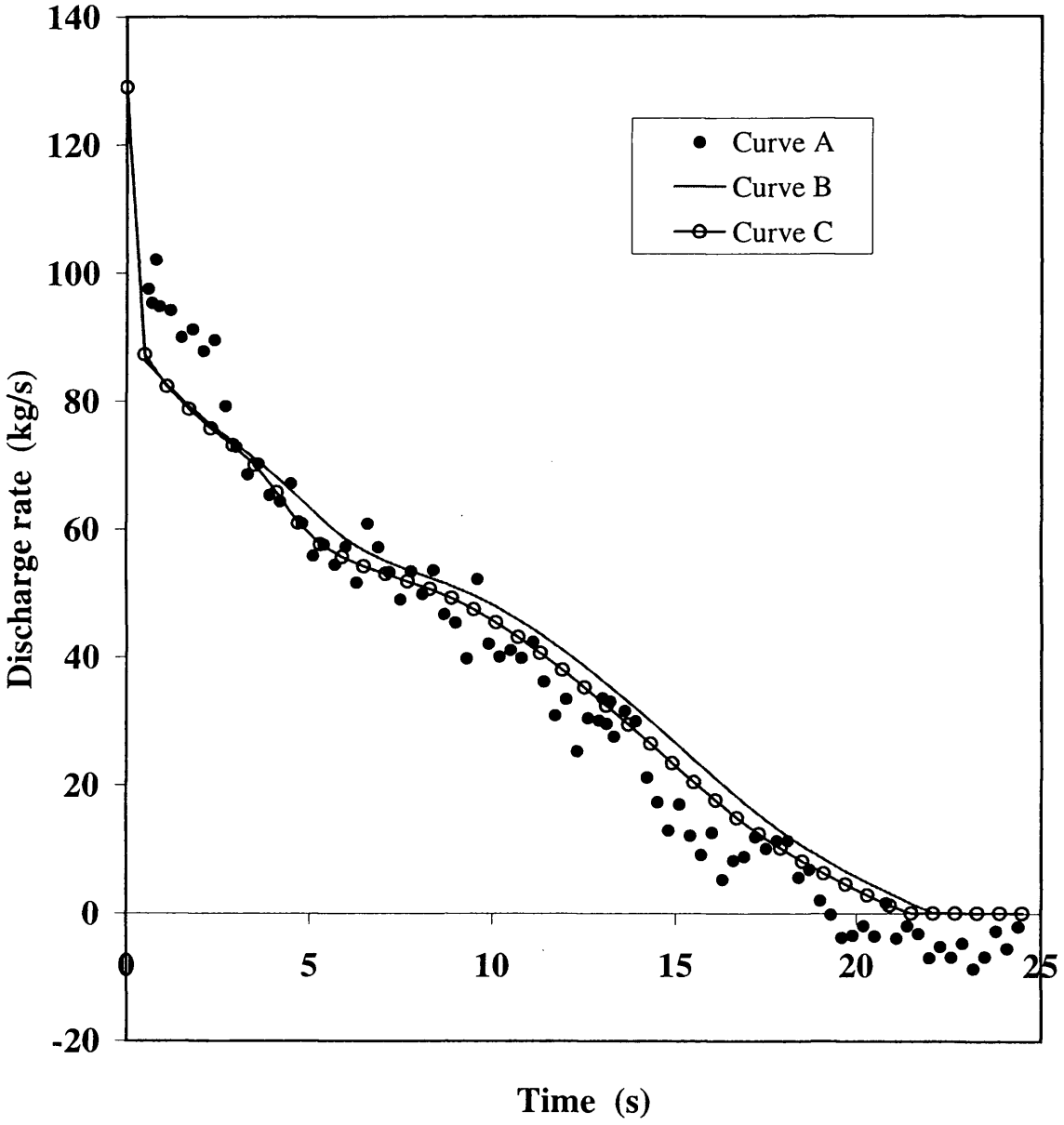

Figure 5.13: FBR discharge rate-time profiles for test P40 (LPG) showing the effect using a smaller time-step in modelling the fluid interface. Simulation data are obtained using 40 simple grids.

Curve A: Measurement (Richardson and Saville, 1996a,b).
Curve B: Simulated data; $0.1\Delta t_{max}$. Run time, 3.5 mins.
Curve C: Simulated data; $0.9\Delta t_{max}$. Run time, 3 mins.

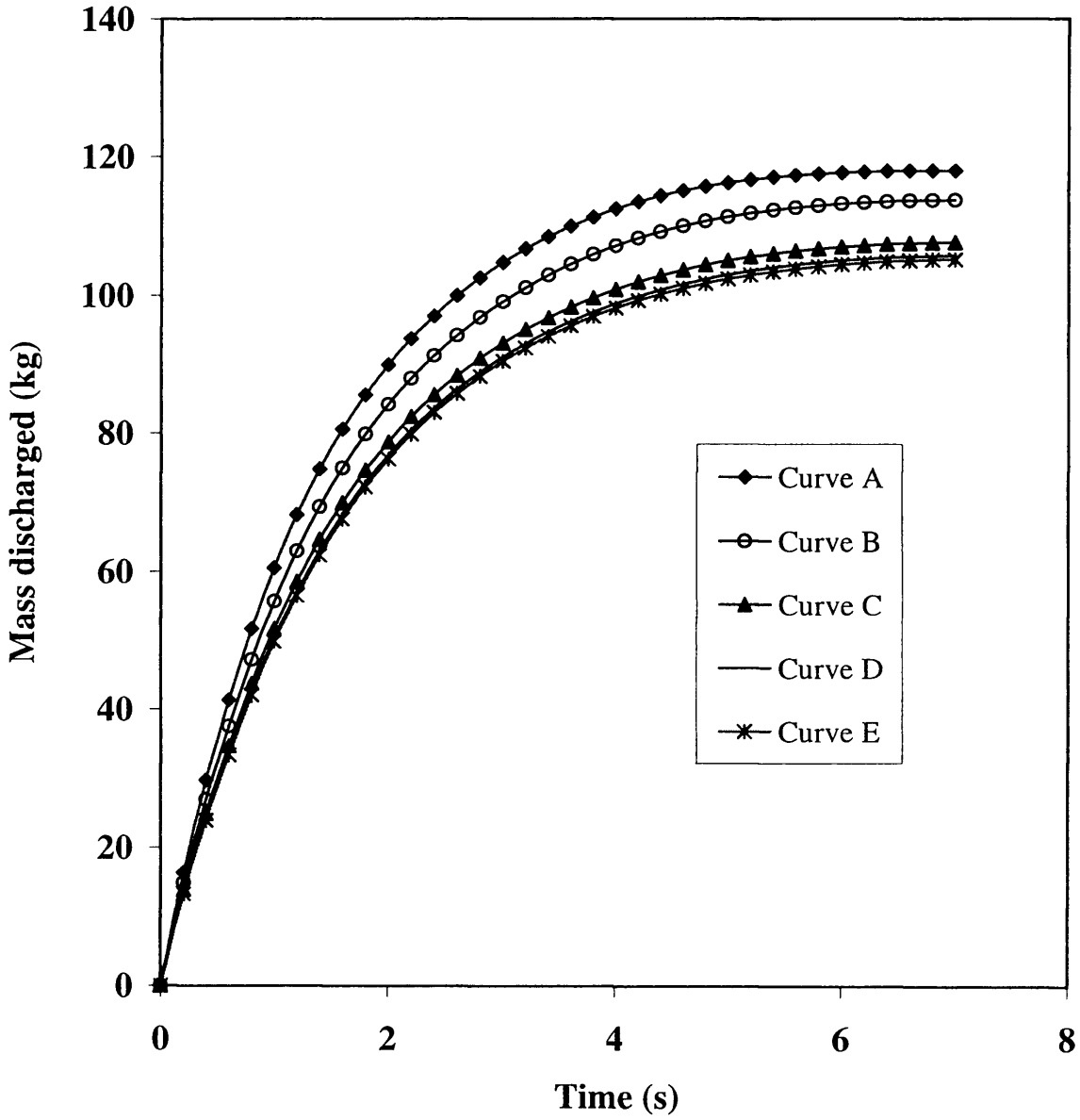

Figure 5.14a: Variation of the cummulative mass discharged with time from a 200 m gas pipeline .

Curve A: 10 simple grids. MCI; 0.82. Runtime; 7 s.
Curve B: 20 simple grids. MCI; 0.91. Runtime; 13 s.
Curve C: 50 simple grids. MCI; 0.97. Runtime; 36 s.
Curve D: 100 simple grids. MCI; 0.99. Runtime; 95 s.
Curve E: 150 simple grids. MCI; 0.99. Runtime; 176 s.

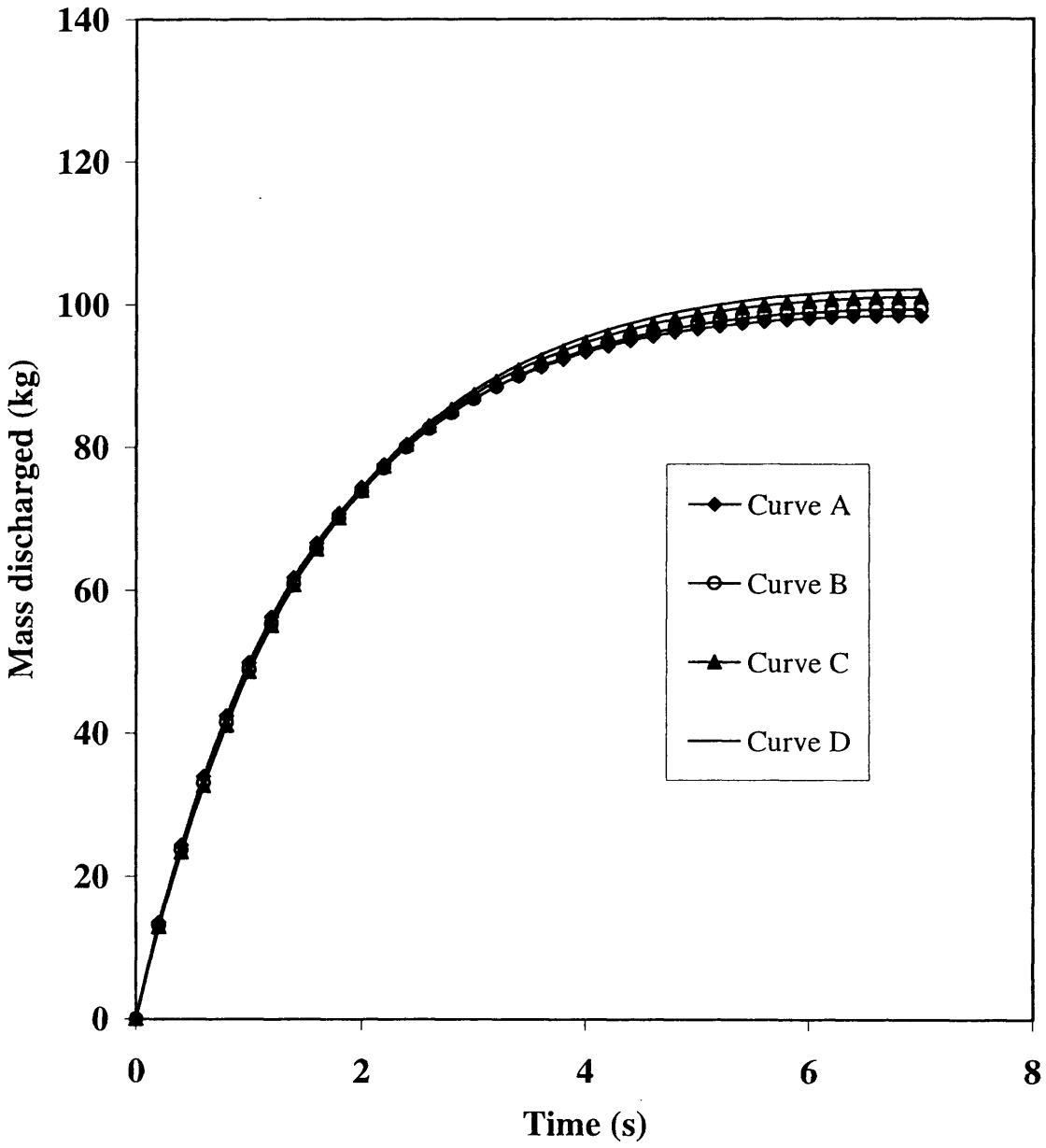

Figure 5.14b: Variation of the cummulative mass discharged with time from a 200 m gas pipeline .

Curve A: 10 nested grids. MCI; 1.06. Runtime; 22 s.
Curve B: 20 nested grids. MCI; 1.05. Runtime; 34 s.
Curve C: 50 nested grids. MCI; 1.03. Runtime; 91 s.
Curve D: 100 nested grids. MCI; 1.02. Runtime; 212 s.

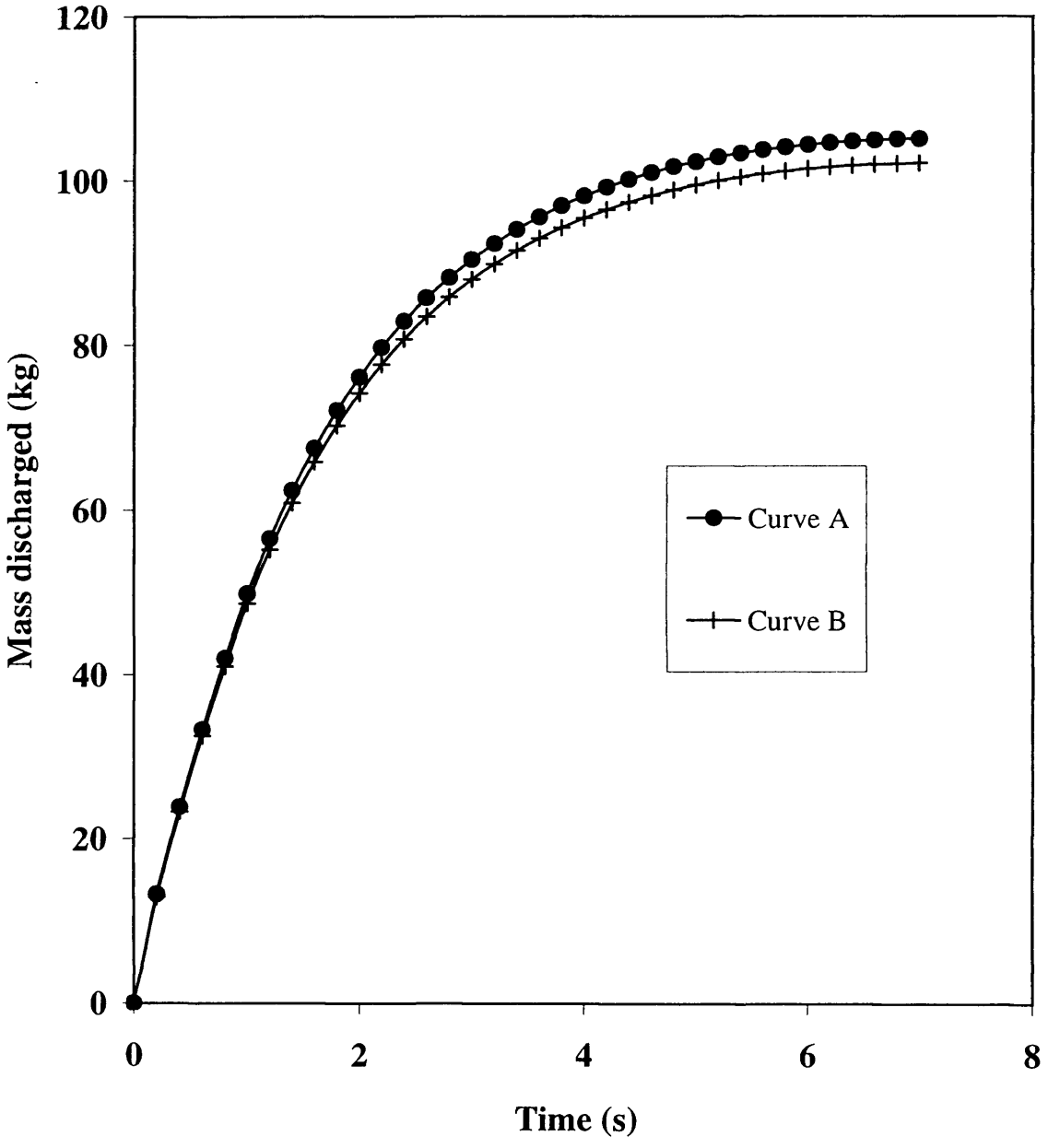

Figure 5.14c: Comparison of the converged cummulative mass discharged profile from a 200 m gas pipeline, based on the simple and nested schemes.

Curve A: 150 simple grids.
Curve B: 100 nested grids.

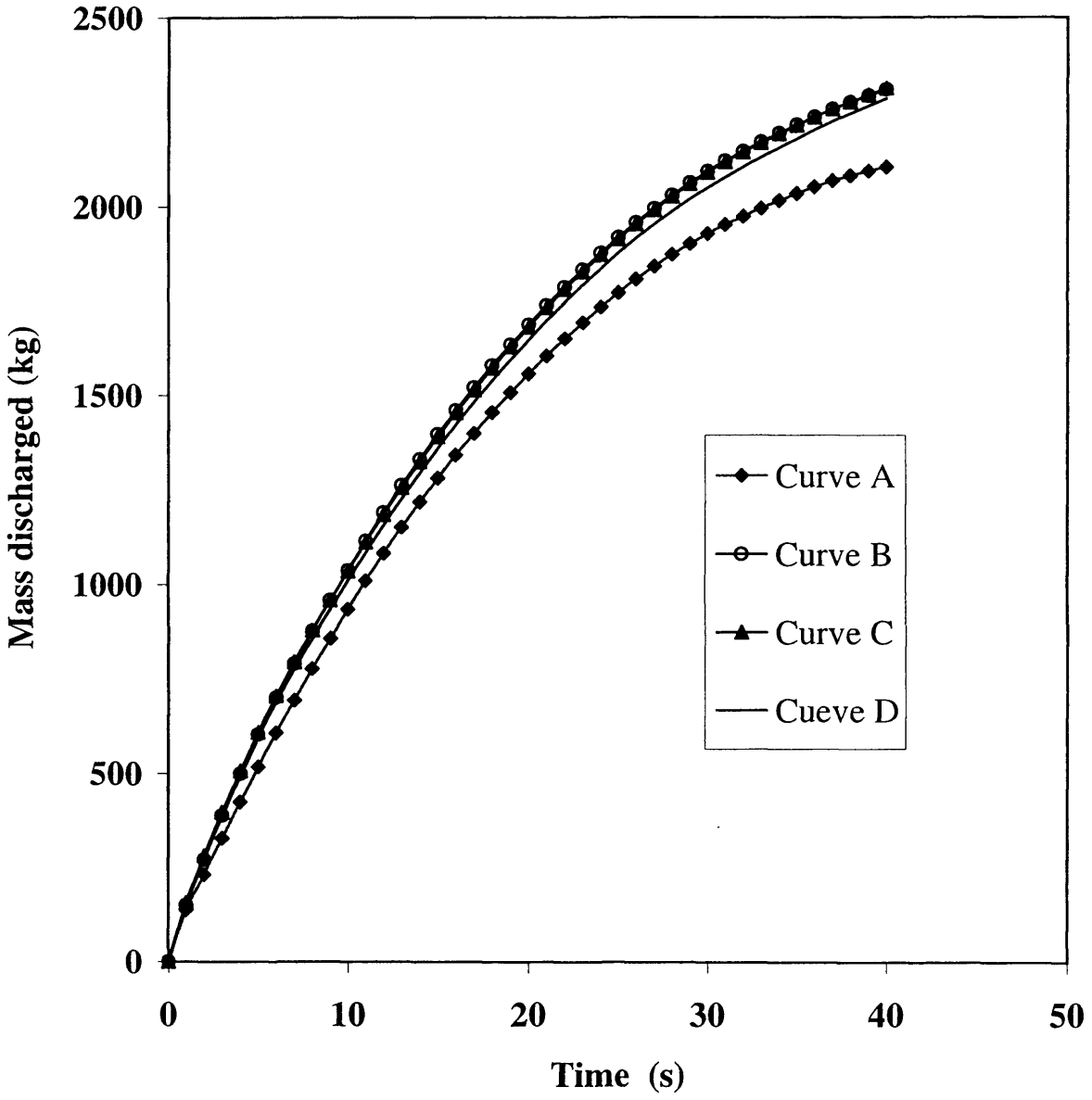

Figure 5.15a: Variation of the cummulative mass discharged with time from a 200 m two- phase pipeline.

Curve A: 10 simple grids. MCI; 1.07. Runtime; 1.2 mins.
Curve B: 20 simple grids. MCI; 0.97. Runtime; 2.7 mins.
Curve C: 50 simple grids. MCI; 0.95. Runtime; 3.9 mins.
Curve D: 100 simple grids. MCI; 0.95. Runtime; 7.6 mins.

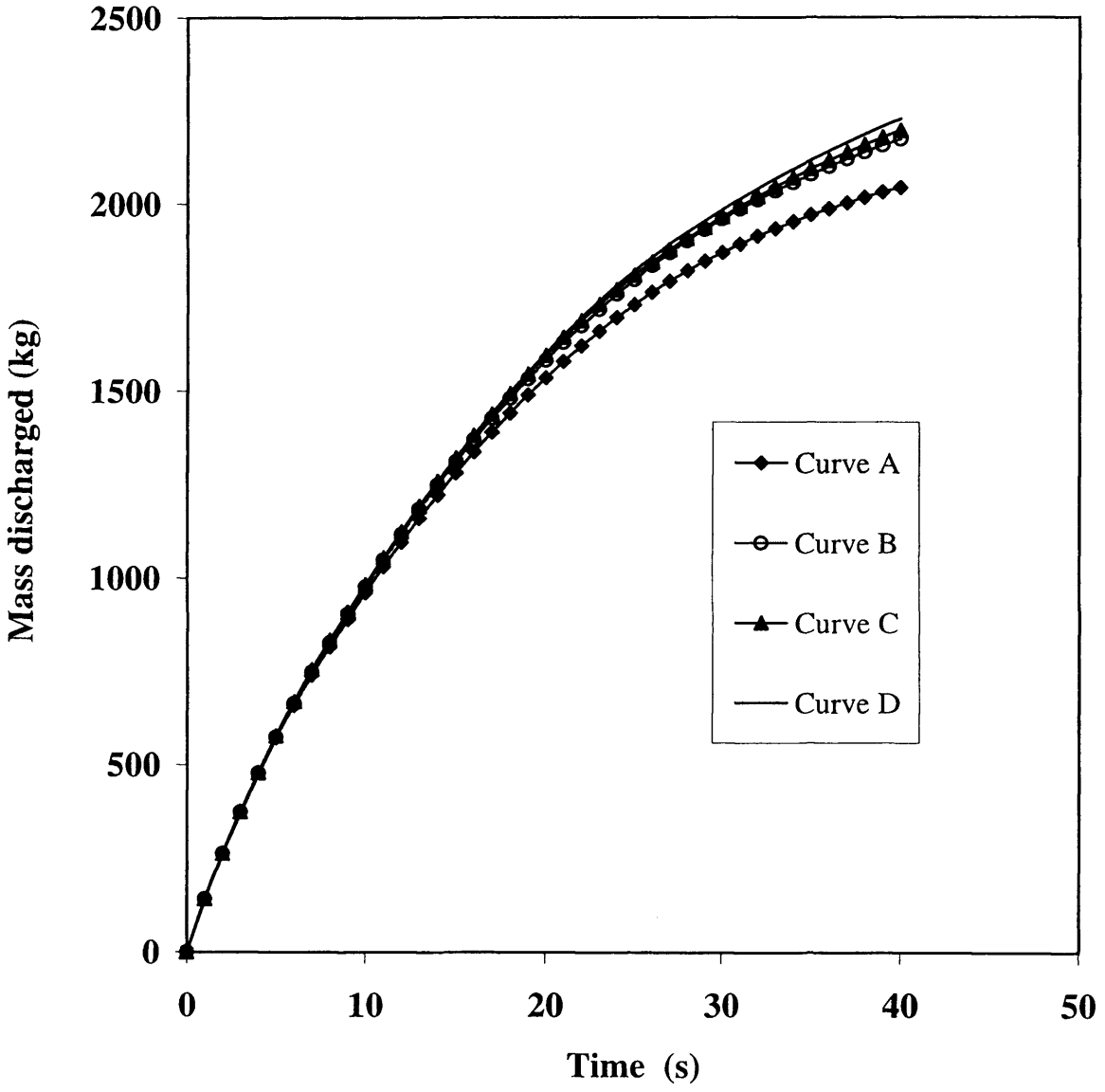

Figure 5.15b: Variation of the cummulative mass discharged with time from a 200 m two- phase pipeline.

Curve A: 10 nested grids. MCI; 1.10. Runtime; 7.5 mins.
Curve B: 20 nested grids. MCI; 1.01. Runtime; 11.1 mins.
Curve C: 50 nested grids. MCI; 0.99. Runtime; 18.5 mins.
Curve D: 100 nested grids. MCI; 0.97. Runtime; 38.6 mins.

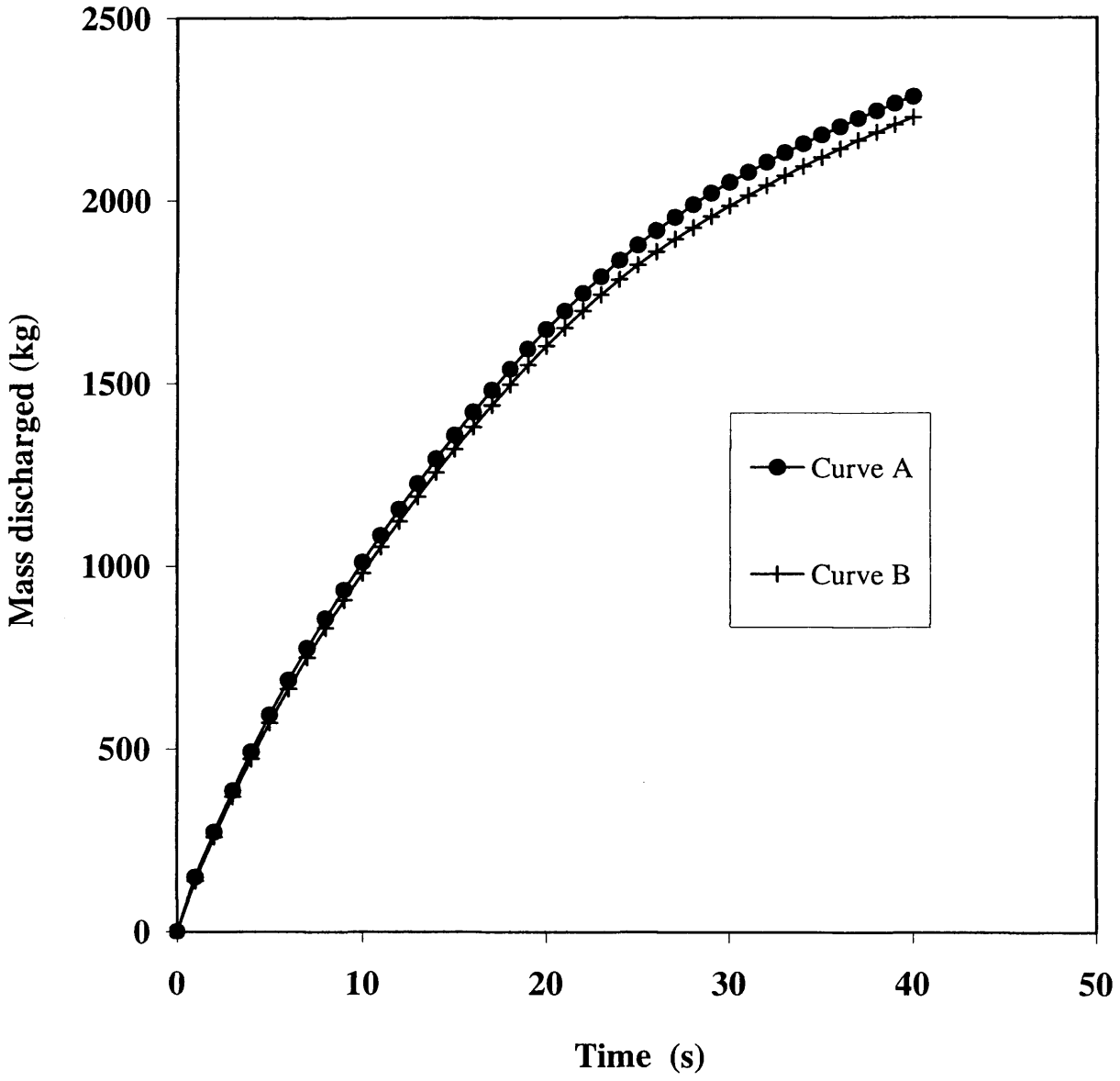

Figure 5.15c: Comparison of the converged cummulative mass discharged profile from a 200 m two phase pipeline, based on the simple and nested schemes.

Curve A: 100 simple grids.
Curve B: 100 nested grids.

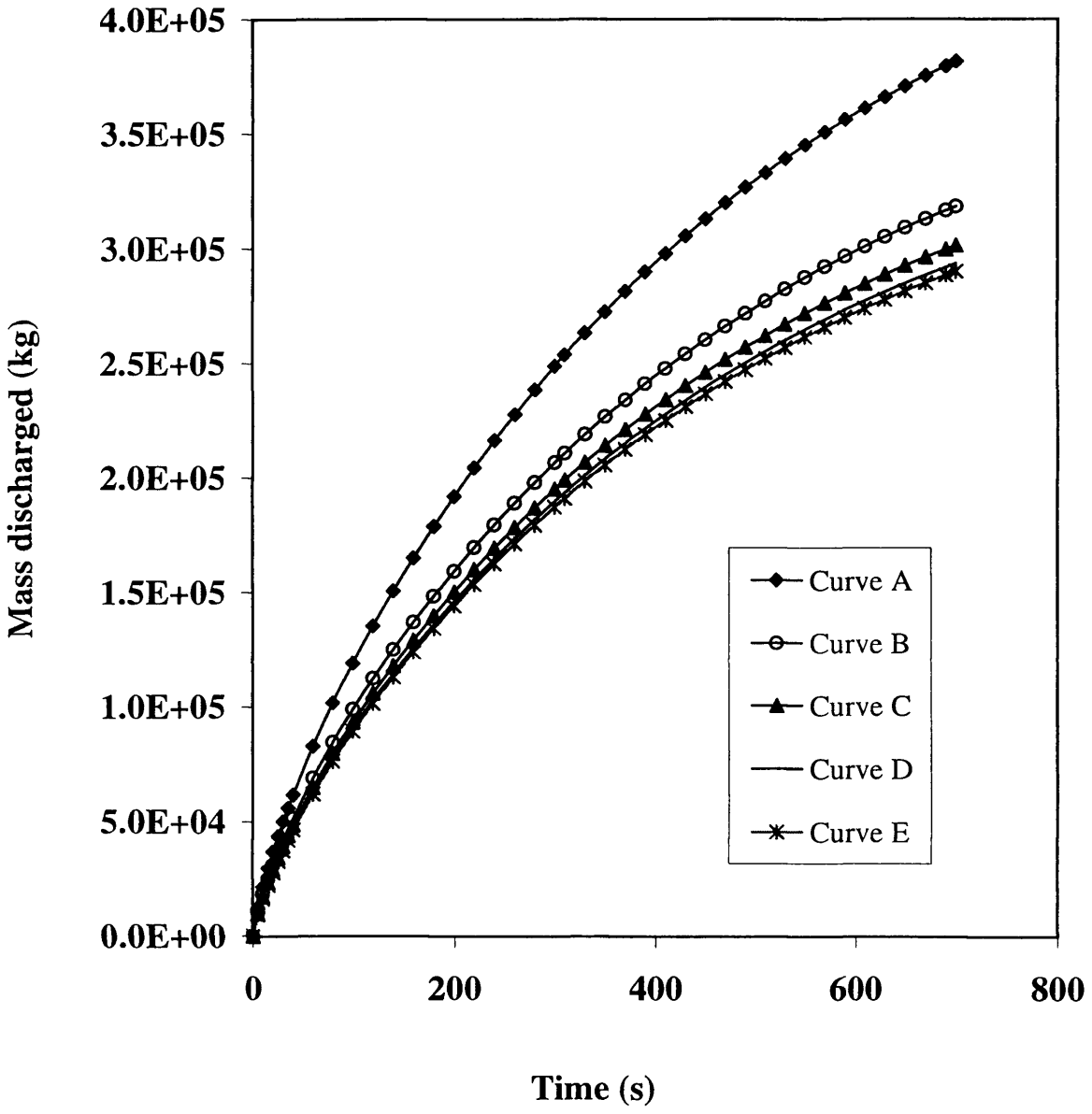

Figure 5.16a: Variation of the cummulative mass discharged with time from a 20 km gas pipeline.

Curve A: 100 simple grids. MCI; 0.77. Run time; 1.7 mins.
Curve B: 250 simple grids. MCI; 0.9. Run time; 7.6 mins.
Curve C: 500 simple grids. MCI; 0.96. Run time; 25.8 mins.
Curve D: 1000 simple grids. MCI; 0.98. Run time; 98.2 mins.
Curve E: 2000 simple grids. MCI; 0.99. Run time; 197.7 mins.

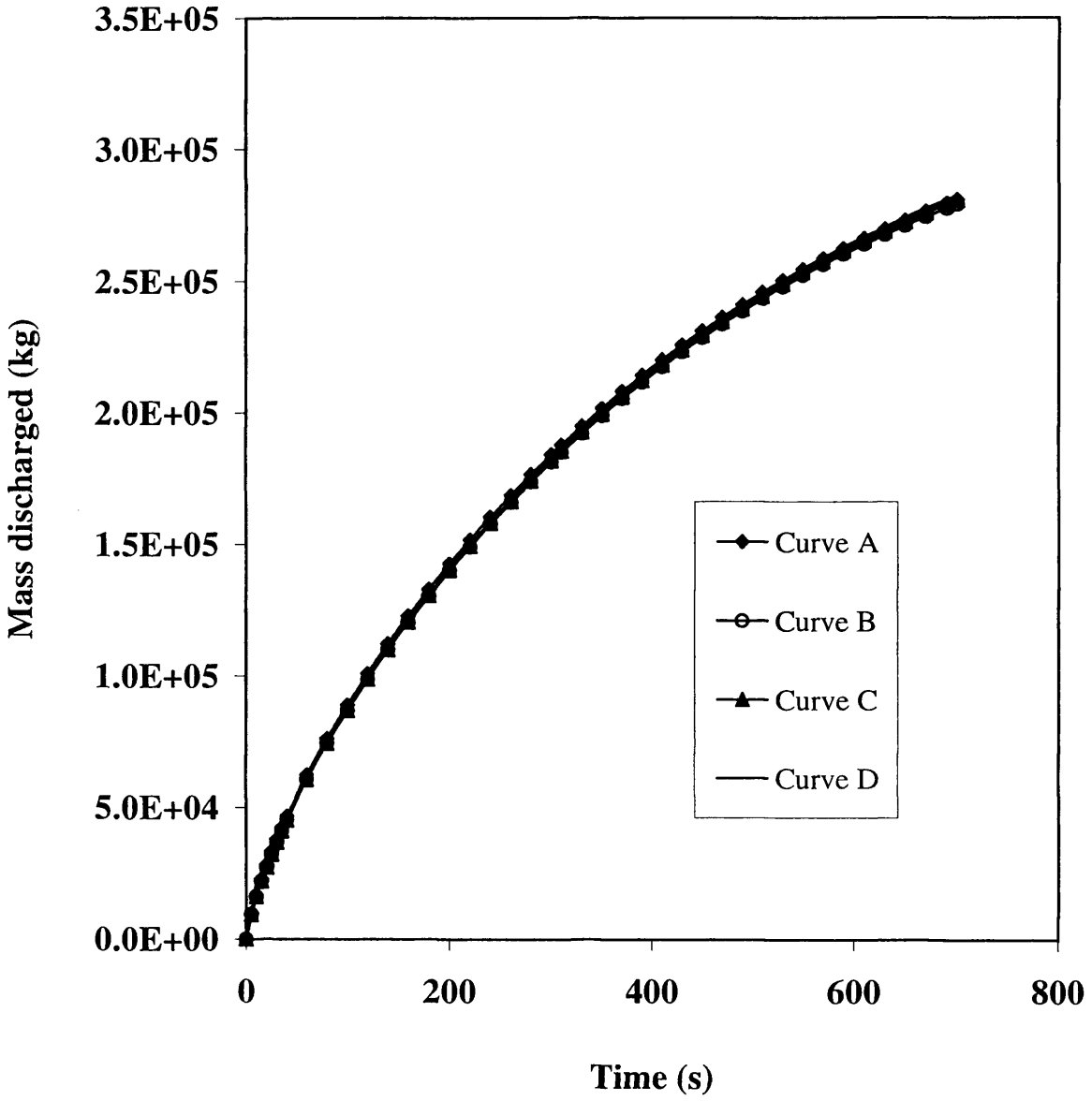

Figure 5.16b: Variation of the cummulative mass discharged with time from a 20 km gas pipeline.

Curve A: 100 nested grids. MCI; 1.04. Run time; 4.9 mins.
Curve B: 250 nested grids. MCI; 1.04. Run time; 12.3 mins.
Curve C: 500 nested grids. MCI; 1.03. Run time; 36.2 mins.
Curve D: 1000 nested grids. MCI; 1.02. Run time; 124.0 mins.

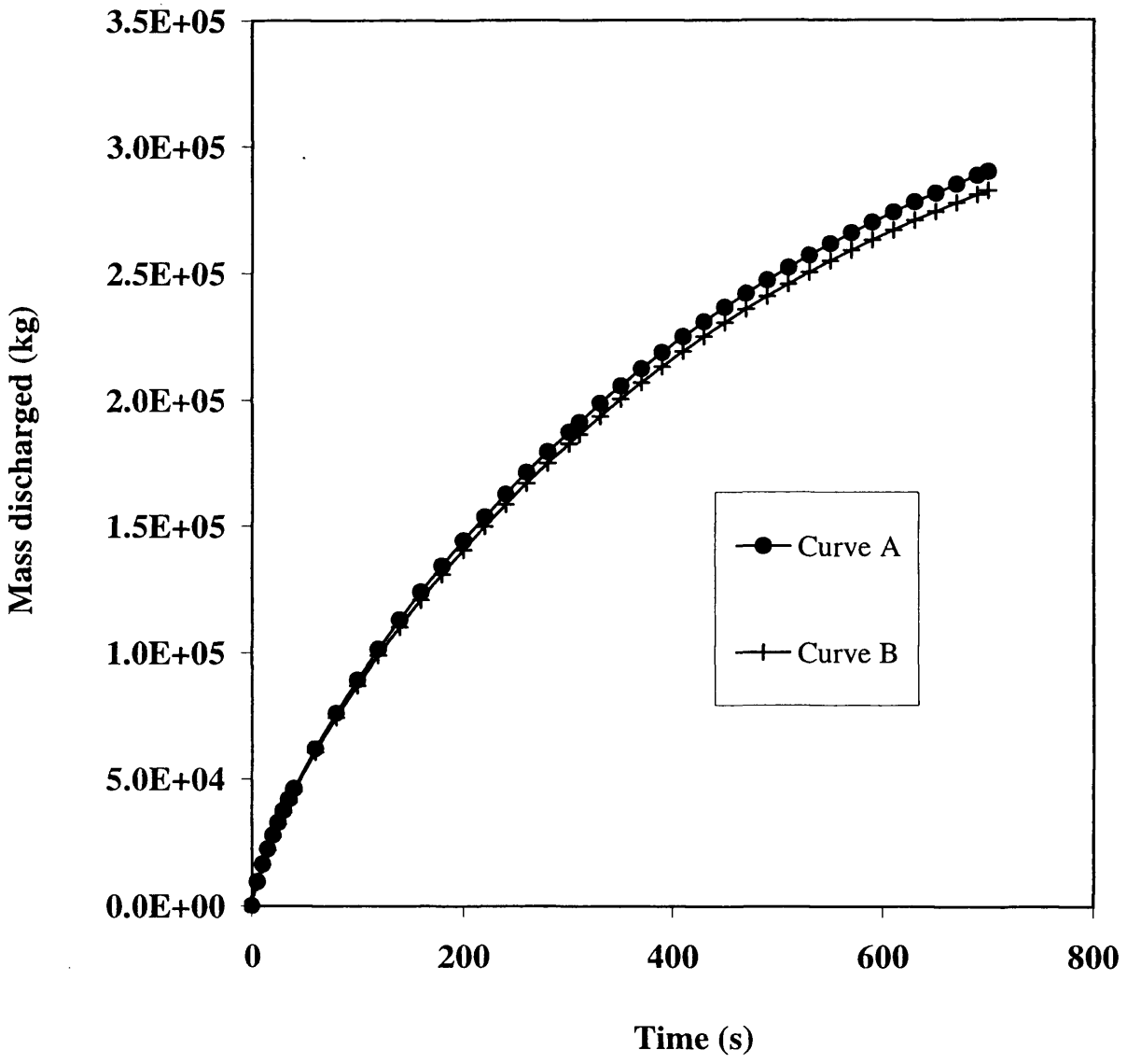

Figure 5.16c: Comparison of the converged cummulative mass discharged profile from a 20 km gas pipeline, based on the simple and nested schemes.

Curve A: 2000 simple grids.
Curve B: 100 nested grids.

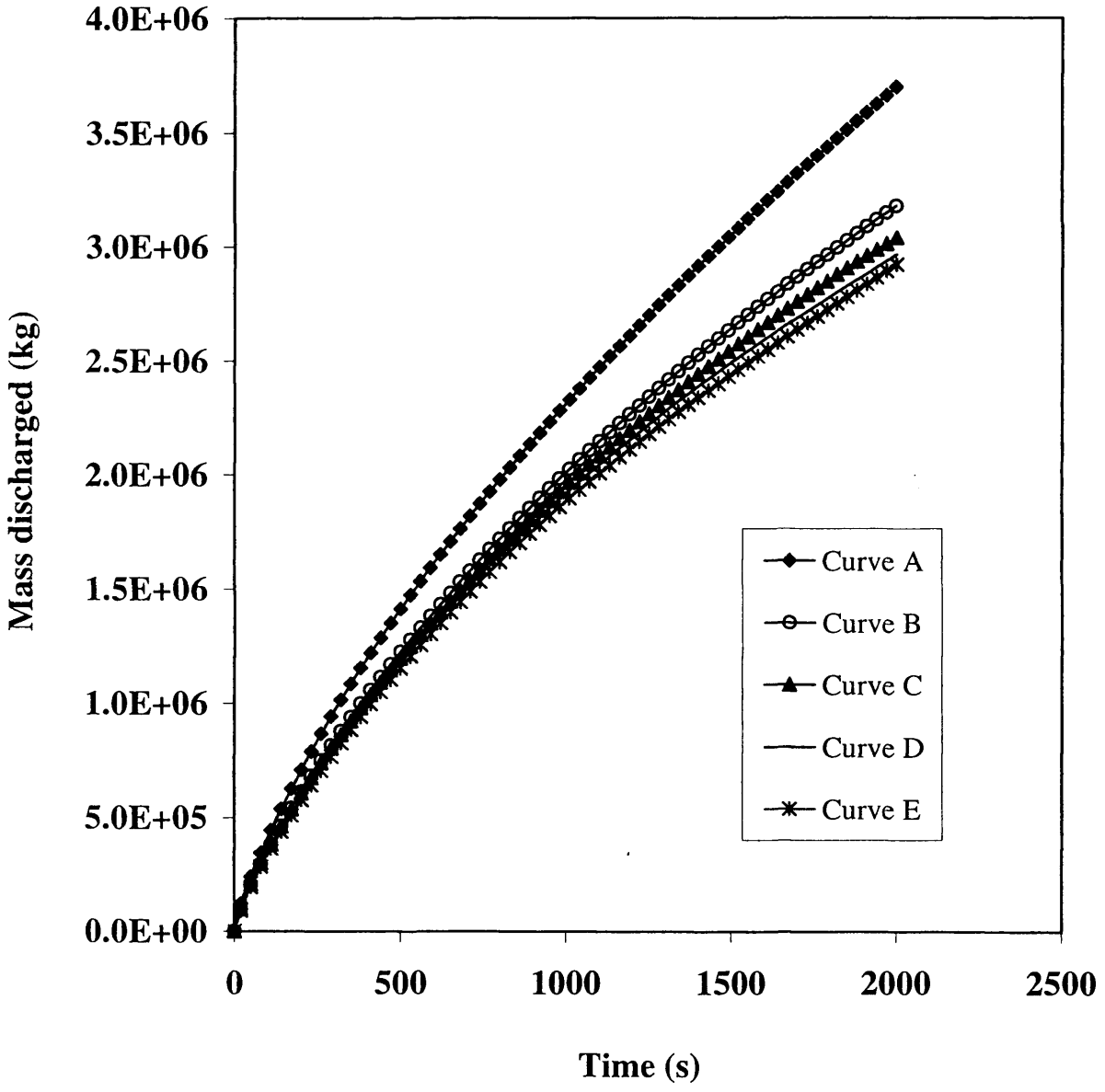

Figure 5.17a: Variation of the cummulative mass discharged with from a 20 km two-phase pipeline.

Curve A: 100 simple grids. MCI; 0.82. Run time; 5.5 mins.
Curve B: 250 simple grids. MCI; 0.92. Run time; 12.2 mins.
Curve C: 500 simple grids. MCI; 0.96. Run time; 19.5 mins.
Curve D: 1000 simple grids. MCI; 0.95. Run time; 46.0 mins.
Curve E: 2000 simple grids. MCI; 0.96. Run time; 112.2 mins.

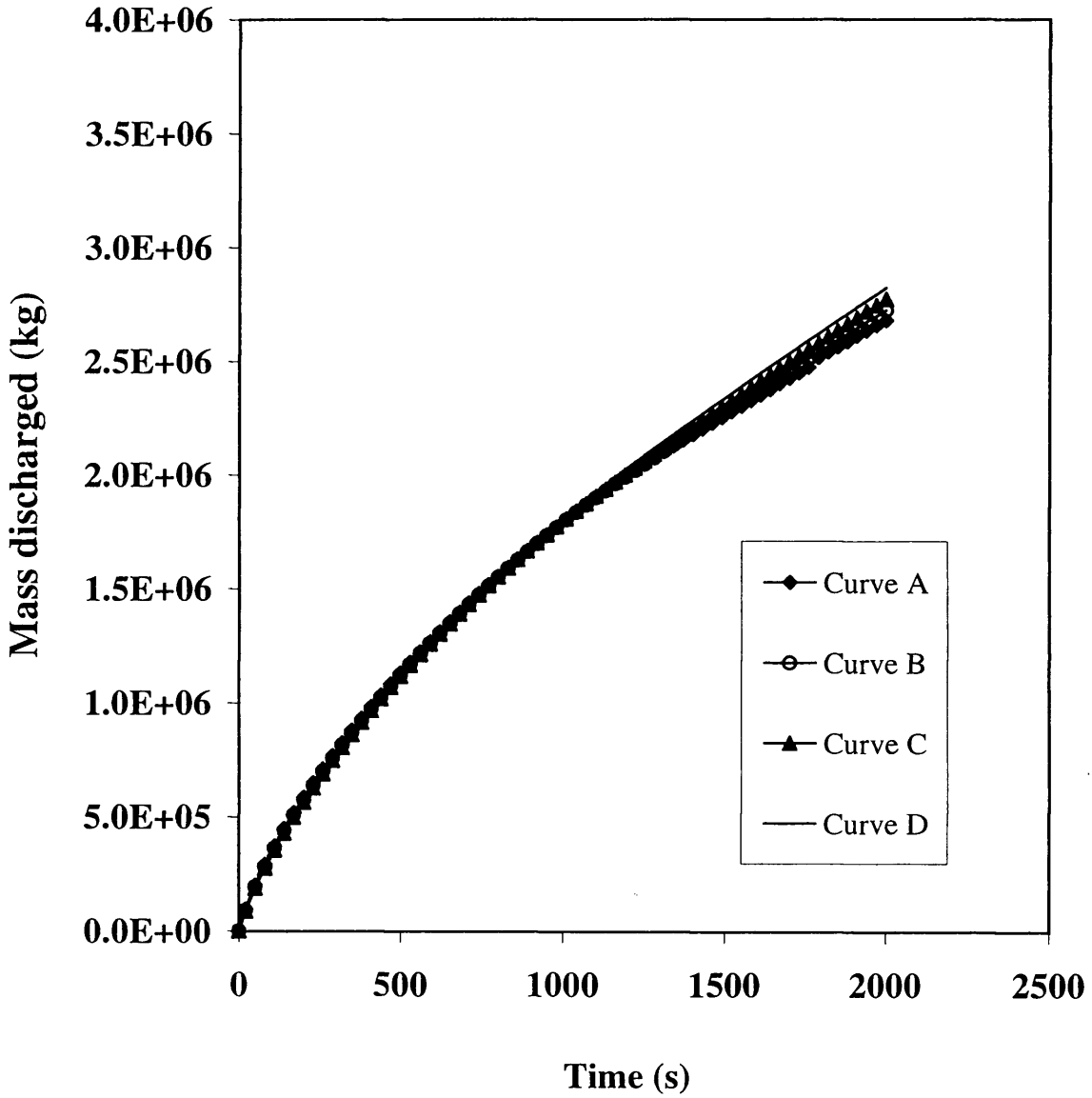

Figure 5.17b: Variation of the cummulative mass discharged with from a 20 km two- phase pipeline.

Curve A: 100 nested grids. MCI; 1.17. Run time; 24.7 mins.
Curve B: 250 nested grids. MCI; 1.07. Run time; 57.3 mins.
Curve C: 500 nested grids. MCI; 1.03. Run time; 110.1mins.
Curve D: 1000 nested grids.MCI; 1.00. Run time; 287.5 mins.

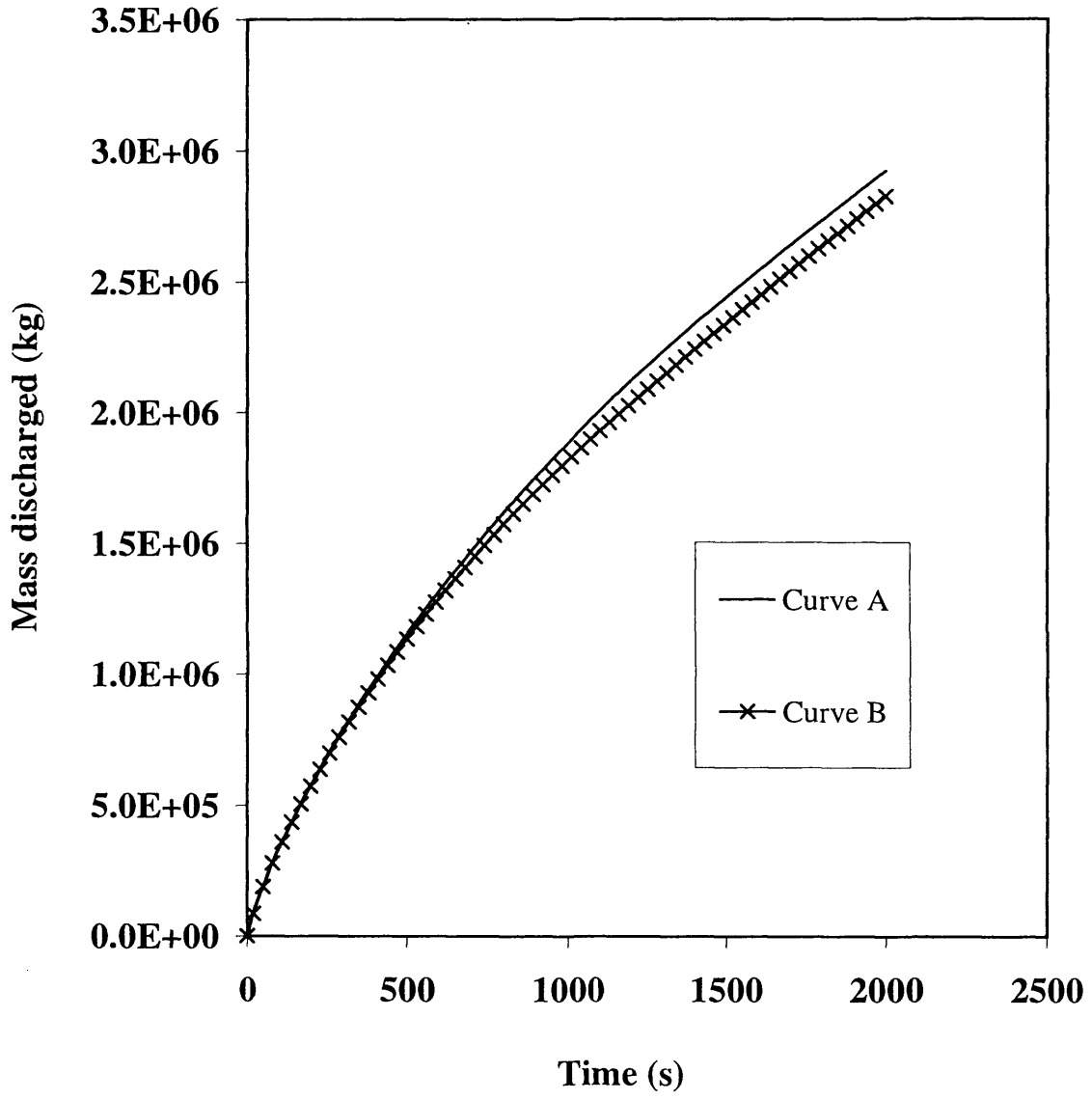

Figure 5.17c: Comparison of the converged cummulative mass discharged profile from a 20 km two- phase pipeline, based on the simple and nested schemes.

Curve A: 2000 simple grids.
Curve B: 1000 nested grids.

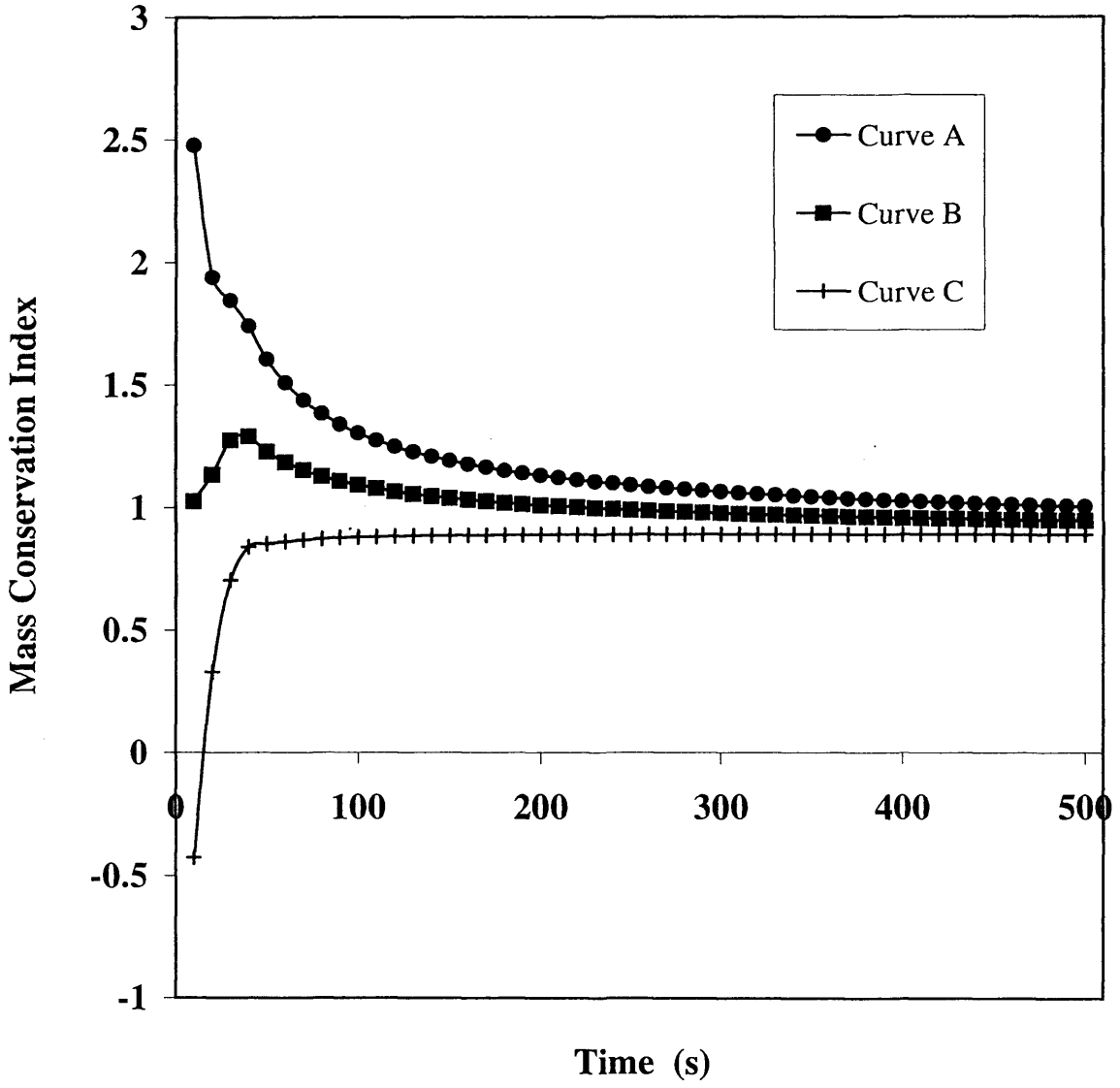

Figure 5.18: Variation of the mass conservation index with time generated during the depressurisation of a 20km two- phase pipeline .

Curve A: Mass conservation index computed with -1% error in the data.
Curve B: Actual mass conservation index .
Curve C: Mass conservation index computed with +1% error in the data.

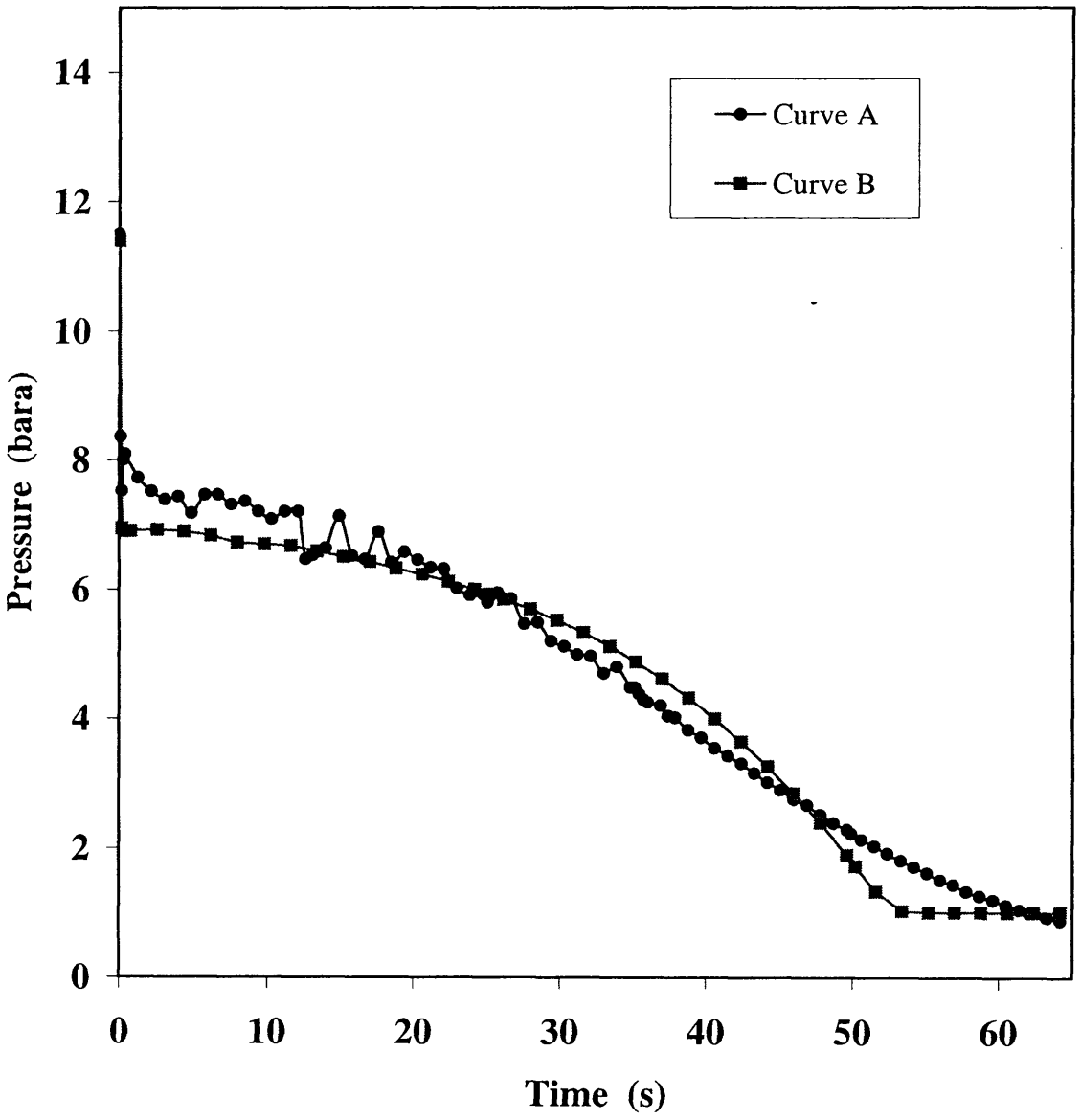

Figure 5.19: Variation of open end pressure with time following a 0.095m diameter axisymmetric puncture for test P45 (LPG). Simulated data are obtained using 40 simple grids.

Curve A: Measurement (Richardson and Saville, 1996a).
Curve B: Simulated data.

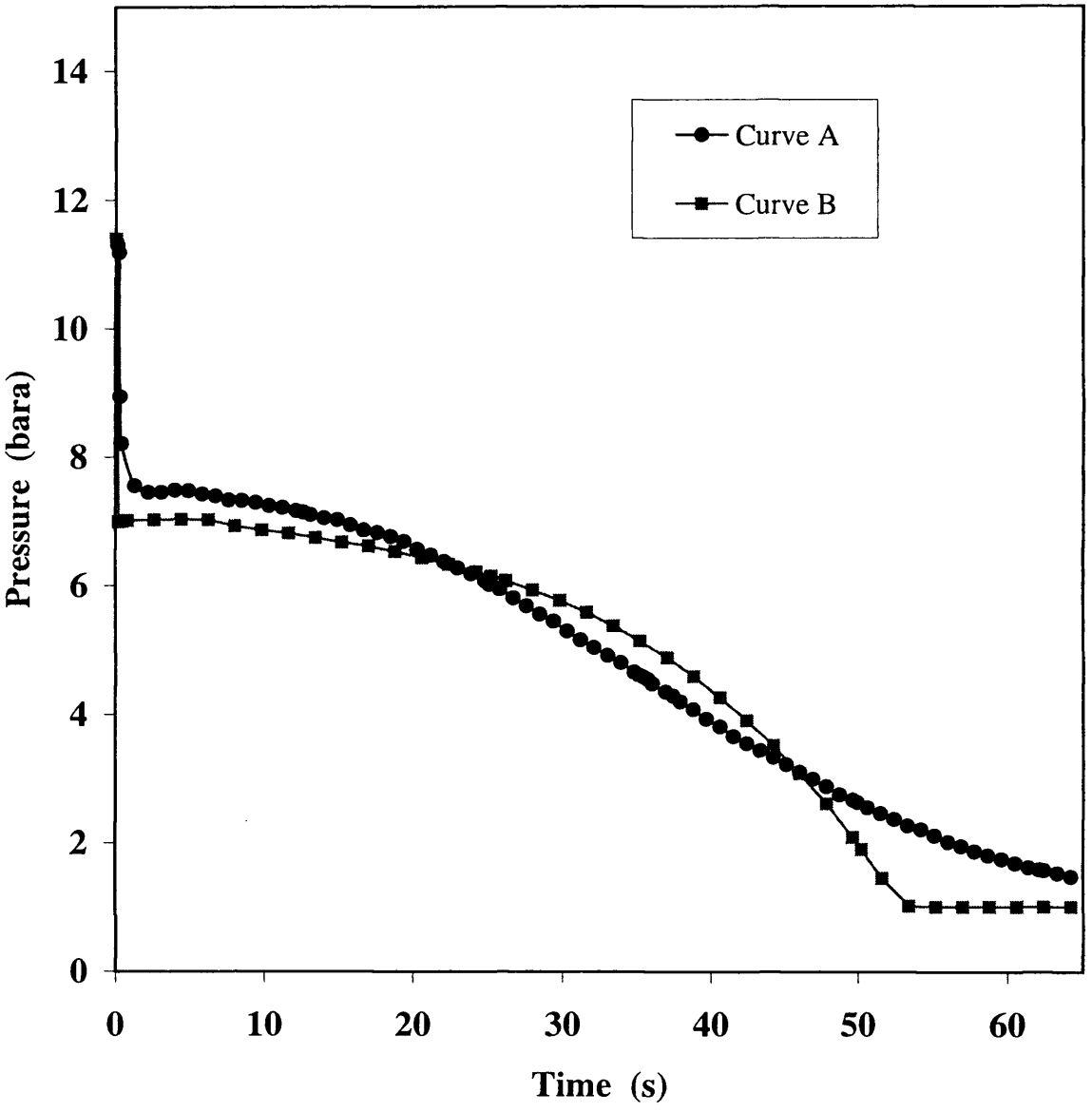

Figure 5.20: Variation of closed end pressure with time following a 0.095m diameter axisymmetric puncture for test P45 (LPG). Simulated data are obtained using 40 simple grids.

Curve A: Measurement (Richardson and Saville, 1996a).
Curve B: Simulated data.

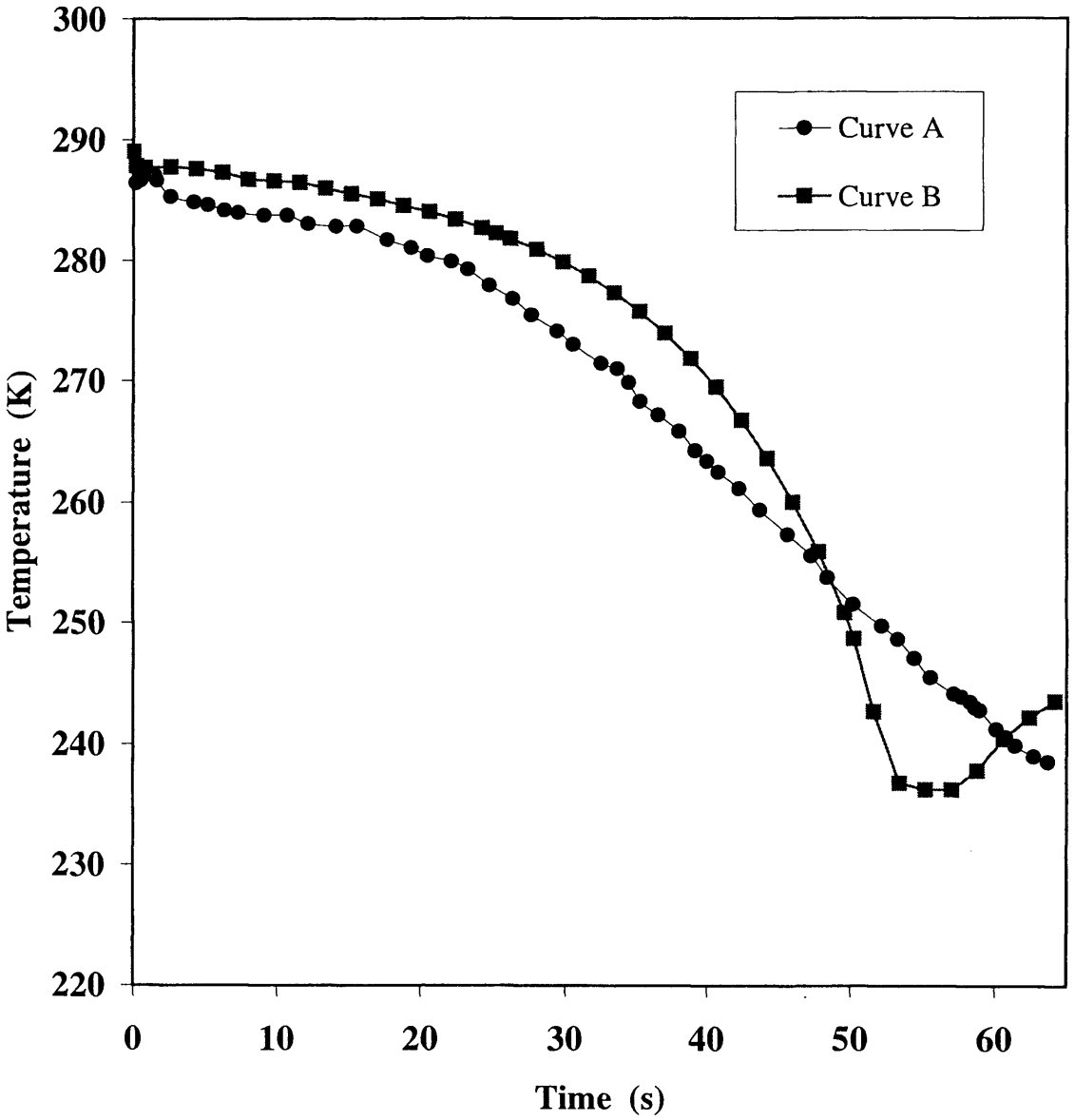

Figure 5.21: Variation of open end temperature with time following a 0.095m diameter axisymmetric puncture for test P45 (LPG). Simulated data are obtained using 40 simple grids.

Curve A: Measurement (Richardson and Saville, 1996a).
Curve B: Simulated data.

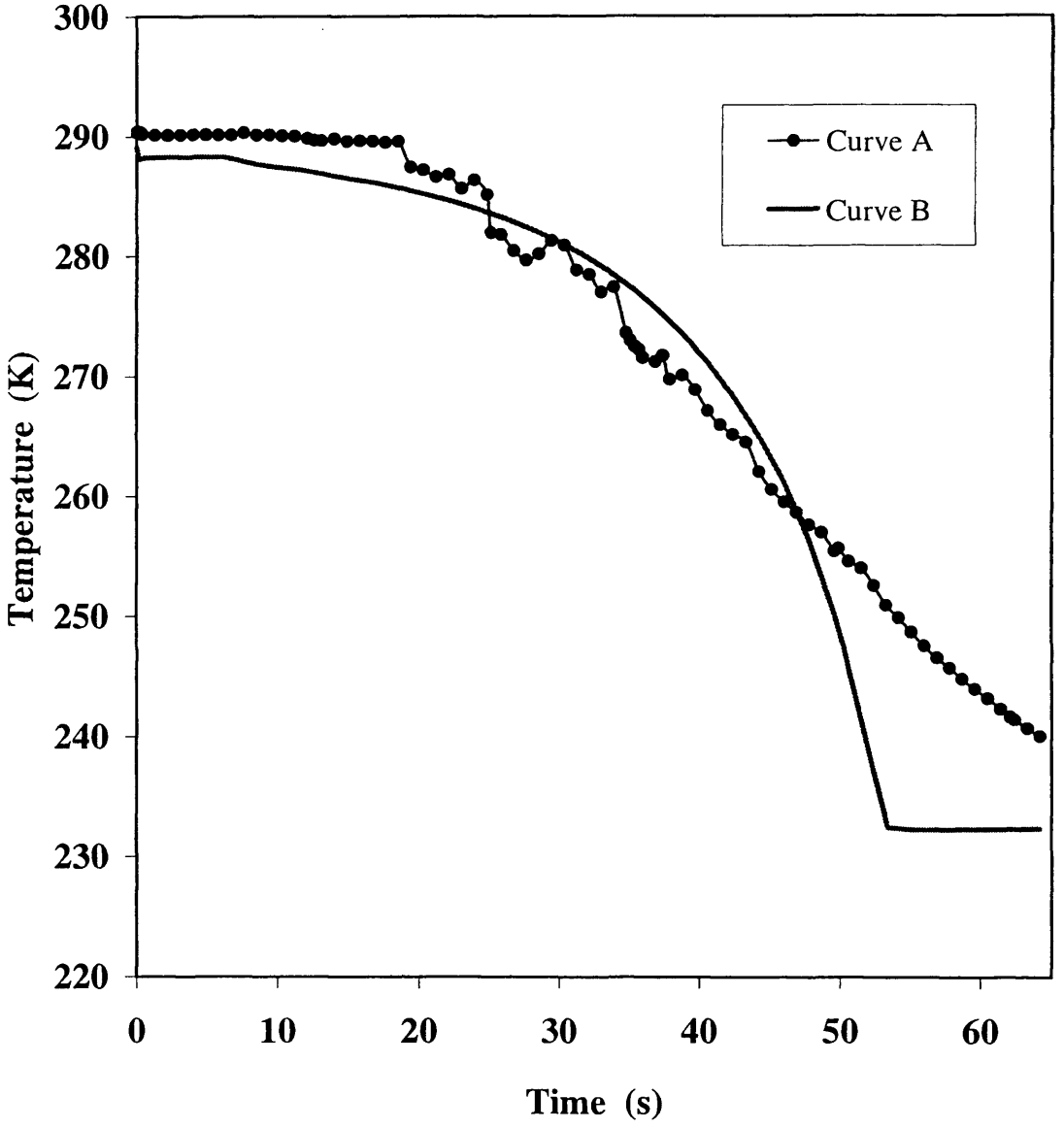

Figure 5.22: Variation of closed end temperature with time following a 0.095m diameter axisymmetric puncture for test P45 (LPG). Simulated data are obtained using 40 simple grids.

Curve A: Measurement (Richardson and Saville, 1996a).
Curve B: Simulated data.

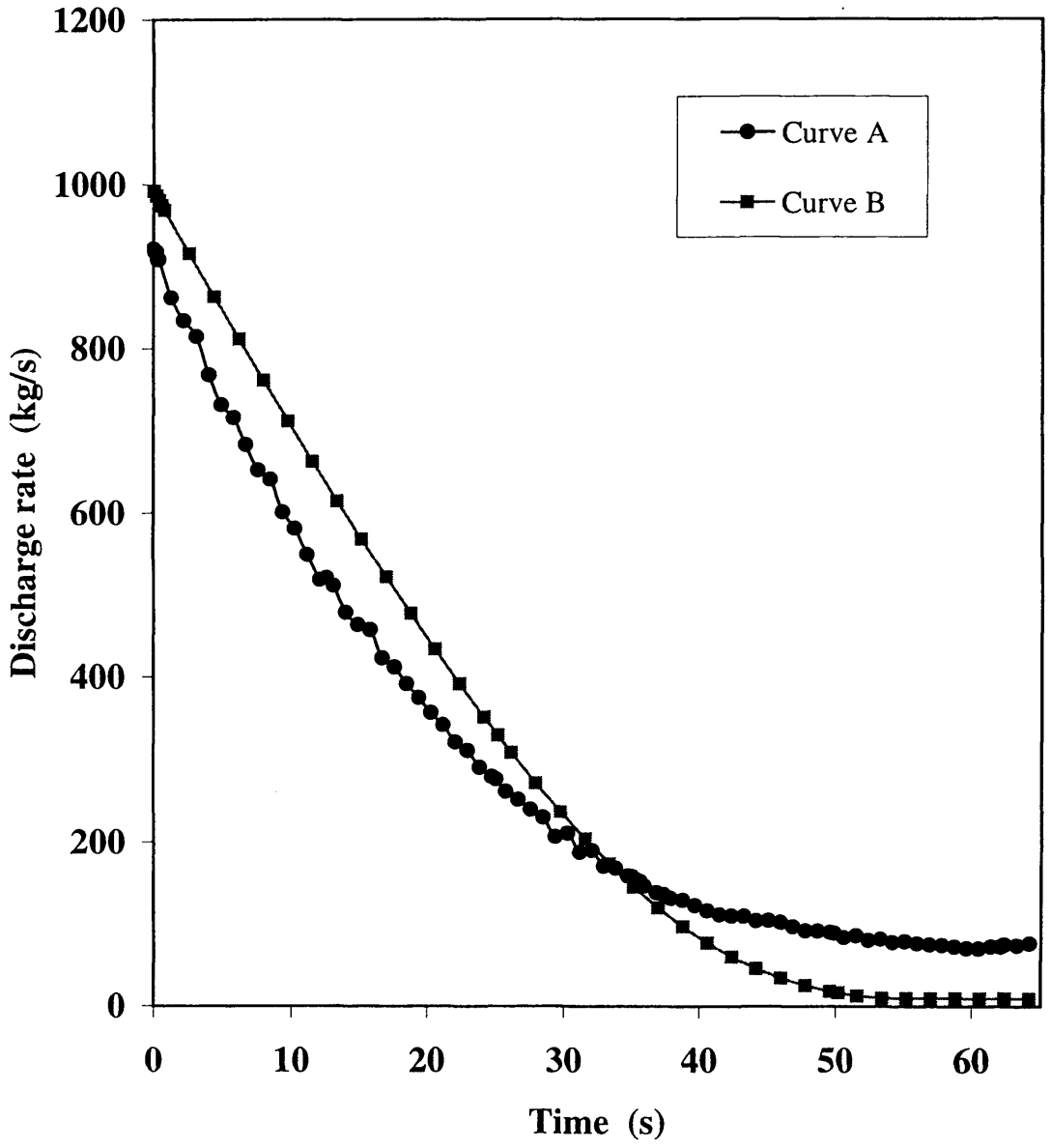

Figure 5.23: Variation of line inventory with time following a 0.095m diameter axisymmetric puncture for test P45 (LPG). Simulated data are obtained using 40 simple grids.

Curve A: Measurement (Richardson and Saville, 1996a).
Curve B: Simulated data.

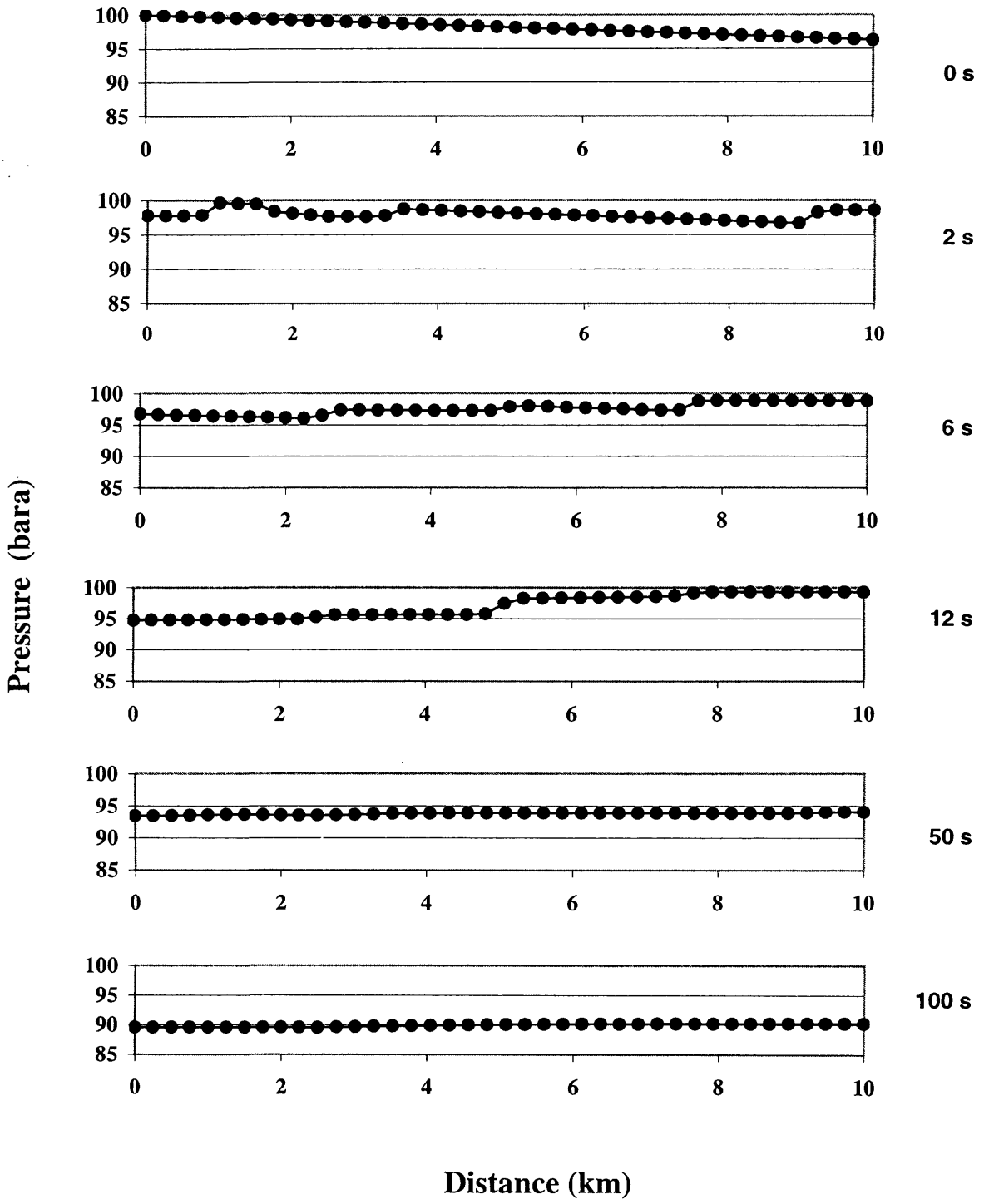

Figure 5.25: Pressure -distance profiles following the 0.1 m puncture of a pipeline, highlighting the depressurisation induced pressure transients.

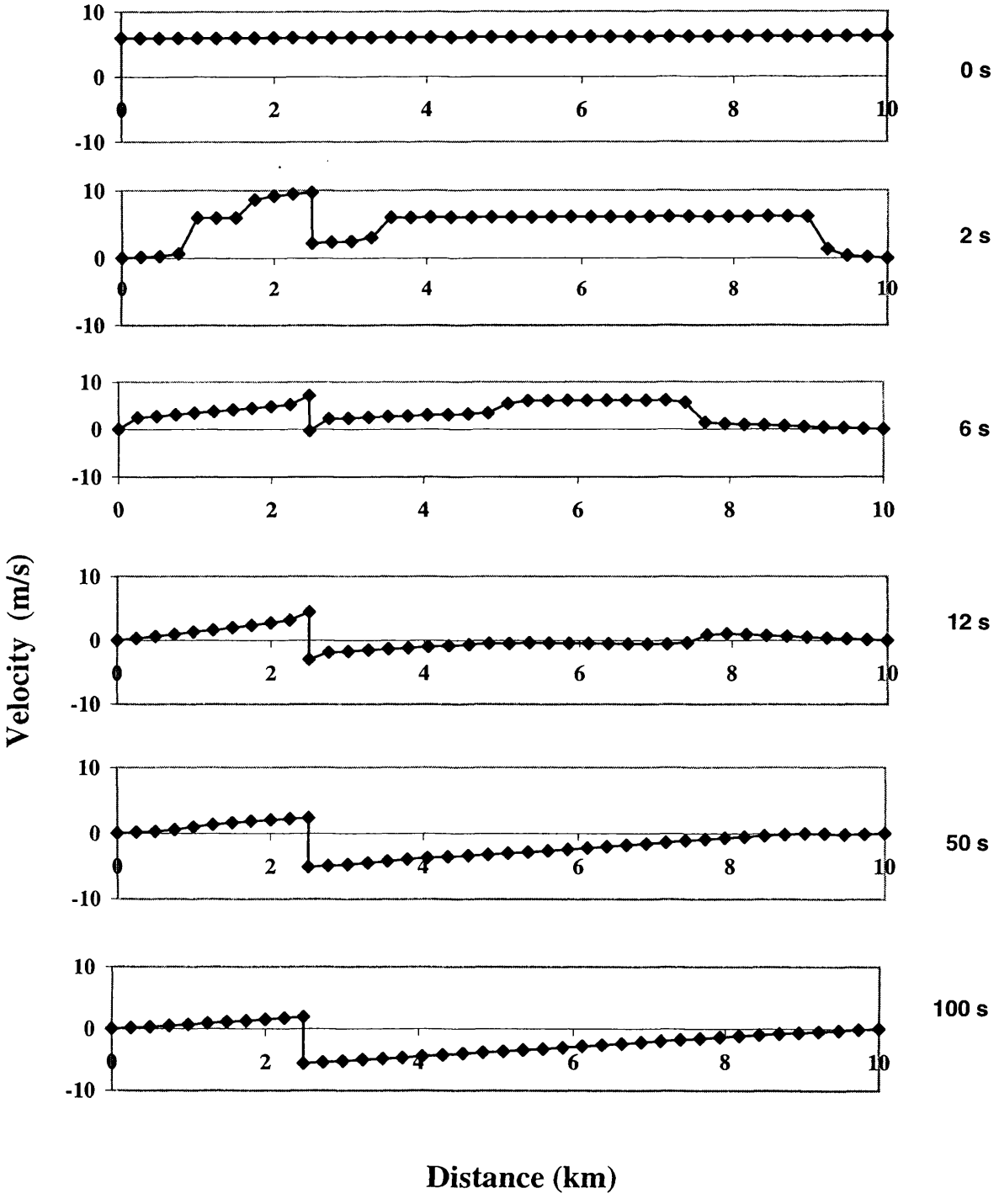

Figure 5.24: Velocity -distance profiles following the 0.1 m puncture of a pipeline, highlighting the depressurisation induced velocity transients.

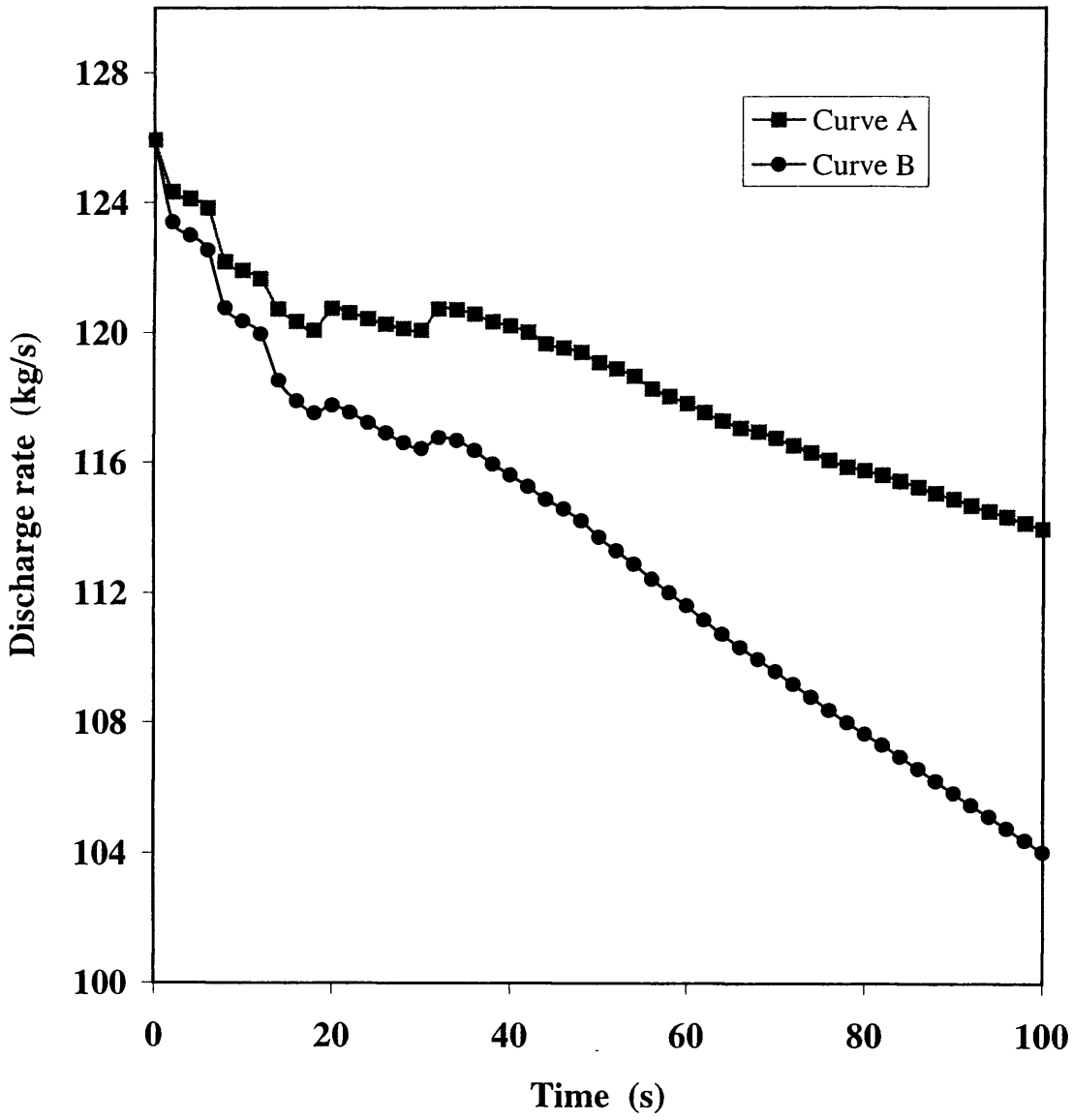

Figure 5.26: Discharge rate-time profiles following the 0.1m puncture of a hypothetical pipeline.

Curve A: Current model; Mass conservation index; 0.99.
Curve A: Oke et al's model; Mass conservation index; 1.61.

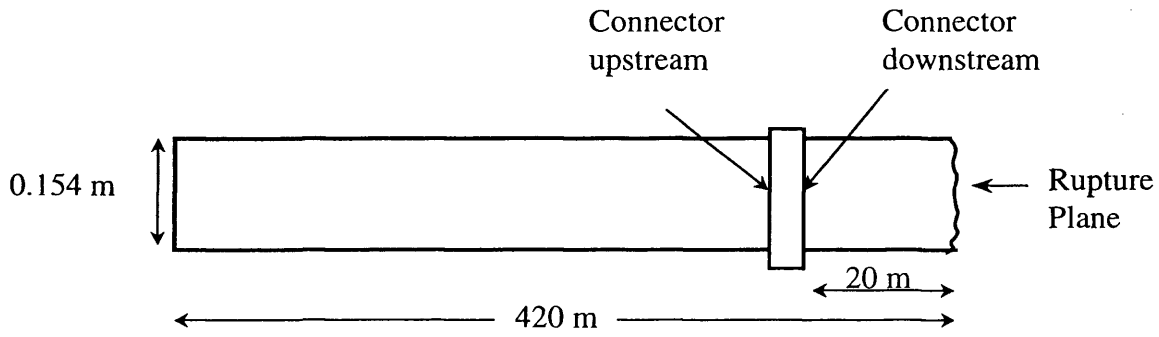

Figure 5.27: Schematic representation of the ruptured pipeline employed for evaluating the pipeline network model.

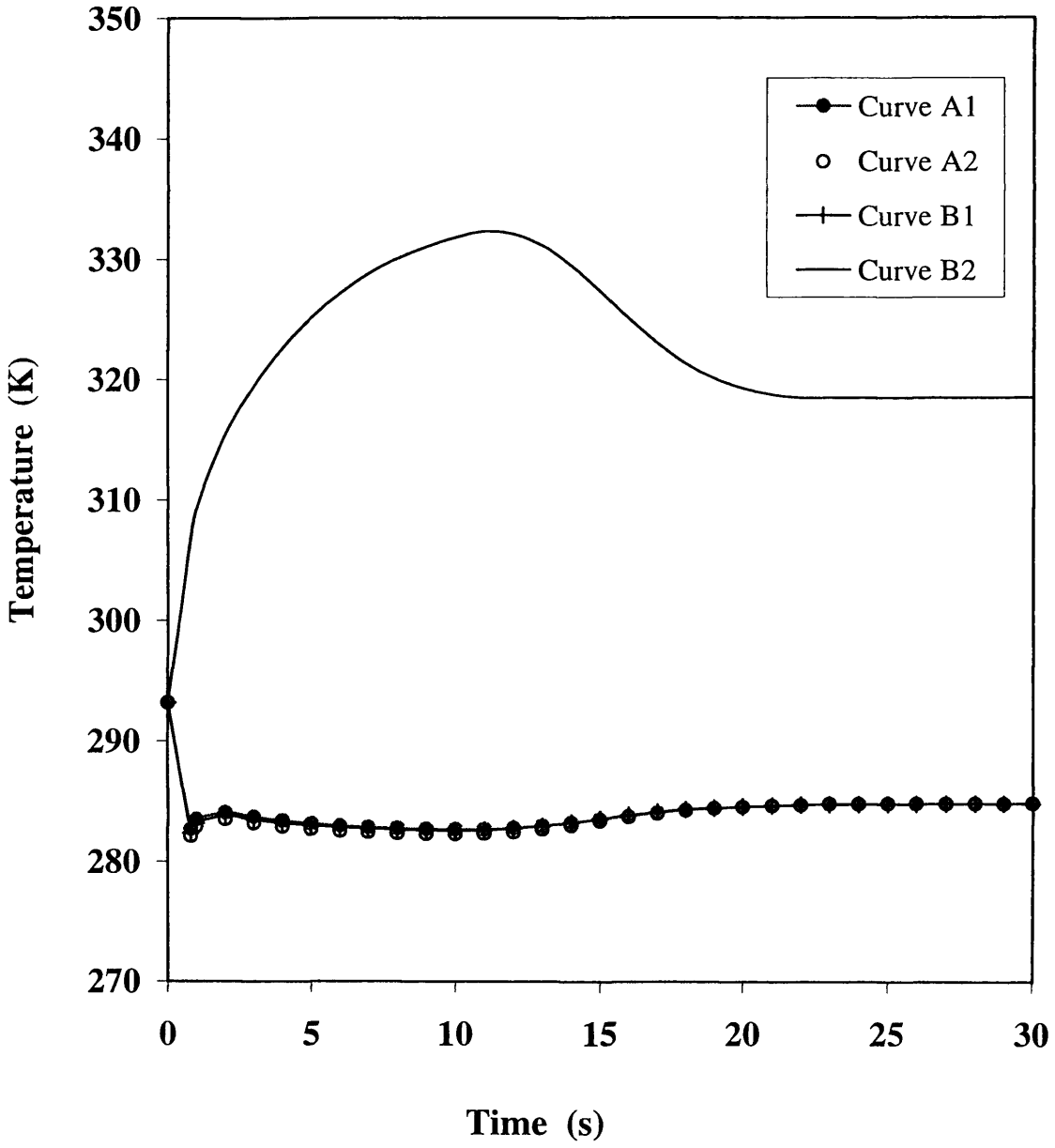

Figure 5.28: Temperature-time profile upstream and downstream of a connector following the FBR of a hypotetical pipeline network.

Curves A1 and A2: Upstream and downstream temperature respectively. Current model. Mass conservation index; 0.97.

Curves B1 and B2: Upstream and downstream temperatures respectively. Oke's (2004) model. Mass conservation index; 0.89.

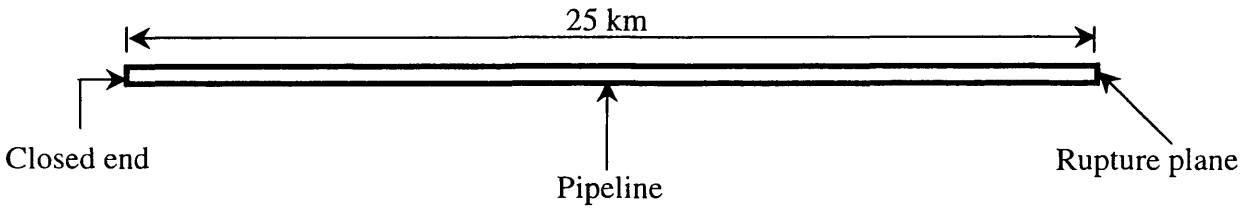

Figure 5.29a: Schematic representation of pipeline configuration A.

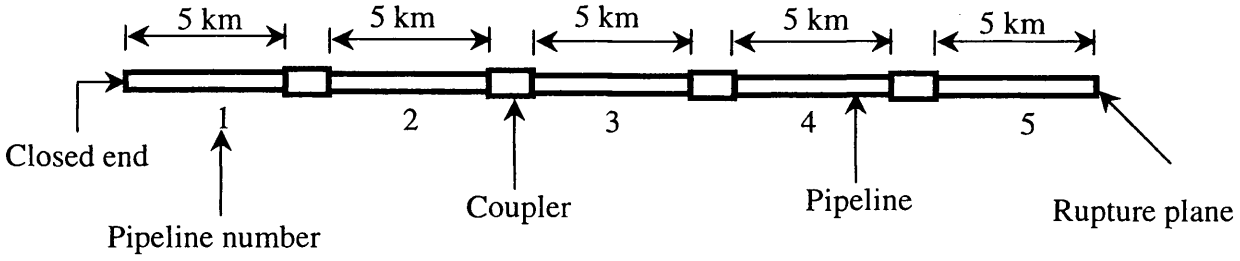

Figure 5.29b: Schematic representation of pipeline configuration B.

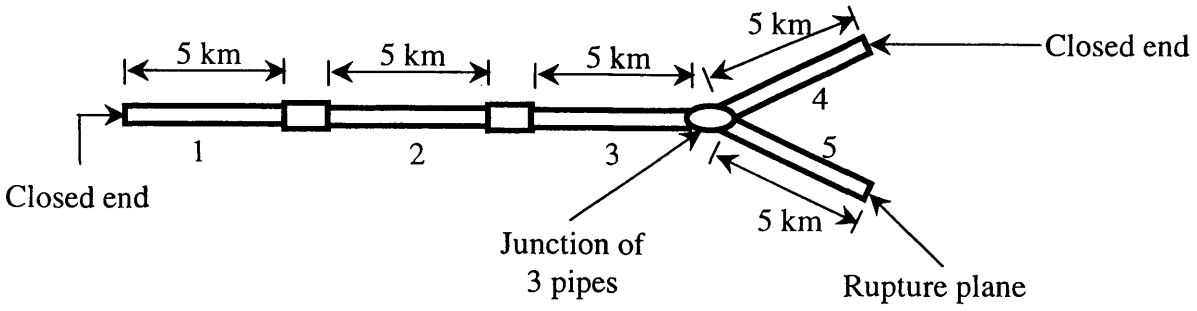

Figure 5.29c: Schematic representation of pipeline configuration C.

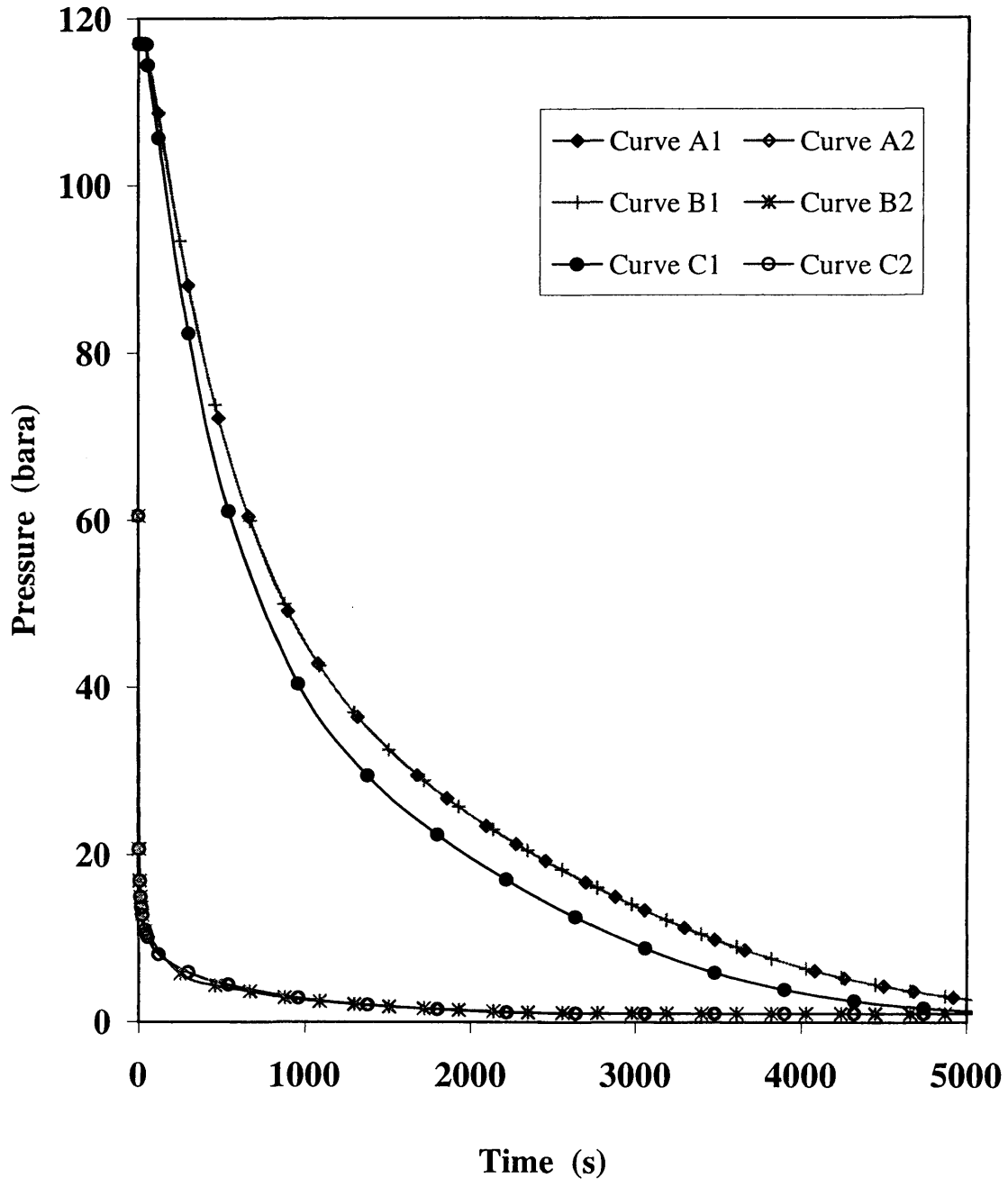

Figure 5.30: Comparison of intact end and rupture plane pressure-time profiles following FBR for the three pipeline configurations.

Curves A1, A2: Intact end and rupture plane pressures respectively: Configuration A.
Curves B1, B2: Intact end and rupture plane pressures respectively: Configuration B.
Curves C1, C2: Intact end and rupture plane pressures respectively: Configuration C.

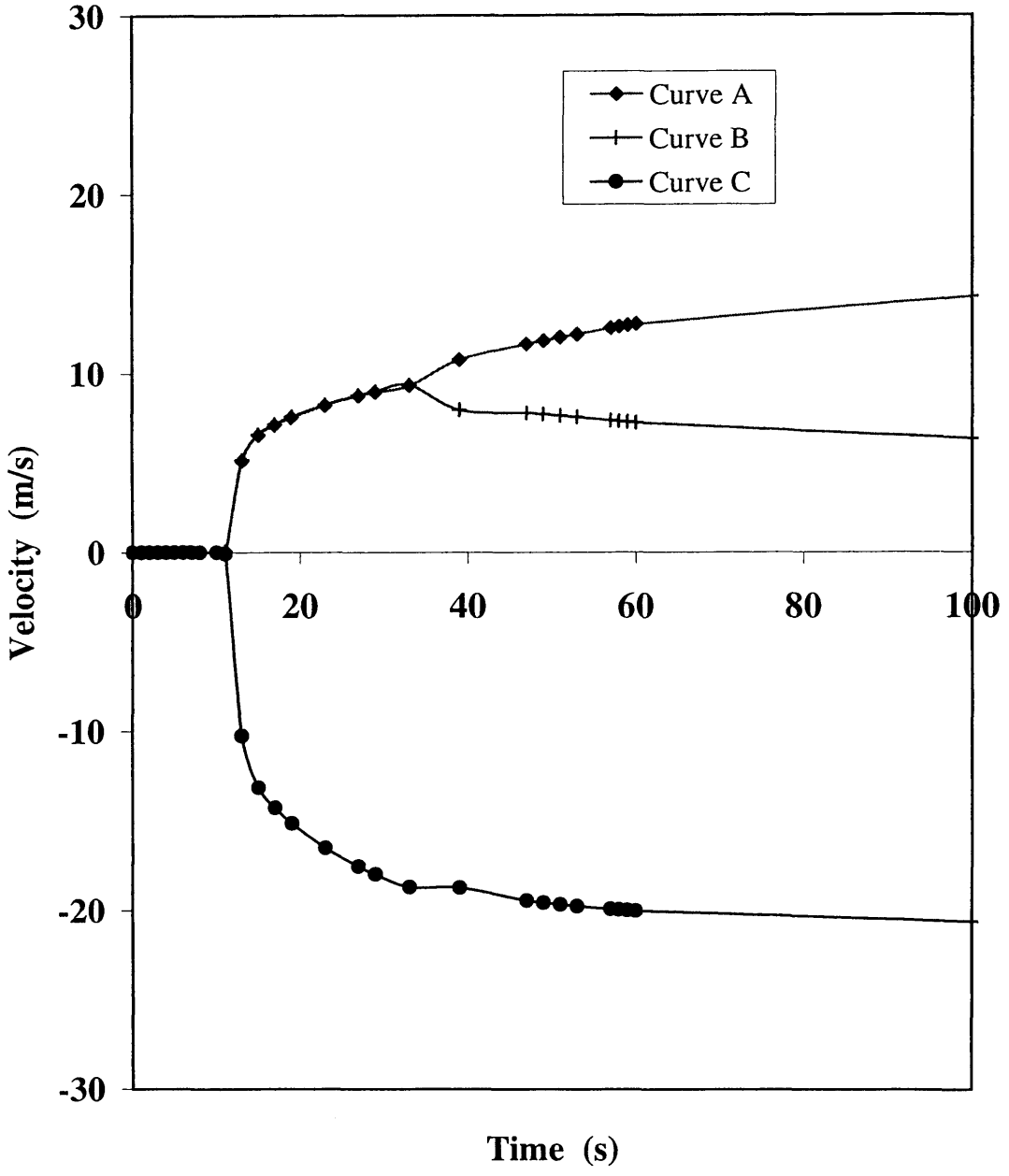

Figure 5.31: Comparison of inlet (pipe sections 3 and 4) and exit (pipe section 5) velocity-time profiles at branch junction for pipeline configuration C following FBR.

Curve A: Fluid velocity into branch junction from pipe section 3.
Curve B: Fluid velocity into branch junction from pipe section 4.
Curve C: Fluid velocity out of branch junction into pipe section 5.

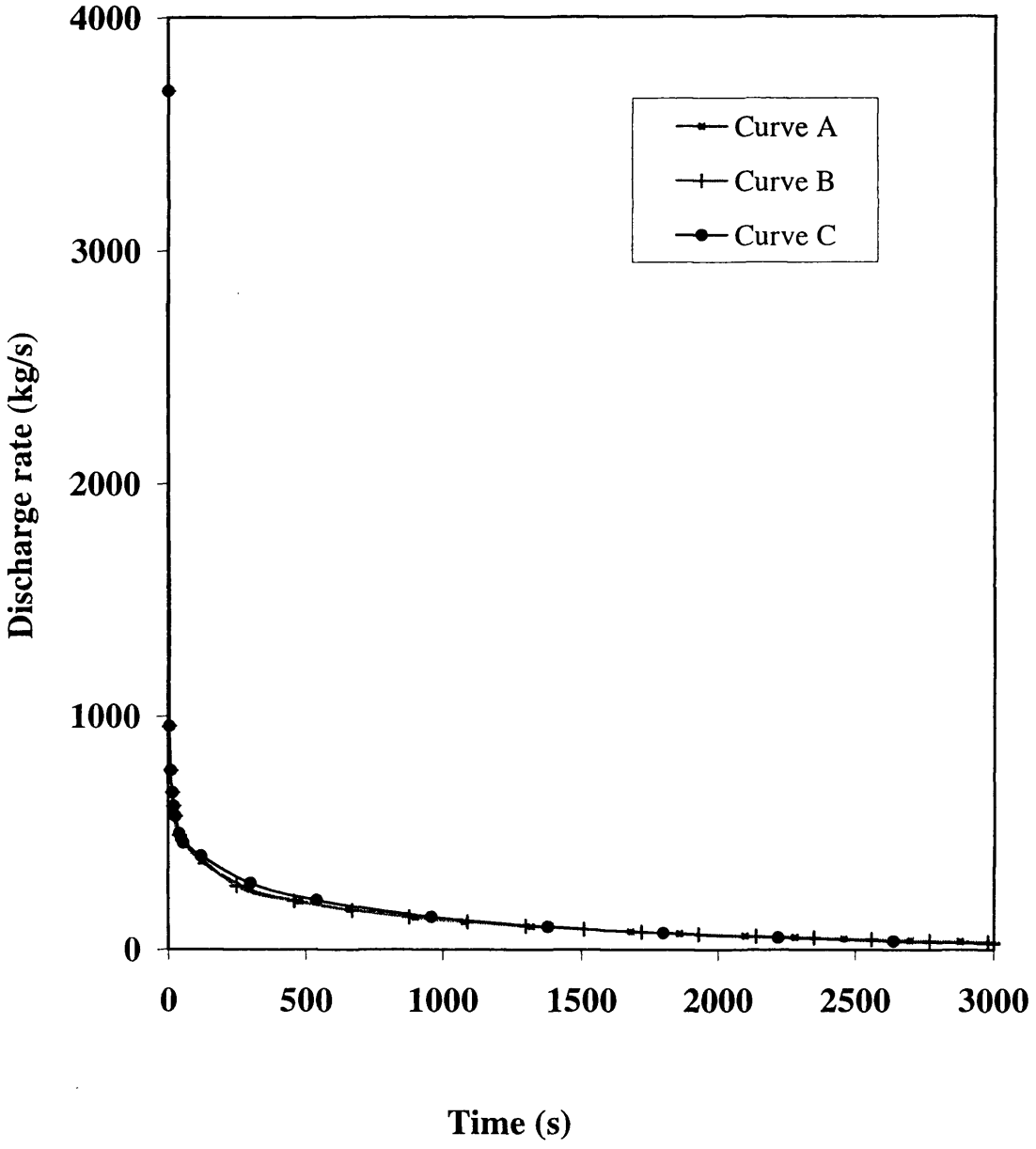

Figure 5.32: Comparison of discharge rate-time profiles following FBR for the three pipeline configurations.

Curve A: Discharge rate-time profile: Configuration A.
Curve B: Discharge rate-time profile: Configuration B.
Curve C: Discharge rate-time profile: Configuration C.

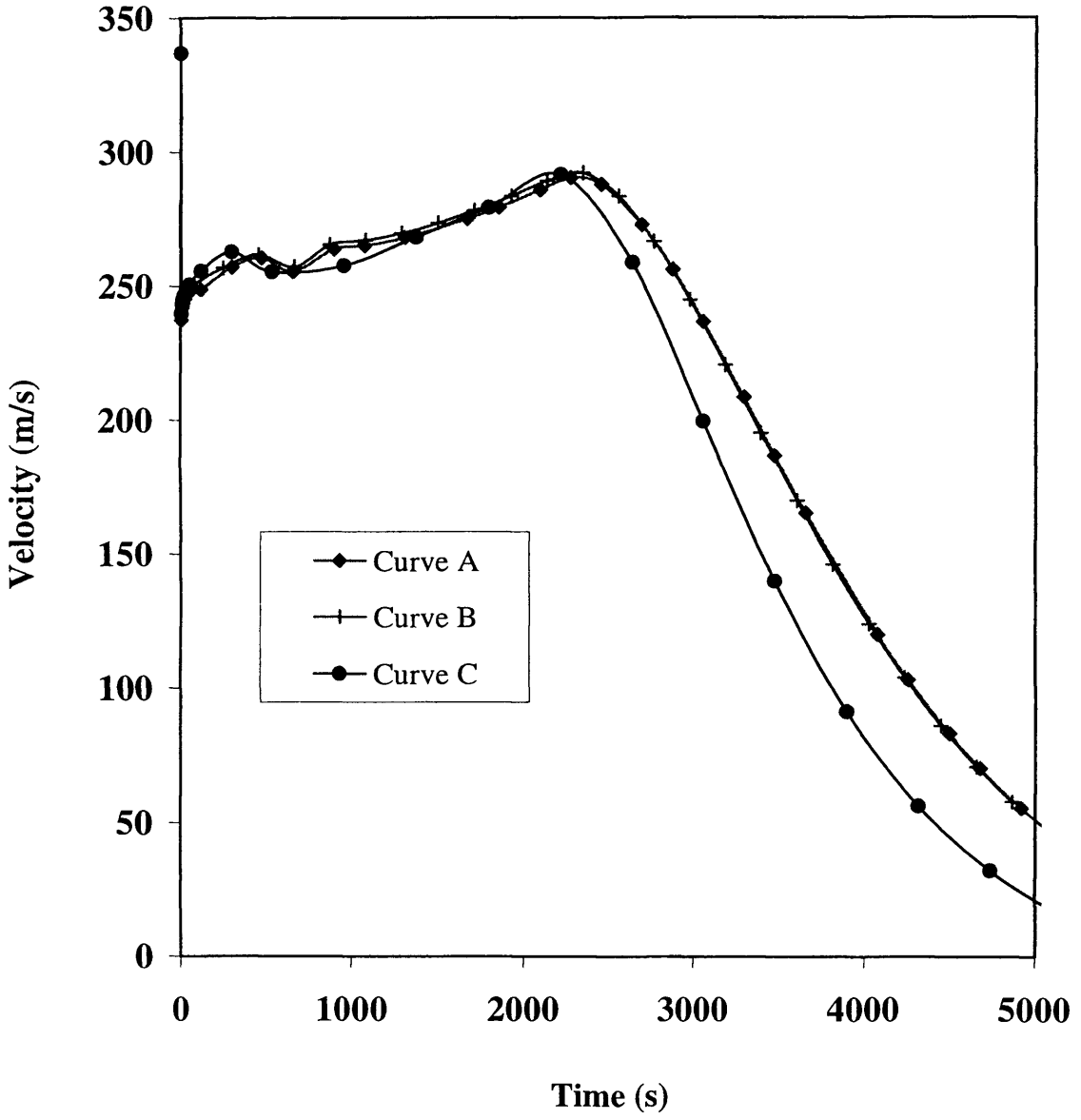

Figure 5.33: Comparison of fluid velocity at the rupture plane following FBR for the three pipeline configurations.

Curve A: Fluid velocity at the rupture plane: Configuration A.
Curve B: Fluid velocity at the rupture plane: Configuration B.
Curve C: Fluid velocity at the rupture plane: Configuration C.

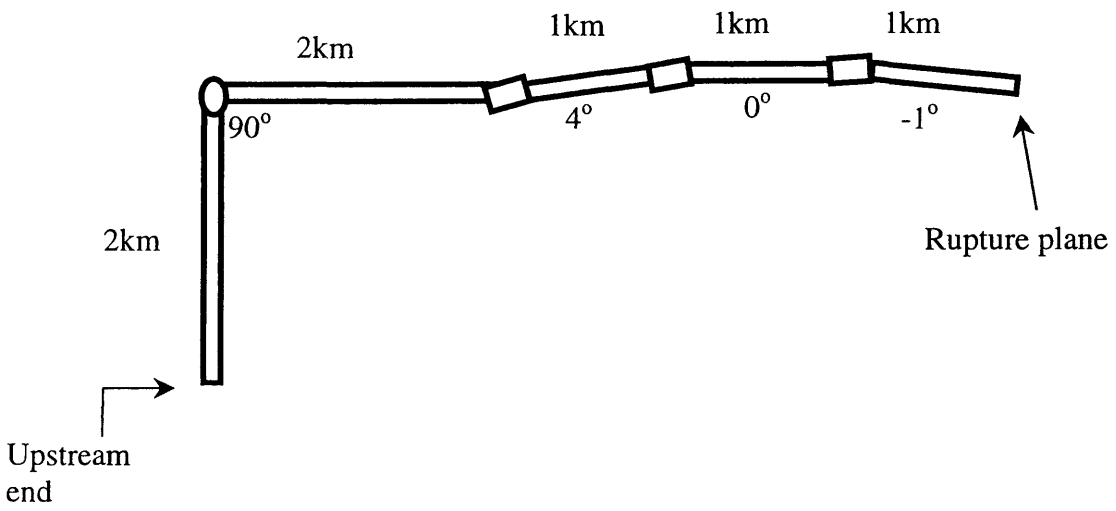

Figure 5.34a: Schematic representation of pipeline configuration A.

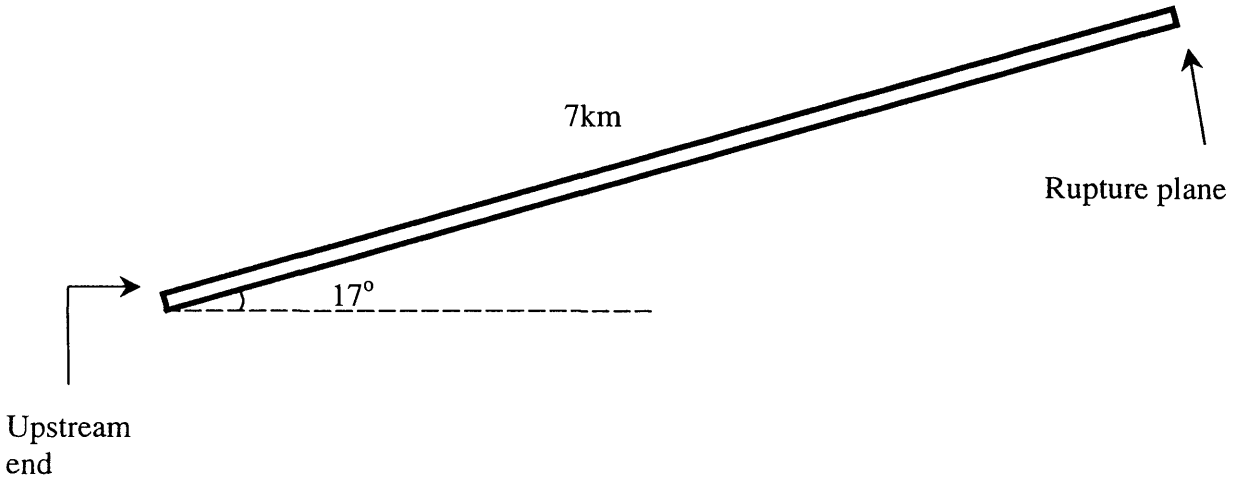

Figure 5.34b: Schematic representation of pipeline configuration B.

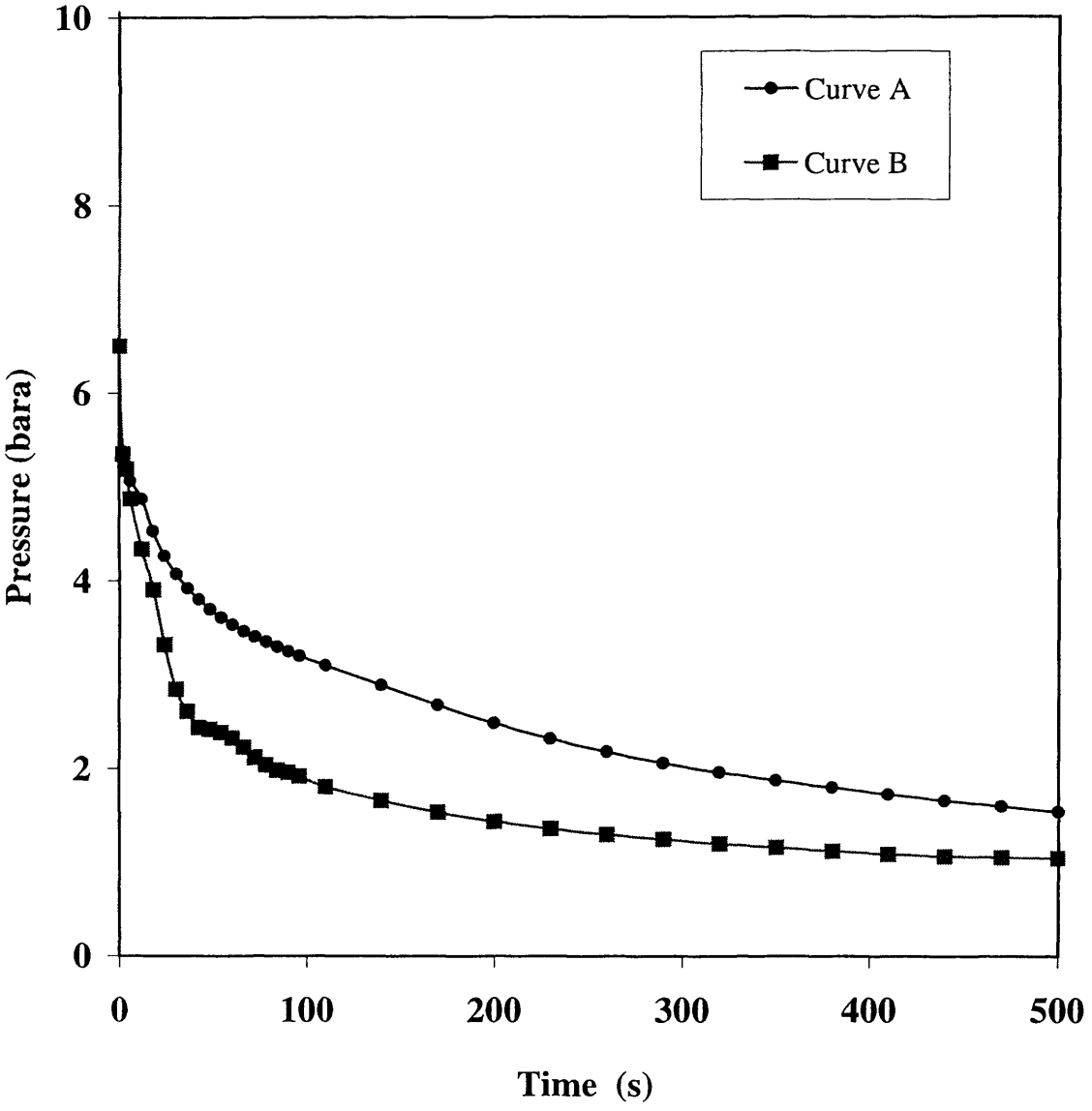

Figure 5.35: Open end pressure-time profile following the FBR of a hypothetical pipeline, showing the effect of inclination in pipeline networks.

Curve A: Pressure-time profile: Configuration A.
Curve B: Pressure-time profile: Configuration B.

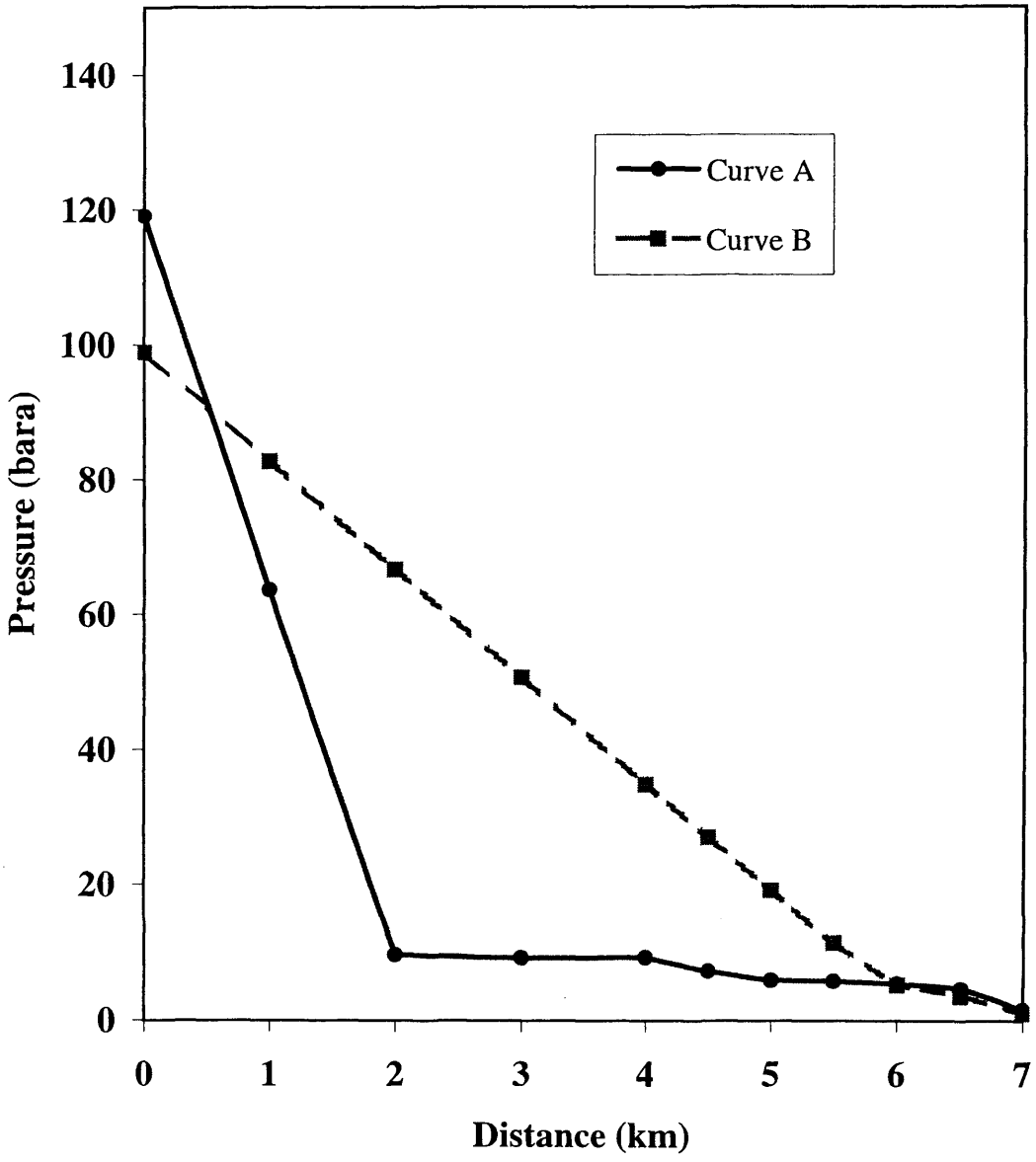

Figure 5.36: Pressure -distance profile at 500 s following the FBR of a hypothetical pipeline, showing the effect of inclination in pipeline networks.

Curve A: Pressure -distance profile: Configuration A.
Curve B: Pressure -distance profile: Configuration B.

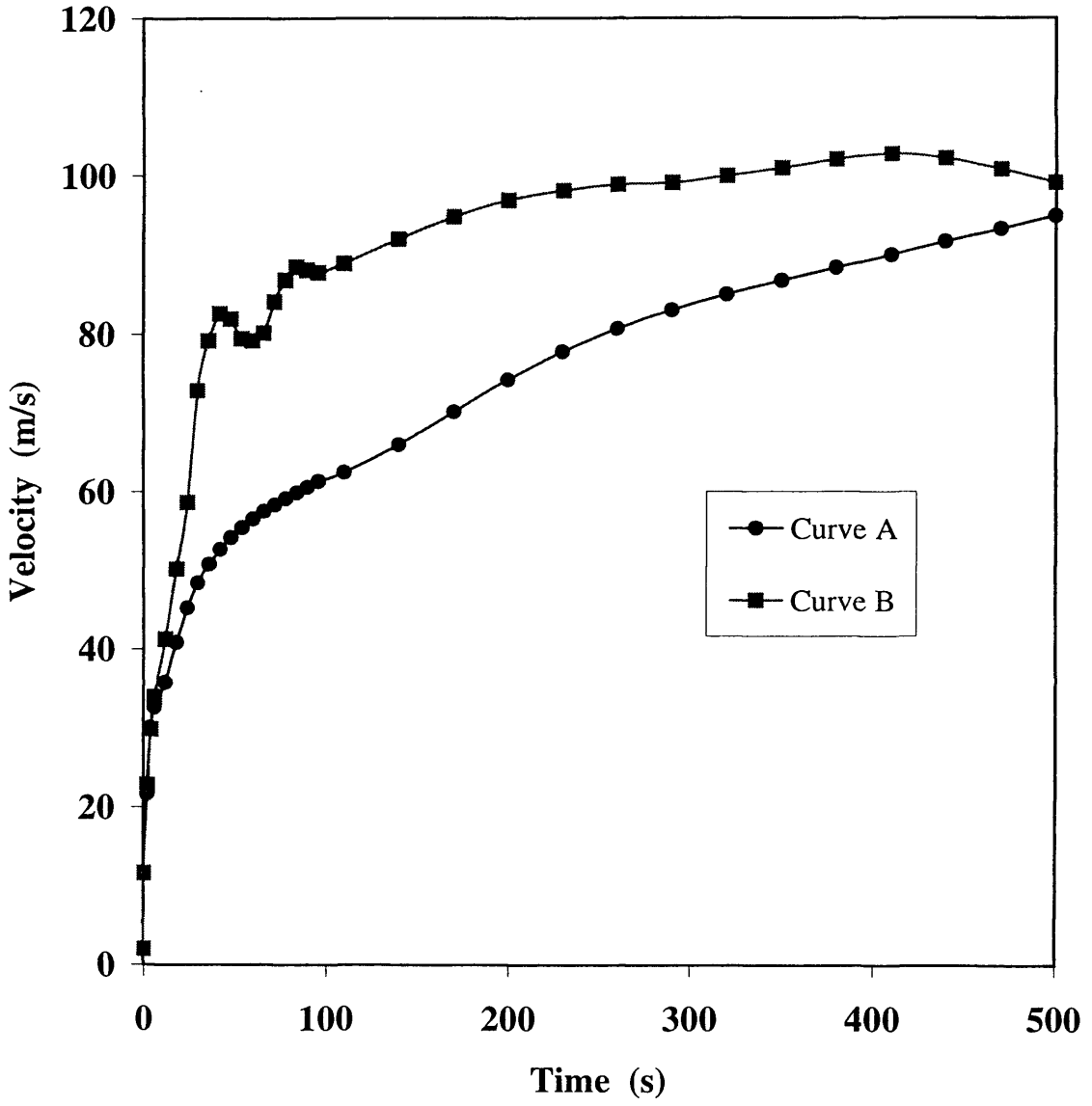

Figure 5.37: Velocity-time profile following the FBR of a hypothetical pipeline, showing the effect of inclination in pipeline networks.

Curve A: Velocity-time profile: Configuration A.
Curve B: Velocity-time profile: Configuration B.

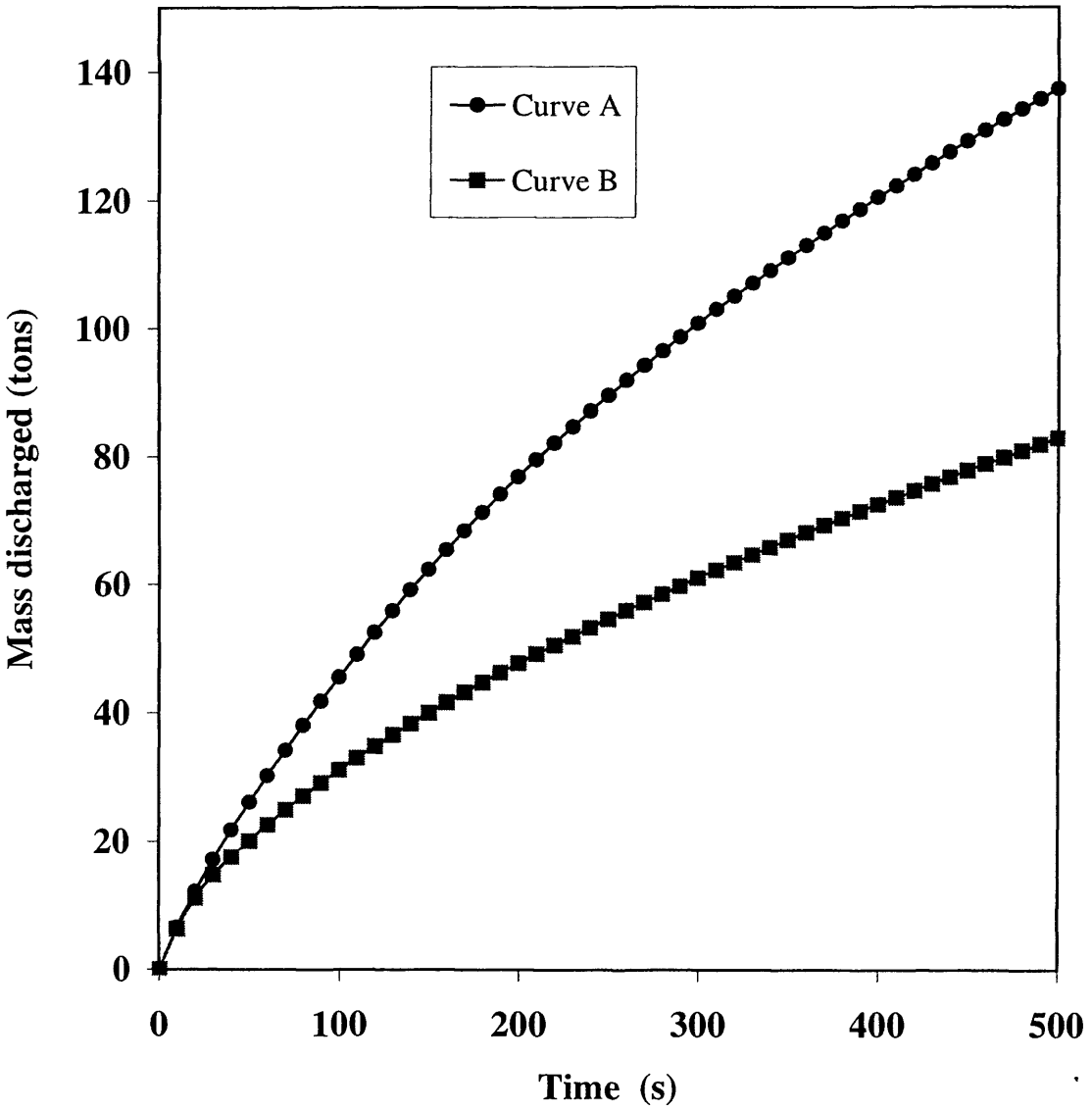

Figure 5.38: Mass discharged-time profile following the FBR of a hypothetical pipeline, showing the effect of inclination in pipeline networks.

Curve A: Mass discharged-time profile: Configuration A.
Curve B: Mass discharged-time profile: Configuration B.

CHAPTER 6

LOW TEMPERATURE INDUCED CRACK PROPAGATION IN PIPELINES

6.1 Introduction

In the case of pipelines containing pressurised gases or condensed liquids, the rapid depressurisation as a result of pipeline puncture will result in significant cooling of the escaping fluid inventory. This leads to a reduction in the pipe wall's temperature possibly to below its ductile-brittle transition temperature. The purpose of this chapter is to develop a mathematical model for predicting whether the prevailing thermal and pressure stresses in the pipe material under such conditions will be sufficient to cause secondary failure through a propagating crack.

A brief overview of the different types of pipeline defects and their origins, including their propagation mechanism is given first.

Defects are introduced into pipelines during steel and pipe making, and also during construction. Although significant pre-service defects are not common in recently constructed pipelines, the initial defect population could expand as pipelines continue in service. This could be due to defects that nucleate and grow or those that are introduced by external forces such as mechanical damage. With the exception of punctures that are due to external forces, defects begin as part-through-wall (PTW) features, which may be blunt (e.g. due to corrosion.) or sharp (e.g. due to hydrogen embrittlement).

Depending on the operating conditions and the properties of the pipeline steel, defects fall into one of three categories of behaviour:

1) Inactive through service.

2) Grow in a stable manner but remain benign because they do not grow through-wall (TW), and the crack length is below critical.

3) Grow through wall in service.

The defects of the third category can further be subdivided into three categories as follows:

3a) TW defect which may grow, but generally remains benign.

3b) Defects that immediately become unstable as the PTW transits to TW defects resulting in catastrophic pipeline failure.

3c) TW defects which continue to grow until they reach a critical length, resulting in catastrophic failure.

Catastrophic failure as a result of case (3b) depends largely on the decompression behaviour of the fluid inventory, i.e. whether the pipeline contains a liquid or a gas. It has been known (Horsley, 2002) that a pipeline conveying a gas can experience a propagating fracture that can run for long distances, whereas those transporting liquids at most support rupture over a few metres. In a pressurised pipeline, rupture/failure allows the fluid to decompress, which initiates a decompression front propagating away from the origin at a speed that is within the limit of the fluids' acoustic velocity. In a liquid, the acoustic velocity is several times greater than in a gas and generally greater than the fracture velocity, so the decompression front outpaces the fracture and the propagation arrests.

In a gas however, the acoustic velocity, hence the decompression front is slower than the fracture velocity, and therefore fracture continues. Due to the speed and inertial forces involved, the process is called running fracture or dynamic fracture propagation. Studies relating to understanding dynamic fracture propagation and crack growth in general have been extensive over the past few decades.

For example, Maxey et al. (1974, 1975) developed a model to predict the arrest toughness in pipelines based on coupling the decompression trajectory of a fluid with an empirically calibrated correlation for fracture behaviour.

Ives et al. (1974) reported that the primary driving force for ductile fracture propagation in pipelines containing high-pressure gases is the residual pressure of the escaping fluid acting on the wall interior downstream of the crack.

Some experimental studies carried out by Baum and Butterfield (1979) to determine the rates of depressurisation generated within ductile steel pipes during rupture showed good agreement between experimental and theoretical data. Based on the experimental data, they also determined the conditions under which a defect would propagate along the entire pipeline length.

Picard and Bishnoi (1988) highlighted the importance of accounting for real fluid behaviour and non-isentropic effects for predicting the correct fluid discharge pressure in fracture propagation analysis.

In case (3c) above, sub critical cracks can grow by a variety of mechanisms until they reach the critical length required for the onset of dynamic fracture propagation. The most common mode for crack growth or propagation is by fatigue. During fatigue crack propagation, the process is brittle, taking place without any appreciable deformation at the crack tip. The rate of fatigue crack propagation and hence the time taken for the initial crack to become critical can be estimated from the Paris equation (Paris, 1960) given by:

$$\frac{da}{dN} = A(\Delta K)^m \tag{6.1}$$

Where a is the half crack length, N is the number of stress cycles, K is the stress intensity factor (see later), while A and m are constants.

Other variations of the Paris equation, which are of improved accuracy, such as the Walker, Bilinear, NASGRO and Collipriest equations (AP1 RP579, 2000) can also be used. Studies, and the application of fatigue to crack growth and eventual structure

failure have also been extensive (see for example Singh et al., 2003; Lewis and Weidmann (1998)).

Apart from fatigue, there are other mechanisms of crack propagation which include stress corrosion cracking, hydrogen embrittlement, creep and liquid metal induced cracking (Borek, 1988).

In most applications, internal pressure and mechanical loading are the principal sources of stress from which fracture ensues. Nonetheless, thermal shock has been shown to be capable of inducing fracture. It is based on the principle that rapidly cooling a hot surface may induce stresses greater than that which the structure can bear, thus resulting in fracture. For example, Chawla et al. (2000) presented a model for simulating crack growth and arrest in a pressure vessel under thermal shock. They demonstrated that a crack would grow when an initially hot vessel is suddenly cooled, and then arrests as it propagates into a region with a lower stress. This phenomenon is however more likely to be experienced in thick-walled vessels such as pressurised water reactors where emergency core cooling may be required. Chapuliot et al. (2005) noted that fracture due to thermal shock is unlikely in vessels with a thin wall when uniformly cooled.

Even in cases where a component does not fail by thermal shock, it may fail due to thermal fatigue. Such failures are common in systems with cyclic changes in temperature such as boilers. Tokiyoshi et al. (2001) presented a model capable of predicting the crack propagation life of a perforated plate under thermal fatigue.

Tsu et al. (1986) exploited the fact that the Joule-Thompson expansion of a pressurised fluid may cause its temperature to drop significantly as it exits a pipe through a crack. This consequently led to a significant amount of stress due to the highly localised temperature gradient around the crack. In determining the fracture behaviour based on the combined thermal and pressure stresses, they concluded that the thermal stresses induced by the expansion were significant, and cannot be ignored.

In the above reviewed cases, it should be noted that the temperature effects were capable of causing fracture by inducing stress in the component.

Another mode by which a crack can grow, which is the focus of this chapter, is also by thermo-fracture, in which a thermal gradient is imposed on a material under stress. In this case however, the temperature gradient eventually causes fracture, not by being a source of stress, but by altering the material's ability to withstand fracture. This mechanism of crack propagation forms the basis for determining the fracture toughness of materials by the Robertson method (Jawad and Farr, 1983).

In the Robertson method, a temperature gradient is imposed across a notched specimen by heating it at one end and cooling it at the other, prior to subjecting it to stress. When stress is applied, the crack grows from the cold end into the warm metal, and then stops at some distance away (Jawad and Farr, 1983). Figure 6.1 is a schematic representation of a propagating crack under the influence of a thermal gradient.

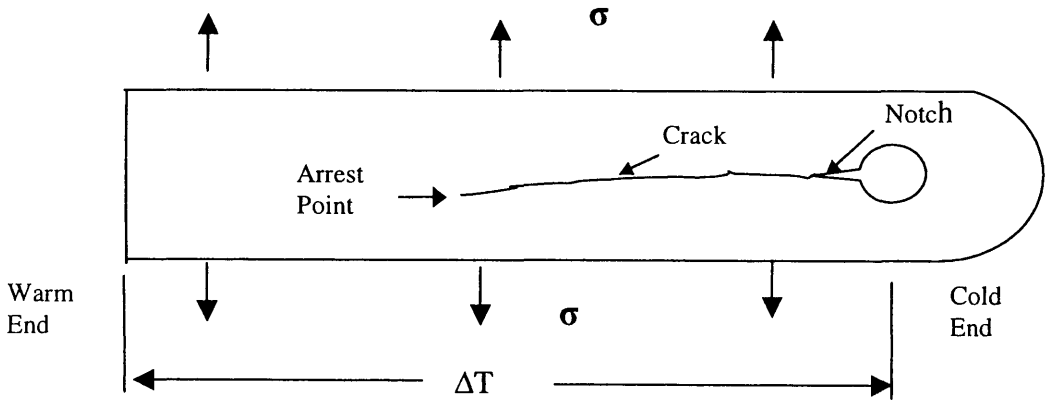

Figure 6.1: Schematic diagram showing crack propagation and arrest during the Robertson test.

Now, consider a case where the cold temperature front is moving. This can occur when the warm source is removed, resulting in a transient decrease in metal temperature across its length due to heat transfer. Consequently, the crack tip grows colder with time, propagating further into the material until it gets to a warmer spot before stopping (as in the Robertson's method). However, the metal at the crack tip soon becomes cold, thus forcing the crack to move further still.

This cyclic process of crack propagation and arrest due to the moving temperature front can therefore lead to fracture.

In the event of a puncture or leak in a pressurised pipeline, the discharging fluid escapes at a low temperature, which in turn cools the pipe metal at the edge of the puncture. The cold exiting fluid acts as a cooling source thereby making the pipe wall in the vicinity of the puncture grow colder with time, and may therefore mimic the cyclic crack propagation and arrest effect described above. If the pipe wall temperature at the crack tip reaches its ductile/brittle transition temperature (typically -10 to –60 °C), a rapid marked decrease in the pipeline's fracture toughness will occur thereby making it more susceptible to fracture (Rinebolt and Harris, 1951; Sandstram et al., 2005).

Under these circumstances, it is imperative to be able to predict *a priori* whether the prevailing stresses at the crack tip would lead to its transformation into a running fracture. In such a case, the delayed ignition of the massive amount of escaping inventory may in turn result in an enormous vapour cloud explosion causing significant damage and fatalities in populated areas.

Experiments by Baum (1985) have indicated that the cooling effect of an expanded fluid can cause the mode of crack propagation to change from ductile to brittle. In the experiment, a pipeline whose ductile-brittle transition temperature (DBTT) was 5 K below ambient, was ruptured by over pressurising it with a gas. From the ruptured pipe, it was observed that there was a sudden transition from ductile to brittle fracture, with the fracture at 90° to the pipe surface. This is thus indicative of the fact that the

exiting gas may have rapidly cooled the crack tip to a temperature below its DBTT thereby changing the fracture mode from ductile to brittle.

Despite its obvious importance, no previous study has provided a quantitative account for the role of fluid-structure interactions on the fracture propagation process during pipeline depressurisation. This chapter therefore describes the development of a mathematical model for predicting if and when an initial TW defect in a pressurised pipeline may develop into a running fracture based on the cyclic propagation and arrest mechanism described above.

A 3-dimensional heat transfer model coupled with the puncture outflow model described in chapter 4, is used to determine the transient temperature profile (hence material toughness) in the vicinity of the defect. Furthermore, the concept of stress intensity factors (SIF) is used to evaluate the pipeline's ability to withstand fracture propagation.

6.2 Model Development

The physical problem under consideration is the sequence of events following the formation of a stable through-wall defect or puncture in a pipeline containing a gas at high pressure. Loss of gas causes depressurisation at the rupture plane, and a wave of low pressure will travel away from the rupture site, typically starting as an expansion fan. Within this fan, the gas may condense, forming a two-phase flow. The objective is to determine the conditions of flow within the pipe, the exiting fluid properties, as well as the accompanying fluid/structure interactions manifested in the localised thermal and pressure stresses in the pipe wall. This task requires the modelling of the following interacting processes:

i) The escaping fluid temperature and pressure at the defect plane using a real fluid model.

ii) Heat transfer effects between the escaping fluid, pipe wall and the surrounding ambient.

iii) Pressure and thermal stresses within the defect plane.

iv) Fracture propagation.

The governing theory for determining the fluid dynamics such as the fluid temperature and pressure following its puncture was described in chapters 3 and 4, hence only steps (ii) to (iv) are presented here.

6.2.1 Heat Transfer

The radial, axial and tangential temperature profiles in the pipe wall in the proximity of the puncture are governed by the following modes of heat transfer as depicted in figure 6.2:

i) Conductive heat transfer within the pipe wall (H_1).
ii) Natural/forced convective heat transfer between the outside ambient and the pipe wall (H_2).
iii) Axial forced convective heat transfer between the escaping fluid and the puncture plane (H_3).
iv) Convective heat transfer between the flowing fluid and the pipe wall (H_4).

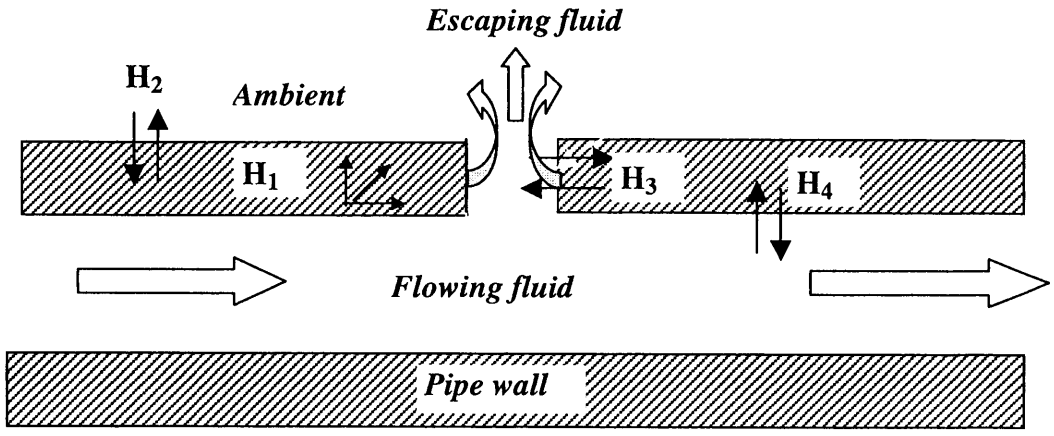

Figure 6.2: A schematic representation of the various heat transfer boundaries following pipeline puncture.

Heat transfer within the pipe wall: H_1

The radial (r), tangential (ϕ) axial (z) temperature profiles within the pipeline due to conductive and convective heat transfer are determined from the numerical solution of the heat transfer equation given by Osizik (1980):

$$\frac{\partial^2 T}{\partial r^2}+\frac{1}{r}\frac{\partial T}{\partial r}+\frac{1}{r^2}\frac{\partial^2 T}{\partial \phi^2}+\frac{\partial^2 T}{\partial z^2}=\frac{1}{\alpha}\frac{\partial T}{\partial \tau} \qquad (r_{in} < r < r_{out}) \qquad (6.2)$$

$$\kappa\frac{\partial T}{\partial r}=h_\infty T_\infty - h_\infty T \qquad (r= r_{out}) \qquad (6.3)$$

$$-\kappa\frac{\partial T}{\partial r}=h_f T_f - h_f T \qquad (r= r_{in}) \qquad (6.4)$$

Where T is the temperature at any point within the pipeline with r_{in}, r_{out}, α and τ respectively denoting the inner and outer pipeline radius, thermal diffusivity and time. The subscripts ∞ and f refer to the ambient and fluid respectively.

In this study, the pipeline wall is divided into nodal points, and the conduction equation solved numerically at each node to obtain its temperature at the next time step. The central difference explicit finite difference scheme (Holman, 1986) is used to resolve the above equations.

Figure 6.3 shows the discretisation within the pipeline used in modelling the temperature profile. T_2-T_7 represents the corresponding temperature at the six nodes surrounding T_1 whose temperature is to be determined at the next time step. T_8 however corresponds to the temperature at a fictitious node, which is employed in solving the convective nodal temperature (T_7) the subsequent time step.

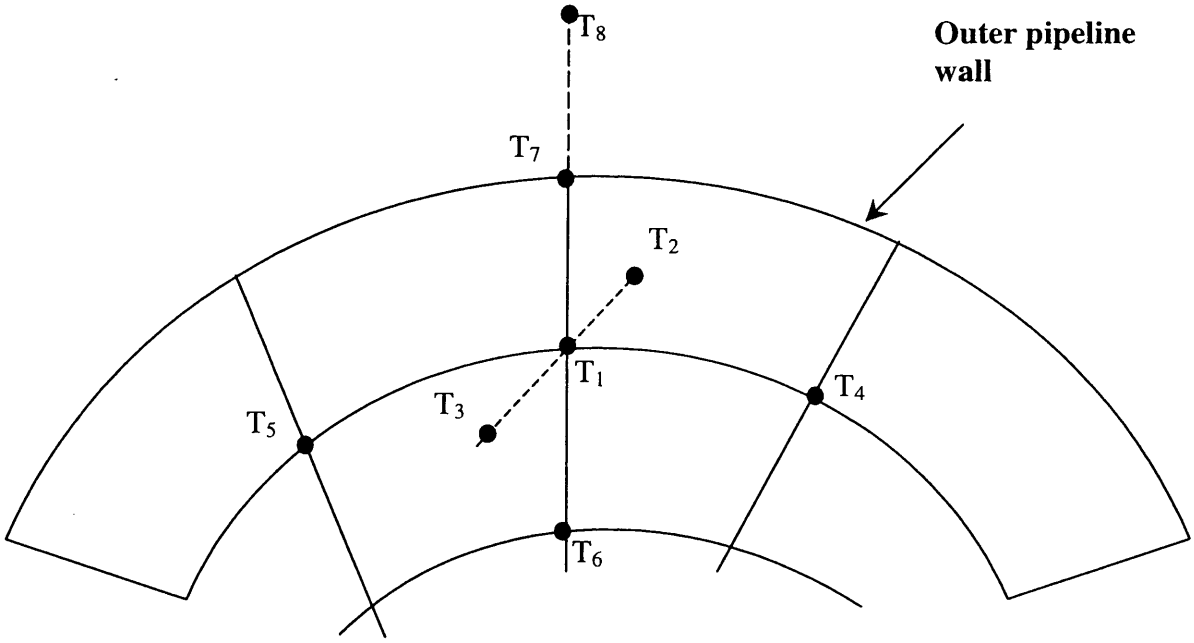

Figure 6.3: Schematic representation of the pipeline discretistion employed in modelling the temperature profile around the puncture plane.

Using the central difference method, equations (6.2-6.4) can be resolved as follows

$$\frac{\partial^2 T}{\partial r^2} = \frac{T_7 - 2T_1 + T_6}{\Delta r^2} = C_1 \tag{6.5}$$

$$\frac{\partial T}{\partial r} = \frac{T_7 - T_6}{2\Delta r} = C_2 \tag{6.6}$$

$$\frac{\partial^2 T}{\partial \phi^2} = \frac{T_5 - 2T_1 + T_4}{\Delta \phi^2} = C_3 \tag{6.7}$$

$$\frac{\partial^2 T}{\partial z^2} = \frac{T_3 - 2T_1 + T_2}{\Delta z^2} = C_4 \tag{6.8}$$

$$\frac{\partial T}{\partial \tau} = \frac{T_1^* - T_1}{\Delta t} \tag{6.9}$$

Hence substituting the above relation into equation 6.2 and rearranging yields temperature at the conduction node T_1 at the next time step (T_1*)

$$T_1^* = T_1 + \alpha\Delta t\left[C_1 + \frac{C_2}{r} + \frac{C_3}{r^2} + C_4\right] \tag{6.10}$$

When the pipeline is exposed to some convection boundary, the temperature at the surface such as T_7 must be computed differently. In this study, the fictitious node concept (Osizik, 1980) is used in resolving the convective boundary temperatures. Using the pipeline boundary exposed to the atmosphere as an example, the convection equation, (i.e. equation 6.2) can be discretised as

$$k\frac{T_8 - T_1}{2\Delta r} = h_\infty T_\infty - h_\infty T_7 \tag{6.11}$$

Rearranging equation (6.11) yields,

$$T_8 = T_1 + \frac{2\Delta r}{k}h_\infty(T_\infty - T_7) \tag{6.12}$$

If $J_2 = \frac{1}{r^2}\frac{\partial^2 T}{\partial\phi^2} + \frac{\partial^2 T}{\partial z^2}$, then the conduction equation can be written as

$$\frac{T_1 - 2T_7 + T_8}{\Delta r^2} + \frac{T_8 - T_1}{2r\Delta r} + J_2 = \frac{1}{\alpha}\frac{T_7^* - T_7}{\Delta t} \tag{6.13}$$

Where T_8 is as defined in equation (6.12).

Hence, the temperature at the next time step T_7* can be obtained by rearranging the above equation

$$T_7^* = T_7 + \alpha\Delta t\left[\frac{T_1 - 2T_7 + T_8}{\Delta r^2} + \frac{T_8 - T_1}{2r\Delta r} + J_2\right]. \tag{6.14}$$

For the above heat transfer computations, the time steps are chosen in accordance with the stability requirement (Osizik, 1980) such that

$$Fo_{max} \leq \frac{1}{6} \quad \text{and} \quad Fo_{max}(3+Bi_{max}) \leq \frac{1}{2}$$

Where Fo_{max} and Bi_{max} are the maximum Fourier and Biot numbers respectively obtained for the three co-ordinates.

As can be observed from figure 6.2 and equations (6.3-6.4), the modelling of the heat transfer process along the convective boundaries requires the determination of various heat transfer coefficients as dictated by the fluid phase or flow characteristics. The different correlations employed at various fluid-wall boundaries are given below.

Fluid/ pipeline wall heat transfer: H_2/H_3

In this study, it is assumed that flow through the orifice following pipeline failure is fully developed and turbulent. This is a reasonable assumption considering the relatively high Reynolds numbers ($>10^6$) following puncture. Consequently, heat exchange between the discharging fluid and the pipe wall is due to forced, as opposed to natural convection. Depending on the size of the orifice and conditions downstream of the puncture, the heat transfer due to fluid flow within the pipeline may be laminar or turbulent.

For single-phase fully developed flow in smooth pipes, the correlation proposed by Gnielinski (1976) is used to calculate the fluid/wall heat transfer coefficient due to its wide range of applicability and accuracy (Rohsenow et al., 1998). It is given by:

$$Nu = \frac{(\mathrm{Re}-1000)\mathrm{Pr}(f/2)}{1+12.7(f/2)^{0.5}\left[\mathrm{Pr}^{2/3}-1\right]} \tag{6.15}$$

Where Nu, Pr and Re are the Nusselt, Prandtl and Reynolds numbers respectively:

The Fanning friction factor, f in equation (6.15), is calculated from the expression proposed by Techo et al. (1965) as given by:

$$\frac{1}{\sqrt{f}} = 1.7372 \ln \frac{\mathrm{Re}}{1.964 \ln \mathrm{Re} - 3.8215} \tag{6.16}$$

For laminar flows, the relation proposed by Holman (1986) is employed

$$Nu = 3.66 + \frac{0.0668(d/L)\,\mathrm{Re}\,\mathrm{Pr}}{1 + 0.04\left[(d/L)\,\mathrm{Re}\,\mathrm{Pr}\right]^{2/3}} \tag{6.17}$$

Where d and L are the pipeline diameter and length respectively.

In the case of two-phase flows, the correlation proposed by Steiner and Taborek (1992) is employed for calculating heat transfer coefficient (h_f) within the pipeline. Apart from its relative simplicity and ease of use, the correlation has been shown (Rohsenow et al., 1998) to produce good agreement with experimental data for a wide range of flow regimes. It is given by:

$$\frac{h_f}{h_l} = \left[(1-x)^{1.5} + 1.9 x^{0.6} \left(\frac{\rho_l}{\rho_g} \right)^{0.35} \right]^{1.1} \tag{6.18}$$

Where, x is the fluid quality, ρ_g and ρ_l are the vapour and liquid densities respectively. h_l is the heat transfer coefficient for the liquid phase in turn given by:

$$\frac{h_l D_{in}}{\kappa_l} = 0.023 \left[\frac{\rho_{mix} u (1-x) D_{in}}{\mu_l} \right]^{0.8} \left[\frac{\mu_l C_{pl}}{\kappa_l} \right]^{0.4} \tag{6.19}$$

ρ_{mix} represents the two-phase mixture density.

Ambient/ pipeline wall heat transfer: H_4

The heat transfer coefficient, h_{amb} between the pipe wall and the surrounding ambient is given by (Incropera and DeWitt, 1996; Rohsenow et al., 1998):

$$h_{amb} = \left(h_{nat}^3 + h_{for}^3\right)^{1/3} \tag{6.20}$$

Where, h_{nat} and h_{for} are the natural and forced heat transfer coefficients respectively.

For natural convection, the correlation proposed by Churchill and Chu (1975) is used:

$$\frac{h_{nat} D_{out}}{\kappa_{film}} = \left[0.60 + \frac{0.387 Ra_D^{1/6}}{\left[1 + \left(0.559/\mathrm{Pr}_{film}\right)^{9/16}\right]^{8/27}} \right]^2 \tag{6.21}$$

The dimensionless groups are defined as:

$$Ra_D = Gr_{film}\,\mathrm{Pr}_{film} \quad \text{(Rayleigh number)} \tag{6.22}$$

$$Gr_{film} = \frac{\rho_{film}^2 g \xi_{film} \left(T_s - T_{amb}\right) D_{out}^3}{\mu_{film}^2} \quad \text{(Grashof number)} \tag{6.23}$$

$$\mathrm{Pr}_{film} = \frac{C_{pfilm}\mu_{film}}{\kappa_{film}} \quad \text{(Prandtl number)} \tag{6.24}$$

Where, g represents the gravitational acceleration, the subscript, *film* represents ambient properties evaluated at the film temperature [$T_{film} = (T_s + T_{amb})/2$], T_s the surface temperature, and ξ_{film} the isobaric volumetric expansion coefficient. ξ_{film} is a thermodynamic property which can be obtained from the equation of state. It is given by (Incropera and DeWitt, 1996):

$$\xi_{film} = -\frac{1}{\rho_{film}} \left(\frac{\partial \rho_{film}}{\partial T_{film}} \right)_P \tag{6.25}$$

For forced convection, the heat transfer correlation proposed by Churchill and Bernstein (1977) is employed. The correlation is said to cover the entire range of Reynolds number for which data are available as well as a wide range of Prandtl numbers.

$$\frac{h_{for}D_{out}}{\kappa_{film}} = \left[0.30 + \frac{0.62\,\mathrm{Re}_{film}^{1/2}\,\mathrm{Pr}_{film}^{1/3}}{\left[1+\left(0.4/\mathrm{Pr}_{film}\right)^{2/3}\right]^{1/4}}\left[1+\left(\frac{\mathrm{Re}_{film}}{282{,}000}\right)^{5/8}\right]^{4/5}\right] \tag{6.26}$$

It should be noted that all the above heat transfer relations were developed using a specific test fluid under specific conditions. As such, its extrapolation to other fluids may introduce inaccuracies in the simulated results.

6.2.2 Pressure and Thermal Stresses

Tangential (hoop) and axial stresses are the driving forces responsible for fracture propagation in the longitudinal and circumferential directions respectively with the latter leading to full bore rupture. In this study, the contribution of the radial stresses in driving fracture has been ignored. However a more advanced stress analysis based on Von Misses stresses is required for a more detailed study of this aspect. In addition, local thermal gradient effects in the vicinity of the crack tip have not been fully accounted for.

Thermal shock stress may develop as a result of rapid cooling of the pipe wall. The equations below, given by (Popov, 1999; Timoshenko and Goodier, 1987) show the corresponding equations for determining the pressure and thermal stresses.

Tangential pressure stress:

$$\sigma_t^{\,P} = A_1\left(1+\frac{b^2}{r^2}\right) \tag{6.27}$$

Axial pressure stress:

$$\sigma_a^{\,P} = A_1 \tag{6.28}$$

Tangential thermal stress:

$$\sigma_t^T = \frac{M_1}{r^2}\left[\frac{r^2+a^2}{b^2-a^2}\int_a^b Trdr + \int_a^r Trdr - Tr^2\right] \tag{6.29}$$

Axial thermal stress:

$$\sigma_a^T = M_1\left[\frac{2}{b^2-a^2}\int_a^b Trdr - T\right] \tag{6.30}$$

Thermal shock:

$$\sigma^T{}_s = \tau E \Delta T \tag{6.31}$$

$$M_1 = \frac{\tau E}{1-\mu} \qquad A_1 = \frac{Pi}{R^2-1} \qquad R = \frac{b}{a}$$

a, b,τ, E and μ are respectively inner and outer pipe radius, coefficient of thermal expansion, modulus of elasticity, and Poisson's ratio. ΔT, T and P_i are the change in initial wall temperature, pipe wall temperature at a particular point and internal pressure respectively.

6.2.3 Crack Propagation

As mentioned earlier, the quasi-adiabatic expansion of the escaping fluid will result in a cold temperature front propagating away from the puncture plane. If this temperature falls below the pipeline material ductile to brittle transition, a drop in the material fracture toughness would occur. At temperatures below the DBTT, the ability of the metal to deform plastically is greatly reduced and the process of crack propagation is brittle. Depending on the prevailing thermal and pressure stresses in the defect plane, the reduction in temperature could lead to a growing crack which in turn may transit into a secondary more catastrophic running ductile fracture resulting in a massive release of the pressurised inventory.

Griffith (1920) laid down the basis for fracture mechanics in the 1920's and used an energy balance approach to determine the conditions of fracture. A major step forward came with Irwin's (Irwin, 1957) studies of the stress analysis of cracks, in which he evaluated the stresses in the area surrounding the tip of the crack as a function of distance (r) polar co-ordinates (θ).

Over the past few decades, different approaches have been developed to evaluate the conditions necessary for fracture, with each approach applicable under certain conditions. Figure 6.4 shows a typical transition curve highlighting the conditions under which different fracture mechanics approach are applicable.

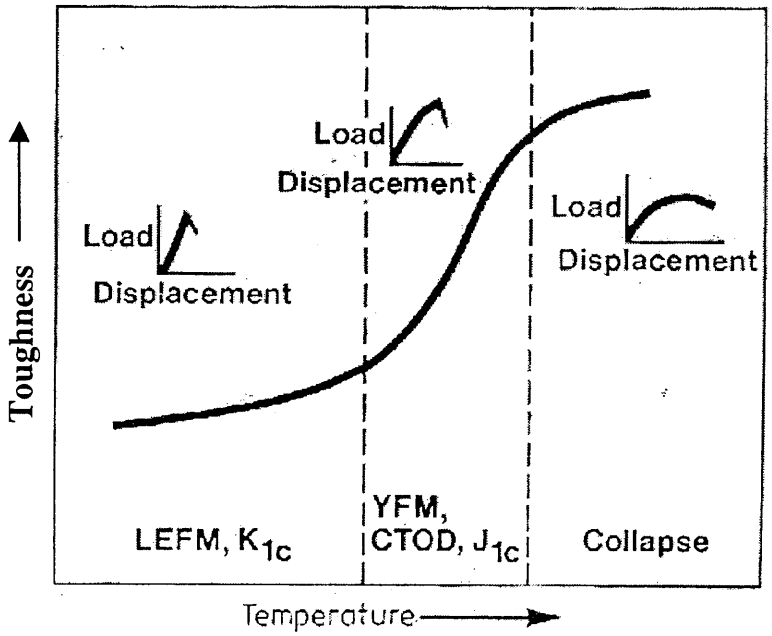

Figure 6.4: Schematic representation of the transition curve showing the applicability of the different fracture mechanics approach (Harrison, 1979).

In the first region, the concept of Linear Elastic Fracture Mechanics (LEFM), which employs the elastic energy release rate, G, and Stress Intensity Factors (K_I) are used in characterising fracture. LEFM is applicable to materials with limited plasticity at

the crack tip, i.e. brittle materials, or materials thick enough that the plastic zone is considered small relative to the overall crack geometry. For materials or operations characterised by some degree of yielding, the basis of stress intensity approach breaks down. Under this situation, Yield Fracture Mechanics (YFM), which employs methods such as Crack Tip Opening Displacement (CTOD) and the J-integral (J_{1c}) (Rice, 1968), becomes applicable in defining fracture conditions.

In this study, the mode of crack propagation is brittle; hence the LEFM- K_1 approach is used in defining fracture conditions. The condition for fracture stipulates that if the crack driving force (expressed as the stress intensity factor, K_1) is equal to or greater than the material fracture toughness (K_{mat}) crack propagation or fracture will occur. In mathematical form, fracture can be said to occur if

$$K_1 \geq K_{mat} \tag{6.32}$$

This fracture criterion is relatively simple, and further work may involve advanced models, including a failure assessment diagram approach.

For brittle materials, the critical fracture toughness, K_I is given by (Irwin, 1957)

$$K_1 = Y\sigma\sqrt{\pi a_l} \tag{6.33}$$

Where, σ is the applied stress i.e. sum of the pressure and thermal stresses. Y is the shape factor (see later) depending on the crack length and geometry with, a_l representing the half crack length.

6.3 Case Studies

The following describes the results of the application of the above fracture propagation model to the hypothetical puncture of pipelines containing hydrocarbons. Two scenarios namely crack propagation in pipelines exposed to air, and crack propagation in buried pipelines are modelled in order to highlight the interesting yet important thermal effects that may occur.

6.3.1 Crack Propagation in Exposed Pipelines

Table 6.1 presents the prevailing conditions prior to puncture as used in the implementation of the fracture model.

The pipe wall is assumed to be made of carbon steel with a ductile to brittle transition temperature (DBTT) of –15 °C (Roberts, 1999). The fracture toughness above and below DBTT are taken as 95 MPa $m^{0.5}$ and 40 MPa $m^{0.5}$ respectively (Roberts, 1999). These values are assumed to remain constant at any temperature away from the DBTT.

In this study, it is assumed that the initial defect is in the form of a 0.005 m diameter circular puncture with a 0.05 m longitudinal hairline crack extending from its side. This type of failure geometry is typical of corrosion-induced defects. The isolated pipeline length is taken as 1 km with the defect being formed at a distance of 250 m from the high-pressure end. Since the pipeline is exposed to the atmosphere, it is reasonable to assume that the expanded jet only cools the pipe wall orifice as it discharges. Hence, the escaped inventory does not contribute to the cooling of the pipe wall.

Parameter	Data
Feed pressure (bara)	117
Feed temperature (K)	293
Feed flow rate (kg/s)	34.5
Pipeline thickness (mm)	19
Pipeline nominal inner diameter (m)	0.419
Pipeline Density (kg/m^3)	7854
Pipeline thermal conductivity (W/mK)	53.6
Poission ratio	0.3
Coefficient of thermal expansion (K^{-1})	12×10^{-6}
Modulus of elasticity (MPa)	20.7×10^4
Wind velocity (m/s)	6.5

Table 6.1: Pipeline rupture data. Pipeline inventory (molar %): CH_4 (98.2), C_2H_6 (1.15), C_3H_8 (0.48), i-C_4H_{10} (0.11), N_2 (0.06).

Two credible failure scenarios involving isolated and un-isolated releases are considered in order to investigate their effect on the defect stability. In the isolated case, it is assumed that pumping ceases 120 s following pipeline failure while in the un-isolated case, pumping continues throughout the discharge process. For the above simulations, the pipeline is discretised into 100 simple grids.

Results and Discussion

Figure 6.5 shows the variation of the radial temperature profile (across the pipeline thickness) at the puncture plane at different time intervals during the depressurisation for the isolated failure scenario. For the conditions tested, the data indicates that the temperature variation across the pipe wall thickness is negligible. The maximum temperature drop is only 5 K following depressurisation. Consequently, the associated thermal stress due to temperature change in the radial direction is minimal.

Figures 6.6 and 6.7 show the corresponding transient axial pipe temperature profiles at different time intervals in the proximity of the puncture plane for the isolated and un-isolated failure scenarios respectively. The corresponding DBTT is also indicated for reference. Referring to the isolated pipeline data (figure 6.6), it is clear that the rapid expansion of the escaping inventory results in significant cooling of the pipe wall with the effect becoming more pronounced with time and distance towards the puncture plane.

Although the uneven cooling may induce stresses in the bulk pipeline material since it cannot contract freely, in this scenario however, it is assumed that the contractions can take place unhindered along the exposed surface of the defect. Consequently, there would be negligible thermal stresses at the crack tip due to thermal shock. However, in the case of an embedded crack the bulk material surrounding it may be prevented from freely contracting, thereby giving rise to thermal shock stresses around the (embedded) defect.

Returning to figure 6.6, the pipe wall temperature reaches the DBTT of 258 K, 30 s following puncture dropping to 240 K at 2 700 s. However, as compared to the un-isolated release (figure 6.7), the expansion induced cold temperature front moving away from the rupture plane is confined to significantly smaller distances (c.f. 0.2 m at 2,700 s with 0.6 m at 2,700 s).

Clearly, under these circumstances, it is imperative to ascertain whether the significant reduction in the pipe wall fracture toughness coupled with the accompanying pressure and thermal stresses may be sufficient to undermine the pipeline's mechanical integrity.

Figure 6.8 shows the transient variations of the prevailing pressure (hoop: curve A) and thermal (tangential: curve B) stresses at the crack tip during depressurisation for the isolated pipeline. Curve C shows the corresponding total stresses. As it may be observed, the thermal stresses are insignificant (probably due to the fact that some stress components has been neglected) as compared to the pressure stresses...However, it should be noted that the expansion induced cooling of the

pipeline plays a major role in weakening the pipeline's mechanical integrity by reducing its fracture toughness and hence its resistance to withstanding the pressure stresses.

Figure 6.9 shows the corresponding calculation algorithm for determining the defect length accounting for the pertinent fluid dynamics, heat transfer and fracture mechanics.

Figures 6.10 a-d is a pictorial time line presentation corresponding to 4 critical stages of crack growth for the isolated pipeline failure scenario. The shape factors, Y required for the calculation of the critical fracture toughness (equation 6.32) for each of the stages of fracture propagation is obtained from the literature, and given in the same figure.

Stage1: 0 – 30 s following depressurisation; Figure 6.10(a)

Crack growth occurs when the temperature at any point at the defect/pipeline boundary drops below the DBTT and $K_c > K_{mat}$. This occurs 30 s following depressurisation and is marked by the onset of crack growth from the LHS of the puncture plane. It is note worthy that at this early stage of depressurisation, the pre-existing crack on the RHS of the puncture does not grow since the temperature at its tip (0.05 m from the puncture plane) has not yet reached the DBTT.

Stage 2: 30 – 1,080 s following depressurisation; Figure 6.10(b)

During 30 – 1,080 s following depressurisation, the crack on the left of the puncture continues to grow. There is no crack growth on the right hand of the puncture since the temperature at the crack tip to the right is still above the DBTT. This stage of crack propagation ends when the crack lengths on either side of the puncture plane are equal.

Stage 3: 1,080 – 2,100 s following depressurisation; Figure 6.10(c)

The onset of stage 3 is marked by the crack length on the left side of the puncture becoming equal to the right side initial crack length (0.05 m). Further depressurisation induced cooling results in both cracks propagating at the same rate.

Stage 4: Catastrophic pipeline rupture (>2 100 s); Figure 6.10(d).

At stage 4 the crack length is the maximum value that the pipe wall toughness can withstand, thus becoming unstable. This leads to a running fracture and catastrophic pipeline failure.

Figure 6.11 shows the transient variation of defect length with time following puncture for the isolated release. The defect length is taken as the summation of the crack length and the puncture diameter. Curve A shows the actual defect length whereas curve B shows the corresponding critical defect length required to cause catastrophic failure. Depressurisation of the pipeline results in a significant and rapid increase in defect length. Catastrophic failure corresponding to the point of intersection for curves A and B occurs some 2,100 s following puncture as indicated above.

Figure 6.12 shows the same data as in figure 6.11 but for un-isolated release. Curve A indicates no crack growth for the first 30 s of discharge. This initial stability is because during the early depressurisation period, the metal's temperature at the edge of the defect is higher than DBTT. However, after this period, the defect length increases by *ca.* 15 mm some 200 s after depressurisation, remaining stable thereon. Throughout the depressurisation process, the actual defect length remains well below the critical defect length (curve B), and catastrophic pipeline failure during unisolated discharge is highly unlikely.

Figure 6.13 shows the corresponding data for the variation of crack length with time for isolated release but assuming isothermal decompression. The data clearly

demonstrates the importance of taking into account the expansion induced cooling effects of the depressurising medium. Ignoring such effects will lead to the erroneous conclusion of a stable defect.

Interestingly, the results of a similar analysis assuming an initial circumferential defect orientation and taking full account of heat transfer effects fail to indicate crack propagation. This is due to the fact that for a cylindrical geometry, the axial stresses required for crack growth in the circumferential direction is double that for crack propagation in the longitudinal direction.

6.3.2 Crack Propagation in Buried Pipelines

The case study dealt with in section 6.3.1 involved crack propagation in exposed pipelines, in which the expanded fluid is released as a jet into the atmosphere.

In the case of buried pipelines in which there is no blowout of materials, the high momentum jet may displace some soil around the pipe thus creating a crater. In this situation, the rapid quasi-adiabatic depressurisation of certain low molecular weight hydrocarbons such as methane or ethylene into the crater space can result in the significant cooling of the escaping fluid to temperatures lower than $-100\ ^{0}C$. This low temperature fluid will in turn form a cold blanket around the exposed part of the pipeline, consequently cooling the pipe wall. Figure 6.14 gives a schematic representation of the buried pipeline undergoing such depressurisation.

The following investigates the effect of the significant depressurisation induced cooling on an embedded crack in the puncture region. Unlike the failure studied in section 6.3.1 in which the defect may contract unrestrictedly, the pipeline wall embedding the crack is significantly hindered from contracting. This hindrance may result in significant thermal shock stresses, which should be accounted for in crack propagation analysis.

The importance of accounting for the thermal stresses when determining the critical stress required for initiating failure in a pipeline containing an embedded defect is thus described below.

The crack propagation model is applied to a 2 km pipeline conveying ethylene, punctured at 500 m from the high-pressure end. Table 6.2 gives the pipeline data used in implementing the model. The puncture size is taken to be 50 mm, and it is assumed that the released jet is of sufficient momentum to form a crater with a 3 m radius around the puncture. The released jet then expands isentropically to ambient conditions, reaching temperature *ca.* –104°C.

Parameter	**Data**
Fluid pressure (bara)	60
Fluid temperature (°C)	5
Puncture location (m)	500
Puncture size (mm)	50
Feed flow rate (kg/s)	120
Pipeline thickness (mm)	10
Pipeline nominal inner diameter (m)	0.30
Pipeline Density (kg/m^3)	7854
Pipeline thermal conductivity (W/mK)	53.6
Coefficient of thermal expansion (K^{-1})	12×10^{-6}
Modulus of elasticity (MPa)	20.7×10^4

Table 6.2: Pipeline rupture data. Pipeline inventory: Ethylene (100 %).

The following assumptions have been employed in the modelling.

1. The pipeline has a DBTT OF –15 °C, with its toughness below and above the DBTT 40 $MPam^{-0.5}$ and 100 $MPam^{-0.5}$ respectively.

2. The soil is in perfect contact with the pipeline, and has a conductivity of 0.6 W/mK, and a thermal diffusivity of 0.15 mm^2/s (Abu-Hamdeh et al., 2001).
3. The stresses around the crack tip due to soil loading are practically non-existent due to the formation of a crater by the expanded jet. Soil loading consists of both axial constraint on the pipe and circumferential pressure. The former could in reality be significant. For scenarios where soil loading is important, the resultant stresses may be estimated using the correlation given by Amirat et al. (2005)
4. The embedded crack is 0.01 m in length, located mid-way within the pipe wall and is oriented axially along the pipeline, close to fluid-soil boundary (see figure 6.14).

Fluid flow is maintained during the depressurisation, resulting in a pseudo-steady state discharge process after a short while.

Results and Discussion

Figure 6.15 shows the mid- thickness axial temperature profile (i.e. along the crack plane) at 100 s, i.e. when steady state conditions have been reached. The fluid-soil boundary has also been included for reference.

As may be observed from the figure, the wall temperature drops rapidly from -1^0C at the puncture site to –30 °C, 30 mm away from it. The pipeline then maintains a relatively constant temperature of –30 °C along the exposed pipeline section. Although not shown in the figure, the surface and inner wall temperatures of the pipeline reaches a minimum of –52 °C and –7 °C respectively. This represents a temperature gradient of 45 °C across the pipe wall. The wall temperature at the puncture site (-1 °C) is unsurprisingly the same as the fluid just before it completely exits the puncture hole.

Towards the ambient-soil boundary, a sharp rise in temperature may also be observed. This is because the buried pipeline section is kept relatively warm by the soil. It

should be noted that the pipe wall itself is not cooled to –104 °C as the cooling effect is countered to some extent by the warm bulk fluid flowing through the pipeline.
At a distance of 0.2 m from the crack, the pipeline's temperature remains at 5 °C, (hence no thermal contraction) and can therefore be considered as a rigid boundary. As such, the pipeline material surrounding the crack is restrained (although not totally), and would therefore experience some stresses due to thermal shock.

In order to account for the degree of contraction, the thermal shock stress determined from equation (6.31) is multiplied by a factor, estimated to be 0.6. Equation (6.29) is also employed for determining the additional thermal stresses as a result of the 45 °C temperature gradient across the pipe wall thickness.

In this case study, the contribution of the thermal stresses (85 MPa) to the total stress (175 MPa) at the crack is significant and should therefore not be ignored.

Figure 6.16 shows the critical fluid pressure required to cause pipeline failure as a function of the crack length. Curve A shows the data when the thermal stresses are ignored, while curve B shows the data when the thermal stresses are incorporated.

The data is generated using the expression for the fracture criteria (equation (6.33)) and that for the relevant stresses (equations (6.27-6.31)) to obtain the critical fluid pressure as a function of crack length.

From the figure, it may be observed that discounting the thermal stresses may result in overestimation of the critical pressure required to propagate a defect. This will in turn result in an over estimation of the safe working pressure. For example, for a crack length of 0.02 m, discounting the thermal stresses indicates that the pipeline would fail due to crack propagation at a pressure of 145 bar. However, the corresponding pressure when the thermal stresses are accounted for is only 91 bar.

6.4 Concluding Remarks

In this study, the development of a model for simulating low temperature induced failure of pressurised pipelines is presented. This model accounts for the important processes taking place during depressurisation including real fluid behaviour as well as the accompanying thermal and pressure stresses in the pipe wall.
Two cases involving defects in exposed and buried pipelines were simulated and the results discussed.

In the case of the exposed pipeline, a pictorial timeline presentation starting with the puncture of an isolated pressurised pipeline containing a multi-component hydrocarbon mixture is used to elucidate the sequence of events leading to its catastrophic failure. The expansion induced cooling of the escaping hydrocarbon results in a cold temperature front moving away from the puncture plane reaching temperatures below the pipeline material's ductile to brittle transition temperature. This results in a significant drop in the fracture toughness thereby weakening the pipe wall.

The combination of low material fracture toughness and the accompanying pressure stresses in the pipe wall are found to ultimately undermine the pipeline's mechanical integrity by transforming the initial defect into a running fracture. Thermal stress magnitudes calculated using the simplified approach in this study were small; however in reality, they could be significant due to the local axial thermal gradient at the crack tip.

Although a delay in isolation of the pipeline by maintaining the feed flow results in a similar orders of magnitude drop in the pipe wall temperature and stresses as compared to the isolated pipeline, such effects are found to be confined to close proximity of the defect plane. This has the effect of limiting the growth of the defect length to that below which is necessary to initiate a running fracture.

The above finding presents an interesting dilemma, as in practice whenever possible, the puncture of the pipeline is universally followed by its immediate isolation using

emergency shutdown valves. Although the above has the effect of limiting the amount of inventory released to the isolated pipeline section, it may well exasperate low temperature induced effects leading to brittle fracture of the pipeline.

In the case of buried pipelines, the study shows the importance of accounting for thermal stresses in crack propagation analysis. These stresses are due to the significant temperature gradients induced by the cold expanded jet, coupled with the embedded crack's inability to contract freely. This in turn reduces the critical pressure required to initiate crack propagation. Hence, ignoring the thermal stresses may result in an overestimation of 'the safe working pressure'.

.

The results of this study highlight the importance of accounting for low temperature induced fracture as a potentially serious failure scenario when undertaking the safety assessment of pressurised pipelines. The model described in this chapter can be used as an effective tool for mitigating such failures through better pipeline design, improved material selection and appropriate emergency action.

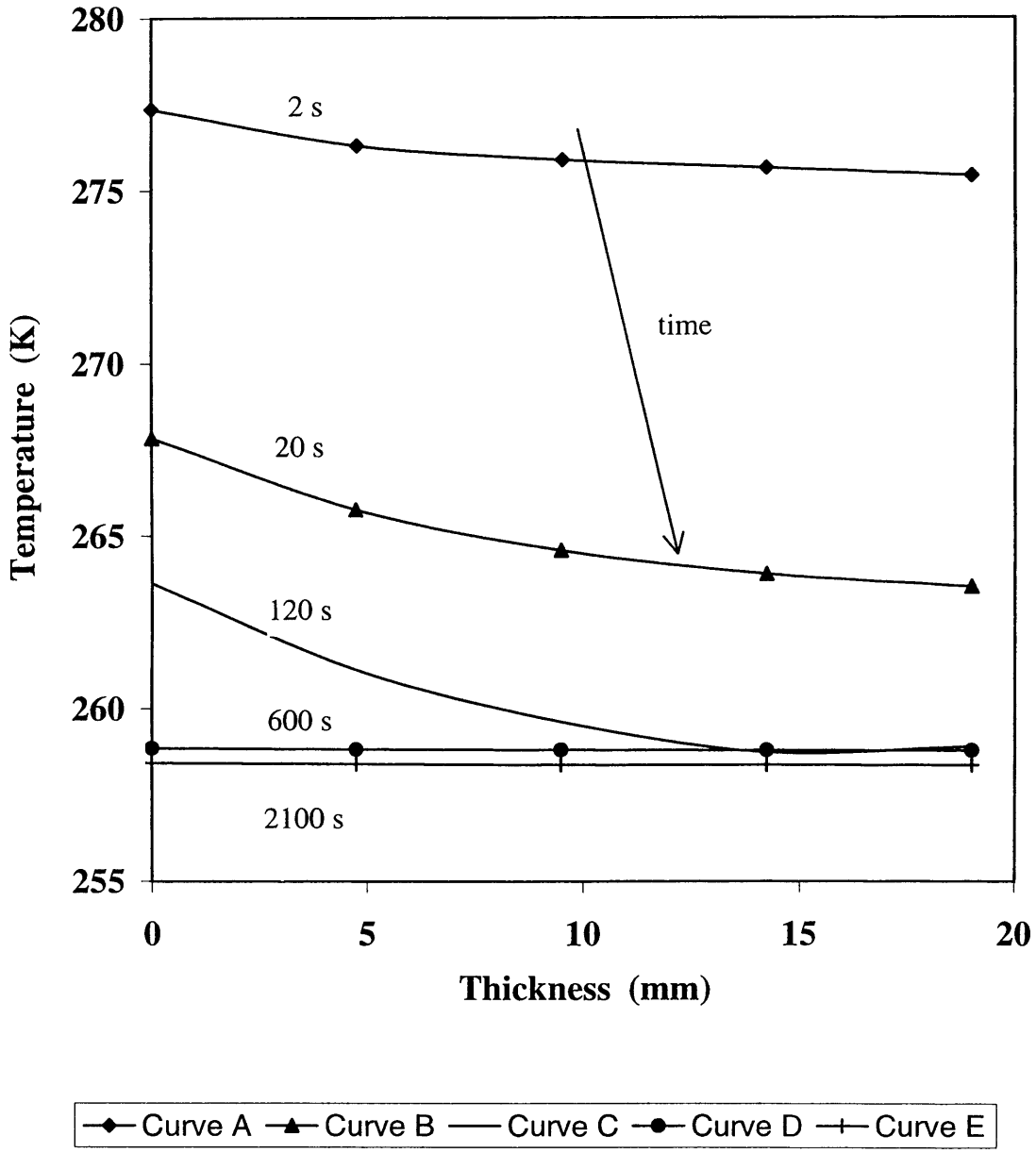

Figure 6.5: Transient variation of the radial temperature profile at the crack tip at different time intervals following depressurisation for isolated release.

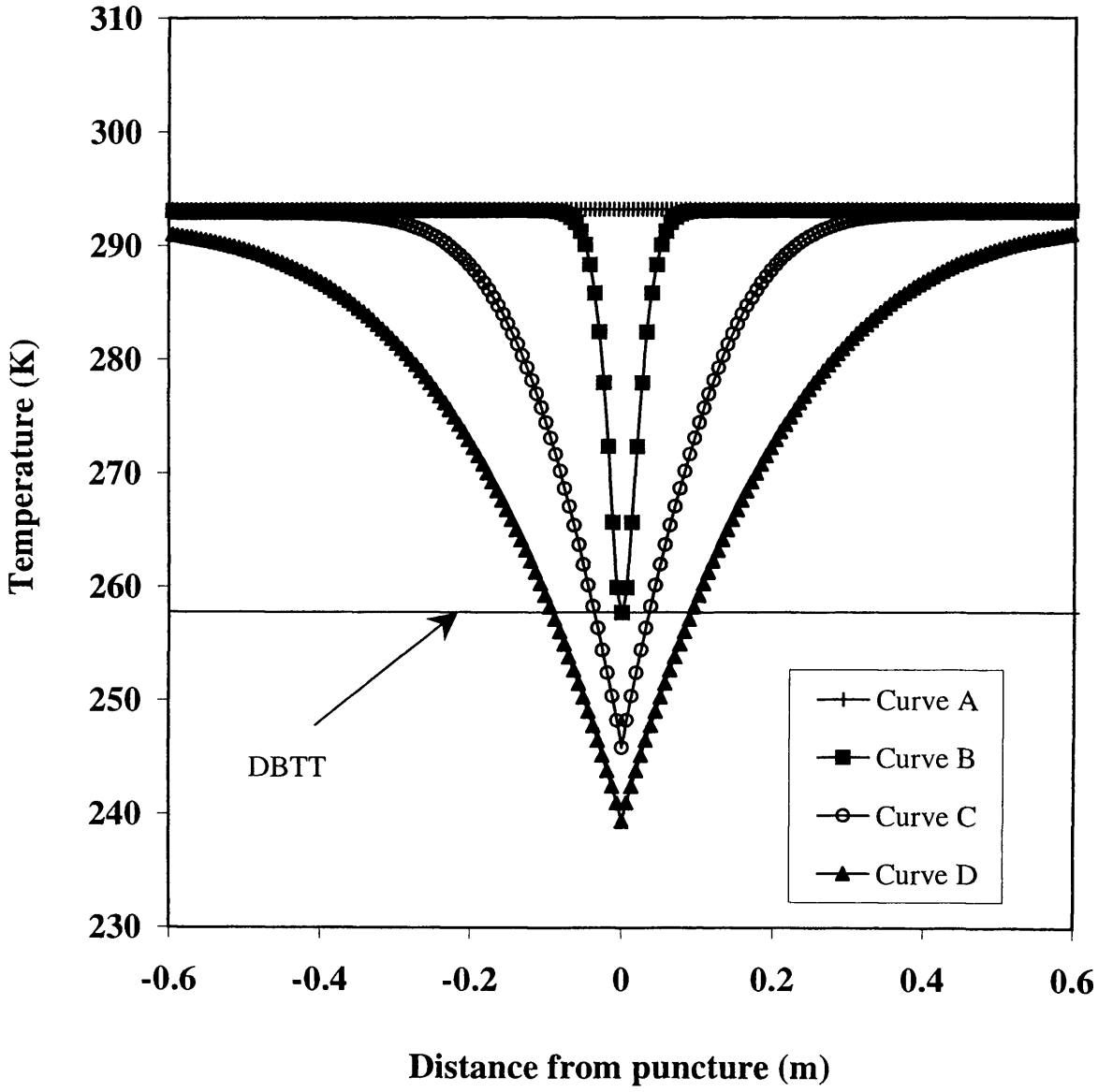

Figure 6.6: Transient variation of the axial temperature profiles in the vicinity of the puncture plane for isolated discharge.

Curve A: 0s; Curve B: 30s; Curve C: 600s; Curve D: 2700s.

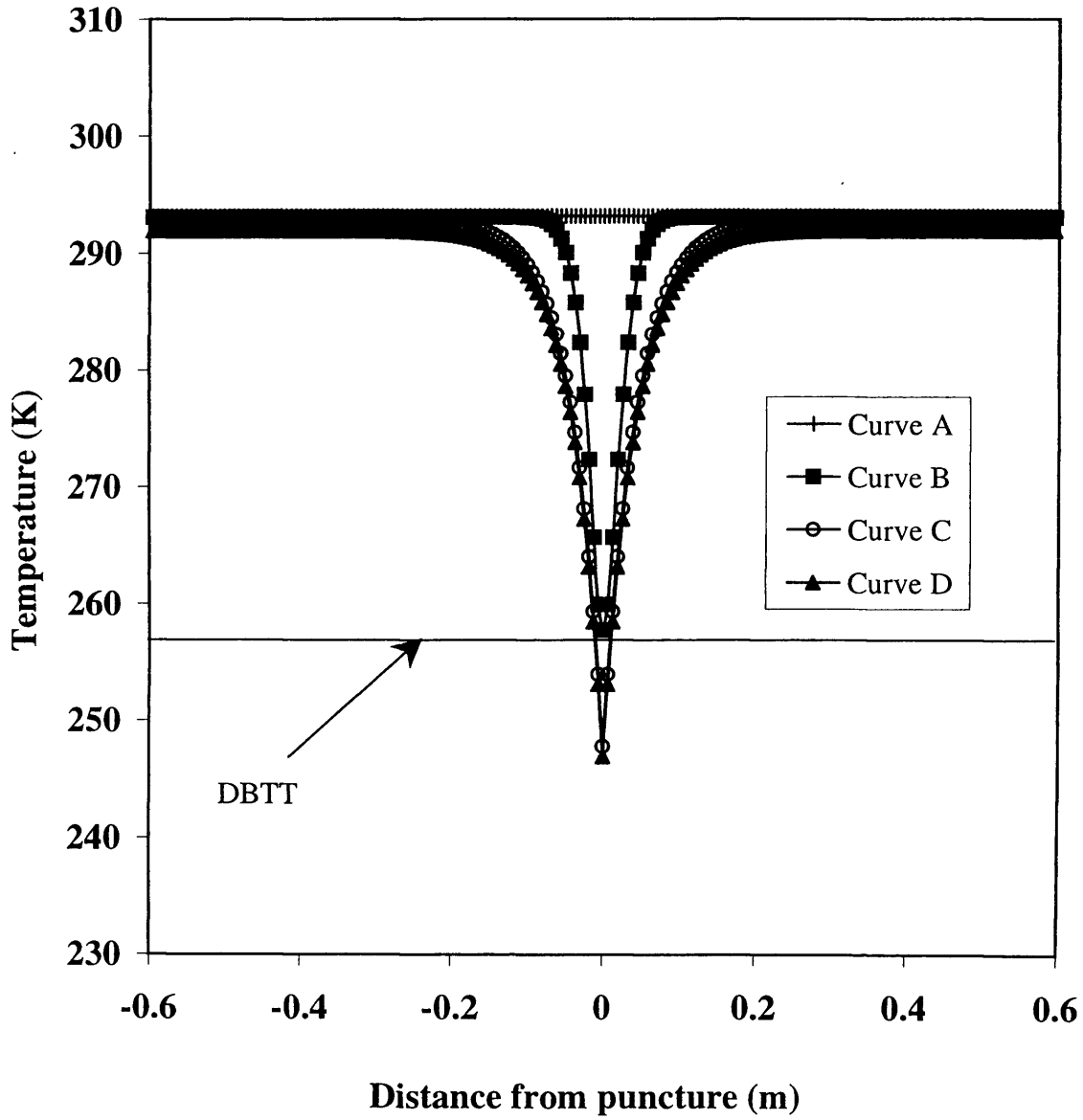

Figure 6.7: Transient variation of the axial temperature profiles in the vicinity of the puncture plane for unisolated discharge.

Curve A: 0s; Curve B: 30s; Curve C: 600s; Curve D: 2700s.

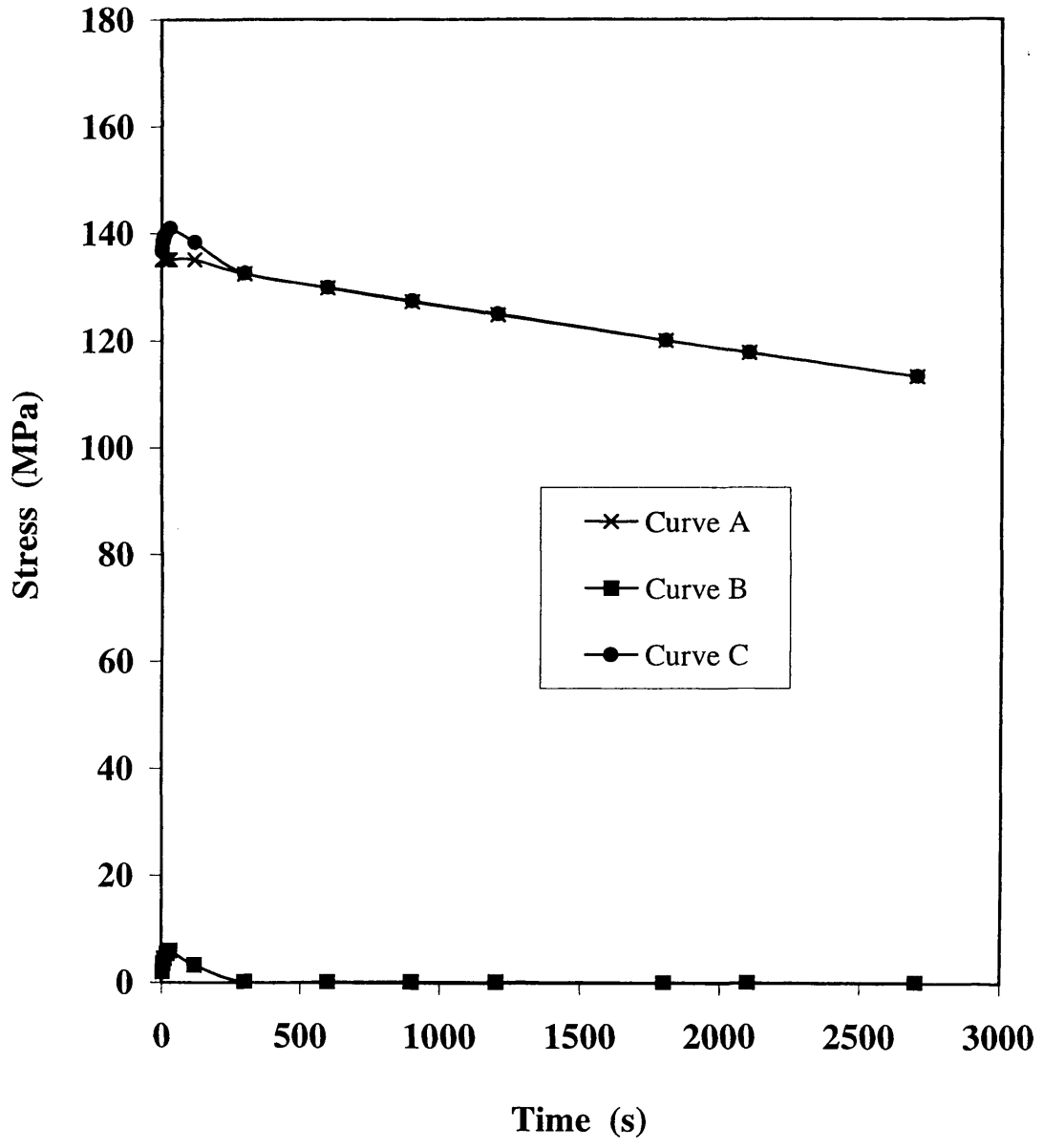

Figure 6.8: Variation of stress at crack tip with time during isolated discharge.

Curve A: Pressure stress.
Curve B: Thermal stress.
Curve C: Total stress.

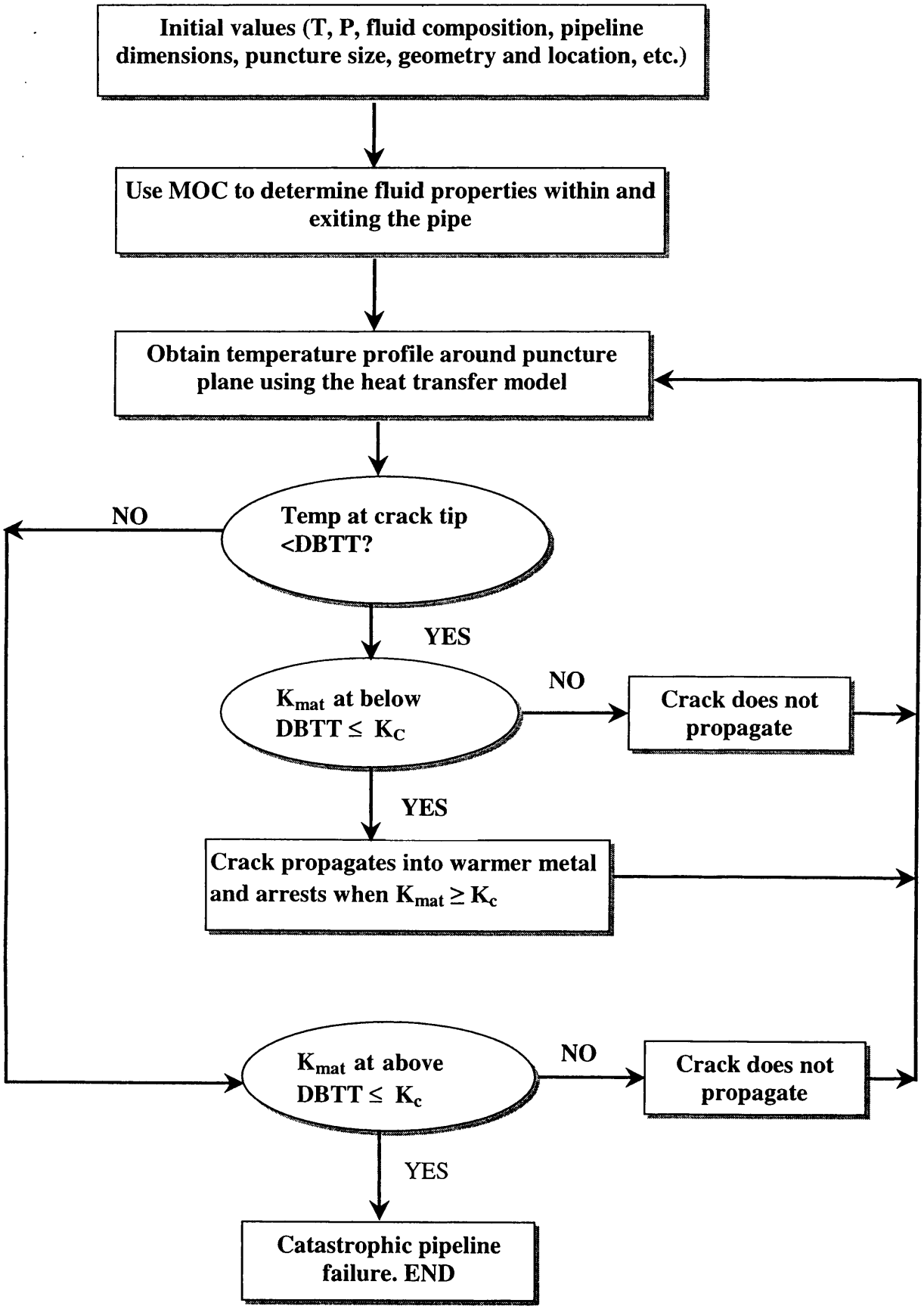

Figure 6.9: Crack propagation calculation flow algorithm.

0 – 30s

(a)

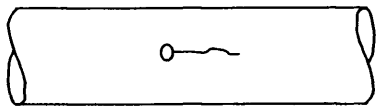

$$Y = \left[1 + 0.2(1-s) + 0.3(1-s)^6\right] Y_O \quad (6.33)$$

$$Y_o = 2.243 - 2.64s + 1.352s^2 - 0.248s^3 \quad (6.34)$$

$$s = \frac{a_i}{r_h + a_i} \quad (6.35)$$

(Tada et al., 2000)

30 – 1080 s

(b)

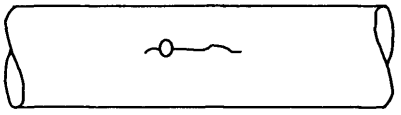

$$Y(\lambda) = (1+1.25\lambda^2)^{0.5} \quad 0 \le \lambda \le 1 \quad (6.36)$$

$$Y(\lambda) = 0.6+0.9\,\lambda \quad 1 \le \lambda \le 5 \quad (6.37)$$

$$\lambda = ((a_i + a_j) + dh)/2\ .[\ Rt]^{-0.5} \quad (6.38)$$

(Folias 1965; Erdogan and Kibbler, 1969)

1080 – 2100 s

(c)

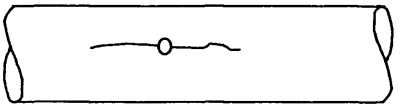

$$Y = 1 + (1-s)\left[0.5 + 0.743(1-s^2)\right] \quad (6.39)$$

(Newman 1971; Tada et al., 2000)

>2100 s

(d)

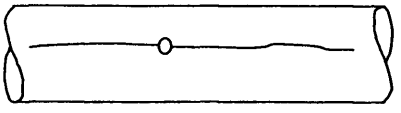

Figure 6.10: Schematic representation of various critical stages of fracture growth at different time intervals during isolated release.

R and t are respectively the inner radius pipe thickness with a_i and a_j representing the respective crack lengths to the right and left of the defect. d_h and r_h are the puncture diameter and radius respectively.

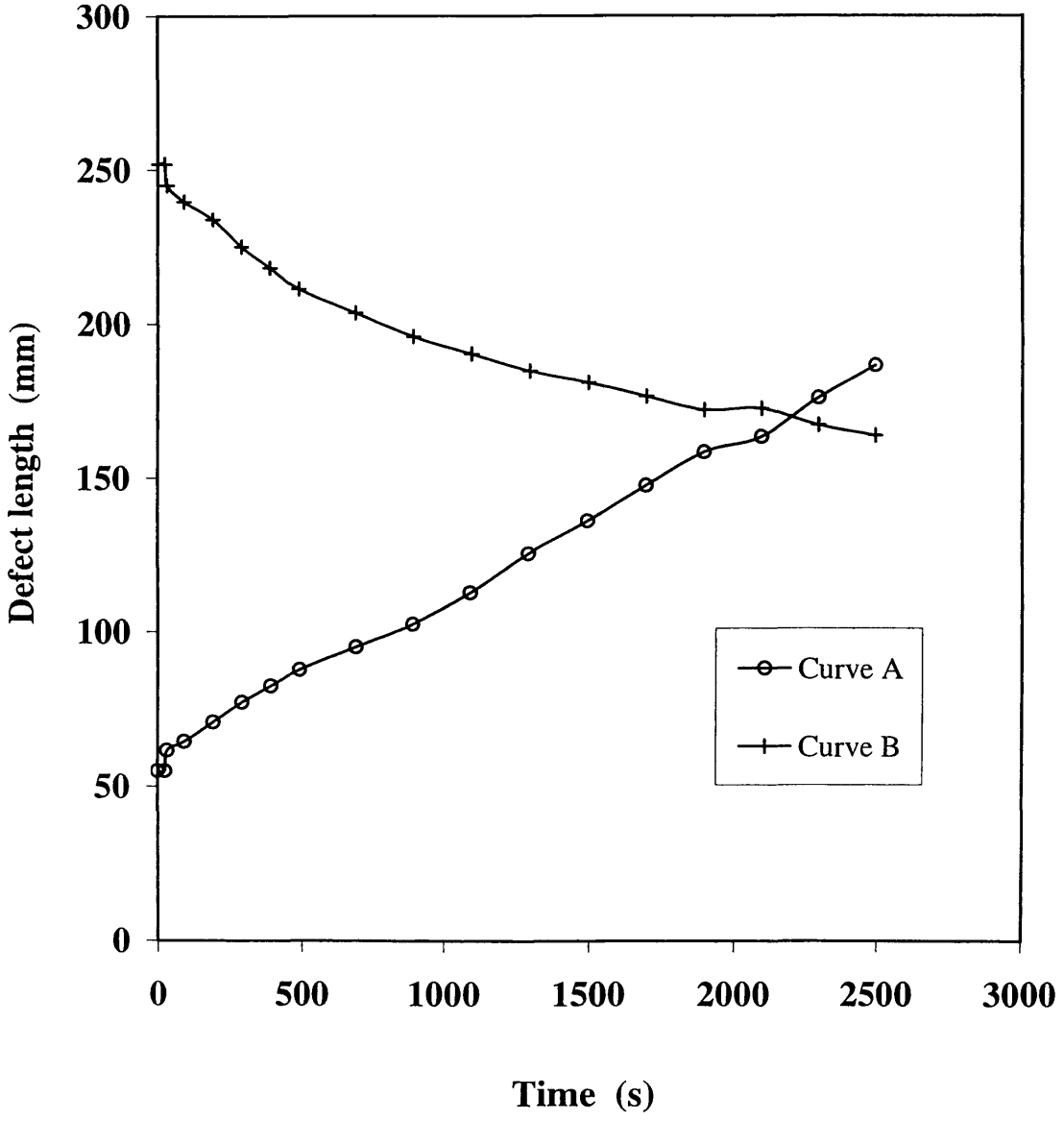

Figure 6.11: Variation of defect length with time for isolated discharge.

Curve A: Actual defect length.
Crave B: Defect length required to cause running fracture.

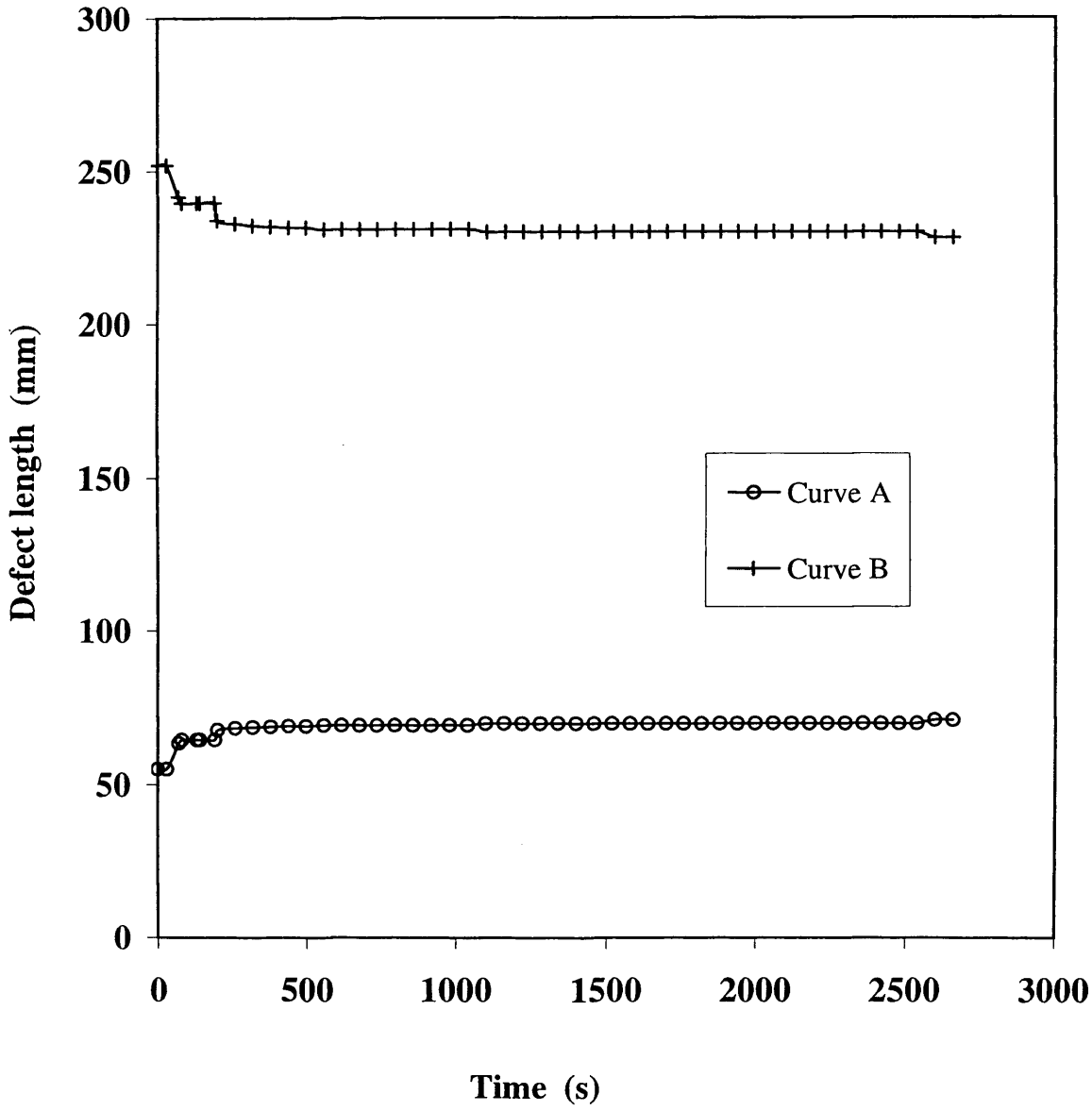

Figure 6.12: Variation of defect length with time for un- isolated discharge.

Curve A: Actual defect length.
Curve B: Defect length required to cause running fracture.

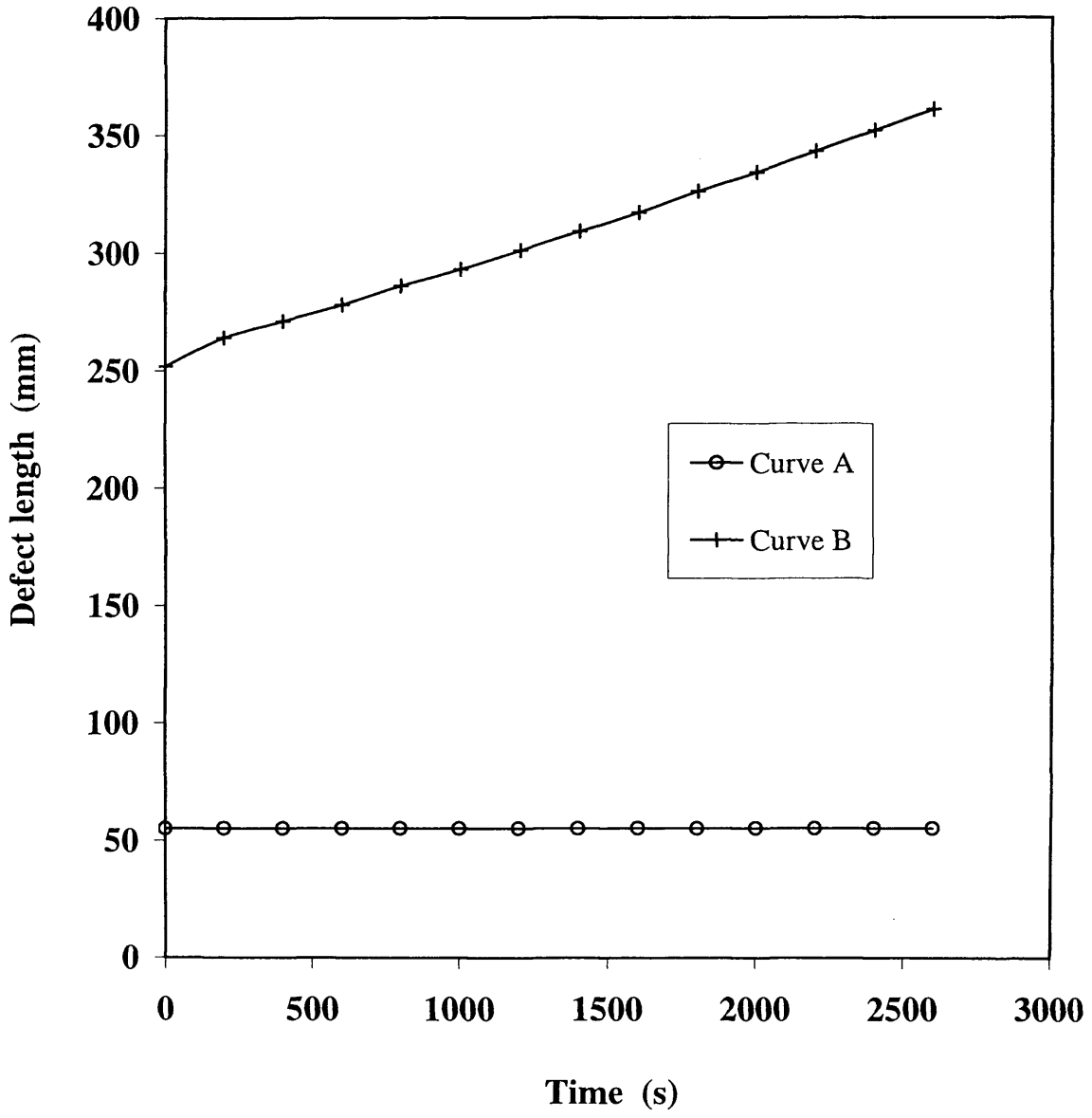

Figure 6.13: Variation of defect length with time for isolated discharge assuming isothermal release.

Curve A: Actual defect length.
Curve B: Defect length required to cause catastrophic failure.

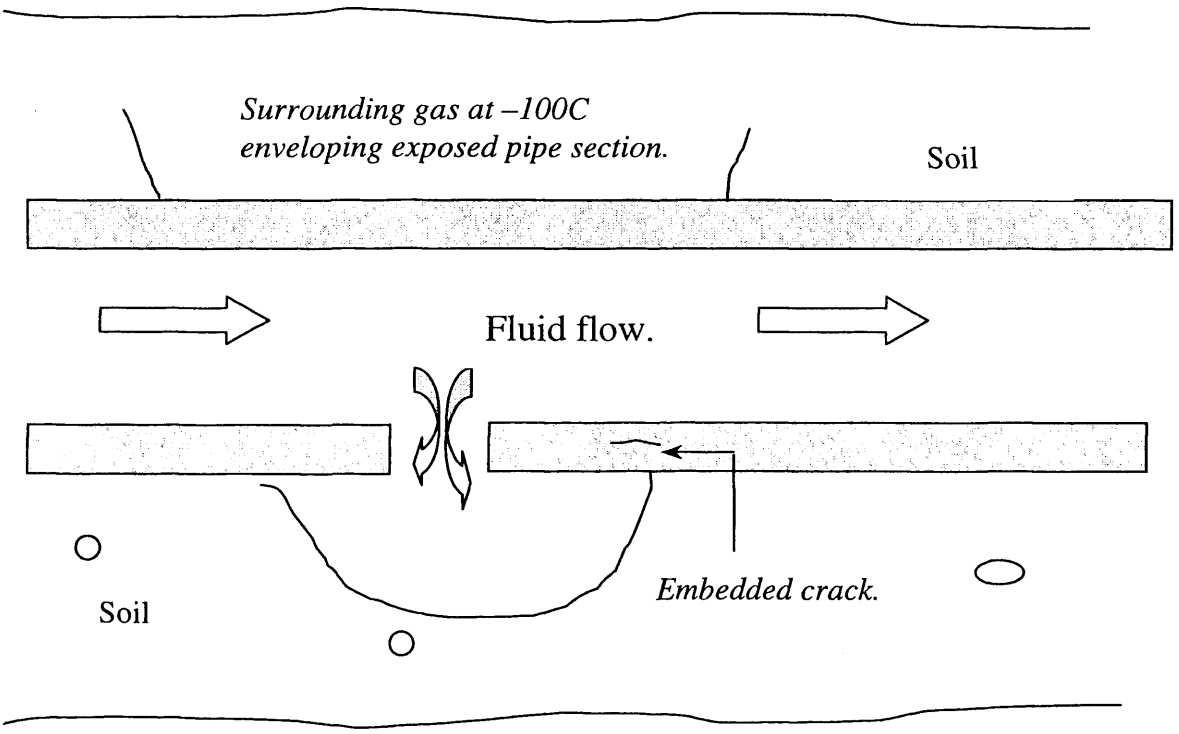

Figure 6.14: Schematic diagram showing the depressurisation of a buried pipeline.

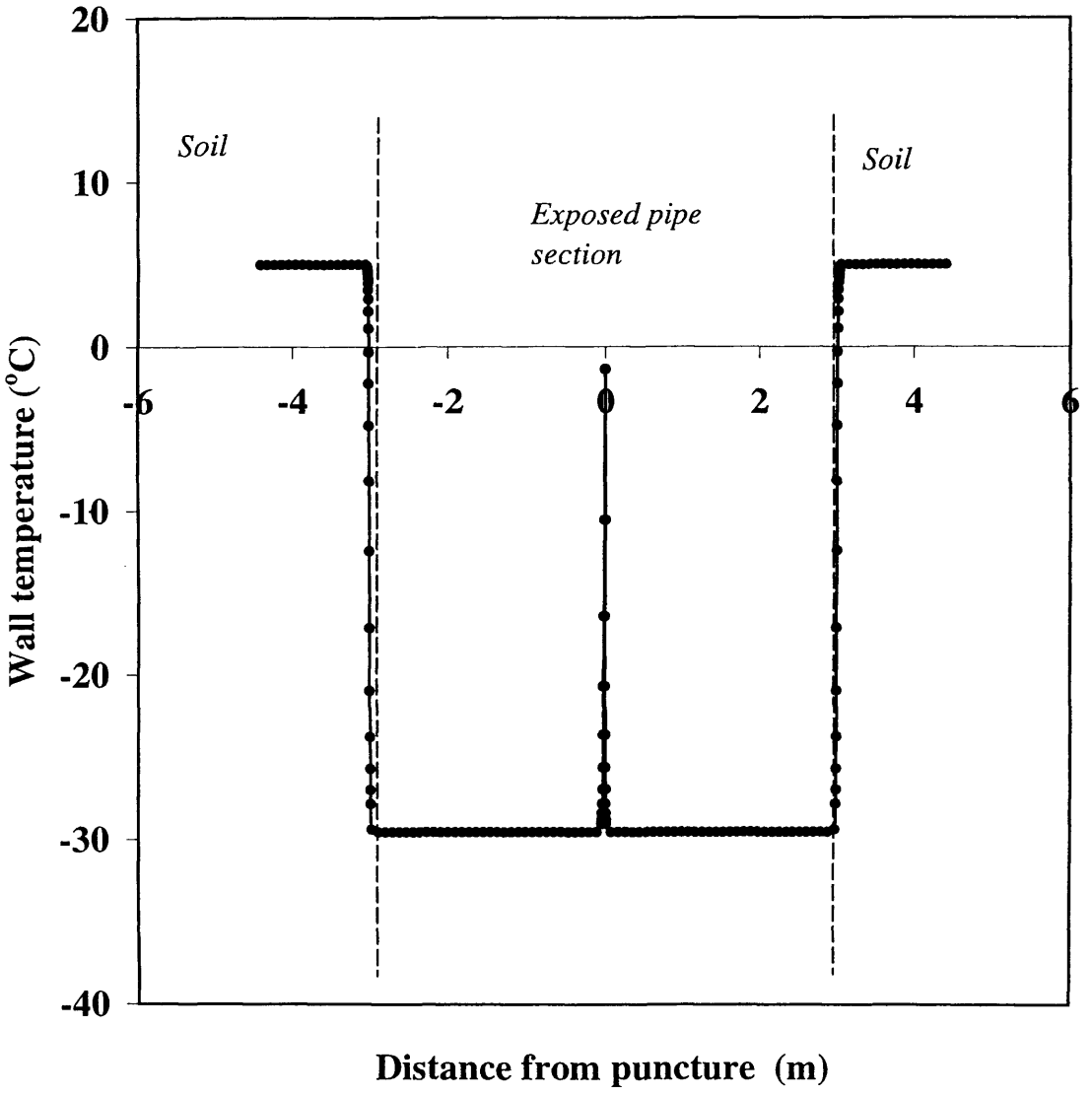

Figure 6.15: Variation of the axial temperature profile along the embeded crak plane at steady state (t=100 s) in the buried pipeline.

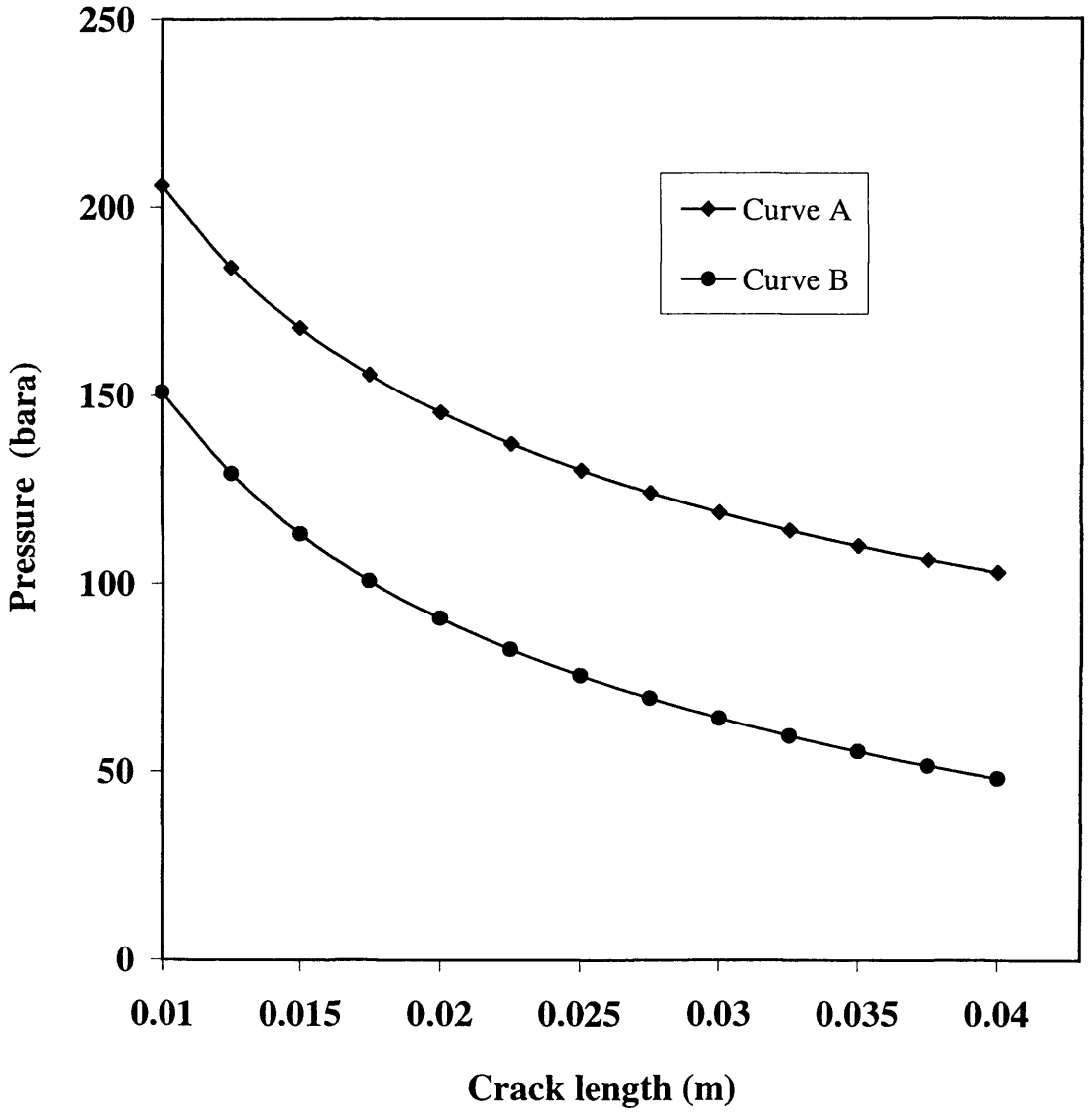

Figure 6.16: Variation of critical fluid pressure required to cause failure as a function of crack length .

Curve A: Data obtained when thermal stresses are ignored.
Curve B: Data obtained when thermal stresses are incorporated.

CHAPTER 7

CONCLUSION AND SUGGESTIONS FOR FUTURE WORK

7.1 Conclusion

This thesis described the development of a rigorous mathematical model for simulating the fluid dynamics following puncture or full bore rupture of pressurised pipelines containing multi-component hydrocarbon mixtures. The same was then extended to simulate the depressurisation induced crack propagation as a secondary mode of failure following the puncture of such pipelines.

The following summarises the main conclusions reached in this work.

A state of the art review presented in chapter 2 showed that there is still significant scope for improving pipeline rupture models reported in the open literature.

For example, several of these models fail due to the assumption of perfect gas behaviour, or ignoring depressurisation induced wave propagation phenomena. Others employ incorrect boundary conditions, ignore frictional and heat transfer effects or treat the pipeline as a vessel discharging through an orifice when simulating puncture. Such shortcomings inevitability undermine the accuracy of the simulated data.

Based on the above review the Homogeneous Equilibrium (HE) assumption, in which the constituent fluid phases (i.e. liquid and vapour) are assumed to be at thermodynamic equilibrium and travel at the same velocity, is adopted in this work. This is because studies by Chen et al. (1993) have shown that the HE model performs better than the heterogeneous equilibrium model when compared with field data. The failure of other heterogeneous equilibrium models, such as PLAC and OLGA to successfully simulate field data together with the associated significant computational expense involved also make the HE assumption more attractive.

Of the those reviewed, the homogenous equilibrium based models by Mahgerefteh et al. (1999), Chen et al. (1995a, b) and Oke (2004) were found to be the most robust with the latter performing best in terms of accuracy and computational run time. Nonetheless, when simulating the complete blowdown of long pipelines (>100 km), the computational run times associated with all of these models remain rather long.

In chapter3, the equations describing mass, momentum and energy conservation were derived. Of important note was the formulation of the mass conservation equation in terms of pressure, enthalpy and flow velocity as opposed to the conventional pressure, density and velocity approach. The former formulation has been shown (Oke, 2004) to significantly reduce the computational run time and produce improved accuracy as compared to real data.

The various hydrodynamic and thermodynamic expressions for predicting important parameters including the speed of sound in two-phase media, fluid viscosity as well as fluid flow and phase dependent friction coefficient were presented. In addition, the mathematical expression for the quantity of heat transferred to the fluid from the ambient based on the lumped body approach was derived. This approach eliminated the need for assuming a constant overall heat transfer coefficient.

Furthermore, the steady state isothermal pressure drop model based on a real fluid was derived.

The chapter concluded by showing that the conservation equations derived are quasi-linear and hyperbolic in nature. The MOC was chosen to solve these, as it is well suited to handling the fast transients at the rupture plane.

In chapter 4, the compatibility equations obtained from the resolution of conservation equations were discretised using the Euler predictor-corrector technique. By assuming that the fluid properties varied linearly with distance, algebraic expressions for the fluid variables at the next time step along the pipeline length were obtained.

These expressions in conjunction with suitable boundary conditions and solution methodologies were applied to model the fluid dynamics following rupture/puncture in both single and pipeline networks. Of particular note are the following:

- The boundary conditions and solution methodology required in modelling outflow from pipeline puncture and pipeline networks were reformulated.
- A Double Sweep Quadratic Interpolation Scheme was developed capable of drastically reducing the computational run time by eliminating the need for frequent flash calculations.

In chapter 5 the full bore rupture and puncture models described in chapter 4 were validated. This exercise involved investigating the effects of the interpolation and the nested grid schemes on the computational run time and the simulation accuracy as compared to real data. In cases where real data were not available, a mass conservation index was used as a means of determining the numerical solution accuracy of the models developed. For the full bore rupture validations, tests P40 and P42 from the Isle of Grain experiments and the pressure data logged during the Piper Alpha tragedy were used. For the puncture simulation, the Isle of Grain test P45 data was employed for validation.

In general, good agreement between the field and simulated data were observed, with the finite discrepancies between them attributed to errors in VLE calculations, measurements uncertainties or errors, as well as the homogenous flow assumption.

The application of the interpolation scheme was shown to reduce the computational runtime by up to 80 % without loss in accuracy.

However the use of the nested grid system showed that reduction in the computational run time was confined to long pipelines containing gases. Surprisingly the nested grid system was found to be more computationally expensive as compared to the simple grid system for other cases such as short pipelines and two-phase fluids.

These investigations showed that discretisation errors (based on the mass conservation index) lower than 5 % can be obtained in reasonable time scales using interpolation coupled with the appropriate numerical discretisation scheme.

Rigorous modelling of the heat transfer across the pipeline and accounting for the presence of a single/two-phase interface during blowdown resulted in improved accuracy of the model predictions.

The limitations of the homogenous equilibrium model with respect to the blowdown of pipelines conveying flashing/ two-phase fluids discharging through a small orifice were highlighted. Under these conditions, the flow becomes highly stratified and hence non-homogenous. As such different outflow characteristics may be expected during top and bottom blowdown.

Different hypothetical case studies demonstrating the fluid transients following pipeline puncture and rupture of pipeline networks were presented and the results discussed.

The puncture simulations case study indicated that under the same operating conditions, a gas approaching a closed valve may produce a greater pressure surge than a two-phase flow due to its higher speed of sound.

In addition, the results showed that the puncture boundary conditions presented in this study gave better predictions in comparison to Oke et al.'s (2003) model. Likewise, the modified boundary condition and solution methodology in the network model addressed the errors associated with Oke's (2004) model.

Studies of the outflow characteristics in a horizontal pipeline network indicated that the depressurisation process during FBR is strongly influenced by the distance the depressurisation wave travels from the open to the closed end of the pipeline. For the same overall length, the more branches a pipeline may have, the faster the depressurisation. However, the flow rate through the open end does not seem to be a function of the number of couplers or branches.

Application of the network model to outflow in inclined pipelines highlighted the importance of taking into account the topography over which the pipeline is laid. The simulation results indicated that a multi-inclined pipeline cannot be modelled as a straight pipeline inclined at an 'equivalent' angle.

Chapter 6 was concerned with the development of a model for simulating low temperature induced fracture of pressurised pipelines. This work was initiated in the first instance due to the observed significant drop in the temperature of the escaping fluid following rupture as reported in several of the publications reviewed. This will inevitably affect the mechanical strength of the pipe wall in contact with the escaping fluid. As such the hazards associated with such low temperature effects needed to be quantitatively modelled.

The fracture propagation model presented in this study accounted for the important processes taking place during depressurisation including real fluid behaviour as well as the accompanying thermal and pressure stresses in the pipe wall.

Two cases involving defects in exposed and buried pipelines were simulated using the above model and the results discussed.

In the case of the exposed pipeline, a pictorial timeline presentation starting with the puncture of an isolated pressurised pipeline containing a multi-component hydrocarbon mixture was used to elucidate the sequence of events leading to its catastrophic failure. The expansion induced cooling of the escaping hydrocarbon resulted in a cold temperature front moving away from the puncture plane reaching temperatures well below the pipeline material's ductile to brittle transition temperature. This resulted in a significant drop in the fracture toughness thereby weakening the pipe wall.

The combination of low material fracture toughness and the accompanying pressure stresses in the pipe wall were found to ultimately undermine the pipeline's mechanical integrity by transforming the initial defect into a running fracture. Although a delay in isolation of the pipeline by maintaining the feed flow resulted in similar orders of magnitude drop in the pipe wall temperature and stresses as compared with the

isolated pipeline, such effects were found to be confined to close proximity of the defect plane. This has the effect of limiting the growth of the defect length to that below which is necessary to initiate a running fracture.

In the case of buried pipelines, the study showed the importance of accounting for thermal stresses in crack propagation analysis. These stresses are due to the significant temperature gradients around the crack, coupled with the crack's inability to contract freely. This in turn reduces the critical pressure required to initiate crack propagation. Hence, ignoring the thermal stresses may result in an overestimation of 'the safe working pressure'.

The results of this part of the study highlighted the importance of accounting for low temperature induced fracture as a potentially serious failure scenario when undertaking the safety assessment of pressurised pipelines. The model described can be used as an effective tool for mitigating such failures through better pipeline design, improved material selection and appropriate emergency action.

In summary, the results of this thesis demonstrate the importance of the correct solution methodology, boundary conditions, and domain discretisation on the overall performance of an MOC based real fluid numerical model. The development of an efficient and accurate interpolation scheme has facilitated the reduction in computational run times by up to 80 % without loss of accuracy. This permits the accurate simulation of pipeline outflow failure in practical computational run times using simple computational resources.

The susceptibility of pipelines to crack propagation as a result of the drop in fluid temperature following its depressurisation has been shown to be significant, and should be accounted for in pipeline safety analysis. This type of hazard is currently not considered in the pipeline industry. Although isolating a pipeline following a puncture will reduce the amount of inventory lost, it may increase the risk of crack propagation in pipelines. The risk becomes even more significant in the case of buried pipelines as the escaping fluid envelops the pipeline cooling it further, resulting in significant thermal stresses.

7.2 Suggestions for Future Work

Modelling other transient flow scenarios

The present model can easily be extended to deal with other transient fluid flow scenarios in pipeline networks such as the effect of operating in line valves and pumps during failure. In addition, in the case of the ignition of the released inventory, a useful extension would be to determine if the resulting thermal stress coupled with the mechanical weakening of the pipeline might lead to its secondary catastrophic failure during the discharge process. The model may also be usefully modified in order to account for fire impingement on the pipeline from a secondary source.

Modelling the dynamics of the above processes can help pipeline safety engineers to determine the likelihood of accident escalation.

Incorporation of heterogeneous equilibrium

Despite the success of the method of characteristics (MOC) based model in predicting outflow, the technique is based on a homogeneous equilibrium model in which the constituent phases are assumed to be in thermal and mechanical equilibrium with one another. In practice the general validity of such an assumption especially in the case of release from a small puncture for flashing liquids or release from inclined pipelines is in doubt due to the possibility of stratified flows.

A heterogeneous equilibrium model ascribing separate conservation equations to each constituent phase and accounting for cross-phase concentration changes is expected to address the above limitation.

Further reduction in computational run time

Although significant reductions in the computational run time have been achieved by the use of the interpolation scheme and appropriate grid discritisation, further reduction is still desirable. This is especially so in the case of release from complex

pipeline systems such as networks where the computational run time can still be significant (e.g. a few days).

Further reduction in the computational workload may be obtained by using an implicit scheme for modelling the fluid dynamics in regions far from the rupture plane where the Mach number is less than 0.5. This has the advantage that discretisation time steps are no longer restricted by the CFL stability criteria, thus allowing the use of larger time steps. In addition, by extending the characteristic lines into adjacent nodes, the maximum allowable time step may be further increased, while still satisfying the CFL stability criteria. Finally, the use of a dynamic grid system, in which the number of grids is continually updated based on the upstream flow conditions may be an efficient way of reducing the computational run time. This would allow the use of the optimum number of grid numbers thereby reducing computational run time and improving accuracy.

Abu-Hamdeh, N. H., A. I. Khdair, and R. C. Reeder, "A comparison of two methods used to evaluate thermal conductivity for some soils," *Int. J. of Heat and Mass Transfer*, **44 (5)**, 1073 (2001).

Amirat, A., A. Mohamed-Chateauneuf, and K. Chaoui, "Reliability assessment of underground pipelines under the combined effect of active corrosion and residual stress," *Int. J. Ves. and Piping,* **83 (2)**, 107 (2006).

American Petroleum Institute (API), Recommended Practice 579. *Fitness-for-Service.* 1st ed., American Petroleum Institute (2000).

APIGEC: Alberta Petroleum Industry Government Environmental Committee, "Hydrogen sulphide isopleth prediction-phase I: model sensitivity study," (1978).

APIGEC: Alberta Petroleum Industry Government Environmental Committee, "Hydrogen sulphide isopleth prediction-phase II: pipe burst study," (1979).

Andritsos, N., "Effect of pipe diameter and liquid viscosity on horizontal stratified flow (two-phase, wave generation)," Ph.D. Thesis, University of Illinois at Urbana-Champaign (1986).

Assael, M. J., J. P. M., Trusler, and T. F., Tsolakis, *Thermophysical properties of fluids: an introduction to their prediction*, Imperial College Press, London (1996).

Battara, V., C. Canuto, and A. Quarteroni, "A Chebyshev spectral method for gas transients in pipelines," *Computer Methods in Appl. Mech. Eng.*, **48**, 329 (1985).

Baum, M. R., "Axial rupture of large-diameter gas-pressurised steel pipes," *Int. J. Ves. and Piping,* **21 (1)**, 21 (1985).

Baum, M. R., and J. M. Butterfield, "Studies of the depressurization of gas pressurized pipes during rupture," *J. Mech. Eng. Sci.*, **21,** 253 (1979).

Bell, R. P., 'Isopleth Calculations for Ruptures in Sour Gas Pipelines', *Energy Processing/Canada*, 36, (1978).

Bergeron, L., *Waterhammer in hydraulics and wave surges in electricity*, J. Wiley, New York, (1961).

Bendiksen, K. H., I. Brandt, P. Fuchs, H. Linga, D. Malnes, and R. Moe, "Two-phase flow research at SINTEF and IFE. Some experimental results and a demonstration of the dynamic two-phase flow simulator OLGA." *The Offshore Northern Seas Conference*, Stavanger (1986).

Bendiksen, K. H., D. Malnes, R. Moe, and S. Nuland, "The dynamic two-fluid model OLGA: theory and applications," *SPE Production Eng.*, **6**, 171 (1991).

Boldy, A. P., "Analysis of waterhammer in hydroelectric installation," *UKSC Conference on Computer Simulation*, Bowness-on-Windermere (May 1975).

Bond, J., "IChemE accidents database," IChemE, Rugby, UK (2002).

Borek, D., *The practical use of fracture mechanics*, Kluwer Academic Publishers, The Netherlands, (1988).

Chawla, D. S., R. Bhate, and H. S. Kushwaha ,"Numerical simulation of crack growth and arrest in a vessel under pressure thermal shock," *Int. J. Ves. and Piping,* **77 (5)**, 261 (2000).

Chapuliot, S., M. H. Lacire, S. Marie, and M. Nédélec, "Thermomechanical analysis of thermal shock fracture in the brittle/ductile transition zone. Part I: description of tests," *Engng. Fract. Mech.,* **72**, 661 (2005).

Chen, J. R., S. M. Richardson, and G. Saville, "Numerical simulation of full-bore ruptures of pipelines containing perfect gases," *Trans. Inst. Chem. Eng. Part B*, **70**, 59 (1992).

Chen, J. R., "Modelling of transient flow in pipeline blowdown problems," PhD Thesis, University of London, (1993).

Chen, J. R., S. M. Richardson, and G. Saville, "A simplified numerical method for transient two-phase pipe flow," *Trans IChemE*, **71A**, 304 (1993).

Chen, J. R., S. M. Richardson, and G. Saville, "Modelling of two-phase blowdown from pipelines – I. A hyperbolic model based on variational principles," *Chem. Eng. Sci.*, **50**, 695 (1995a).

Chen, J. R., S. M. Richardson, and G. Saville, "Modelling of two-phase blowdown from pipelines – II. A simplified numerical method for multi-component mixtures," *Chem. Eng. Sci.*, **50**, 2173 (1995b).

Chen, N. H., "An explicit equation for friction factor in pipes," *Ind. Eng. Chem. Fundam.*, **18**, No. 3, 296 (1979).

Churchill, S. W., and M. Bernstein, "A correlating equation for forced convection from gases and liquids to a circular cylinder in cross-flow," *J. Heat Transfer*, **99**, 300 (1977).

Churchill, S. W., and H. H. S. Chu, "Correlating equations for laminar and turbulent free convection from a horizontal cylinder," *Int. J. Heat Mass Transfer*, **18**, 1049 (1975).

Colebrook, C. F., "Turbulent flow in pipes with particular reference to transition region between the smooth and rough pipe laws," *J. Inst. Civil Eng.*, **11**,133, (1939).

Courant, R., K. O. Friedrichs, and H. Lewy, "Uber die partiellen differentialgleichungen der mathematischen, physik," *Mathematische Annalen*, **100**, 32 (1926).

Crowl, D. A., and J. F. Louvar, *Chemical process safety: fundamentals with application*, Prentice-Hall, New Jersey (1990).

Cullen, W. D., "The public inquiry into the Piper Alpha disaster," Dept. of Energy, HMSO, (1990).

Cunliffe, R. S., "Condensate flow in a wet-gas line can be predicted," *Oil and Gas Journal*, Oct 30 (1978).

Daubert, T. E., and R. P. Danner, "Tables of physical and thermodynamic properties of pure compounds," DIPPR Project 801 Data Compilation (1990).

Ely, J. F., and H. J. M. Hanley, "Prediction of transport properties. 1. Viscosity of fluids and mixtures," *Ind. Eng. Chem. Fundam.*, **20**, 323 (1981).

Ely, J. F., and H. J. M. Hanley, "Prediction of transport properties. 2. Thermal conductivity of pure fluids and mixtures," *Ind. Eng. Chem. Fundam.*, **22**, 90 (1983).

Environmental Defence, News Release, 3 Feb 1999, New York.

Erdogan, F., and Kibbler, J. J., "Cylindrical and Spherical Shells with Cracks," *Int. Journal of Fracture Mechanics*, **5**, 229 (1969).

Faille, I., and E. Heintze, "A rough finite volume scheme for modeling two-phase flow in a pipeline," *Comput. Fluids*, **28,** (1999).

Fairuzov, Y. V., "Blowdown of pipelines carrying flashing liquids," *AIChE J.*, **44,** No. 5, 245 (1998).

Fannelop, T. K., and I. L. Ryhming, "Massive release of gas from long pipelines," *J. Energy*, **6**, 132 (1982).

Flatt, R., "A singly-iterative second order method of characteristics for unsteady compressible one-dimensional flows," *Comm. in Applied Num. Meth.*, **1**, 269 (1985a).

Flatt, R., "On the application of numerical methods of fluid mechanics to the dynamics of real gases," *Forschung im Ingenieurwesen*, **51(2)**, 41, in German (English translation: British Gas Translation No. T07823/BG/LRS/LRST817/86), (1985b).

Flatt, R., "Unsteady compressible flow in long pipelines following a rupture," *Int. J. Num. Meth. Fluids*, **6**, 83 (1986).

Flatt, R., "Unified approach of calculation of mono-phase and bi-phase/homogeneous flows of condensable pure fluids," *Revue Entropie*, **149**, 48 (French), (1989).

Fletcher, S., "US senate ready to act on pipeline safety," *Oil & Gas Journal*, **99.6**, 58 (February 2001a).

Folias, E. S., "An Axial Crack in a Pressurised Cylindrical Shell," *Int. Journal of Fracture Mechanics*, **1**, 104 (1965).

Gato, L. M. C., and J. C. C. Henriques, "Dynamic behaviour of high-pressure natural-gas flow in pipelines," *Int. Journal of Heat and fluid flow*, **26 (5)**, 817 (2005).

Griffith, A.A., "The phenomenon of Rupture and Flow in Solids," *Phil. Trans. Roy. Soc.*, London, Series A, **(221)**, (1920).

Gnielinski, V., "New equations for heat and mass transfer in turbulent pipe and channel flow," *Int. Chem. Eng.*, **16**, 359 (1976).

Hall, A. R. W., E. R. Butcher, and C. E. Teh, "Transient simulation of two-phase hydrocarbon flows in pipelines," *Proceedings of the European Two-Phase Flow Group Meeting*, Hannover (1993).

Haque, M. A., S. M. Richardson, and G. Saville, "Blowdown of pressure vessels. I. Computer model," *Trans IChemE Part B: Process Safety Environmental Protection*, **70 (BI)**, 1 (1992a).

Haque, M. A., S. M. Richardson, G. Saville, G. Chamberlain, and L. Shirvill, "Blowdown of pressure vessels. II. Experimental validation of computer model and case studies," *Trans IChemE Part B: Process Safety Environmental Protection*, **70 (BI)**, 10 (1992b).

Harrison, J. D., "The brittle fracture story" *Engineering applications of fracture analysis*, Vol I, Garrett, G.G., and D.L. Marriott, *eds.*, *Proceedings of the first national conference on fracture*, South Africa (1979).

HMSO., *A guide to pipeline safety regulations 1996*, Health and Safety Executive, Bootle, UK (1996).

Hoffman, J. D., *Numerical methods for engineers and scientists*, McGraw-Hill, New York (1992).

Horsley, D. J., "Background to the use of CTOA for Prediction of Dynamic Fracture Arrest in Pipelines," *Engineering Fracture Mechanics* **70**, 547 (2002).

Hyprotech, *PROFES-Transient user manual*, Aspentech, Houston (2001).

Incropera, F. P., and D. P. De Witt, *Fundamentals of heat and mass transfer*, 4th Ed., John Wiley and Sons, New York (1996).

Irwin G. R., "Analysis of Stresses and Strains Near the End of a Crack Transversing a Plate," *Transactions, ASME, Journal of Applied Mathematics*, **24** , 361 (1957).

Ives, K. D., A. K. Shoemaker, and R. F. McCartney, "Deformation During a Running Shear Fracture in Line Pipe," *ASME J. of Eng. Materials and Tech.*, **96,** (1974).

Jawad, M., and Faar, J., *Structural Analysis and Design of Process Equipments*, John Wiley and Sons, New York (1983).

Jones, D. G., and D. W. Gough, "Rich gas decompression behaviour in pipelines," *AGA-EPRG Pipeline Research Seminar IV*, Duisburg, British Gas, Report No. ERSE 293, (1981).

Ke, S. L., and Ti, H. C., "Transient analysis of isothermal gas flow in pipeline network," *Chemical Engineering Journal*, **76**, 169, (2000).

Kimambo, C. Z., and A. Thorley, "Computer modelling of transients ruptured high-pressure natural gas pipelines: a review of experimental and numerical studies," *IMechE*, C502/003, 55 (1995).

Kunsch, J. P., K. Sjoen, and T.K. Fannelop, "Simulation of unsteady flow, massive release and blowdown of long high-pressure pipelines," *Int. Gas Conf.*, Cannes, France (1995).

Lang, E., "Gas flow in pipelines following a rupture computed by a spectral method," *J. Appl. Math. and Physics (ZAMP)*, **42**, 183 (1991).

Lang, E., and T. K. Fannelop, "Efficient computation of the pipeline break problem," *3rd Symp. on Fluid-Transient in Fluid Structure Interaction*, **56**, 115 (1987).

Lewis P. R., and G. W., Weidmann, "Catastrophic failure of a polypropylene tank Part i: primary investigation," *Engng Fract Mech.*, **6 (4),** 197 (1997).

Lister, M., "The numerical solution of hyperbolic partial differential equations by the method of characteristics," *Numerical methods for digital computers*, Ralston, A., and H. S. Wilf, eds., John Wiley and Sons, New York (1960).

Lydell, B. O. Y., "Pipe failure probability-the Thomas paper revisited," *Reliability Engineering and System Safety*, **68**, 207 (2000).

Mahgerefteh, H., P. Saha, and I. G. Economou, "A study of the dynamic response of emergency shutdown valves following full-bore rupture of gas pipelines," *Trans. Inst. Chem. Eng., Part B*, **75**, 201 (1997).

Mahgerefteh, H., P. Saha, and I. G. Economou, "Fast numerical simulation for full-bore rupture of pressurized pipelines," *AIChE J.*, **45,** No. 6, 1191 (1999).

Mahgerefteh, H., P. Saha, and I. G. Economou, "Modelling fluid phase transition effects on dynamic behaviour of ESDV," *AIChE J.*, **46**, No. 5, 997 (2000).

Mahgerefteh, H., and S. M. A., Wong, "A numerical blowdown simulation incorporating cubic equations of state," *Computers in Chemical Engineering,* **23(9)**, 1309 (1999).

Maxey, W. A., "Fracture Initiation, Propagation and Arrests," *Fifth Symposium on Line Pipe Research, American Gas Association* (1974).

Maxey, W. A., Kiefner, J. F., Eiber, R. J., "Ductile Fracture Propagation Resistance of Rising Shelf controlled Steels", *ASM Symposium on What does Charpy Energy Really Mean*? (1975).

Montiel, H., J. A. Vilchez, J. Arnaldos, and J. Casal, "Pipeline rupture," *J. Hazard. Mater.*, **51**, 77 (1996).

Montiel, H., J. A. Vilchez, J. Casal, and J. Arnaldos, "Mathematical modelling of accidental gas releases," *J. Hazard. Mater.*, **59**, 211 (1998).

Myers, G. E., *Analytical methods in conduction heat transfer*, McGraw-Hill, New York, 10 (1971).

Nakamura, S., Berger, M. A., and Spencer, A. C., "One Dimensional Implicit Characteristic Method for Compressible Two-Phase Coolant Flow," *Proc. Of the Conf. On Comp. Methods in Nuclear Eng.*, NYIS conf-750413, American Nuc. Soc., (April 1975).

Newman, J. C., " An Improved Method of Collocation for the Stress Analysis of Cracked Plates with Various Shape Boundaries," NASA Technical Note, NASA TN D-6376. (1971).

Offshore Technology Report, OTO 98 162, *Subsea hydrocarbon pipeline failure: survey of available prediction schemes*, HSE, (1998).

Oke, A., H. Mahgerefteh, I. Economou, and Y. Rykov, "A transient outflow model for pipeline puncture," *Chem. Eng. Sci.*, **58(20)**, 4591 (2003).

Oke, A., "An efficient numerical simulation for modelling outflow following rupture or puncture of pressurised pipeline networks," PhD Thesis, University College London (2004).

Olorunmaiye, J. A., and N. E. Imide, "Computation of natural gas pipeline rupture problems using the method of characteristics," *J. Hazard. Mater.*, **34**, 81 (1993).

Ouyang, L., and K. Aziz, "Steady-state gas flow in pipes," *J. Pet. Sci. Eng.*, **14**, 137 (1996).

Ozisik, M. N., *Heat conduction*, John Wiley and Sons, New York, (1980).

Parmakian, J., *Water Hammer Analysis*, Dover, New York, (1963).

Peng, D. Y., and D. B. Robinson, "A new two-constant equation of state," *Ind. Eng. Chem. Fund.*, **15**, 59 (1976).

Perry, R. H., and D. W. Green, *Perry's chemical engineers' handbook*, 7th Ed., McGraw Hill, London (1997).

Peterson, C. E., V. K. Chexal, and T. B. Clements, "Analysis of a hot-leg small break LOCA in a three loop Westinghouse PWR plant," *Nuc. Tech.*, **70,** No.1, 104 (1985).

Philbin, M. T., and A. H. Govan, "Pipeline analysis code," UKAEA Report AEA-APS-0031 (1990).

Philbin, M. T., "The simulation of transient phenomena in multiphase production systems," AEA Harwell Report AEA-APS-0177 (1991).

Picard, D. J., and P. R. Bishnoi, "Calculation of the thermodynamic sound velocity in two-phase multi-component fluids," *Int. J. Multiphase Flow*, **13(3)**, 295 (1987).

Picard, D. J., and P. R. Bishnoi, "The importance of real-fluid behaviour and non-isentropic effects in modelling compression characteristics of pipeline fluids for application in ductile fracture propagation analysis," *Can. J. Chem. Eng.*, **66**, 3 (1988).

Picard, D. J., and P. R. Bishnoi, "The importance of real-fluid behaviour in predicting release rates resulting from high pressure sour-gas pipeline ruptures," *Can. J. Chem. Eng.*, **67**, 3 (1989).

Prasad, P., and R. Ravindran, *Partial differential equations*, Wiley Eastern Limited, New Delhi (1985).

Press, W. H., S. A. Teukolsky, W. T. Vetterling, and B. P. Flannery, *Numerical recipes in FORTRAN 77: the art of scientific computing*, 2nd ed., Cambridge University Press, Cambridge, U.K. (1992).

Rice, J. R., "A Path Independent Integral and the Approximate Analysis of Strain Concentration by Notches and Cracks," *ASME J. Appl. Mech.*, **35**, 379 (1968).

Rich, G. R., *Hydraulic transients*, Dover, New York, (1963).

Richardson, S. M., and G. Saville, "Blowdown of pipelines," *Society of Petroleum Engineers Europe 91*, paper SPE 23070, Aberdeen, UK, 369 (1991).

Richardson, S. M., and G. Saville, "Isle of Grain pipeline depressurisation tests," HSE OTH 94441, HSE Books, HSE, Bootle, U.K. (1996a).

Richardson, S. M., and G. Saville, "Blowdown of LPG pipelines," *Trans. IChemE*, **74B**, 236 (1996b).

Richardson, S. M., G. Saville, A. Fisher, A. J. Meredith, and M. J. Dix, "Experimental Determination of Two-Phase Flow Rates of Hydrocarbons Through Restrictions," *Trans IChemE, Part B: Process Safety and Environmental Protection*, **84 (B1)**, 40, (2006).

Rinebolt, J. A., and Harris, W. J., "Effect of Alloying Elements on Notch Toughness of Pearlitic Steels," *Transaction of the American Society of Metals,* **43** (1951) .

Roberts, S. G., "Multiscale Phenomena in Plasticity: From Experiments to Phenomenology," *Modelling and Materials Engineering*, 8 Sep.1999 - 19sep 1999, Ouranopolis, Greece (1999).

Rohsenow, W. M., J. P. Hartnett, and Y. I. Cho, eds., *Handbook of heat transfer*, 3rd ed., McGraw-Hill, New York (1998).

Saha, P., "Modelling the dynamic response of emergency shutdown valves following full-bore rupture of long pipelines," PhD Thesis, University College London (1997).

Sandsträm,R., P. Langenberg and H. Sieurin, "Analysis of the brittle fracture avoidance model for pressure vessels in European standard," *Int.J. Ves. and Piping,* **82 (11)**, 872 (2005).

Saville, G., and R. Szczepanski, "Methane-based equations of states for a corresponding states reference substance," *Chem. Eng. Sci.,* **37**, 719 (1982).

Sens, M., P. Jouve, and R. Pelletier, "Detection of a break in a gas line," *11th International Gas Conference*, Moscow, Paper No. IGU/C37-70, in French, (English Translation: British Gas, Translation No. BG. TRANS 4910) (1970).

Serghides, T. K., "Estimate friction factor accurately," *Chem. Eng.*, **91**, 63 (1984).

Shoup, G., J. J. Xiao, and J. O. Romma, "Multiphase pipeline blowdown simulation and comparison to field data," *1st North American Conference on Multiphase*

Technology, BHR Group Conference Series No. 31, Banff, Canada, **3**, June 10-11 (1998).

Singh, P. K., K. K. Vaze, V. Bhasin, H. S. Kushwaha, P. Gandhi, and D. S. Ramachandra Murthy, "Crack initiation and growth behaviour of circumferentially cracked pipes under cyclic and monotonic loading," *Int. J. Ves. and Piping,* **80 (9)**, 629 (2003).

Soave, G., "Equilibrium constants from a modified Redlich-Kwong equation of state," *Chem. Eng. Sci.*, **27**, 1197 (1972).

Steiner, D., and J. Taborek, "Flow boiling heat transfer in vertical tubes correlated by an asymptotic method," *Heat Transfer Eng.*, **13(2)**, 43 (1992).

Stroud, K. A., *Engineering mathematics: programmes and problems*, 4th ed., Macmillan, London (1995).

Swaffield, J. A., "Column separation in an aircraft fuel system," *Procs. 1st Int. Conf. Pressure Surges*, Canterbury, England, Paper C2, BHRA Fluid Eng., 13 (Sept 1972).

Swaffield, J. A., and A. P. Boldy, *Pressure surge in pipe and duct systems*, Ashgate Publishing Limited, Vermont, USA, (1993).

Tada, H., Paris, P., and Irwin, G., *The Stress Analysis of Cracks Handbook*, 3rd ed. ASME New York. (2000).

Tam, V. H. Y., and L. T. Cowley, "Consequences of pressurised LPG releases: the Isle of Grain full scale experiments," *Proceedings of GASTECH 88 (13th Int. LNG/LPG Conf.)*, Kuala Lumpur, 2 (1988).

Tao, W. Q., and Ti, H. C., "Transient analysis of gas pipeline network," *Chemical Engineering Journal*, **69**, 47 (1998).

Techo, R., R. R. Tickner, and R. E. James, "An accurate equation for the computation of the friction factor for smooth pipes from the Reynolds number," *J. Appl. Mech.*, **32**, 443 (1965).

Tiley, C. H., "Pressure transient in a ruptured gas pipeline with friction and thermal effects included," PhD Thesis, City University, London (1989).

Timoshenko S. P., and J. N. Goodier, *Theory of Elasticity*, McGraw-Hill, New York, (1987).

Tokiyoshi, T., F. Kawashima, T. Igari and H. Kino, "Crack propagation life prediction of a perforated plate under thermal fatigue," *Int.J. Ves and Piping*, **78 (11-12)**, 837 (2001).

True, W. R., "Regulatory actions loom for US pipelines in 2001," *Oil & Gas Journal*, **99.1**, 70 (January 2001).

Tsu T. R., G. G. Chen, Z. L. Gong,, and N. S. Sun, "On thermofracture behaviour of leaking thin-wall pipes," *Int. J. Ves. and Piping*, **24 (4)**, 269 (1986).

Uhl, A. E., K. B. Bischoff, R. F. Bukacek, P. V. Elllington, D. V. Kniebes, W. R. Staats, D. A. Worcester, and the NB-13 Committee, "Steady flow in gas pipelines," *Institute of Gas Technology (IGT) Report No. 10*, Am. Gas Assoc. Inc., New York (July 1965).

U.S. Department of Transport, Code of Federation Regulations (CFR) Title 49D, Part 195, *Transportation of hazardous liquids by pipeline*, Accident Report Data Base.3 (1982 – 1997).

Vahedi, S., "Modelling the effects of inclination and pipeline enlargement on outflow following pipeline rupture," PhD Thesis, University College London (2003).

Walas, S. M., *Phase equilibrium in chemical engineering*, Butterworth Publisher, Boston, (1987).

Woodward, J. L., and K. S. Mudan, "Liquid and gas discharge rates through holes in process vessels," *J. Loss Prev. Process Ind.*, **4**, 161 (1991).

Wylie, E. B., and V. L. Streeter, *Fluid transients*, McGraw-Hill Inc., New York (1978).

Zigrang, D. J., and N. D. Sylvester, "Explicit approximations to the solution of Colebrook's friction factor equation," *AIChE J.*, **28**, 514 (1982).

Zucrow, M. J., and J. D. Hoffman, *Gas dynamics,* volume I and II, Wiley, New York, 297 (1976).